TESI DOCTORAL

Modeling Semiconductor Ring Lasers

Antonio Pérez-Serrano

Tesi presentada al Programa oficial de doctorat en Física de la Universitat de les Illes Balears, per optar al grau de Doctor en Física.

Palma, Setembre 2011

Alessandro Scirè	Salvador Balle	Antonio Pérez Serrano
Director	Co-director	Doctorand

Instituto de Física Interdisciplinar y Sistemas Complejos, IFISC (UIB-CSIC)
Departament de Física, Universitat de les Illes Balears, UIB.

Modeling Semiconductor Ring Lasers

Antonio Pérez-Serrano
Instituto de Física Interdisciplinar y Sistemas Complejos
IFISC (UIB-CSIC)
antonio@ifisc.uib-csic.es

PhD Thesis
Director: Alessandro Scirè
Co-director: Salvador Balle

Aquest document s'ha creat amb LaTeX 2_ε.

Resum

La present tesi tracta sobre el modelatge de làsers d'anell de semiconductor centrant-se en la dinàmica no lineal, la propietats modals i l'estabilitat dinàmica que mostren aquests dispositius.

Per a aquesta fi s'usen diferents models basats en una descripció semiclàssica. En aquesta aproximació, la radiació electromagnètica es descriu mitjançant les equacions de Maxwell, mentre que la interacció radiació-matèria es descriu per mitjà de les equacions de Bloch, provinents de la física quàntica. Aquests models es poden dividir en dos grans blocs: (1) els models anomenats d'equacions de balanç (*rate equations*), basats en equacions diferencials ordinàries que no tenen en compte els efectes espacials i que històricament han tingut molt èxit en oferir bons resultats en ser comparats amb els experiments; i (2) els models basats en equacions diferencials parcials que tenen en compte els efectes espacials. En el cas tractat en aquesta tesi, on es té en compte la dimensió espacial longitudinal, aquests models d'ones viatgeres (*traveling waves*) presenten més complicacions des del punt de vista de l'anàlisi matemàtica i el tractament numèric que les equacions de balanç, no obstant això presenten avantatges com la descripció de forma natural el comportament multimode i el poder ser aplicats a diferents tipus de làsers després de mínimes modificacions. De fet, aquest segon bloc de models inclou el primer sota aproximacions o límits on la dependència espacial pot ser simplificada. No obstant això, últimament amb l'ús de nous materials i noves cavitats òptiques, aquests límits i aproximacions deixen de ser vàlids i es requereix una descripció física més detallada. Aquest és el cas dels làsers d'anell de semiconductor.

Els làsers d'anell són dispositius que mostren una gran riquesa de comportaments dinàmics. Aquesta riquesa es deu a la presència de dos camps elèctrics que es propaguen en sentits oposats dins de la cavitat òptica, i a la interacció entre ells a través del medi actiu, que és el responsable de proporcionar el guany dels camps. D'entre la varietat de comportaments dinàmics, el règim d'emissió unidireccional biestable ha acaparat l'interès de la comunitat científica en l'última dècada pel seu ús en memòries òptiques. En aquest règim l'emissió és principalment en una direcció en un règim biestable, és a dir, el dispositiu és sensible a estímuls que poden fer canviar el sentit de l'emissió. Aquest interès també ha estat motivat pel perfeccionament de les tècniques de litografia que han fet possible l'aparició dels làsers d'anell fets de material semiconductor, i que també han permès la integració de diferents dispositius en un mateix xip per realitzar diferents funcions analògiques o digitals en el domini òptic. Aquestes noves aplicacions motiven la creació de models més complexos que els existents, per servir de guia en el disseny de dispositius optimitzats per a situacions específiques.

En el capítol II d'aquesta tesi, primer s'introdueixen des d'un enfocament fenomenològic a la dinàmica de làsers els anomenats models de fotons. Aquests models simples ens permeten introduir els conceptes de dinàmica no lineal i les equacions de balanç. A continuació es tracta la descripció de la llum dins de la teoria de l'electrodinàmica clàssica, i la descripció de la matèria i la seva interacció amb la llum per mitjà de la física quàntica. Trobarem una col·lecció d'equacions generals en el domini espai-temporal que ens permetran descriure diferents tipus de làsers, i que conformen el nostre model d'ones viatgeres. Finalment, a partir del model d'ones viatgeres es deriven els models d'equacions de balanç per als casos de làsers d'anell unidireccionals i bidireccionals.

En el capítol III es mostren els estudis basats en models d'equacions de balanç. El primer estudi tracta sobre l'aplicació dels làsers d'anell de semiconductor al mesurament de rotacions inercials, és a dir, el seu ús com a giroscopi. Aquest estudi teòric

mostra una nova tècnica per al mesurament de rotacions en la anomenada *locking band*, on els dos camps contrapropagants tenen la mateixa freqüència i per tant no hi ha freqüència de batut induda per la rotació. També es discuteix com aquesta tècnica pot ser exportada a altres tipus de làsers. El segon estudi que es tracta des del modelatge amb equacions de balanç és l'efecte del soroll d'emissió espontània en la dinàmica. Aquest efecte es tradueix en l'aparició d'un pic en l'espectre que pot ser usat per a una millor caracterització dels paràmetres d'aquests dispositius.

A més d'aquests estudis basats en equacions de balanç, en el capítol IV es mostren estudis basats en el model d'ones viatgeres per al cas d'un medi format per àtoms de dos nivells. Malgrat la simplicitat d'aquesta descripció del medi, aquests estudis serveixen com a primera aproximació al modelatge del medi semiconductor i són bones aproximacions als làsers de gas i estat sòlid. En aquest capítol es presenten eines per a l'obtenció de les solucions monocromàtiques i la realització de l'anàlisi d'estabilitat lineal d'aquest model. Aquesta eines s'utilitzen per estudiar l'estabilitat de la solucions monocromàtiques en aquests làsers i la coexistència de diferents solucions estables, d'acord amb evidències experimentals. Aquests resultats mostren que la longitud d'ona d'emissió d'aquests làsers pot ser seleccionada per injecció d'un camp extern.

La dinàmica multimode també s'ha estudiat amb el model d'ones viatgeres per a un medi format per àtoms de dos nivells. Aquest estudi ens mostra una gran varietat de comportaments pel que fa al cas monomode, entre ells cal destacar l'emissió bicromàtica, on els dos camps elèctrics contrapropagants emeten en diferent longitud d'ona, i el comportament pulsat o *mode-locking* unidireccional que apareix per a grans amplàries de la corba de guany.

El cas del mig semiconductor es tracta en el capítol V. En ell s'han estudiat de forma experimental i teòrica les propietats modals de dispositius reals formats per una cavitat d'anell i guies d'ona per a la injecció i extracció de la llum. Els resultats mostren que l'impacte de la cavitat composta és notable en les modes de cavitat freda del làser. A més, l'estructura modal explica els salts en longitud d'ona que ocorren en connexió al canvi de direcció d'emissió en augmentar el bombament quan el làser està encès.

En el capítol V també es construeix un model d'ones viatgeres per a pous quàntics al que se li apliquen les eines desenvolupades en el capítol IV per a la simulació i l'anàlisi d'estabilitat lineal del sistema. Finalment, es mostra un estudi experimental i teòric sobre un nou tipus de làser basat en el làser d'anell de semiconductor, el làser de caragol o *snail laser*. En ell es demostra per primera vegada la seva fabricació i la seva caracterització, que des del punt de vista teòric es realitza per mitjà del model d'ona viatgeres i el formalisme de matriu de *scattering* per obtenir la seva estructura modal.

Resumen

La presente tesis trata sobre el modelado de láseres de anillo de semiconductor centrándose en la dinámica no lineal, la propiedades modales y la estabilidad dinámica que muestran estos dispositivos. Para este fin se usan distintos modelos basados en una descripción semiclásica. En esta aproximación, la radiación electromagnética se describe mediante las ecuaciones de Maxwell, mientras que la interacción radiación-materia se describe por medio de las ecuaciones de Bloch, provenientes de la física cuántica. Estos modelos se pueden dividir en dos bloques: (1) Ecuaciones de balance (*rate equations*), basados en ecuaciones diferenciales ordinarias que no tienen en cuenta los efectos espaciales y que históricamente han tenido mucho éxito al ofrecer buenos resultados al ser comparados con los experimentos; y (2) los modelos basados en ecuaciones diferenciales con derivadas parciales que tienen en cuentan los efectos espaciales. En el caso tratado en esta tesis, donde se tiene en cuenta la dimensión espacial longitudinal, estos modelos de ondas viajeras (*traveling waves*) presentan más complicaciones desde el punto de vista del análisis matemático y el tratamiento numérico que las ecuaciones de balance, no obstante presentan ventajas como la descripción de forma natural del comportamiento multimodo y el poder ser aplicados a diferentes tipos de láseres tras mínimas modificaciones. De hecho, este segundo bloque de modelos incluye el primero bajo aproximaciones o límites donde la dependencia espacial puede ser simplificada. Sin embargo, últimamente con el uso de nuevos materiales y nuevas cavidades ópticas, estos límites y aproximaciones dejan de ser válidos y se requiere una descripción física más detallada. Este es el caso de los láseres de anillo de semiconductor.

Los láseres de anillo son dispositivos que muestran una gran riqueza de comportamientos dinámicos. Esta riqueza se debe al efecto que tiene la geometría de la cavidad óptica en los dos campos eléctricos que se propagan en sentidos opuestos dentro de la cavidad, y a la interacción entre estos campos a través del medio activo, que es el responsable de proporcionar la ganancia a los campos. De entre la variedad de comportamientos dinámicos, el régimen de emisión unidireccional biestable ha acaparado el interés de la comunidad científica en la última década por su uso en memorias ópticas. En este régimen la emisión es principalmente en una dirección en un régimen biestable, es decir, el dispositivo es sensible a estímulos que pueden hacer cambiar el sentido de la emisión. Este interés también ha sido motivado por el perfeccionamiento de las técnicas de litografía que han hecho posible la aparición de los láseres de anillo hechos de material semiconductor, y que también han permitido la integración de distintos dispositivos en un mismo chip para realizar distintas funciones analógicas o digitales en el dominio óptico. Estas nuevas aplicaciones motivan la creación de modelos más complejos que los existentes, para servir de guía en el diseño de dispositivos optimizados para situaciones específicas.

En el capítulo II de esta tesis, primero se introducen desde un enfoque fenomenológico a la dinámica de láseres los llamados modelos de fotones. Estos modelos simples permiten introducir los conceptos de dinámica no lineal y las ecuaciones de balance. A continuación se trata la descripción de la luz dentro de la teoría de la electrodinámica clásica, y la descripción de la materia y su interacción con la luz por medio de la física cuántica. Se encontrarán una colección de ecuaciones generales en el dominio espacio-temporal que permitirán describir diferentes tipos de láseres, y que conforman nuestro modelo de ondas viajeras. Finalmente, a partir del modelo de ondas viajeras se derivan los modelos de ecuaciones de balance para los casos de láseres de anillo unidireccionales y bidireccionales.

En el capítulo III se muestran los estudios basados en modelos de ecuaciones de

balance. El primer estudio trata sobre la aplicación de los láseres de anillo de semiconductor a la medición de rotaciones inerciales, es decir, su uso como giroscopio. Este estudio teórico muestra una nueva técnica para la medición de rotaciones en la llamada *locking band*, dónde los dos campos contrapropagantes tienen la misma frecuencia y por lo tanto no hay frecuencia de batido inducida por la rotación. También se discute como esta técnica puede ser exportada a otros tipos de láseres. El segundo estudio que se trata desde el modelado con ecuaciones de balance es el efecto del ruido de emisión espontánea en la dinámica. Dicho efecto se traduce en la aparición de una resonancia en el espectro de radiofrecuencia que puede ser usado para una mejor caracterización de los parámetros de estos dispositivos.

Además de estos estudios basados en ecuaciones de balance, en el capítulo IV se muestran estudios basados en el modelo de ondas viajeras para el caso de un medio formado por átomos de dos niveles. Pese a la simplicidad de esta descripción del medio, estos estudios sirven como primera aproximación al modelado del medio semiconductor y son buenas aproximaciones a los láseres de gas y estado sólido. En este capítulo se presentan herramientas para la obtención de las soluciones monocromáticas y la realización del análisis de estabilidad lineal de este modelo. Esta herramientas se utilizan para estudiar la estabilidad de la soluciones monocromáticas en estos láseres y la coexistencia de diferentes soluciones estables, de acuerdo con evidencias experimentales. Estos resultados muestran que la longitud de onda de emisión de estos láseres puede ser seleccionada por inyección de un campo externo.

La dinámica multimodo también se ha estudiado con el modelo de ondas viajeras para un medio formado por átomos de dos niveles. Este estudio muestra una gran variedad de comportamientos con respecto al caso monomodo, entre ellos cabe destacar la emisión bicromática, dónde los dos campos eléctricos contrapropagantes emiten en distinta longitud de onda, y el comportamiento pulsado o *mode-locking* unidireccional que aparece para grandes anchuras de la curva de ganancia.

El caso del medio semiconductor se trata en el capítulo V. En él se estudian de forma experimental y teórica las propiedades modales de dispositivos reales formados por una cavidad de anillo acoplada a guías de onda para la inyección y extracción de la luz. Los resultados muestran que el impacto de la cavidad compuesta es notable en los modos de cavidad fría del láser. Además, la estructura modal explica los saltos en longitud de onda que ocurren en conexión al cambio de dirección de emisión al aumentar el bombeo cuando el láser está encendido.

En el capítulo V también se construye un modelo de ondas viajeras para pozos cuánticos al que se le aplicarán las herramientas desarrolladas en el capítulo IV para la simulación y el análisis de estabilidad lineal del sistema. Finalmente, se muestra un estudio experimental y teórico sobre un nuevo tipo de láser basado en el láser de anillo de semiconductor, el láser de caracol o *snail laser*. En él se demuestra por primera vez su fabricación y su caracterización, que desde el punto de vista teórico se realiza por medio del modelo de onda viajeras y el formalismo de matriz de *scattering* para obtener su estructura modal.

Agradecimientos

En primer lugar me gustaría agradecer la financiación económica que ha hecho posible esta tesis. Durante los tres primeros años la financiación corrió a cargo del proyecto europeo "IOLOS: Integrated Optical Logic and Memory Using Ultrafast Micro-ring Biestable Semiconductor Lasers" (IST-2005-034743). En los últimos años la financiación ha sido en forma de beca FPI de la Conselleria d'Economia, Hisenda i Innovació del Govern de les Illes Balears. Muchas gracias por haber confiado en mí y haberme permitido llevar a cabo esta investigación.

En segundo lugar quiero agradecer a Alessandro Scirè la oportunidad que me brindó proponiéndome trabajar en el proyecto IOLOS e introduciéndome en el mundo de la investigación científica. Tambíen quiero agradecerle sus enseñanzas, la libertad que me ha dado durante estos años y la confianza que ha depositado en mí. Gracias por todo.

En tercer lloc, vull agrair a Salvador Balle la seva implicació des de un principi per que aquesta tesis arribés a bon port. També li haig d'agrair que m'hagi encomanat la seva passió per la ciència i la seva bona forma de fer les coses tant a un nivell científic i acadèmic com a un nivell humà. A més estic content d'haver compartit bons moments amb en Salvador, com per exemple quan vàrem recórrer el sud d'Itàlia en cotxe entre converses filosòfiques i bon menjar italià o parlant de física i prenent cerveses a Munich amb els col·laboradors del projecte IOLOS. Moltes gràcies.

En cuarto lugar, quiero agradecer a Julien Javaloyes que haya compartido sus conocimientos conmigo y que hayamos logrado formar un buen grupo de trabajo. Sin duda esta tesis no hubiera sido posible sin su ayuda, gracias. También quiero agradecer tanto a Julien como a Sandrine su hospitalidad y amistad durante mi estancia en Glasgow. Merci beaucoup mon amis.

Fifthly I want to thank the IOLOS project partners, especially Sandor Fürst, Michael J. Strain, Marc Sorel, Guido Giuliani and Siyuan Yu. It's been a pleasure working with you.

A parte de las personas implicadas directamente en la tesis me gustaría dar las gracias a mis amigos Niko Komin, Fernando Galve y Xavier Porte. También quisiera agradecer a los compañeros con los que he compartido cubículo y muchas cosas más: Ismael Hernández, Juan Carlos González-Avella, Adrián Jacobo, Pedro Sánchez y Pablo Fleurquin. Así como agradecer a todo el personal del IFISC por haber contribuido a esta enriquecedora experiencia vital, en especial a Rubén Tolosa, Eduardo Herraiz, Daniel Brunner, Roberta Zambrini, Damià Gomila, Rosa María Rodríguez, Manuel Matías, Pere Colet y a los miembros del 'IFISC-OSA Student Chapter': María Moreno, Konstantin Hicke, Neus Oliver y Jade Martínez. También agradecer a todos los compañeros, personal administrativo, personal de limpieza y profesores del departamento de física de la UIB por todos estos años. Parece que fue ayer cuando tuve la primera clase de cálculo con Lluís Mas acompañado de aquella pandilla inicial formada por Xavier Porte, Marc Farré, Victor Huarcaya, Miquel Roig y Toni Melis. También quiero agradecer al personal del bar del Mateu Orfila: Lianca, Núria, la *simpática* de Cati y Tomeu. Gracias a todos.

Fuera del ámbito universitario, quiero agradecer a mis amigos que me han dado ánimos durante todos estos años y me han ayudado de distintas formas. Gracias a Javi, Irene e Itxiar; a Jaume y Xisca; a Johan, Juan, Rafa, Àngel y a toda la gente de Can Angel; y por descontado a mis compañeros en las bandas con las que he estado tocando durante todo este tiempo: *Helio*, *Citizen Dick* y *Neotokyo*, es decir, Miquel, Marc, Biel, Mónica, Sebas, Jaume, Yamil, Rafa, Ginés y Jordi. Gracias a todos por haber hecho que me olvidase de los láseres aunque sólo fuera por un rato.

Por último, quiero dar las gracias a toda mi familia. A mi familia de Badalona, Torelló y Sevilla; a los que se han ido en estos años, siempre os llevaré conmigo; y a los que acaban de llegar, bienvenidos. Y sobre todo gracias a mis padres, Encarna y Toni, por darme la vida y por apoyarme siempre en todo lo que he hecho. Este trabajo os lo dedico a vosotros.

- Antonio Pérez, 29 de Septiembre de 2011.

- Ernest Shackleton's ad for his expedition in search of the South Pole, 1913.
(Thanks to S. Balle)

But apart from the sanitation, the medicine, education, wine, public order,
irrigation, roads, the fresh-water system, and public health,
what have the Romans ever done for us?

- Monty Python, *Life of Brian*, 1979.

The great tragedy of Science – the slaying of a beautiful hypothesis by an ugly fact.

- T.H. Huxley, 1870.

Karma police, arrest this man
He talks in maths
He buzzes like a fridge
He's like a detuned radio

- Radiohead, *Karma police*, from *Ok Computer*, 1997.

Contents

Introduction

In the last decades the field of communications has grown very quickly with the popularization of the Internet. The society requires information access everywhere at any time, and the demand grows day by day. This is due in part to the enormous development of the optical communications systems and technology.

Optical communications have well known technological advantages, i.e. huge bandwidth (nearly 50 Tb/s), low signal attenuation (as low as 0.2 dB/km), low signal distortion and small space requirement. A single-mode fiber's potential bandwidth is nearly 50 Tb/s, which is almost four orders of magnitude higher than electronic data rates of a few Gb/s. This opto-to-electronic bandwidth mismatch can be avoided at a physical level by using all-optical processing, e.g. in the 80s the invention of the Erbium Doped Fiber Amplifier (EDFA) removed the bottleneck created by electronic amplifiers used to regenerate the optical signal between fibers. However, this limitation cannot be overcome at some stages, e.g. the maximum rate at which an end-user can access the network is limited by the electronic speed, but it can be overcome at the network level by using different architectures and protocols. For instance, Wavelength Division Multiplexing (WDM) is an approach that can exploit the huge opto-to-electronics bandwidth mismatch by requiring that each end-user's equipment operates only at electronic rate, but multiple WDM channels from different end-users may be multiplexed on the same fiber [1]. Telecommunications market demands have motivated the research and development of new physical devices and components to improve system performance. Among the most important devices are the *laser*[1] [2] sources. Telecommunications market requires small, cheap, stable, powerful and versatile laser sources. These factors have motivated numerous experimental and theoretical studies. These studies have unveiled the behavior of the different kinds of laser structures, and they have motivated the use of these devices to perform complex operations. Although the basic rules that determine the behavior of lasers are in general well known, there is a lot of research still to be performed regarding more detailed aspects. A detailed understanding of the physical processes that take place in lasers is needed in order to model the novel cavity geometries and materials used in nowadays laser devices [3].

In the case of optical communications systems, the lasers employed are Semiconductor Lasers (SLs) [4], due to their small size, easy integration in electronic circuits and low cost. In fact, these kind of lasers represent more than the 50 % of the lasers produced per year, and they represented more than 3 billion of dollars in sales in 2008 [5]. An important dynamical feature of SLs is that they permit ultrashort pulsed emission (around a few ps) that can be transmitted by a fiber-optics communication system containing digital information. There are some different techniques

[1] Light Amplification by Stimulated Emission of Radiation

that lead to pulsed operation [6], e.g. gain switching, Q-switching or Mode-locking [7]. These techniques are based on the study of the physical mechanisms that take place in the laser operation, e.g. fast pulsed lasers are fabricated by using saturable absorbers (SA) [8]. The SA is an optical component with intensity dependent optical losses, which decrease for high optical intensities.

Laser sources with high spectral purity are also useful in optical communications, like Distributed Feedback Lasers (DFBs) [9] and Distribute Bragg Reflector (DBR) lasers [10]. A DFB is a laser where the whole resonator consists of a periodic structure, which acts as a distributed reflector in the wavelength range of laser action, and contains a gain medium. A DBR is a laser, where the resonator is made with at least one distributed Bragg reflector outside the gain medium.

Other common laser sources are the Vertical-Cavity Surface-Emitting Lasers (VCSELs) [11], which are in fact DFB lasers. The cavity is realized with two semiconductor Bragg mirrors. Between which, there is an active region containing (typically) several quantum wells and a total thickness of only a few μm. The short resonator makes it easy to achieve single-frequency operation, even combined with some wavelength tunability. Also, VCSELs can be modulated at high frequencies making them useful for optical fiber communications.

An important practical advantage of VCSELs, as compared with edge-emitting semiconductor lasers, is that they can be tested and characterized directly after growth, i.e. before the wafer is cleaved. This makes possible to identify quality problems early on. Furthermore, it is possible to combine a VCSEL wafer with an array of optical elements (e.g. collimation lenses) and then dice this composite wafer instead of mounting the optical elements individually for every VCSEL. This allows for cheap mass production of laser products.

In addition, fiber-optics communications have motivated the development of other components that perform all-optical processing [12], e.g. filters, power divisors, routers, switches, multiplexers and de-multiplexers in time and in frequency (for WDM), etc... Those perform different functions in the communication structure. These devices share some characteristics with lasers, e.g. the gain materials and the optical cavities. The Fabry-Pérot cavity and Bragg gratings [13] have been used to produce filters, besides they have been used in the fabrication of lasers [14]. Recently, passive ring resonators have been used as filters, using a single resonator [15] or arrays of resonators [16]. Four Wave Mixing (FWM) enables the use of these devices as wavelength converters [17], and they have been proposed to realize logic gates [18]. Recently good integration with electronic circuits has been achieved by using silicon materials [19, 20].

Nowadays the technology challenge is to produce Photonic Integrated Circuits (PICs) that will process the information in the all-optical domain by the integration of different components avoiding electronic conversion [21]. The research is active in seeking new optoelectronic devices, able to integrate in the same substrate several all-optical functions [22, 23, 24]. These new devices demand a full description of their spatiotemporal dynamics including propagation effects in order to be properly modeled. One of the most promising and interesting all-optical application is to use a bistable optical device as an optical memory [25]. The memory application was investigated in optical bistable devices such as semiconductor diode lasers [26] and VCSELs [27], where the bistability comes from the different polarization modes.

The research in lasers has found many applications, ranging from medical to industrial and military applications. E.g. they are routinely used to store data in optical discs, like the Compact Disc (CD), the Digital Versatile Disc (DVD) and more recently in the Blu-ray disc. Other everyday applications are found in printers and

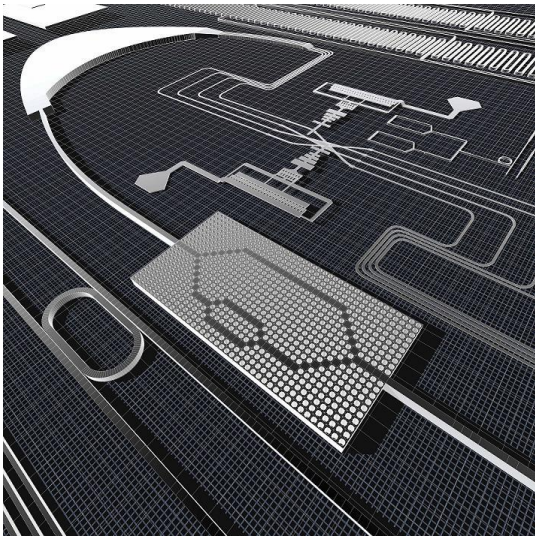

Fig. 1.0.1 – A representation of a Photonic Integrated Circuit (PIC). The circuit is composed by different components to perform complex all-optical signal processing. *From www.esa.int.*

barcode readers. As industrial applications lasers are used to weld, melt or vaporize materials with high precision, to cut microelectronics components, to warm up semiconductors chips, to cut textile patterns or synthesize materials. Another important field for laser applications is medicine, surgery in particular, where the full control and noninvasive character of the laser light show its advantages in front of traditional techniques.

Lasers are used extensively in research. They are used to measure the pollution in the atmosphere and to measure the Moon-Earth distance. They are used in relativity experiments and to measure the speed of light with a great precision. Moreover, lasers are used for characterizing materials and molecular structures and they can induce chemical reactions in selective form. In metrology, lasers are used to make accurate measurements of rotations and distances. The LIDAR (Light Detection And Ranging) is an optical remote sensing technology that measures properties of scattered light to find range and other information of a distant target. The gyroscope is a device that measures inertial rotations used in navigation systems for aircrafts and missiles. Other very large devices have been used to measure earth's rotation [28, 29].

I.1 Ring lasers

To build a laser, three ingredients are required: an *active medium* that provides the gain (or amplification), an energy *pump* that generates population inversion (or excitation of the atoms), and an *optical cavity* that confines the electric field and acts as a resonator. In particular Ring Lasers (RLs) have been studied due to their peculiar cavity characteristics. The RL cavity is a closed loop that allows two counter-propagating electric fields. The electric fields in ring cavities show a traveling wave character in contrast with the standing wave character of the fields in Fabry-Pérot cavities.

The first systematic formulation of the theory of RLs by Lamb et al. [30, 31] already evidenced that symmetry issues and even minute intra-cavity reflections have

a major impact on the modal structure in RLs; i.e. pure counter-propagating traveling waves are ideal states only allowed in closed loop optical cavities without any localized reflection; localized reflections destroy the rotational invariance of the RL, and the cavity modes become non-degenerate standing waves with fixed phase relationship. These effects together with the nonlinear interaction of the counter-propagating waves, mediated by the active medium, lead to a large variety of operating regimes and dynamics that are profoundly different from those of Fabry-Pérot lasers and that have posed problems for the development of practical devices (specially semiconductor-based) for the above applications in spite of the tremendous advances achieved by technology [32, 33].

RLs have been initially applied to inertial rotation sensing [34] because they do not need moving parts as the mechanical gyroscopes. During the 70s and 80s the research was focused on gas, solid-state and fiber RLs. The main part of these studies was related to the aspects of practical importance in understanding the limitations of the laser gyroscope. The idea behind using the RL as a gyroscope comes from the Sagnac effect [35]. It consists of a measure of the interference pattern formed by the two counter-propagating light fields in the RL and extract, from the pattern, information of the rotation rate of the laser relative to an inertial frame. In other devices the rotation can be detected by a beat signal. The information of the rotation is extracted from the dephasing between the two counter-propagating fields which is induced by the the different path lengths that the two counter-propagating fields follow. In this context the problems treated were the effects of rotation [35], the stability of the different modes of operation [36], behavior of the beat note, the effect of frequency lock-in at slow rotation rates [37, 38], influence of backscattering of radiation in frequency lock-in phenomena [39], hysteresis effects [40], the Noise Equivalent Rotation (NER) effects [41] and polarization-induced effects in solid-state RLs [42].

From the theoretical point of view, the usual approach is to describe the laser with the semiclassical theory [30]. It consists in a classical description of the light and its interaction with matter in a quantum mechanical way. The classical description of the light comes from the Maxwell's equations while the material quantum description comes from the Bloch equations.

The most studied case is the single-mode unidirectional operation, which can be obtained by using an intracavity element, or from the theoretical point of view, in the good cavity limit, i.e. lossless, and with a negligible reflectivity. As pointed in [43], in the absence of reflectivity only unidirectional emission is stable. In this case the laser can emit in different regimes as continuous wave [44], mode-locked and chaotic behavior [45]. In fact, the chaotic behavior comes from an instability of the single-mode continuous wave solution as found in the Haken-Lorenz model [46]. Multi-mode instabilities were studied theoretically in [47], where a Linear Stability Analysis (LSA) is performed for the unidirectional single-mode steady-state solution. It was found that this solution is unstable depending on the laser parameters. The instability generates pulses by locking different modes of the cavity. It was observed experimentally in ref. [48] thanks to the possibility, offered by fiber RLs, of achieving large gain in large cavities. These studies were made to analyze the conditions to get mode-locked operation [49, 50, 51].

The analytical description of the bidirectional case poses severe problems due to the non linear interaction between the fields and the fields and the active medium. This has motivated the study of the unidirectional regime in great detail [52, 53]. However, in the last decades, using approximations and computer simulations many results have been obtained. Single-mode instabilities in bidirectional RLs in the good

cavity limit were studied theoretically by Zeghlache et al. [54], this work highlighted the effect of a detuned cavity in the single longitudinal operating mode, that produces unidirectional stable emission, alternate direction of emission or even chaotic bidirectional emission depending on the pump and the detuning values. Other theoretical studies were dedicated to the effect of the different coupling sources, conservative and dissipative backscattering [55] and the role of saturation effects [56]. Bistability was observed in solid state RLs [40]. Stochastic resonance between the direction of emission was observed in [57] and then explained theoretically [58]. Other noise properties were studied focusing on their effect in the relaxation oscillations [59, 60].

Although, the main motivation on the study of RLs was their application as gyroscopes, other applications have been developed. The unidirectional continuous wave regime was used to develop high power RLs, e.g. Nd:YAG RL [61]. However, this scenario has changed with the maturity of Semiconductor Ring Lasers (SRLs), because they show the same variety of dynamical regimes of their gas or solid-state counterparts, in smaller and cheaper devices. Moreover, SRLs are candidates to be important components in integrated optics circuits for performing complex operations.

I.2 Semiconductor ring lasers

SRLs are highly integrable and show interesting dynamical behaviors. The reversibility of the optical path and the (in principle) absence of reflectivity allow for two degenerate counter-propagating electric fields in the same gain medium. This property is not exclusive of RLs [62], it is common to all systems possessing rotational symmetry as e.g. micro-disk lasers [63, 64, 65]. This fact has important consequences on the dynamics and potential applications. SRLs exhibit a great variety of dynamical operating regimes characterized by bidirectional-continuous waves or alternate oscillations [66], to bistability [67], mode locking [68] and chaos [69]. In particular, the bistable regime is interesting for applications to integrated optical logics, optical gating and reshaping [70], whereas the bidirectional regime can be used for rotation sensing applications [71].

The demonstration of the first memory application using SRLs was performed in 2004 [70]. The device was formed by two SRLs of 16 μm radius coupled to a waveguide via evanescent coupler, all placed in a photonic circuit of InP/InGaAsP. The device was fabricated with two rings and a semicircular inter-laser waveguide in order to enhance the memory state switching. Light from one of the lasers injection-locks the other laser, forcing it to lase only in one direction. Then pulses of light at the chosen input set the system in one of the two states. The experiments show that the memory state switched within 20 ps with 5.5 fJ optical switching energy.

The first experimental devices were half-SRLs [72] fabricated by liquid-phase epitaxial growth of GaAlAs and GaAs layers over etched channels in GaAs substrates. The fabricated half-ring waveguides had 5 μm width and 185 μm radius. The problem in the fabrication of full-SRLs was that they needed a mechanism to extract the light from the ring. This problem was solved in [73], where a straight waveguide was used as a light extraction section for the light produced in the SRL. This paper analyzes the modal properties of the devices as compared with the half-SRLs and it highlights the importance of the output waveguide as a part of the whole laser structure, evidenced in the excited modes of the cavity. The main result in [73] was the realization that the ring resonator can support resonant modes and can be used as a laser. The second result was the importance of the light extraction sections in the modal properties of the device and in the efficiency.

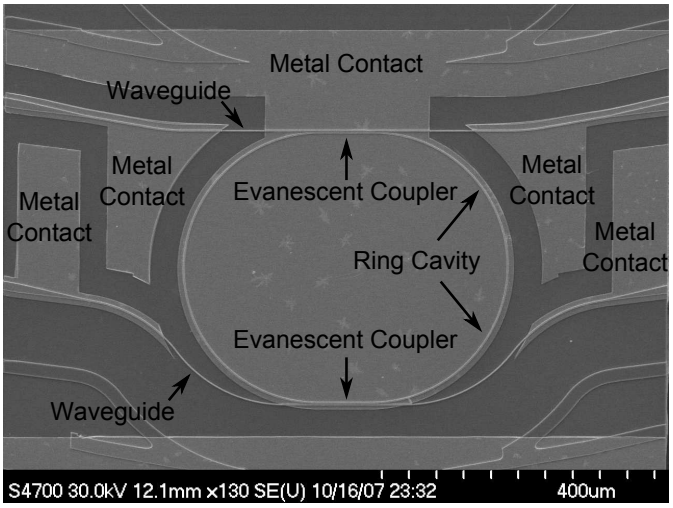

Fig. 1.2.2 – Micrograph of a SRL with output waveguides. The metal contacts are used to pump the ring laser and the output waveguides independently. The active region consists in InAlGaAs/InP quantum well (QW) material. *Courtesy of University of Glasgow.*

In the late 80s and the beginning of the 90s, the research was focused in fabrication of new structures for SRLs that allow extracting the light in a more efficient way. Dry etching techniques become a standard process in the fabrication of optical devices, as lithography features a size less than 1 μm [74]. Circular structures [75], triangular structures [76], and square structures [77] were fabricated. These studies highlighted the effects of the backreflections in the electric fields. While the triangular and square SRLs use total reflection mirrors, the circular SRLs have not (in principle) these sources of reflection; however they possess some degree of backreflection due to the bent waveguides and the light extraction sections [78]. Moreover the circular devices have bending losses, which limit the minimum diameter of these devices and increase the threshold current at high values. In the early 90s, circular cavities of radius $<$ 100 μm showed unreachable thresholds.

In order to minimize the bending losses, some improvements in the etching techniques and different geometries were proposed, such as square [79], triangular [80], racetrack [81], micro-squares [82] and S section [83]. These structures as well as the circular SRLs show the different behaviors found in other RLs, e.g. bistability [67] and alternate oscillations [66].

More recently, other cavities were fabricated in order to minimize the device and obtain smaller switching times. A device constructed with parabolic mirrors was introduced in [84]. This device shows bistability [85], and switching response times of 70 ps approx. [86, 87]. Other strategy used in circular devices is to minimize the waveguide sidewall roughness [88]. This reduces the losses and allows to fabricate devices of 30 μm radius showing directional bistability.

Other experimental studies were dedicated to data processing [89] and reshaping [90]. Logic gates demonstration with SRLs was also obtained [91]. Four Wave Mixing (FWM) produced by an injected field was investigated in [92]. The injected field can produce mode-locked via a FWM process exciting different modes of the SRL. In [93], the mode-locked operation is obtained with a SA.

Various theoretical models were proposed to describe the dynamics of SRLs. Rate

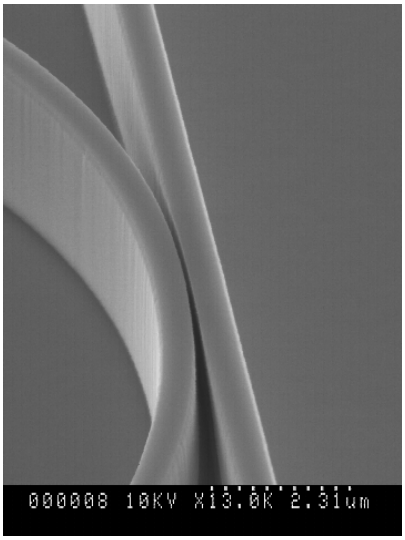

Fig. 1.2.3 – Micrograph showing in detail the evanescent coupler of a SRL. *Courtesy of University of Glasgow.*

Equations (RE) models for two fields showed the different stability scenarios, like single-mode unidirectional operation, bistability and multistability [94] produced by cross-gain saturation [95]. A further improvement to the model was the introduction of backscattering coefficients [66], it showed good agreement with the experiments [96]. Multi-mode dynamics were described in [97], in this paper multistability is discussed, they are able to change the emission wavelength by injection locking.

Switching properties were also studied using this RE model [98] introducing the effects of spontaneous emission and external pulses to the system biased in the bistable regime. Other theoretical studies characterize the different switching regions and locking to the injection fields [99] and the switching response to different signal formats [100]. Moreover, other models appeared in order to describe more accurately smaller devices fast dynamics and their light extraction sections. A Traveling Wave Model (TWM) [101] is able to describe the direction emission and the wavelength jumps observed in SRLs as the pump current is increased. This work highlights the effect of the modulation of the cavity losses imposed by the light extraction section, the thermal shift of the gain spectrum and the spatial hole burning in the direction and wavelength of emission.

Therefore, SRLs display interesting dynamics, e.g. switching in the direction of emission or multistability, with direct applicability to optical telecommunications (pulsed sources, components) for being fast and integrable. However, a detailed understanding of the fast laser dynamics is now required to assess the actual possibilities of these devices. This is the aim of this work.

I.3 Overview of this thesis

Chapter II is devoted to introducing the semiclassical approach to laser modeling as well as the different notations and models used in the thesis. In this chapter photon models are introduced from a phenomenological point of view. These models allow to review the concepts of nonlinear dynamics and introduce the RE. Followed by the description of light in the theory of classical electrodynamics, and the description of matter and its interaction with light through quantum physics, a collection of general equations in space-time domain are introduced. This collection of equations comprise the TWM that will be used to describe different types of lasers in the thesis, in particular for a two level atom medium and for semiconductor quantum well (QW) material, in chapters IV and V respectively. Finally, the RE are derived from the TWM for the cases of unidirectional and bidirectional RLs.

Chapter III presents studies based on the RE model. First, there is a description of the RE model and its use in the literature. Second, there is part dedicated to the bidirectional regime, particularly in the use of the SRL as a gyroscope and the noise properties of these devices.

Chapter IV is devoted to study the nonlinear dynamics of a bidirectional RL which active medium consists of 2-level atoms. The description of the system is based on the TWM, and is a good approximation to gas and solid state lasers. In this chapter, tools for obtaining the monochromatic solutions and the realization of the linear stability analysis of this model are presented. These tools are used to investigate longitudinal modal multistability. Also multimode dynamics are explored with the TWM for the two level atom medium.

The case of the semiconductor medium is discussed in chapter V. The modal properties of real devices consisting in a ring cavity and waveguides for light injection and extraction are studied. Moreover a TWM for the case of semiconductor QW medium is presented. Finally, a experimental and theoretical study is shown for a new type of laser based on semiconductor ring lasers, the snail laser.

II Laser modeling

II.1 General remarks

In a semiclassical frame, an adequate choice of physical variables for the description of the amplifying medium and the electromagnetic wave generated within the resonator are the atomic dipole moment (or polarization), the population inversion of the atoms or molecules of the amplifying medium and the electric field of the generated wave.

In this context, the mathematical frame are the Maxwell-Bloch equations, derived from Maxwell's equations and from Schrödinger equation [30, 102]. The electromagnetic field is treated as a classical quantity, obeying Maxwell's equations, while the motion of the electrons of the atoms in the active medium is treated in a quantum mechanical way. If the spatial dependence is retained, the Maxwell-Bloch equations are Partial Differential Equations (PDEs). Numerical algorithms are mostly implemented in order to simulate the system behavior. General electrodynamics numerical methods, e.g. Finite-Differences Time-Domain (FDTD) methods, have been used to model lasers [3]. But under certain assumptions, less computationally expensive models are used. Such models that focus on longitudinal dynamics (one spatial dimension) are called Traveling Wave (TW) models [101, 103, 104].

If longitudinal dynamics is spatially averaged and one focuses on slow time scales ($1/f_{rel.\ osc.}$) simple Rate Equations (RE) models can be derived. A RE model is a set of Ordinary Differential Equations (ODEs) that describe the temporal evolution of a set of variables. One finds two types of RE models [102], the *photon models*, for the dynamics of cavity averaged photon and atomic inversion number; the *semiclassical model*, where the polarization has been eliminated adiabatically [105], that describe the electric field and the population inversion density. Under certain assumptions and approximations these RE models are equivalent. However, the semiclassical approach can be more general to describe laser dynamics because the Maxwell-Bloch equations include the polarization that the field induces to the medium. This leads to different phenomena such as chaotic behavior. Moreover, if we retain the spatial dependence of the variables, other phenomena can be easily described, e.g. multi-mode operation or Four Wave Mixing (FWM) phenomena.

In the following the photon and semiclassical models are presented and the semiclassical Maxwell-Bloch equations retaining the spatial dependence are derived. Transverse and longitudinal modes of an optical cavity are discussed. The two level atom model for the gain medium and its differences with a semiconductor gain medium are described. Finally, the RE model for the bidirectional RL from the TW Maxwell-Bloch equations are derived.

II.1.1 The photon model

The *photon models* describe the dynamics of photon numbers and the atomic occupation numbers. The used variables are the population inversion density and the photon density n. The photon density equation is of the form

$$\frac{dn}{dt} = \text{generation rate} - \text{annihilation rate.}$$

Supposing that the active medium can be treated as a quantum mechanical system formed by two energy levels, E_1 and E_2, with occupation level numbers $N_1(t)$ and $N_2(t)$, respectively. Without taking into account the spontaneous emission, the equations for the occupation level numbers by using Einstein's results are derived [106],

$$\frac{dN_1}{dt} = -W_{1\to 2}nN_1 + W_{2\to 1}nN_2 \ , \tag{2.1.1}$$

$$\frac{dN_2}{dt} = W_{1\to 2}nN_1 - W_{2\to 1}nN_2 \ , \tag{2.1.2}$$

where $W_{1\to 2} = W_{2\to 1} = W$ are Einstein's coefficients. Introducing a change of variable, defining the population inversion $D = N_2 - N_1$, then Eqs. (2.1.1)-(2.1.2) become

$$\frac{dD}{dt} = -WnD \ . \tag{2.1.3}$$

Now, introducing a posteriori in (2.1.3) the effect of the spontaneous emission by means of relaxation time T_1 and the pump J, the equation reads

$$\frac{dD}{dt} = -2WnD - \frac{1}{T_1}(D - J) \ . \tag{2.1.4}$$

The equation for the photon density is

$$\frac{dn}{dt} = Wn(N_2 - N_1) = WnD - \frac{1}{T_c}n \ , \tag{2.1.5}$$

where the cavity losses are taken into account by the parameter T_c, then the simplest *photon model* describing laser dynamics reads as

$$\frac{dn}{dt} = WnD - \frac{1}{T_c}n \ , \tag{2.1.6}$$

$$\frac{dD}{dt} = -2WnD - \frac{1}{T_1}(D - J) \ . \tag{2.1.7}$$

Eqs. (2.1.6)-(2.1.7) is a non linear dynamical system of dimension two. In this work, non linear system analysis is based on various methods for stability analysis and bifurcation theory, that are described in appendix A.

The light amplification is obtained from (2.1.6) if $WD - 1/T_c > 0$, and this permits to the define a threshold density, above which light amplification will take place. The condition

$$D > D_{th} = \frac{1}{WT_c} \ , \tag{2.1.8}$$

means population inversion, i.e. $N_2 > N_1$ which is a necessary condition for laser operation. The stationary solutions for Eqs. (2.1.6)-(2.1.7), are a trivial solution, $n = 0$ and $D = J$, and a non trivial solution (operation condition),

$$D = \frac{1}{WT_c} = D_{th} = J_{th} \ , \tag{2.1.9}$$

$$n = \frac{T_c}{2T_1}(J - J_{th}) \ , \tag{2.1.10}$$

The condition $D = J$, defines a pump threshold J_{th}. The linear stability analysis of solutions (2.1.9)-(2.1.10) produces the bifurcation diagram shown in Fig. 2.1.1. There is no laser emission for pump values $0 < J < J_{th}$, where the *off* solution is the only stable. At threshold, the laser emission becomes stable and grows linearly with the pump J, whereas D saturates at $J_{th} = D_{th}$. This type of bifurcation is called transcritical bifurcation.

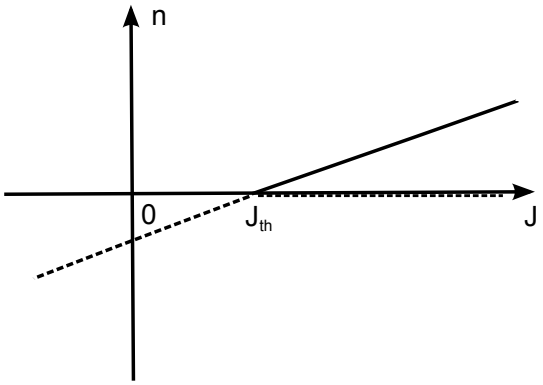

Fig. 2.1.1 – Bifurcation diagram for the simplest *photon model*. Dashed (solid) lines represent unstable (stable) solutions. For $J > J_{th}$ a transcritical bifurcation appears and the laser operation takes place.

II.2 Light and matter description

II.2.1 Maxwell's equations

The starting point for laser dynamics description within the semiclassical approach are Maxwell's equations [107],

$$\nabla \cdot \vec{\mathcal{D}}(\vec{r},t) = \rho_f(\vec{r},t) \ , \tag{2.2.11}$$

$$\nabla \times \vec{\mathcal{E}}(\vec{r},t) = -\frac{\partial \vec{\mathcal{B}}(\vec{r},t)}{\partial t} \ , \tag{2.2.12}$$

$$\nabla \cdot \vec{\mathcal{B}}(\vec{r},t) = 0 \ , \tag{2.2.13}$$

$$\nabla \times \vec{\mathcal{H}}(\vec{r},t) = \frac{\partial \vec{\mathcal{D}}(\vec{r},t)}{\partial t} + \vec{J}_f(\vec{r},t) \ , \tag{2.2.14}$$

for the displacement field $\vec{\mathcal{D}}(\vec{r},t)$, the electric field $\vec{\mathcal{E}}(\vec{r},t)$, the magnetic induction $\vec{\mathcal{B}}(\vec{r},t)$, and the magnetic field $\vec{\mathcal{H}}(\vec{r},t)$. In Eq. (2.2.11) $\rho_f(\vec{r},t)$ is the free charge density and $\vec{J}_f(\vec{r},t)$ is the free density current in Eq. (2.2.14). Maxwell's equations when are combined with Lorentz force equation[1] and Newton's second law of motion, provide a complete description of the classical dynamics of interacting charged particles and electromagnetic fields.

In a laser, light propagates inside a dielectric medium, and interacts with it. In case of a linear and isotropic material, then the constitutive relations take the form

$$\vec{\mathcal{D}}(\vec{r},t) = \epsilon\vec{\mathcal{E}}(\vec{r},t) = \epsilon_0\vec{\mathcal{E}}(\vec{r},t) + \vec{\mathcal{P}}(\vec{r},t) \ , \tag{2.2.15}$$

$$\vec{\mathcal{B}}(\vec{r},t) = \mu\vec{\mathcal{H}}(\vec{r},t) = \mu_0\vec{\mathcal{H}}(\vec{r},t) + \vec{\mathcal{M}}(\vec{r},t) \ , \tag{2.2.16}$$

[1] $\vec{F} = q(\vec{\mathcal{E}} + \vec{v} \times \vec{\mathcal{B}})$

where ϵ is the dielectric constant and μ is the magnetic permeability of the given medium, ϵ_0 is the electric vacuum permittivity[2] and μ_0 is the magnetic vacuum permeability[3]. Finally, the polarization $\vec{\mathcal{P}}(\vec{r},t)$ and the magnetization $\vec{\mathcal{M}}(\vec{r},t)$ of the medium are the response function that describe light-matter interaction at a mesoscopic scale. Laser media are usually non-magnetic, i.e. $\vec{\mathcal{M}}(\vec{r},t) \sim 0$ then $\vec{\mathcal{B}}(\vec{r},t) = \mu_0\vec{\mathcal{H}}(\vec{r},t)$ and $\mu \simeq \mu_0$. On the other hand, the polarization plays an important role in the laser dynamics, and it is usually related to the frequency dependent electric field by the electric susceptibility of the medium $\chi_e(\omega)$ as follows

$$\vec{\mathcal{P}}(\vec{r},\omega) = \epsilon_0\chi_e(\omega)\vec{\mathcal{E}}(\vec{r},\omega) \ . \tag{2.2.17}$$

The electric susceptibility is a complex scalar quantity here, because the medium is considered as isotropic. The relation between the susceptibility and dielectric constant is given by

$$\epsilon = \epsilon_0[1 + \chi_e(\omega)] \ . \tag{2.2.18}$$

The response of a medium is frequency dependent, so ϵ and μ are in general complex functions of ω. With the constitutive relations for a medium, the equations for $\vec{\mathcal{E}}(\vec{r},\omega)$ and $\vec{\mathcal{H}}(\vec{r},\omega)$ are

$$\nabla \times \vec{\mathcal{E}}(\vec{r},\omega) = i\omega\mu\vec{\mathcal{H}}(\vec{r},\omega) \ , \tag{2.2.19}$$

$$\nabla \times \vec{\mathcal{H}}(\vec{r},\omega) = -i\omega\epsilon\vec{\mathcal{E}}(\vec{r},\omega) + \vec{J}_f(\vec{r},\omega) \ , \tag{2.2.20}$$

where the Fourier transform in time reads

$$\mathcal{F}\{F(t)\} = F(\omega) \equiv \int_{-\infty}^{\infty} dt \ e^{i\omega t}F(t) \ . \tag{2.2.21}$$

Concerning the material electrical conductivity, using Ohm's law, a further constitutive relation is

$$\vec{J}_f(\vec{r},\omega) = \sigma\vec{\mathcal{E}}(\vec{r},\omega) \ , \tag{2.2.22}$$

by combining the Eqs. (2.2.19)-(2.2.20) the Helmholtz wave equation for $\vec{\mathcal{E}}(\vec{r},\omega)$ reads

$$\nabla \times [\nabla \times \vec{\mathcal{E}}(\vec{r},\omega)] = (\mu\epsilon\omega^2 + i\omega\mu\sigma)\vec{\mathcal{E}}(\vec{r},\omega) \ , \tag{2.2.23}$$

with the corresponding equivalent equation for $\vec{\mathcal{H}}(\vec{r},\omega)$. One possible solution for (2.2.23) is a plane wave traveling in the z direction, of the form

$$\vec{\mathcal{E}}(z,\omega) = \mathcal{E}_x(z,\omega)\vec{e}_x + \mathcal{E}_y(z,\omega)\vec{e}_y + \mathcal{E}_z(z,\omega)\vec{e}_z \ , \tag{2.2.24}$$

where $\mathcal{E}_x(z,\omega) = \mathcal{E}_z(z,\omega) = 0$ and

$$\mathcal{E}_y(z,\omega) = e^{iqz-i\omega t} \ . \tag{2.2.25}$$

Using the vector calculus identity,

$$\nabla \times (\nabla \times \vec{\mathcal{E}}) = -\nabla^2\vec{\mathcal{E}} + \nabla \cdot (\nabla \cdot \vec{\mathcal{E}}) \ , \tag{2.2.26}$$

Eq. (2.2.23) becomes

$$\frac{\partial^2\mathcal{E}_y(z,\omega)}{\partial z^2} = -(\mu\epsilon\omega^2 + i\omega\mu\sigma)\mathcal{E}_y(z,\omega) \ . \tag{2.2.27}$$

[2] $\epsilon_0 = 8.854\ 10^{-12}\ F\ m^{-1}$
[3] $\mu_0 = 4\pi\ 10^{-7}\ N\ A^{-2}$

Using (2.2.25) in (2.2.27), with (2.2.18) and a non-magnetic medium $\mu = \mu_0$, the wavenumber q can be written as

$$q^2(\omega) = \frac{\omega^2}{c^2}\left[1 + \chi_e(\omega)\right] + i\mu_0\sigma\omega \ . \tag{2.2.28}$$

In this case, the wavenumber is a complex quantity $q(\omega) = q_R(\omega) + iq_I(\omega)$, then the electric field reads

$$\mathcal{E}_y(z,\omega) = e^{i[q_R(\omega)z - \omega t]}e^{-q_I(\omega)z} \ , \tag{2.2.29}$$

where the real part of $q(\omega)$ set the refractive index of the medium as corresponding to a monochromatic component ω. The refractive index frequency dependence imposes a different phase velocity to each monochromatic component, this causes a light packet to spread its spectrum during the propagation. Being the electrical susceptibility $\chi_e(\omega)$ a complex quantity, the refractive index can be written as

$$n(\omega) = \sqrt{1 + \mathrm{Re}\{\chi_e(\omega)\}} \ . \tag{2.2.30}$$

On the other hand, the imaginary part of $q(\omega)$ is responsible of the wave attenuation or amplification. So the imaginary part of $\chi_e(\omega)$ gives the amplification/attenuation of the medium. The other contribution to the imaginary part of $q(\omega)$ comes from the medium electrical conductivity, which also causes wave attenuation. However, depending on the field of study, it can be found in the literature different conventions for the susceptibility $\chi_e(\omega)$ depending on the definition of the polarization, e.g. in [36] is the $\mathrm{Re}\{\chi_e(\omega)\}$ responsible of providing amplification/attenuation of the medium while the $\mathrm{Im}\{\chi_e(\omega)\}$ gives the modification of the refractive index.

(a) Quasi-monochromatic fields

One can consider that due to the nature of the light source, in our case a laser, only frequencies close to a mean frequency ω_0 are relevant. This is called the quasi-monochromatic approximation [108], and it allows to write the electric field as

$$\mathcal{E}_y(z,t) = E(z,t)e^{-i\omega_0 t} + c.c. \ , \tag{2.2.31}$$

where *c.c.* denotes the complex conjugate. Considering that the amplitude $E(z,t)$ is time dependent, but that its time dependence is much slower than that of the exponential function in (2.2.31). Therefore, the temporal variation of the derivative of the field $E(z,t)$, is smaller than the field. So the quasi-monochromatic field condition can be written as

$$\left|\frac{\partial E(z,t)}{\partial t}\right| \ll \omega_0 |E(z,t)| \ .$$

II.2.2 Medium response to the light

The coupling between light and matter resides in the mutual action of charges and fields, according to electrodynamics. If the charges are bound forming atoms or molecules, their displacement from their equilibrium positions generates an induced macroscopic polarization which acts as a source of re-radiated fields. From a classical point of view, the charges are modeled as dipoles oscillating driven by the electric field, producing an overall polarization (Drude model) [109].

In the following the quantum approaches for the case of a two level atom medium and semiconductor medium are presented. One difference between the quantum and classical approaches is the introduction of the stimulated emission process that leads to amplification of the light in the active medium.

(a) Two level atom medium

The simplest case is to consider the dipole transition between two energy levels which are spaced by $\hbar\omega_A$, see Fig. 2.2.2, assuming the atoms to be identical (homogeneous broadening). This description use to apply to solid-state (e.g. Nd:YAG) and gas lasers, where one can consider the active medium effectively as an ensemble of absorption or amplification centers (like e.g. atoms, molecules) with only two electronic energy levels which couple to the resonant optical field mode.

Considering a weak and quasi-monochromatic electromagnetic field, the complex amplitude of the field at a given point varies slowly compared with the carrier frequency ω_0, which in fact is close to ω_A. Therefore, the spatial variations are also slow compared with the wavelength associated to ω_0. These assumptions are known in the literature as the Rotating Wave Approximation (RWA) [102]. Moreover, a the dipolar

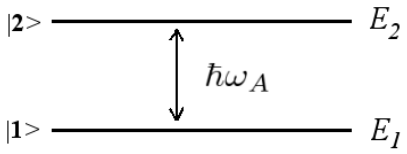

Fig. 2.2.2 – Schematic representation of the energy levels (E_1 and E_2) of the active atoms. The frequency spacing between the upper (2) and the lower (1) levels is ω_A. $|1\rangle$ and $|2\rangle$ are the associated eigenfunctions to each energy level.

approximation for the interaction between the field and the atom is assumed. These approximations allows to describe the two-level atom system by the total Hamiltonian as

$$\mathcal{H} = \mathcal{H}_0 + \mathcal{H}' \ , \tag{2.2.32}$$

where $\mathcal{H}'$ is the Hamiltonian of the light-matter interaction and $\mathcal{H}_0$ is the Hamiltonian of the system in absence of any field, which obeys

$$\mathcal{H}_0|n\rangle = E_n|n\rangle \ , \text{ where } n = 1, 2 \ , \tag{2.2.33}$$

and $|n\rangle$ are the eigenfunctions of unperturbed Hamiltonian, and supposed to be known. The interaction Hamiltonian is of the electric dipole type,

$$\mathcal{H}' = -\widetilde{\mu}\mathcal{E}(t) \ , \tag{2.2.34}$$

where $\widetilde{\mu}$ is the component of the dipole operator along the direction of the field $\mathcal{E}(t)$. In this semiclassical approach, the field $\mathcal{E}(t)$ is still considered as a classical variable. The density matrix [110] reads

$$\hat{\rho} = \begin{pmatrix} \rho_{11} & \rho_{12} \\ \rho_{21} & \rho_{22} \end{pmatrix} \ . \tag{2.2.35}$$

The diagonal matrix elements of $\mathcal{H}'$ are taken as zero, $\widetilde{\mu}_{11} = \widetilde{\mu}_{22} = 0$ as appropriate for transitions between states of definite parity. The phases of eigenfunctions $|2\rangle$ and $|1\rangle$ are taken as $\widetilde{\mu}_{21} = \widetilde{\mu}_{12} = \widetilde{\mu}$. The ensemble average $< \widetilde{\mu} >$ of the atomic dipole moments reads

$$< \widetilde{\mu} >= tr(\hat{\rho}\widetilde{\mu}) = \widetilde{\mu}(\rho_{12} + \rho_{21}) \ . \tag{2.2.36}$$

The density matrix obeys

$$\frac{\partial \hat{\rho}}{\partial t} = \frac{i}{\hbar}[\hat{\rho}, \mathcal{H}] \ , \tag{2.2.37}$$

which reduces to

$$\frac{d\rho_{21}}{dt} = -i\omega_A \rho_{21} + i\frac{\widetilde{\mu}}{\hbar}(\rho_{11} - \rho_{22})\mathcal{E}(t) - \frac{\rho_{21}}{T_2} \ , \tag{2.2.38}$$

and

$$\frac{d}{dt}(\rho_{11} - \rho_{22}) = \frac{2i\widetilde{\mu}\mathcal{E}(t)}{\hbar}(\rho_{21} - \rho_{21}^*) - \frac{(\rho_{11} - \rho_{22}) - (\rho_{11} - \rho_{22})_0}{\tau} \ , \tag{2.2.39}$$

where phenomenological collision terms (τ and T_2) are included a posteriori. The mesoscopic polarization $\mathcal{P}(z,t)$ relates to the density matrix via the dipoles average as follows

$$\mathcal{P}(z,t) = N < \widetilde{\mu} >= N\widetilde{\mu}(\rho_{12} + \rho_{21}) \ , \tag{2.2.40}$$

where N is the number of atoms per volume unit. $\mathcal{P}(z,t)$ is the electric dipole density in the medium, averaged from a microscopic to a mesoscopic scale typical in optics (see Fig. 2.2.3).

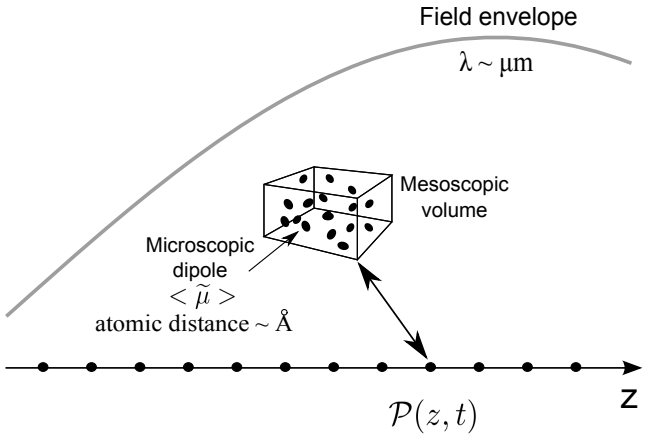

Fig. 2.2.3 – The mesoscopic volume contains statistically relevant quantity of atoms but it is small respect to the spatial variation of the field. This variation is characterized by the wavelength λ of the field of the order of μm (10^{-6} m), which is much bigger than the characteristic distance between atoms, of the order of Å(10^{-9} m).

In the RWA the density matrix elements read

$$\begin{aligned} \rho_{12} &= \sigma_{12} e^{i\omega_0 t} \ , \\ \rho_{21} &= \sigma_{21} e^{-i\omega_0 t} = \rho_{12}^* \ , \end{aligned} \tag{2.2.41}$$

and identifying the quasi-resonant polarization as

$$P(z,t) = -Ni\widetilde{\mu}\sigma_{21} \ . \tag{2.2.42}$$

Next one defines

$$\begin{aligned} D(z,t) &= N(\rho_{22} - \rho_{11}) \ , \\ J &= N(\rho_{22} - \rho_{11})_0 \ , \end{aligned} \tag{2.2.43}$$

where $D(z,t)$ is the population difference and $J(z,t)$ is proportional to the population inversion at zero field, in general $J(z,t)$ can depend on time and space. According to (2.2.38) one finds

$$\frac{\partial P(z,t)}{\partial t} = -i\delta P(z,t) - \frac{\widetilde{\mu}^2}{\hbar} D(z,t)E(z,t) - \gamma_\perp P(z,t) \ , \qquad (2.2.44)$$

where the conventional polarization decay rate is $\gamma_\perp = T_2^{-1}$, and the frequency detuning δ,

$$\delta = \omega_A - \omega_0 \ . \qquad (2.2.45)$$

From Eq. (2.2.44) one notes that the role of the detuning is to produce an oscillation at frequency δ; the second term is a field-inversion coupling due to the radiation-matter interaction; and finally, the third term is the polarization damping factor.

On the other hand, one can write (2.2.39) as

$$\frac{\partial D(z,t)}{\partial t} = \frac{2}{\hbar}[E(z,t)P^*(z,t)+E^*(z,t)P(z,t)]+\gamma_\parallel[J-D(z,t)]+\mathbb{D}\partial_z^2 D(z,t) \ , \qquad (2.2.46)$$

where a diffusion term with $\mathbb{D}$ being the diffusion coefficient is included and the term divided by τ in (2.2.39) is changed by its inverse $\gamma_\parallel$ decay term. However, the decay term for the population difference it is usually written as a more general function that describes the carrier recombination due to spontaneous emission or non-radiative decays, and denoted as $R_{sp}(D)$. Here $R_{sp}(D) = \gamma_\parallel D$. In order to find an expression for the electrical susceptibility $\chi_e(\omega)$, Eq. (2.2.44) is solved in the Fourier frequency space, and comparing with (2.2.17) the susceptibility for the two level atom system reads

$$\chi_e(\omega, D) = -\frac{\widetilde{\mu}^2}{\hbar\epsilon_0} \frac{D}{\gamma_\perp + i(\delta - \omega)} \ . \qquad (2.2.47)$$

The real part of the susceptibility (2.2.47) has a Lorentzian shape and it is the responsible of the gain/absorption. The linewidth of the Lorentzian function is given by the polarization decay rate $\gamma_\perp$. The imaginary part of Eq. (2.2.47) gives a modification of the refractive index around the the transition frequency. Note that Eq. (2.2.47) depends on the population difference $D(z,t)$, this fact gives gain or amplification instead of absorption (see Fig. 2.2.4).

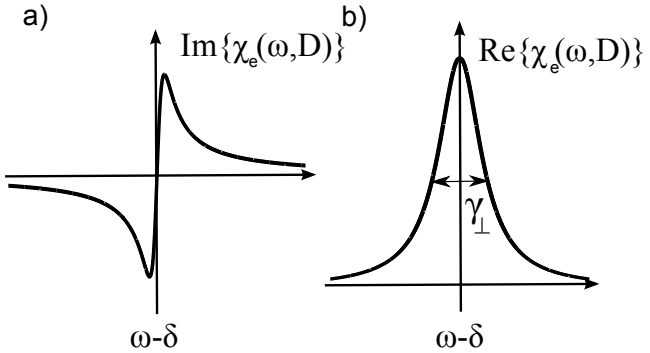

Fig. 2.2.4 – Schematic representation of (a) $\mathrm{Im}\{\chi_e(\omega, D)\}$ and (b) $\mathrm{Re}\{\chi_e(\omega, D)\}$ vs the angular frequency ω. In this case the imaginary part provides a modification of the refractive index around the transition frequency, whereas the real part is the responsible of the material gain. The width of the gain curve is given by the polarization decay rate $\gamma_\perp$.

(b) Semiconductor medium

The electronics of semiconductor lasers are based on the p-n junction of two donor/ acceptor doped semiconductor materials and the laser oscillation is realized by the emission of light due to carrier recombination between the conduction and valence bands (see Fig. 2.2.5). The energy band structure [109] of bulk and quantum well structures is constituted by different inner bands, they usually are completely filled and they do not contribute directly to the dynamical material response $\mathcal{P}(\vec{r}, t)$, as the resonances of the lattice and the strong bound electrons, they are included into the linear static response specified by the background refractive index. Due to the

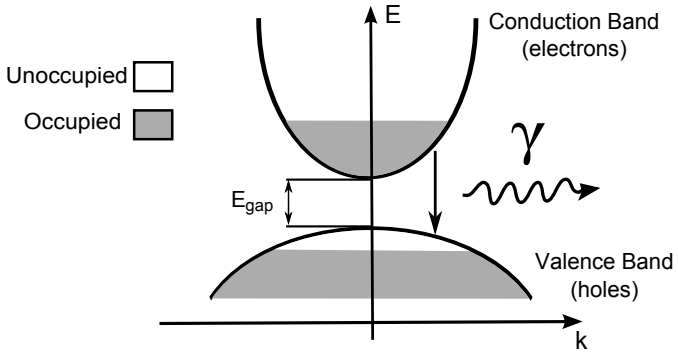

Fig. 2.2.5 – Schematic and simplified representation of the energy (E) band structure of a semiconductor bulk material for a wavenumber k of the reciprocal lattice within the first Brillouin zone [109]. The energy gap E_{gap} is the energy difference between the top of the valence band and the bottom of the conduction band. The electrons of the conduction band recombine with the holes of the valence band producing a photon γ.

band structure present in semiconductors the lasers fabricated with this material show particular characteristics, that are not found in the two level system approach:

- Many-body interactions are important due to high carrier density, particularly in gain structures with quantum confinement. Moreover there is a strong dephasing of the induced polarization.
- Semiconductor gain materials are characterized by a broad gain spectra and a strong coupling of the amplitude and phase dynamics (α factor).
- Semiconductor laser dynamics include different relevant time scales ranging from a few fs (for intraband Coulomb scattering) to several ns (for mesoscopic transport processes such as carrier diffusion).
- Spatial and spectral hole burning, and saturation effects are important, e.g. for fast (ps) dynamics or multimode (THz spectrum) description.
- Modern semiconductor lasers are composed of complex structured cavities, then the lasing modes may strongly differ from the cold-cavity modes because the lasing action and carrier dynamics (e.g. hole burning and thermal effects) change the refractive index structure.

Generally, the gain spectrum of a semiconductor medium is highly asymmetric and shows a typical profile in frequency, i.e. a sharp structure at the direct band edge and absorption for high frequencies (see Fig. 2.2.6).

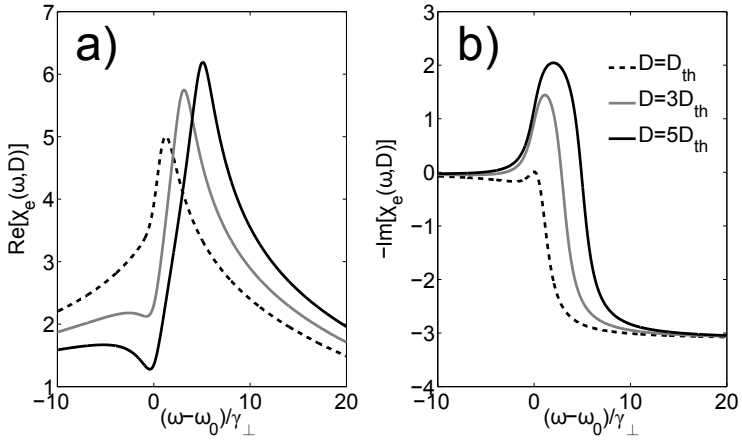

Fig. 2.2.6 – (a) Real part and (b) Imaginary part of the semiconductor susceptibility described in [111] vs the angular frequency ω for different population inversion values, $\chi_0 = 1$ and $b = 100$. The asymmetric gain curve is characterized by a gain region at the transition frequency and absorption for high frequencies.

These characteristics makes that the band structure of actual semiconductor lasers is not well modeled by a simple two-level system. However, the intra-band relaxation within the medium of the semiconductor laser is fast enough of the order of 10^{-13} s compared with the carrier recombination rate of 10^{-9} s [41]. This fact makes it possible to use approximately the model of two-level atoms for the theoretical investigation of the dynamics of semiconductor lasers. This approach has been used sometimes because marginal or medium numerical efforts are required even in a spatio-temporal description. Therefore, this approach allows the possibility to perform extensively parameter scans that one uses to carry out bifurcation analysis of nonlinear laser dynamics, and it is also used in modeling 3D novel microcavity structures [112], where the spatial dynamics can play a fundamental role.

One approach is to consider the semiconductor medium as an ensemble of many two level systems with different transitions frequencies as determined by the electronic band structure and with separated carrier inversions, and then consider the contributions supeerimposed of the various transitions. This would result in an inhomogeneously broadened system. However, due to the high carrier densities in a semiconductor laser and operation at room temperature, many-body effects like carrier-carrier Coulomb interaction and carrier-phonon interaction have to be taken into account [3].

The derivation of the microscopic model can be found in [113]. It uses the single particle approximation in the parabolic band structure approximation. It deals with 10^{23} ($\sim$ N_A) identical, indistinguishable and interacting particles, therefore a probabilistic approach as the density matrix formulation is needed. In this model some phenomenological terms are included to give a more realistic description. These mostly incoherent processes deal with the recombination of the carriers, the most important are nonradiative recombination, spontaneous emission, Auger recombination, carrier leakage and thermionic emission out of the optically active states [3].

The quantum microscopic approach including many-body effects for the semiconductor material is a more precise model, however it is difficult to implement numerically. It motivates the derivation of approximate models from microscopic models

[111] that allow to model the characteristic dynamics of the semiconductor medium without requiring the numerical efforts of the microscopic model. The electrical susceptibility from [111] read as

$$\chi_e(\omega, D) = -\chi_0 \left[2 \ln \left(1 - \frac{D}{u+i} \right) - \ln \left(1 - \frac{b}{u+i} \right) \right] , \qquad (2.2.48)$$

where

$$D = \frac{N}{N_{th}} \ , \ b = \frac{\hbar k_m^2}{2m\gamma_\perp} \ , \ u = \frac{\omega - E_t/\hbar}{\gamma_\perp} \ .$$

The band gap renormalization effects due to screened Coulomb interaction between electrons and holes have not be taken into account in (2.2.48), however they are introduced by a band gap shrinkage of the transition energy E_t, $E_t = E_t^0 - sD^{1/3}$. Other properties of the gain, differential gain, refraction index, and α factor of the active semiconductor medium can be found (see [111] for details). In this case, unlike the case for the two-level atom, the imaginary part provides the gain to the system (see Fig. 2.2.6). This will lead to a modification of the definition of polarization and Eqs. (2.2.44) and (2.2.46).

The coupling between the phase and amplitude dynamics in semiconductor lasers is typically large [114]. It is quantified by means of the linewidth enhancement factor or α factor. It is due essentially to the spontaneous emission noise that gives fluctuations in the phase of the electric field [115]. The increased linewidth result from a coupling between intensity and phase noise, caused by a dependence of the refractive index on the carrier density in the semiconductor. The α factor is a proportionality factor relating phase changes to changes of the amplitude gain. It was found that the linewidth should be increased by a factor of $(1 + \alpha^2)$, which turned out to be in reasonable agreement with experimental data [115]. The linewidth enhancement factor α can be determined as

$$\alpha = \frac{\mathrm{Re}\{\partial \chi_e / \partial D\}}{\mathrm{Im}\{\partial \chi_e / \partial D\}} \ . \qquad (2.2.49)$$

The value of the α factor for non-semiconductor lasers is almost zero, e.g. in the gas laser $\alpha \sim 0$ while in semiconductor lasers $\alpha \sim 2-5$ [116]. In RE models the α factor is usually included phenomenologically in the equations for the fields and has a constant value. In other approaches where the susceptibility for the semiconductor medium is explicitly used, the α factor is implicitly given in the susceptibility and it depends on the frequency and carrier inversion. For the susceptibility (2.2.48) the α factor at the frequency of the gain peak is given by [111]

$$\alpha = 2D - \sqrt{2D^2 - 1} - \frac{s}{3} D^{1/3} \ . \qquad (2.2.50)$$

II.3 Light dynamics in an optical cavity

II.3.1 Transverse and longitudinal cavity modes

Maxwell's equations have to be completed with the appropriate boundary conditions for each problem. The light in a laser, is characterized by a radiation field having slow transverse variations propagating in devices that have overall dimensions much larger than the optical wavelength. A first case is that of cavities used in gas and solid-state lasers [117]. These cavities consist of two end-reflectors having proper transverse (or lateral) shape such as a flat surface or a part of a large sphere (curved mirrors), known as Fabry-Pérot (FP) cavities. They are also called FP etalons or interferometers, and take its name after Charles Fabry and Alfred Pérot. FP cavities support fields that can be approximated as Transverse Electric and Magnetic (TEM) waves. In TEM waves the electric and the magnetic field lie approximately in the plane perpendicular to the direction of propagation.

The second case corresponds to waveguide modes. The modes for structures that have uniform transverse cross-section in the direction of propagation can be divided into TE (transverse electric) and TM (transverse magnetic) types. They are not TEM modes. However the two cases lead to an equivalent wave equation for the longitudinal mode that it will be discussed in the following.

(a) Mirror based cavity

In the case of a FP cavity with curved mirrors (see Fig. 2.3.7), the beam has a narrow aperture in the direction transverse to the propagation, it diverges from the propagation direction due to diffraction. The linearly polarized electric field can be projected to separated transverse and longitudinal modes,

$$\mathcal{E}_y(\vec{r},\omega) = \sum_{m,l,n} \mathcal{E}_m(z,\omega)\psi_{l,n}(x,y,\omega) \ . \tag{2.3.51}$$

The cavity selects the modes that resonate within it, mathematically it consists of applying boundary conditions to the wave equations. The solutions are labeled with the integer m corresponding to the longitudinal mode and the integers l and n corresponding to the transverse modes. In this case the transverse amplitude distributions for the waves can be described [61] as

$$\psi_{l,n}(x,y) = H_l\left(\frac{\sqrt{2}x}{w}\right) H_n\left(\frac{\sqrt{2}y}{w}\right) e^{-(x^2+y^2)/w^2} \ , \tag{2.3.52}$$

where $H_l(u)$ are the Hermite polynomials, that take the form

$$H_l(u) = (-1)^l e^{u^2} \frac{d^l(e^{-u^2})}{du^l} \ . \tag{2.3.53}$$

and w is the beam waist. The spatial intensity distribution is the square root of the amplitude distribution function. The transverse modes are designated TEM_{ln}. The lowest order is given by TEM_{00}, which has a circular distribution with gaussian shape (often referred to as the gaussian mode, see Fig. 2.3.7) and has the smallest divergence of any of the transverse modes.

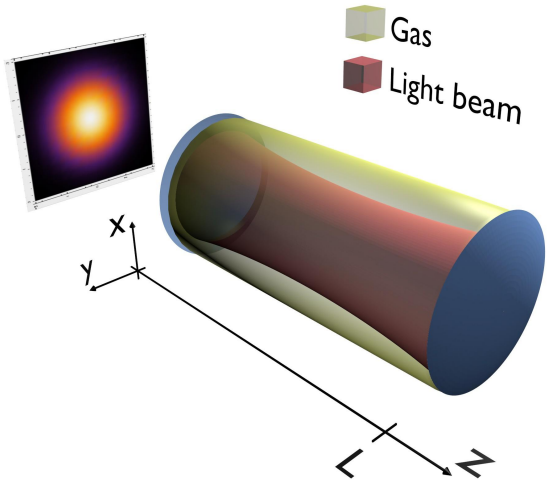

Fig. 2.3.7 – Schematic representation of a FP laser of length L. The gas is composed by an active material and a host material. The light beam is waisted because the curvature of the mirrors. In the rear part it is shown the projection of the transverse mode, a TEM_{00}.

(b) Waveguide

In semiconductors lasers the cavity is defined by lithography in the same semiconductor medium, and the mirrors are usually sketched by cutting the semiconductor medium and forming a refractive index jump between the semiconductor medium and air. The transversal cross-section is constant in this case, and the transverse modes are those corresponding to a rectangular waveguide. Assuming a waveguide as depicted in Fig. 2.3.8. In this case due to the symmetry of the waveguide, an expression like (2.3.52) can not be found. The rectangular structure leads to a separation of the transverse solutions of the electric field in TE and TM modes instead of TEM waves [118]. One of the most important characteristics of waveguide modes are the exponential decay of their evanescent tails. This enables to interact with the waveguide mode by placing perturbations close to the surface of the waveguide, e.g. the evanescent coupler formed by two adjacent waveguides (see Fig. 1.2.3) or a grating filter fabricated on the top of a waveguide.

Assuming that L goes to infinity, that there are not variations in the y direction. In the case of TE solutions, the electric and the magnetic fields read as

$$\vec{E} = A(x)e^{i\beta z}\vec{e}_y \ , \qquad \boxed{2.3.54}$$

$$\vec{H} = \left[B(x)\vec{e}_x + C(x)\vec{e}_z\right] e^{i\beta z} \ , \qquad \boxed{2.3.55}$$

Applying boundary conditions on x we found

$$A(x) = \begin{cases} A_0 e^{qx} & \text{for } x > 0 \\ A_0 \left[\cos hx - \frac{q}{h}\sin hx\right] & \text{for } -a < x < 0 \\ A_0 \left[\cos ha + \frac{q}{h}\sin ha\right] e^{p(x+a)} & \text{for } x < -a \end{cases}$$

where

$$q = \sqrt{\beta^2 - \frac{\omega^2}{c^2}n_1^2} \ , \ h = \sqrt{\frac{\omega^2}{c^2}n_2^2 - \beta^2} \ , \ p = \sqrt{\beta^2 - \frac{\omega^2}{c^2}n_3^2}$$

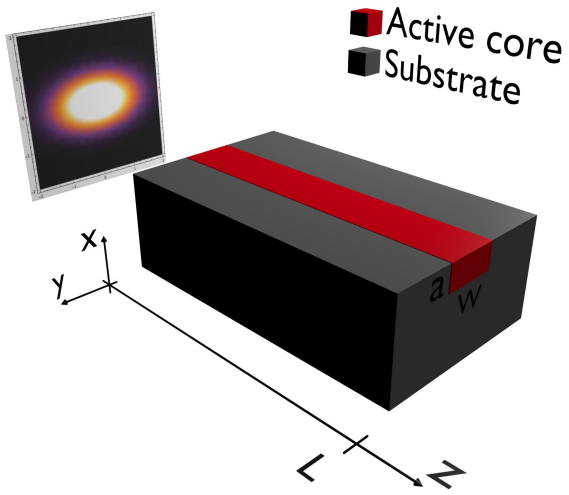

Fig. 2.3.8 – Schematic representation of a waveguide of length L. The active core dimensions are w, a and L.

where n_1, n_2 and n_3 denote the different refractive indexes of the materials. Note that $(\omega/c)n_2 \geq \beta \geq (\omega/c)n_3$. Now $A(x)$ is continuous at $x = 0$ and $x = -a$ and $d_x A(x)$ is continuous at $x = 0$. Imposing continuity of $d_x A(x)$ at $x = -a$, one finds

$$\tan(ha) = h\frac{p+q}{h^2 - pq} \ , \qquad \boxed{2.3.56}$$

this transcendental equation determines numerically the allowed propagation constants β for a given ω, a and the refractive indexes. It has multiple solutions, $l = 0, ..., M$, each corresponds to a transverse mode, TE_l. Once β_l is known, p, q and h can be determined, and therefore the spatial profile of the corresponding TE_l solution. Analogously an expression for the TM mode can be found.

(c) Wave equation for the longitudinal modes amplitudes

Optical materials are non-magnetic and possess an electrical conductivity σ. The field is assumed transversal, a TEM_{00} wave. With these assumptions, Eqs. (2.2.12) and (2.2.14) read in the Fourier frequency space

$$\nabla \times \vec{\mathcal{E}}(\vec{r},\omega) = i\mu_0\omega\vec{\mathcal{H}}(\vec{r},\omega) \ , \qquad \boxed{2.3.57}$$

$$\nabla \times \vec{\mathcal{H}}(\vec{r},\omega) = -i\epsilon_0\omega\vec{\mathcal{E}}(\vec{r},\omega) - i\omega\vec{\mathcal{P}}(\vec{r},\omega) + \sigma\vec{\mathcal{E}}(\vec{r},\omega) \ , \qquad \boxed{2.3.58}$$

by combining the last two equations and making use of (2.2.26), the wave equation takes the form

$$\nabla^2\vec{\mathcal{E}}(\vec{r},\omega) + \frac{\omega^2}{c^2}\vec{\mathcal{E}}(\vec{r},\omega) = -\mu_0\omega^2\vec{\mathcal{P}}(\vec{r},\omega) - i\mu_0\omega\sigma\vec{\mathcal{E}}(\vec{r},\omega) \ . \qquad \boxed{2.3.59}$$

The polarization $\vec{\mathcal{P}}(\vec{r},\omega)$ is usually expressed as the superposition of two contributions,

$$\vec{\mathcal{P}}(\vec{r},\omega) = \vec{\mathcal{P}}_{back}(\vec{r},\omega) + \vec{\mathcal{P}}_{act}(\vec{r},\omega) \ , \qquad \boxed{2.3.60}$$

where $\vec{\mathcal{P}}_{back}(\vec{r},\omega)$ is due to the background medium, i.e. the dielectric material in a semiconductor laser or the host gas in a gas laser. The role of the background polarization is to give an effective refractive index frequency independent, on the other hand $\vec{\mathcal{P}}_{act}(\vec{r},\omega)$, the polarization of the active medium describes the gain/absorption and dispersion of the active medium. The polarization of the background medium can be written as

$$\vec{\mathcal{P}}_{back}(\vec{r},\omega) = \epsilon_0 \widetilde{\chi}_e(\omega)\vec{\mathcal{E}}(\vec{r},\omega) \ , \tag{2.3.61}$$

also defining an effective refractive index,

$$n_{ef}(\omega) = \sqrt{1+\widetilde{\chi}_e(\omega)} \ . \tag{2.3.62}$$

By using the background and the active medium polarizations, Eq. (2.3.59) becomes

$$\nabla^2\vec{\mathcal{E}}(\vec{r},\omega) + \frac{\omega^2}{c^2}n_{ef}^2\vec{\mathcal{E}}(\vec{r},\omega) = -\mu_0\omega^2\vec{\mathcal{P}}_{act}(\vec{r},\omega) - i\mu_0\omega\sigma\vec{\mathcal{E}}(\vec{r},\omega) \ , \tag{2.3.63}$$

using (2.3.51) in the above wave equation one arrives to

$$\sum_{m,l,n}\left[\left(\frac{\partial^2\psi_{l,n}}{\partial x^2}+\frac{\partial^2\psi_{l,n}}{\partial y^2}+\frac{\omega^2}{c^2}n_{ef}^2\psi_{l,n}\right)\mathcal{E}_m\left(\frac{\partial^2\mathcal{E}_m}{\partial z^2}+i\mu_0\omega\sigma\mathcal{E}_m\right)\psi_{l,n}\right] = -i\mu_0\omega^2\vec{\mathcal{P}}_{act} \ . \tag{2.3.64}$$

recalling

$$\frac{\partial^2\psi_{l,n}}{\partial x^2}+\frac{\partial^2\psi_{l,n}}{\partial y^2}+\frac{\omega^2}{c^2}n_{ef}^2(\omega)\psi_{l,n} = \beta^2\psi_{l,n} \ , \tag{2.3.65}$$

and projecting on the transversal modes, the following wave equation for the longitudinal modes amplitudes is obtained,

$$\frac{\partial^2\mathcal{E}_m}{\partial z^2}+\beta^2\mathcal{E}_m = -\mu_0\omega^2\widetilde{\mathcal{P}}_{act} - i\mu_0\omega\sigma\mathcal{E}_m \ , \tag{2.3.66}$$

where

$$\widetilde{\mathcal{P}} = \epsilon_0\int_{act.reg.}\chi_e(\omega)\psi^*\psi \ dx \ dy \ \mathcal{E}_m \ , \tag{2.3.67}$$

where *act.reg.* denotes the active region. The polarization $\vec{\mathcal{P}}_{act}$ is nonvanishing in the active region. Assuming that in our case all the medium is active as depicted in Fig. 2.3.7, therefore $\widetilde{\mathcal{P}} = \mathcal{P}_{act} = \mathcal{P}$ and $\beta = \omega_m n_{ef}/c$. Under this assumption and dropping out the subindex m, the wave equation reads

$$\frac{\partial^2\mathcal{E}}{\partial z^2}+\frac{\omega^2}{c^2}n_{ef}^2\mathcal{E} = -\mu_0\omega^2\mathcal{P} - i\mu_0\omega\sigma\mathcal{E} \ . \tag{2.3.68}$$

Now returning to the spatio-temporal picture, performing the inverse Fourier transform in time of Eq. (2.3.68), one obtains

$$\frac{\partial^2\mathcal{E}}{\partial z^2}-\frac{n_{ef}^2}{c^2}\frac{\partial^2\mathcal{E}}{\partial t^2} = \mu_0\frac{\partial^2\mathcal{P}}{\partial t^2}-\mu_0\sigma\frac{\partial\mathcal{E}}{\partial t} \ . \tag{2.3.69}$$

The background material is taken into account by the effective refractive index n_{ef}, while the active material is accounted by the polarization $\mathcal{P}(z,t)$ term, which electrical susceptibility will characterize the interaction between the light and the active medium. The last term in (2.3.69) takes into account the presence of free currents that will cause losses in the propagation of the electric field.

For a waveguide, the derivation of the wave equation of the longitudinal modes is equivalent. However, in this case the light is not only confined in the active medium or core of the waveguide. The wave equation for the longitudinal modes amplitudes in a waveguide reads

$$\frac{\partial^2 \mathcal{E}}{\partial z^2} + \beta^2 \mathcal{E} = -\Gamma \frac{\omega^2}{c^2} \chi_e(\omega, N)\mathcal{E} - i\mu_0 \omega \sigma \mathcal{E} \quad , \tag{2.3.70}$$

where Γ is the confinement factor [119] that can be written as

$$\Gamma_{TE}^{(l)} = \frac{\int_{-a}^{0} |A_l(x)|^2}{\int_{-\infty}^{\infty} |A_l(x)|^2} \quad . \tag{2.3.71}$$

Note that Eq. (2.3.70) is written in the frequency domain, this is due because the response of the semiconductor medium is only known in the frequency domain (see Eq. (2.2.48)) in contrast with the response of the two level atom, that was found in the time domain. However, it is equivalent to Eq. (2.3.68). To translate Eq. (2.3.70) to time domain, a convolution of the susceptibility $\chi_e(\omega, D)$ with the electric field $\mathcal{E}$ has to be done. However, this convolution is very difficult to do, and only can be approximated via a Padé and parabolic approximations [101], or by numerical calculation of the convolution [120].

II.3.2 The slowly varying envelope approximation

Usually when describing laser dynamics, the electric field components are written in an approximation allowing to write the wave equation (2.3.69) in a more convenient way for treating it. The Slowly Varying Envelope Approximation (SVEA) consists in neglecting the fast variations of the field due to its optical frequency and to retain the slow variations. Assuming a quasimonochromatic field $\mathcal{E}(z,t)$ around the optical carrier frequency ω_0. In order to obtain a general solution, the field can be decomposed in their different propagation directions and positive and negative frequency parts,

$$\mathcal{E}(z,t) = [E_+(z,t)e^{iq_0 z} + E_-(z,t)e^{-iq_0 z}]e^{-i\omega_0 t} + c.c. \ , \tag{2.3.72}$$

where the amplitudes for the two propagation directions $E_+(z,t)$ and $E_-(z,t)$, have a time and space dependence much smoother than that of the exponential function in (2.3.72) and the wavenumber q_0 is related to ω_0 by $q_0 = \omega_0 n_{ef}/c$. The decomposition (2.3.72) in the different slow and fast temporal components can be seen as the Amplitude Modulation (AM) used in radio broadcasting, in this case the signal is the slow component of the field, and the carrier radiofrequency wave is our optical frequency.

In the same way one decomposes the polarization $\mathcal{P}(z,t)$, in the rotating wave approximation, i.e. supposing a quasi-resonant light-matter interaction. The polarization can be written as

$$\mathcal{P}(z,t) = i\left\{[P_+(z,t)e^{iq_0 z} + P_-(z,t)e^{-iq_0 z}]e^{-i\omega_0 t} - c.c.\right\} \ , \tag{2.3.73}$$

substituting (2.3.72) and (2.3.73) in (2.3.69). At this point is when the SVEA is called, under the assumption that

$$\left|\frac{\partial^2 E_\pm}{\partial z^2}\right| \ll \left|\frac{\partial E_\pm}{\partial z}\right| \ll q_0|E_\pm| \quad \text{and} \quad \left|\frac{\partial^2 E_\pm}{\partial t^2}\right| \ll \left|\frac{\partial E_\pm}{\partial t}\right| \ll \omega_0|E_\pm| \ ,$$

where $E_\pm(z,t) = E_\pm$ and $P_\pm(z,t) = P_\pm$ to simplify the notation. Then under the SVEA, one obtains

$$\begin{aligned}\left(2iq_0\mathcal{F}_z(E_+,E_-)e^{-i\omega_0 t}+c.c.\right) &+ \frac{n_{ef}^2}{c^2}\left(2i\omega_0\mathcal{G}_t(E_+,E_-)e^{-i\omega_0 t}+c.c.\right) \\ &= -i\mu_0\omega_0^2\left[\left(P_+e^{iq_0z}+P_-e^{-iq_0z}\right)e^{-i\omega_0 t}-c.c.\right] \\ &- i\mu_0\sigma\omega_0\left[\left(E_+e^{iq_0z}+E_-e^{-iq_0z}\right)e^{-i\omega_0 t}+c.c.\right]\end{aligned} \tag{2.3.74}$$

where

$$\mathcal{F}_z(E_+,E_-) = \frac{\partial E_+}{\partial z}e^{iq_0z} - \frac{\partial E_-}{\partial z}e^{-iq_0z}\ ,\ \mathcal{G}_t(E_+,E_-) = \frac{\partial E_+}{\partial t}e^{iq_0z} + \frac{\partial E_-}{\partial t}e^{-iq_0z}\ ,$$

and the bigger contribution in each term is retained. Multiplying (2.3.74) by $e^{i\omega_0 t}$ and making an average in a time interval τ taking into account the characteristic time scales $\lambda/v \ll \tau \ll L/v$, e.g. for the first term in (2.3.74) one obtains

$$\frac{2iq_0}{2\tau}\int_{t-\tau}^{t+\tau}\left[\mathcal{F}_z(E_+,E_-) - \mathcal{F}_z^*(E_+,E_-)e^{2i\omega_0 t}\right]dt = 2iq_0\left(\frac{\partial E_+}{\partial z}e^{iq_0z} - \frac{\partial E_-}{\partial z}e^{-iq_0z}\right)\ ,$$

where after the integration the limit $\tau \to 0$ is taken. Then repeating this process in all the terms in (2.3.74), one obtains

$$\begin{aligned}&2iq_0\left(\frac{\partial E_+}{\partial z}e^{iq_0z} - \frac{\partial E_-}{\partial z}e^{-iq_0z}\right) + \frac{2i\omega_0}{c^2}\left(\frac{\partial E_+}{\partial t}e^{iq_0z} + \frac{\partial E_-}{\partial t}e^{-iq_0z}\right) \\ &\quad = -i\mu_0\omega_0^2(P_+e^{iq_0z}+P_-e^{-iq_0z}) - i\mu_0\sigma\omega_0(E_+e^{iq_0z}+E_-e^{-iq_0z})\ .\end{aligned} \tag{2.3.75}$$

In the same way as the time average, the spatial average of (2.3.75) is done for the two counter-propagating fields (multiplying (2.3.75) by e^{-iq_0z} or e^{iq_0z} in each case), by taking a space Δ that accomplish $\lambda \ll \Delta \ll L$. The two wave equations obtained can be written as

$$\pm\frac{\partial E_\pm}{\partial z} + \frac{n_{ef}}{c}\frac{\partial E_\pm}{\partial t} = -\frac{\mu_0\omega_0 c}{2n_{ef}}P_\pm - \frac{\mu_0\sigma c}{2n_{ef}}E_\pm\ . \tag{2.3.76}$$

The wave equations (2.3.76) describe the propagation of the two counterpropagating electric fields $E_\pm(z,t)$ in a medium characterized by the polarizations $P_\pm(z,t)$ associated to each electric field.

II.3.3 Longitudinal modal properties of ring cavities

The longitudinal modes treated here are *cold* or *passive* cavity modes, it means that the gain in the material is zero. The contribution of the material susceptibility is not included. Mathematically, these modes form a complete orthogonal set, meaning that any radiation field can be expressed as a superposition of these modes. The longitudinal modes characterize the wavelength output of the laser. In the literature the term single-mode laser is extensively used, it refers to one single longitudinal mode operating or lasing. While multimode operation refers to different longitudinal modes lasing, that will lead to different phenomena including chaos and mode-locked operation [61].

The ring cavity consists in three or four corner mirrors placed in a configuration that they form a closed loop. In this case one of the mirrors has a non zero transmitivity which defines the output, while the other mirrors have ideally full reflectivity

and no transmitivity. In order to create a laser, an active medium can be placed in one of the arms formed by the cavity. On the other hand, Semiconductor Ring Lasers (SRLs) can not have mirrors. They can have circular, triangular or rectangular shapes because they are defined by lithography, and the active medium can be placed all along the cavity. However, those that are fabricated without mirrors, e.g. the circular ones, have reflections and losses due to the curvature of the waveguides or the light-extraction sections.

In a ring resonator, the optical electric field can have two components traveling in opposites directions. In the absence of any reflective point the light waves are pure traveling waves, in contrast with the standing waves developed in a FP cavity. However, in real devices there are always sources of reflection due to different factors, e.g. the light extraction sections, the back-reflections at the mirrors or the impurities in a semiconductor material. Therefore the electric fields in a ring cavity show a mix between a standing waves and traveling waves behaviors allowing this devices to show different behaviors than the shown by FP devices.

Considering a ring cavity where the propagation direction z is running along the ring. Each monochromatic component at frequency ω of electric field can be written as the superposition of two counter-propagating components

$$E(z,\omega) = A_F(\omega)e^{iq(\omega)z} + A_B(\omega)e^{-iq(\omega)z} \ , \qquad (2.3.77)$$

the boundary constraints set a value of the wavevector q for each Fourier component, shaping a dispersion relationship. A lossless circular cavity would yield

$$q_m(\omega) = \frac{2\pi m}{L} \quad \text{where} \quad m = 0, \pm 1, \pm 2, ... \ , \qquad (2.3.78)$$

where a subindex m is introduced for denoting a particular solution of the infinite set of solutions. Ideal circular symmetry is never met in real devices, e.g. due to fabrication imperfections, so it is interesting to evaluate the effect of the circular symmetry breaking consequent to the presence of a localized defect (see Fig. 2.3.9). A special point in the cavity introduces complex reflection $r_{1,2}$ and transmission $t_{1,2}$

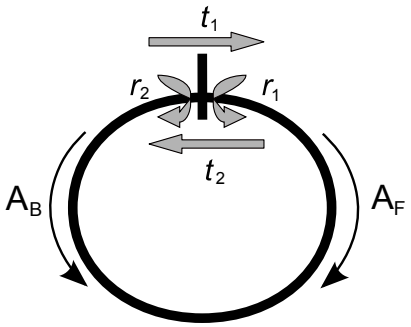

Fig. 2.3.9 – Schematic representation of a ring laser with a special point. The special point is characterized by reflection (r_1 and r_2) and transmission (t_1 and t_2) coefficients. The electric field has two components inside the cavity, a forward field A_F and backward field A_B.

coefficients, which in general, can depend on ω. A natural choice is to set the point $z = 0$ in correspondence of the defect. The continuity of the electric field (2.3.77) leads to boundary conditions that can be written as

$$A_F = r_1 A_B + t_1 A_F e^{iq(\omega)L} \ , \qquad (2.3.79)$$

$$A_B e^{-iq(\omega)L} = r_2 A_F e^{iq(\omega)L} + t_2 A_B \ . \qquad (2.3.80)$$

This system of equations has a non-trivial solution iff

$$(1 - Te^{iq(\omega)L})^2 = R^2 e^{2iq(\omega)L} \ , \tag{2.3.81}$$

where $t_1 = t_2 = T$ and $r_1 = r_2 = R$ is supposed for simplicity. This assumption reflects the fact that the typical structure of light extraction used in semiconductor ring lasers is considered, where light from the ring cavity is evanescently coupled into a bus waveguide. In these structures, reflections come mostly from the end of the bus waveguide after passing twice through the evanescent coupler. In such a situation the transmission and reflection coefficients are determined mainly by propagation along the coupler and the bus and they have no predetermined relationships, like in the scattering matrix formalism of lossless mirrors, where if r is real t must be purely imaginary [121]. Solving Eq.(2.3.81) for q, one obtains

$$q_m^{\pm}(\omega) = \frac{2\pi m}{L} + \frac{i}{L}\ln(T \pm R) \quad \text{where} \quad m = 0, \pm 1, \pm 2, ... \tag{2.3.82}$$

Eq. (2.3.82) shows that the degeneracy characterizing the solutions of the ideal ring has been removed by the introduction of a defect. The consequence of the symmetry breaking is the appearance of two families of solutions (+ and −) for the wavenumber q.

In order to further understanding, one can consider that defect can be regarded as a point with no associated losses, T and R fulfill the following conservation law and reciprocity conditions, respectively yielding (see [121])

$$\begin{cases} |T|^2 + |R|^2 = 1 \\ RT^* + R^*T = 0 \end{cases} \rightarrow |T \pm R| = 1 \ , \tag{2.3.83}$$

and then writing the transmission and reflection coefficients through one parameter $\theta_{\pm}$ as

$$T \pm R = e^{i\theta_{\pm}}. \tag{2.3.84}$$

And finally, relating $\theta_{\pm}$ to R as

$$\theta_{\pm} = -\arctan\frac{\mathrm{Im}(R)}{\mathrm{Re}(R)} \pm \arcsin|R| \ . \tag{2.3.85}$$

The relation for the wavenumber becomes

$$q_{\pm}(\omega) = \frac{2\pi m}{L} - \frac{\theta_{\pm}}{L} \quad \text{where} \quad m = 0, \pm 1, \pm 2, ... \tag{2.3.86}$$

Note that the effect of the special point is a displacement of the wave number if $R \in \mathbb{C}$ and a splitting if $0 < |R| < 1$ (see Fig. 2.3.10). In the limit $|R| = 0$ the ideal ring (2.3.78) is found. While for $|R| = 1$ a lossless FP cavity is found.

The same methodology used to find Eq. (2.3.82) can be used to obtain the modes of a FP cavity. Assuming a FP cavity as shown in Fig. 2.3.11, the separation between the mirrors is L and each mirror has a reflection coefficient associated r_1 and r_2. In this case the boundary conditions read as

$$\begin{aligned} A_F(0,\omega) &= r_1 A_B(0,\omega) \ , \\ A_B(L,\omega) &= r_2 A_F(L,\omega) \ , \end{aligned} \tag{2.3.87}$$

and using a plane wave solution, we can write the boundary conditions as

$$\begin{aligned} A_F(0,\omega) &= r_1 A_B(0,\omega) \ , \\ A_B(0,\omega)e^{-iq(\omega)L} &= A_F(0,\omega)e^{iq(\omega)L} \ . \end{aligned} \tag{2.3.88}$$

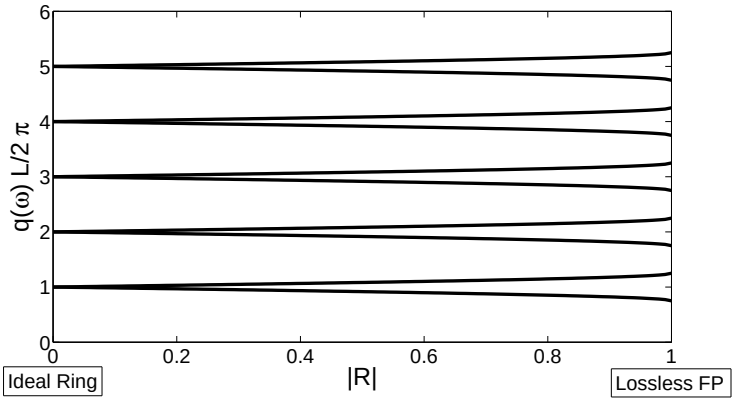

Fig. 2.3.10 – Splitting of the modes $m = 1, 2, 3, 4, 5$ calculated from Eq. (2.3.86) vs $|R|$. The ideal ring case (2.3.78) is obtained for $|R| = 0$, and the lossless Fabry-Pérot case (2.3.90) is obtained for $|R| = 1$. A lossless ring will have a splitting corresponding to the intermediate zone of the figure.

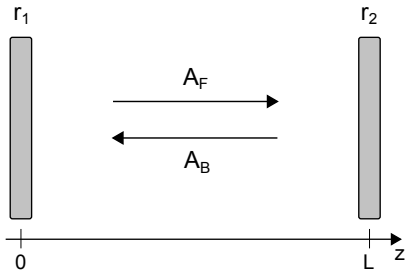

Fig. 2.3.11 – Schematic representation of a Fabry-Pérot cavity of length L. The cavity is composed by two reflective mirrors characterized by the reflective coefficients r_1 and r_2. The electric field has two components inside the cavity, a forward field A_F and backward field A_B.

The system of equations (2.3.88) has the trivial solution $A_F = A_B = 0$ and also has the solution

$$r_1 r_2 e^{2iq(\omega)L} = 1 \tag{2.3.89}$$

then the solution for the wavenumber q is

$$q_m(\omega) = \frac{\pi m}{L} - \frac{i}{2L} \ln \frac{1}{r_1 r_2} \quad \text{where} \quad m = 0, \pm 1, \pm 2, \dots \quad , \tag{2.3.90}$$

If the reflectivities are real numbers, we note that the second term in (2.3.90) are the losses of the electric field due to the mirrors. On the other hand the first term gives the frequencies allowed in the cavity, i.e. the longitudinal modes,

$$\omega_m = \frac{\pi m}{L n_{ef}} c \quad \text{where} \quad m = 0, \pm 1, \pm 2, \dots \ . \tag{2.3.91}$$

The varying transmission function of a FP etalon is caused by interference between the multiple reflections of light between the two reflecting surfaces. Constructive interference occurs if the transmitted beams are in phase, and this corresponds to a high-transmission peak of the etalon. If the transmitted beams are out-of-phase,

destructive interference occurs and this corresponds to a transmission minimum. It depends on the wavelength of the light and the length of the etalon to this interference to be constructive. Therefore standing waves are formed in a FP cavity.

II.4 Hierarchy of ring lasers dynamical models

The semiclassical models are based in the description of three variables: the complex electric field, the polarization of the medium and the population inversion, by means of their dynamical equations derived from Maxwell's equations and the Schrödinger equation. The different longitudinal and transverse modes inside an optical cavity have been discussed. For the rest of the thesis only the longitudinal modes are taking into account. The longitudinal modes wave equation for the slowly varying electric fields $E_\pm$ reads

$$\pm \frac{\partial E_\pm}{\partial z} + \frac{n_{ef}}{c}\frac{\partial E_\pm}{\partial t} = -\frac{\mu_0\omega_0 c}{2n_{ef}}P_\pm - \frac{\mu_0\sigma c}{2n_{ef}}E_\pm \ . \tag{2.4.92}$$

Using (2.3.72) and (2.3.73) into (2.2.44) and (2.2.46) evidences that the presence of counter-propagating fields creates a spatial modulation of the population inversion. This important property follows from the iterative relationship between the diagonal and off-diagonal matrix elements of the density matrix $\hat{\rho}$ [122]. As a result only odd harmonics appear in the expansion of $\mathcal{P}$ and only even harmonics appear in the expansion of the population difference D. This spatial modulation acts as a Bragg grating and creates a coupling between the counter-propagating fields. In order to get the dynamics of this grating explicitly the population difference is decomposed in different spatial contributions as

$$D = D_0 + D_{+2}e^{2iq_0z} + D_{-2}e^{-2iq_0z} + \dots \ . \tag{2.4.93}$$

Such a decomposition yields an infinite hierarchy of equations that has to be truncated in order to keep the problem treatable. In systems with large diffusion, the truncation can be justified due to the quadratically increasing damping of the high-order terms [101, 123]; in other cases, the intensity of the fields has to be low compared to the saturation intensity of the medium [54]. To the dominant order, for a two level atom system the medium evolves according to

$$\frac{\partial P_\pm}{\partial t} = -(i\delta + \gamma_\perp)P_\pm - \frac{\widetilde{\mu}^2}{\hbar}(D_0E_\pm + D_{\pm2}E_\mp) \ , \tag{2.4.94}$$

$$\frac{\partial D_0}{\partial t} = \frac{2}{\hbar}(E_+P_+^* + E_-P_-^* + c.c.) + \gamma_\parallel(J - D_0) + \mathbb{D}\frac{\partial^2 D_0}{\partial z^2} \ , \tag{2.4.95}$$

$$\frac{\partial D_{\pm2}}{\partial t} = \frac{2}{\hbar}(E_\pm P_\mp^* + E_\mp^* P_\pm) - (\gamma_\parallel + 4q_0^2\mathbb{D})D_{\pm2} \ , \tag{2.4.96}$$

where $|\partial_z D_{\pm2}| \ll q_0|D_{\pm2}|$ is used twice. The diffusion tries to smear out the grating in the population inversion (2.4.96) by inducing a much larger effective relaxation rate for $D_{\pm2}$ than for D_0. Another characteristic is that the polarization in the forward direction has a contribution from the field in the backward direction and viceversa. This "reflection on the grating" leads to saturation effects of the fields. Eqs. (2.4.92) and (2.4.94)-(2.4.96) form the Traveling Wave (TW) model for a two level atom medium, they have to be completed with the appropriate boundary conditions as shown in II.3.3. This model will be profoundly studied in chapter IV. A modification of this model for the semiconductor medium is presented in section V.2. In the following the RE model for the unidirectional and bidirectional cases from the TW model are derived.

II.4.1 Unidirectional ring laser: The Haken-Lorenz model

Considering the simplest case, a laser with a ring resonator in which only one mode in one direction is allowed (unidirectional single-mode ring laser) with a two-level atom medium (homogeneously broadened laser) as shown in Fig. 2.4.12. Bidirectional emission is not allowed due to the insertion of an optical isolator which is composed by a Faraday rotator. Assuming a uniform refractive index of the laser medium and

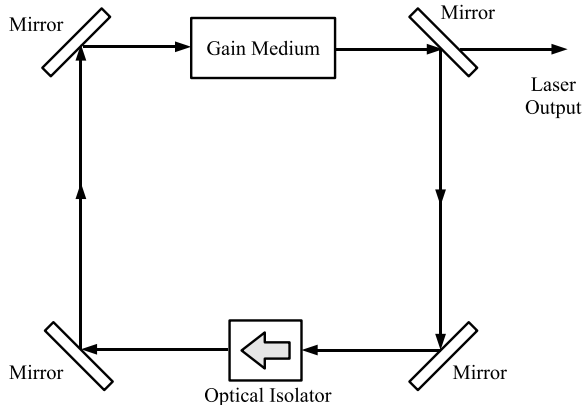

Fig. 2.4.12 – Schematic representation of a unidirectional ring laser. The optical isolator only allows propagation in one direction.

linearly polarized spatial modes for the x and y directions with the propagation for the z axis, the field and the polarization of matter reduce to scalar complex quantities propagating only along the z direction as we see in the previous sections. In this case only one direction of propagation is allowed, i.e. $E_+ \neq 0$ and $E_- = 0$, then $P_+ \neq 0$ and $P_- = 0$ and the grating term vanishes $D_{\pm 2} = 0$. The boundary conditions in this case read as

$$E(0,t) = TE(L,t)e^{iq_0 L} = TE(L,t)e^{i\frac{\omega_0}{c}n_{ef}L} \ , \qquad \boxed{2.4.97}$$

where ω_0 is the carrier frequency introduced in section II.3.2. For simplicity the carrier frequency ω_0 is assumed to correspond to one of the modes of the cavity, therefore $e^{i\frac{\omega_0}{c}n_{ef}L} = 1$. In the single-mode regime the electric field can be written as

$$E_+(z,t) = A(t)e^{iqz} \ , \qquad \boxed{2.4.98}$$

where $A(t)$ does not depend on the space. Then substituting this solution in Eq. (2.4.97) one finds,

$$q_m = \frac{2\pi m}{L} + \frac{i}{L}\ln T \quad \text{where} \quad m = 0, \pm 1, \pm 2, ..., \qquad \boxed{2.4.99}$$

in agreement with Eq. (2.3.82). Substituting (2.4.99) in Eq. (2.4.92) one obtains

$$iqAe^{iqz} + \frac{n_{ef}}{c}\frac{\partial A}{\partial t}e^{iqz} = -\frac{\mu_0\omega_0 c}{2n_{ef}}P_+ - \frac{\mu_0\sigma c}{2n_{ef}}Ae^{iqz} \ , \qquad \boxed{2.4.100}$$

Next, projecting into the dual mode space with

$$\frac{1}{L}\int_0^L dz \ e^{-iqz} \ , \qquad \boxed{2.4.101}$$

and the equation that describes the temporal evolution of each longitudinal mode can be written as

$$\frac{dA}{dt} = -\frac{c}{n_{ef}}\left(\frac{1}{L}\ln T - \frac{\mu_0\sigma c}{2n_{ef}}\right)A - \frac{\mu_0\omega_0 c^2}{2n_{ef}^2}B \ , \tag{2.4.102}$$

where Eq. (2.4.99) have been used and the next definition

$$B(t) = \frac{1}{L}\int_0^L dz\ P_+(z,t)e^{-iqz} \ . \tag{2.4.103}$$

Following the same process with Eq. (2.4.94) for the polarization, one obtains

$$\frac{dB}{dt} = -(i\delta + \gamma_\perp)B - \frac{\widetilde{\mu}^2}{\hbar}\hat{D}_0 A \ , \tag{2.4.104}$$

where D_0 is assumed constant near threshold or/in the Uniform Field Limit (UFL) where the spatial effect are not important. Moreover the hat in $\hat{D}_0$ denotes the space average of this quantity. From Eq. (2.4.95), one obtains

$$\frac{d\hat{D}_0}{dt} = \frac{2}{\hbar}\left[AB^* + A^*B\right] + \gamma_\parallel(\hat{J} - \hat{D}_0) \ , \tag{2.4.105}$$

where the diffusion term are neglected. Supposing that the frequency of this mode is ω_c. To take ω_c into account explicitly one changes the reference frame with $A(t) = a(t)e^{i\omega_c t}$ and $B(t) = b(t)e^{i\omega_c t}$, obtaining

$$\frac{da}{dt} = -(i\omega_c + \alpha_{tot})a - \frac{\mu_0\omega_0 c^2}{2n_{ef}^2}b \ , \tag{2.4.106}$$

$$\frac{db}{dt} = -(i\delta + \gamma_\perp)b - \frac{\widetilde{\mu}^2}{\hbar}\hat{D}_0 a \ , \tag{2.4.107}$$

$$\frac{d\hat{D}_0}{dt} = \frac{2}{\hbar}(ab^* + a^*b) + \gamma_\parallel(\hat{J} - \hat{D}_0) \ , \tag{2.4.108}$$

where one has group together the losses due to the material and to the cavity in a parameter α_{tot},

$$\alpha_{tot} = \frac{c}{n_{ef}}\left(\frac{\mu_0\sigma c}{2n_{ef}} - \frac{1}{L}\ln T\right) \ . \tag{2.4.109}$$

In order to write the laser equations in a form that is usually found in textbooks (see e.g. refs. [102, 124, 125]). The next change of variables

$$E(t) = \sqrt{\frac{2n_{ef}^2}{\hbar\mu_0\omega_0 c^2}}\ a(t) \ , \tag{2.4.110}$$

$$P(t) = -\frac{b(t)}{\widetilde{\mu}} \ , \tag{2.4.111}$$

$$D(t) = \hat{D}_0 \ , \tag{2.4.112}$$

$$J = \hat{J} \ , \tag{2.4.113}$$

can be applied. This allow to write the laser equations (2.4.92), (2.4.94) and (2.4.95), in the form

$$\frac{dE(t)}{dt} = -(i\omega_c + \alpha_{tot})E(t) + gP(t) \ , \tag{2.4.114}$$

$$\frac{dP(t)}{dt} = -(i\delta + \gamma_\perp)P(t) + gE(t)D(t) \ , \tag{2.4.115}$$

$$\frac{dD(t)}{dt} = -\gamma_\parallel(D(t) - J) - 2g(E(t)P(t)^* + c.c.) \ . \tag{2.4.116}$$

Class	Relation between parameters	Equations adiabatically eliminated
A	$\gamma_\perp \approx \gamma_\parallel \gg \alpha_{tot}$	(2.4.115) and (2.4.116)
B	$\gamma_\perp \gg \gamma_\parallel \approx \alpha_{tot}$	(2.4.115)
C	$\gamma_\perp \approx \gamma_\parallel \approx \alpha_{tot}$	none

Table 2.4.1 – Classification of the RE models depending on their damping parameters.

where

$$g = \sqrt{\frac{\mu_0 \omega_c c^2 \widetilde{\mu}^2}{2 n_{ef} \hbar}} \ . \qquad (2.4.117)$$

The set (2.4.114)-(2.4.116) is known as the semiclassical Maxwell-Bloch-type equations. The first term in the Eqs. (2.4.114) and (2.4.115), $-i\omega_0 E(t)$ and $-i\delta P(t)$, describes a fast-oscillating factor in $E(t)$ and $P(t)$ of frequency equal (or close) to ω_c and ω_A. The terms containing α_{tot}, $\gamma_\perp$ and $\gamma_\parallel$ describe the damping of the corresponding variables, and the last term in each equation describes the coupling between the variables brought about by the radiation-matter interaction.

When one of the damping parameters α_{tot}, $\gamma_\perp$ and $\gamma_\parallel$ is larger than the others, the differential equation for the corresponding variable can be adiabatically eliminated [126], e.g. in semiconductor lasers polarization is usually eliminated adiabatically. This leads to a classification of the laser models depending on their characteristic time scales [105], according to this classification, one or two of the relaxation times are in general very fast compared with the other time scales and most lasers are described by the RE with one or two variables (see table 2.4.1). Therefore, they are stable systems that are categorized in class A and B lasers. Only class C lasers require the full description. Class B lasers are characterized by the rate equations for a complex field and population inversion, and they are easily destabilized by an additional degree of freedom as an external perturbation, e.g. solid state lasers, fiber lasers, and CO_2 lasers that are categorized as class B lasers, show unstable oscillations by external optical injection or modulation for accessible laser parameters. Semiconductor lasers, which are also classified into class B lasers, are also very sensitive to self-induced optical feedback, optical injection from different lasers, optoelectronic feedback, and injection current modulation [124]. *Photon models* can also be classified as class B lasers that describe the field intensity and the population inversion, where the polarization has been eliminated adiabatically.

It was demonstrated [46] the analogy between the set (2.4.114)-(2.4.116) and the well-known Lorenz equations [127]. After manipulating the set (2.4.114)-(2.4.116) one obtains [125]

$$\frac{dx}{d\tau} = -\sigma(x-y) \ , \qquad (2.4.118)$$

$$\frac{dy}{d\tau} = -y + rx - xz \ , \qquad (2.4.119)$$

$$\frac{dz}{d\tau} = -bz + xy \ , \qquad (2.4.120)$$

where

$$\sigma = \frac{\alpha_{tot}}{\gamma_\perp} \ , \quad b = \frac{\gamma_\parallel}{\gamma_\perp} \ , \quad r = \frac{g^2 J}{\alpha_{tot}\gamma_\perp} \ . \qquad (2.4.121)$$

Eqs. (2.4.118)-(2.4.120) are exactly the Lorenz equations. This model is also called the Lorenz-Haken model, because Haken in ref. [46] realized that the equations ruling the

simplest laser, i.e. a homogenously broadened single-mode resonantly tuned laser, are isomorphic with the equations obtained by Lorenz for the description of convection flows in fluids. The Lorenz equations are the most representative model that shows

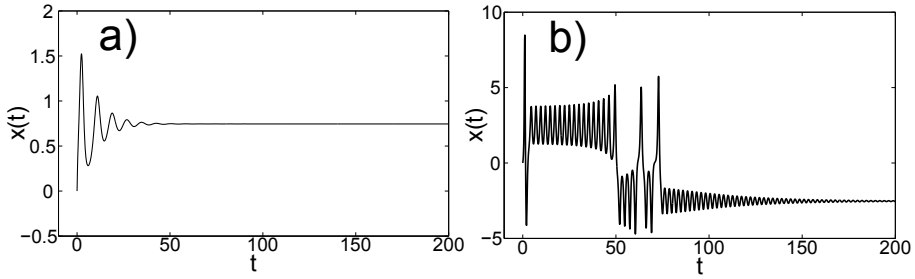

Fig. 2.4.13 – Numerical solution for the dynamical system (2.4.118)-(2.4.120) for $\sigma = 1.4253$ and $b = 0.2778$. Initial conditions: $x(0) = z(0) = 0$ and $y(0) = 1$. (a) The solution for $r = 3$ ends in one of the stable solutions. (b) The solutions for $r = 24$ shows *metastable chaos*, it begins approaching to one solution but ends the other one.

chaotic behavior, therefore this simplified model shows very interesting features for increasing the pump parameter that one summarizes here [125]:

- $0 \leq r \leq 1$

  In this domain the laser is off. Whatever the initial conditions may be, the system will go to the zero solution. The pumping rate is to low for the gain to exceed the losses and there is no laser emission.

- $1 \leq r \leq r_a$

  In this domain the zero point solution still exists, but it is now unstable (see Fig. 2.4.13 (a)). These features are the same found in the *Photon model* shown in the previous section, but in this case two stable solutions $C_\pm$ appear:

  $$C_\pm = \left(\pm\sqrt{b(r-1)}, \pm\sqrt{b(r-1)}, r-1\right) \qquad (2.4.122)$$

  Physically, these two solutions are identical, because they only differ in the sign of x and y, i.e. they differ in the phase of the field and the polarization. For a given initial conditions the laser will approach to the C_+ or the C_- solutions, in some cases it will show *metastable chaos*, i.e. the solution approaches to one of the solutions but finally reach the other one (see Fig. 2.4.13 (b)).

- Unstable behavior

  Considering the fixed points C_+ and C_-, which for $1 \leq r \leq r_a$, were attracting any trajectory. For $r > r_a$ they still exist but now they only attract the trajectories originating close to them. If r is further increased these solutions becomes unstable. It happens after the second laser threshold is reached

  $$r > r_H = \frac{\sigma(\sigma + b + 3)}{\sigma - b - 1} \quad , \qquad (2.4.123)$$

  the solutions $C_\pm$ still exist but they are unstable for $r_H < r < \infty$ (see Fig. 2.4.14). A necessary condition for the fixed points $C_\pm$ become unstable (i.e. $r_H < \infty$) is that

  $$\sigma > b + 1 \quad , \qquad (2.4.124)$$

which in the case of the laser parameters means

$$\alpha_{tot} > \gamma_{\parallel} + \gamma_{\perp} \quad , \tag{2.4.125}$$

which is called as the *bad cavity condition*, because it requires that the cavity looses for the field be larger that the population inversion and polarization relaxation rates.

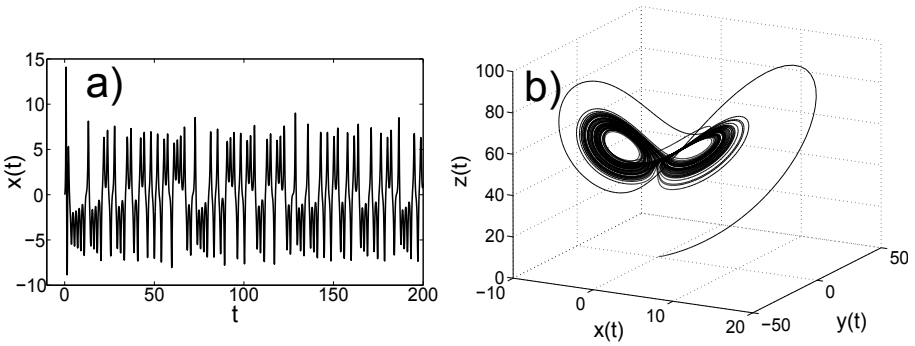

Fig. 2.4.14 – Numerical solution for the dynamical system (2.4.118)-(2.4.120) for $r = 54$, $\sigma = 1.4253$ and $b = 0.2778$. Initial conditions: $x(0) = z(0) = 0$ and $y(0) = 1$.(a) The solution is unstable, for these parameters $r_H = 45.4463$. (b) Portrait in the phase space of the solution shown in (a).

Although the Lorenz-Haken model results can be experimentally confirmed using an ammonia ring laser, in general the simplified model described by Eqs. (2.4.118)-(2.4.120) does not describe a real laser, where nine variables have to be taken into account. However, the Lorenz-Haken model is one of the most studied systems that shows chaotic behavior, and allow us to introduce the concept of single-mode instability [128].

Other instabilities more related to the work developed in this thesis are the multimode instabilities, like the Risken-Nummedal-Graham-Haken instability [47] for unidirectional homogenously broadened ring lasers that leads to pulse generation [48].

II.4.2 Rate equations for a bidirectional ring laser

In this section the RE model for a bidirectional ring laser is derived. As shown in section II.3.3, two families of solutions arise for the wavenumber in a ring laser with reflection and transmission coefficients. However, these solutions are not related to every propagating direction as one can think in principle. Therefore, every counter-propagating component of the field will be composed by two components related to the two families of solutions of the wavenumber q, this will lead to a mixing of the counter-propagating fields via a backscattering coefficient.

In the previous section it was discussed that depending on the different time scales involved in the set (2.4.92)-(2.4.96), one can adiabatically eliminate one or two of the variables. The starting point in this case is to perform the adiabatic elimination of the polarization $P_{\pm}$ and the population difference grating $D_{\pm 2}$. E.g. in the semiconductor case, the polarization evolves at much slower rate than the other variables, therefore its equation can be adiabatically eliminated by taking its stationary state [105], i.e. $\partial_t P_{\pm} = 0$, and obtaining an expression for $P_{\pm}$,

$$P_{\pm} = -\frac{\widetilde{\mu}^2}{\hbar\gamma_{\perp}}(D_0 E_{\pm} + D_{\pm 2} E_{\mp}) \ , \tag{2.4.126}$$

in the resonant case, i.e. $\delta = 0$. Taking $\partial_t D_{\pm 2} = 0$ in (2.4.96) one obtains

$$D_{\pm 2} = \frac{2}{\hbar(\gamma_\parallel + 4q_0^2\mathbb{D})}(E_\pm P_\mp^* + E_\mp^* P_\pm) \ , \tag{2.4.127}$$

and taking into account that by construction $D_{\mp 2}^* = D_{\pm 2}$,

$$D_{\pm 2} = -\frac{2CD_0 E_\pm E_\mp^*}{1 + C(|E_\pm|^2 + |E_\mp|^2)} \ , \tag{2.4.128}$$

where

$$C = \frac{2\widetilde{\mu}^2}{\hbar^2(\gamma_\parallel + 4q_0^2\mathbb{D})\gamma_\perp} \ . \tag{2.4.129}$$

Using (2.4.128) in (2.4.126) the polarization $P_\pm$ can be written in terms of the fields $E_\pm$ and the population difference D_0,

$$P_\pm = -\frac{\widetilde{\mu}^2}{\hbar\gamma_\perp}\left[1 - \frac{2C|E_\mp|^2}{1 + C(|E_\pm|^2 + |E_\mp|^2)}\right] D_0 E_\pm \ , \tag{2.4.130}$$

that it is substituted in the equations for the fields (2.4.92) and the population difference (2.4.95), obtaining

$$\pm \frac{c}{n_{ef}}\frac{\partial E_\pm}{\partial z} + \frac{\partial E_\pm}{\partial t} = \left[G\left(1 - \frac{2C|E_\mp|^2}{1 + C(|E_\pm|^2 + |E_\mp|^2)}\right) D_0 - \alpha_{int}\right] E_\pm \ , \tag{2.4.131}$$

and

$$\begin{aligned} \frac{\partial D_0}{\partial t} &= \gamma_\parallel(J - D_0) - F\left[\left(1 - \frac{2C|E_-|^2}{1 - C(|E_+|^2 + |E_-|^2)}\right)|E_+|^2\right. \\ &+ \left.\left(1 - \frac{2C|E_+|^2}{1 - C(|E_+|^2 + |E_-|^2)}\right)|E_-|^2\right] D_0 \ , \end{aligned} \tag{2.4.132}$$

where

$$G = \frac{\mu_0\omega_0 c^2\widetilde{\mu}^2}{2\hbar\gamma_\perp n_{ef}^2} \ , \ F = \frac{4\widetilde{\mu}^2}{\hbar^2\gamma_\perp} \ , \ \alpha_{int} = \frac{\mu_0\sigma c^2}{2n_{ef}^2} \ .$$

On the other hand, the boundary conditions that complete the set of Eqs. (2.4.92)-(2.4.96) can be written as

$$E_+(0,t) = RE_-(0,t) + TE_+(L,t) \ , \tag{2.4.133}$$

$$E_-(L,t) = RE_+(L,t) + TE_-(0,t) \ , \tag{2.4.134}$$

where in this case R and T are complex numbers. Following the strategy shown in II.3.3, one obtains two families of solutions ($\sigma = \pm 1$) for the wavenumber q,

$$q_m(\omega,\sigma) = \frac{2\pi m}{L} + \frac{i}{L}\ln(T + \sigma R) \ \text{ where } \ \sigma = \pm 1 \ \text{ and } \ m = 0, \pm 1, \pm 2, \ldots \tag{2.4.135}$$

Moreover, from (2.4.133) a relation between the counter-propagating fields amplitudes for the two families of solutions can be written,

$$E_-(\sigma = +1) = \frac{1}{T + R}E_+(\sigma = +1) \ , \tag{2.4.136}$$

$$E_-(\sigma = -1) = \frac{-1}{T - R}E_+(\sigma = -1) \ , \tag{2.4.137}$$

allowing to write the fields as

$$E_+(z,t) = A(t)e^{iq_{+1}z-i\omega_{+1}t} + B(t)e^{iq_{-1}z-i\omega_{-1}t} \ , \quad (2.4.138)$$

$$E_-(z,t) = \frac{A(t)}{T+R}e^{iq_{+1}z-i\omega_{+1}t} - \frac{B(t)}{T-R}e^{iq_{-1}z-i\omega_{-1}t} \ , \quad (2.4.139)$$

where $A(t)$ and $B(t)$ do not depend on space and a new notation was introduced, being $q_{\pm 1} = q(\sigma = \pm 1)$ and $\omega_{\pm 1} = \mathrm{Re}\{q(\sigma = \pm 1)\}$. At this stage performing the uniform field limit (UFL) approximation, i.e. $T \to 1$ and $R \to 0$, the wavenumber can be written as the sum of an average contribution and a smaller contribution due to the complex reflectivity R,

$$q(\omega,\sigma) \simeq \bar{q}(\omega) + \delta q(\sigma) = \frac{2\pi m}{L} + \frac{i}{L}\left(\ln T + \sigma\frac{R}{T}\right) \ . \quad (2.4.140)$$

Finally, using (2.4.138) and (2.4.139) in (2.4.131) and (2.4.132), and taking the UFL that allow to define new fields $\mathcal{E}_\pm(t) = A(t) \pm B(t)$, one obtains the bidirectional single-mode RE model for a ring laser,

$$\frac{d\mathcal{E}_\pm}{dt} = (G\sigma_\pm D_0 - \alpha_{tot})\,\mathcal{E}_\pm + \eta\mathcal{E}_\mp \ , \quad (2.4.141)$$

$$\frac{\partial D_0}{\partial t} = \gamma_\parallel(J - D_0) - F\left(\sigma_-|\mathcal{E}_+|^2 + \sigma_+|\mathcal{E}_-|^2\right)D_0 \ , \quad (2.4.142)$$

where

$$\alpha_{tot} = \alpha_{int} + \alpha_{cavity} = \frac{\mu_0\sigma c^2}{2n_{ef}^2} + \frac{c}{n_{ef}L}\ln T \quad (2.4.143)$$

are the total losses,

$$\eta = \frac{c}{n_{ef}L}R \quad (2.4.144)$$

is the complex backscattering and

$$\sigma_\pm = \left(1 - \frac{2C|\mathcal{E}_\mp|^2}{1 + C(|\mathcal{E}_\pm|^2 + |\mathcal{E}_\mp|^2)}\right) \quad (2.4.145)$$

is the suppression function, where the saturation effects are represented. In this case, developing in series (2.4.145) and taking the first order in C one obtains

$$\sigma_\pm \simeq 1 - 2C|\mathcal{E}_\mp|^2 \ , \quad (2.4.146)$$

where only cross-saturation of the fields appears. This is due to using a two-level atom medium for deriving Eqs. (2.4.141) and (2.4.142).

In the case of a semiconductor medium, the susceptibility of the semiconductor medium can depend on the intensities of the fields,

$$P = \epsilon\chi_e(D, |E|^2)E \ . \quad (2.4.147)$$

Using (2.3.72), (2.3.73) and (2.4.93) and supposing operation near threshold, one obtains

$$P_\pm \approx \epsilon_0\left[\chi_e(D_0,0)E_\pm + \frac{\partial\chi_e(D_0,0)}{\partial N}D_{\pm 2}E_\mp + \frac{\partial\chi_e(D_0,0)}{\partial|E|^2}(|E_\pm|^2E_\pm + 2|E_\mp|^2E_\pm)\right] \ . \quad (2.4.148)$$

In this case, at first order the self-saturation coefficient is present being half the cross-saturation one. Another difference between the semiconductor and the two level atom medium is that one has to introduce the α-factor that couples the phase and the amplitude of the field. In the next chapter a standard RE model, including the α factor and self- and cross-saturation terms, for the bidirectional semiconductor ring laser is presented.

III

Rate equation modeling

In this chapter various contributions making use of Rate Equations (REs) model for a Semiconductor Ring Lasers (SRLs) are presented. In section III.1 the REs model is introduced and analysed in terms of the dynamic/static regimes it shows. Main results found in the literature are reported, ranging from the dynamics and the regime boundaries to the directional switching properties. In section III.2, it is demonstrated theoretically that a SRL can be used for rotation sensing, as a gyroscope. Finally in section III.3, the noise characteristics of a SRL in the bidirectional regime are presented. Noise spectra for field fluctuations are analitically derived from REs in the Langevin form, when spontaneous emission is retained.

III.1 Rate equations model for semiconductor ring lasers

The RE model used to model the dynamics of SRLs is formaly analogous to the model presented in the section II.4.2. Semiconductor REs models rely on the adiabatical elimination of the polarization. Considering single mode operation, then the electric field inside the cavity reads

$$E(z,t) = E_+(t)e^{-i(\Omega t - kz)} + E_-(t)e^{-i(\Omega t + kz)} \ , \tag{3.1.1}$$

where E_+ and E_- are the mean-field (spatially averaged) slowly varying complex amplitudes of the electric field associated with the two propagation directions, E_+ clockwise (CW) and E_- counterclockwise (CCW), respectively, being z the spatial coordinate along the ring, assumed positive in the clockwise direction, and Ω is the optical frequency of the selected longitudinal mode. The other dynamic variable is the average carrier density D. The RE model is composed by the following set of dimensionless rate equations for the time evolution of the electric fields $E_\pm$ and the carrier density D [96],

$$\frac{dE_\pm}{dt} = \mathcal{G}_\pm(D, |E_\pm|^2)\ E_\pm - \eta\ E_\mp \ , \tag{3.1.2}$$

$$\frac{dD}{dt} = \gamma\ \left[\mu - D(1 + \sigma_+\ |E_+|^2 + \ \sigma_-\ |E_-|^2)\right] \ , \tag{3.1.3}$$

where (3.1.3) is a simplified form of the Bloch equation for the carrier dynamics,

$$\mathcal{G}_\pm(D, |E_\pm|^2) = \frac{1}{2}(1 + i\alpha)\{D\ \sigma_\pm - 1\} \tag{3.1.4}$$

is the non linear gain, where the α factor describes the phase-amplitude coupling mechanism present in semiconductor lasers, and

$$\sigma_\pm = 1 - s\ |E_\pm|^2 - c\ |E_\mp|^2 \ ,$$

is the gain saturation function, written in the quadratic approximation, where the parameters s and c are normalized self- and cross-gain saturation coefficients, respectively. The complex backscattering coefficient

$$\eta = k_d + ik_c \ , \tag{3.1.5}$$

with its dissipative (k_d) and conservative (k_c) components [39]. Dissipative backscattering is associated to localized light losses. The conservative component is associated to localized intracavity reflections. SRLs were experimentally found to exhibit strong conservative backscattering, respect to the dissipative one. This feature derives from unavoidable intracavity reflections at the light extraction region (evanescent coupler). The light extraction section is formed by the curved waveguide coupled to a straight waveguide by evanescent wave [129]. This introduces a localized perturbation to the effective refraction index which reverts to a source of localized back-reflections, i.e. conservative backscattering [55, 130]. The parameter μ represents the pump current and is normalized to the threshold current (i.e. $\mu = 1$ at threshold) and γ is the ratio between the photon lifetime and the carrier lifetime. This model describes the

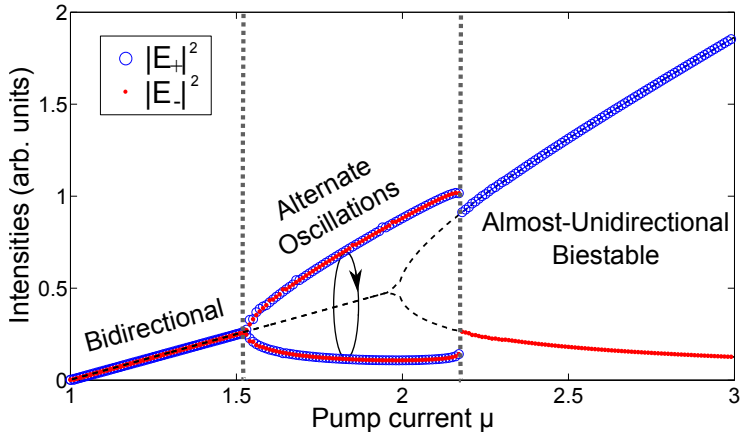

Fig. 3.1.1 – Bifurcation diagram for increasing pump current μ of the SRL RE model (3.1.2)-(3.1.3). Three regimes are shown: CW bidirectional emission, alternate oscillations (AO) regime and almost-unidirectional bistable regime. This diagram was constructed integrating Eqs. (3.1.2)-(3.1.3) with a 4th order Runge-Kutta algorithm plotting the maximum and minimum values of the intesities of the fields after a long transient for each pump current value (blue circles and red dots). The dashed black line are the monochromatic solutions obtained numerically from (3.1.10) with a Newton-Raphson algorithm. It shows the unstable pitchfork bifurcation inside the AO regime. $\alpha = 3.5$, $s = 0.005$, $c = 0.01$, $k_d = 3.27\ 10^{-4}$, $k_c = 4.4\ 10^{-3}$ and $\gamma = 2\ 10^{-2}$.

longitudinal single-mode dynamics of two electric fields traveling in opposite directions within the ring cavity. The model was proven to give excellent agreement with experiments [66, 96] for the slow (ns) dynamics. Writing the fields as

$$E_{\pm}(t) = Q_{\pm}e^{i\omega t \pm i\phi} \ , \tag{3.1.6}$$

and substituting (3.1.6) in the set (3.1.2)-(3.1.3) one obtains

$$D_{st} = \frac{\mu}{1 + \widetilde{\sigma}_{+}|Q_{+}|^2 + \widetilde{\sigma}_{-}|Q_{-}|^2} \ . \tag{3.1.7}$$

Eqs. (3.1.2)-(3.1.3) admit two possible solutions, the *in phase* case

$$\phi_{in} = 0 \rightarrow \omega_{in} = \alpha k_d - k_c \ , \tag{3.1.8}$$

and the *out of phase* case

$$\phi_{out} = \frac{\pi}{2} \rightarrow \omega_{out} = -\alpha k_d + k_c \ . \tag{3.1.9}$$

Depending on the sign of the backscattering parameters one of the solutions is stable and the other unstable, if $k_d > 0$ ($k_d < 0$) the *out of phase* case is stable (unstable). Physically, the two solutions are equivalent because the sign of k_d represent which direction (CW or CCW) is chosen as positive. In the *out of phase* case one obtains,

$$\left\{ i\omega_{out} - \frac{1}{2}(1+i\alpha)[D_{st}\widetilde{\sigma}_{\pm} - 1] \right\} Q_{\pm} = \eta Q_{\mp} \ \ , \tag{3.1.10}$$

where

$$\widetilde{\sigma}_{\pm} = 1 - s|Q_{\pm}|^2 - c|Q_{\mp}|^2 \ \ . \tag{3.1.11}$$

Solving (3.1.10) numerically e.g. by a Newton-Raphson algorithm the dashed black line in Fig. 3.1.1 is plotted. This allows to find the unstable pitchfork bifurcation point that can not be obtained from temporal numerical simulations of the set (3.1.2)-(3.1.3). Focusing on the bidirectional regime, the monochromatic solutions (3.1.6) for the two fields have the same amplitude, i.e. $Q_+ = Q_- = Q$. In this case, the corresponding stationary solution for the carrier density $D = D_{st}$ as a function of the amplitude of the fields and the pump parameter is

$$D_{st} = \frac{\mu}{1 + 2Q^2 - 2(c+s)Q^4} \ . \tag{3.1.12}$$

While for the amplitude Q one finds

$$Q^2 = \frac{D_{st} - 1 + k_d}{(c+s)D_{st}} \ . \tag{3.1.13}$$

These stationary solutions will be useful in the following sections. The behavior of this model can be summarized in the bifurcation diagram shown in Fig. 3.1.1 for a parameter set fitted from experiments [66]. After the threshold the laser begins to operate in a continuous wave (CW) bidirectional regime, i.e. the two counter-propagating fields have the same intensity as the pump current is increased. At $\mu \sim 1.5$ a Hopf bifurcation induced by a competition for the carrier depletion between the two counter-propagating fields, it gives an out-phase oscillation between the two fields, the so-called alternate oscillations (AO) regime [66]. Inside this regime a unstable pitchfork bifurcation from the unstable branch developed from the Hopf bifurcation appears at $\mu \sim 2$. These unstable branches change their stability abruptly as the AO regime ends, and the unidirectional or almost-unidirectional bistable regime is stabilized.

REs models like Eqs. (3.1.2)-(3.1.3) have been studied profoundly in the last years. Among the numerous publications that had used this RE model, we refer here to the most significant ones. The stability analysis of a RE model with a two fields approach considering gain saturation and absorption saturation reveals that different types of stability may occur in these systems, showing single-mode stability, bistability and multistability [94].The appearance of these types of stability depends on the saturation coefficients. An increase of the gain cross saturation tends to enhance bistability, while

increasing the absorption cross saturation tends to prohibit bistability. A RE model used to model SRLs was introduced in [95] including gain saturation terms.

The coupling between fields by means of a backscattering coefficient was introduced to this model in [66], where a experimental fitting of the parameters of the model is achieved and the whole experimental $L - I$ curve is well reproduced. The regimes boundaries were presented in [96], depending on pump and on the backscattering coefficients. The RE with no backscattering, i.e. $k_c = k_d = 0$, would operate in a complete unidirectional and bistable regime because cross-gain saturation selects one of the counter-propagating fields. By including the backscattering, dissipative backscattering coefficient favors continuous wave operation, either bidirectional or unidirectional, while the conservative backscattering acts like a driven force for the alternate oscillations.

The RE model (3.1.2)-(3.1.3) was also used to investigate on the directional switching properties. The theoretical work [98] unveiled that the switching time depends mainly on the energy of the pulses rather than on its amplitude, duration or shape. The directional switching response and the characterization of different switching and locking regions were investigated in [100, 99]. A reduction using asymptotic methods of such REs was performed in [131] in order to investigate the emergence of the different dynamical regimes shown by original REs model. Theoretical and experimental work was performed by using a reduced RE model focused in the switching dynamics [132].

III.2 Semiconductor ring laser gyroscope

[1]In this part of the thesis, it is theoretically showed that a SRL can be used to measure inertial rotation within the so called locking band, i.e. without the need to un-lock the two counterpropagating waves. Indeed, the dephasing accumulated by the two counterpropagating waves due to rotation within the locking region is coupled to the field amplitudes via conservative backscattering. This in turn unbalances the field amplitudes by a quantity proportional to the rotation angular velocity. An analytical expression for the *responsivity* is provided that would characterize a possible rotation sensor. Moreover the quantum fluctuations [71] of the fields are considered to estimate the Noise Equivalent Rotation Rate (NER $\sim 10^{-3}\ Hz$). The obtained NER is higher than what is tipically displayed by He-Ne Ring Laser Gyroscope (RLG); however, the limited cost and size of a S-RLG could make it appealing for rotation sensing applications. Also, this technique can be exported to other ring lasers than SRLs, providing an intracavity mechanism of conservative backscattering.

III.2.1 The rotation sensing problem

The RLG consists of a rotating ring cavity with two optical fields propagating in opposite directions, a measure of the interference pattern formed by extracting and heterodyning portions of the two counter propagating beams provides information about the rotation rate relative to an inertial frame.

The advantage of the RLG as a rotation sensing device is that it has no moving parts and so would seem, potentially, to have a longer repair lifetime than a mechanical gyroscope, but the major advantage is the much higher sensitivity ($0.001°/h$).

Usually these RLGs are fabricated using gas lasers or fiber lasers. The gas ring laser gyroscope is more sensitive than the fiber laser gyroscope and is used in research like the Canterbury gyroscope [28] used to measure the Earth's rotation. Fiber RLGs [133, 134, 135] are cheaper and they are used in commercial applications, like in the navigation systems of aircrafts (sensitivity $\sim 15°/h$).

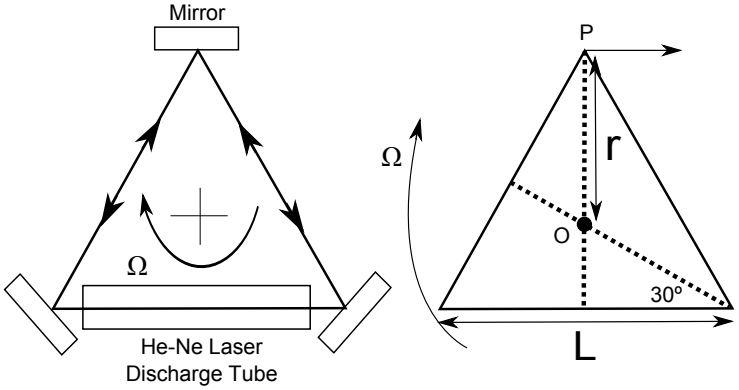

Fig. 3.2.2 – Scheme of the He-Ne triangular ring laser gyroscope. L is the length of the side of the triangle. The cavity is rotating around O with an angular frequency Ω.

[1]This part is based on the letter: "Theoretical Analysis of a New Technique for Inertial Rotation Sensing Using a Semiconductor Ring Laser" by A. Pérez-Serrano and A. Scirè, *IEEE Photon. Techn. Lett.* **21**, no. 13, p. 917 (2009).

Sagnac effect

RLGs are based on the Sagnac effect. By considering the scheme shown in figure 3.2.2, we suppose that the light leaves the point P of the triangular cavity, rotating around O with an angular velocity Ω. The time it takes in return to P making the travel in the ring cavity if $\Omega = 0$ is $t = \frac{3L}{c} = \frac{S}{c}$. Where L is the length of the side of the triangle and $S = 3L$ is the total perimeter. When the gyroscope spins (i.e. $\Omega \neq 0$), the point P moves to a distance $d = \Omega r t = \Omega r \frac{S}{c}$, where r is the distance from P to O, which is $\frac{L}{2}\sec 30^\circ = \frac{L}{\sqrt{3}}$. The change of optical path δS seen by the beam is the component of the movement of P along the direction of the beam, $\delta S = d\cos 60^\circ = d/2$, and making use of d and r, δS can be written as

$$\delta S = \frac{\Omega S L}{2c\sqrt{3}} = \frac{\sqrt{3}\Omega L^2}{2c} \ . \tag{3.2.14}$$

Now using the area of a triangle, $A = \frac{\sqrt{3}L^2}{4}$, one obtains

$$\delta S = \frac{2\Omega A}{c} \ . \tag{3.2.15}$$

To accomplish the cavity resonance condition, the path length is a integer number of times the wavelength, $m\lambda = 3L = S$, therefore for a change δS a change $\delta\lambda$ is produced

$$\delta\lambda = \frac{\delta S}{m} = \frac{\lambda \delta S}{S} \ , \tag{3.2.16}$$

and the correspondent frequency change is $\delta\nu/\nu = \delta\lambda/\lambda = \delta S/S$. Each beam suffers the same change in frequency, but in opposite direction, therefore the beat frequency $f = 2\delta\nu = 2\nu(\delta S/S)$, and using (3.2.15) one obtains

$$f = \frac{4\Omega A\nu}{cS} = \frac{4\Omega A}{\lambda S} \ , \tag{3.2.17}$$

This is the basic equation to measure angular rotations. In [35, 136] derivations of the generalized Sagnac effect in general relativity can be found.

In principle laser gyroscopes should be very sensitive and accurate with a fundamental limit of less than 10^{-6} °/h. In practice the performance is less than this, the limits being set by the accuracy of fabrication, cleanliness and a few inherent operational difficulties. The use of the device as a rotation sensor depends crucially on the extent to which the relation (3.2.17) is valid. In the ideal case (that is, one which obeys (3.2.17)) the relationship between Ω and f is linear as shown in Fig. 3.2.3. There are three main kinds of error that may cause relation (3.2.17) to be invalid.

Null shift (Fig. 3.2.3 (b)). This happens when the frequency difference is "biased", i.e. f is non zero for zero input rate. It amounts to adding a constant term to the right-hand side of (3.2.17), the exact magnitude of which is unpredictable. It can arise from any anisotropy in the cavity respect to the radiation traveling in the two directions. If it is constant and repeatable it can be measured and compensated for in the final output. If it drifts, however, or changes from turn-on to turn-on, it can be a serious problem.

Frequency locking. This occurs when the rotation rate becomes very small. The effect is due to interaction effects between the two counter-propagating fields, when on reflection, a small amount of energy is scattered from the mirror surface back into the oppositely traveling beam. If this difference becomes too small the counter-propagating beams lock together in the same way that coupled mechanical oscillators

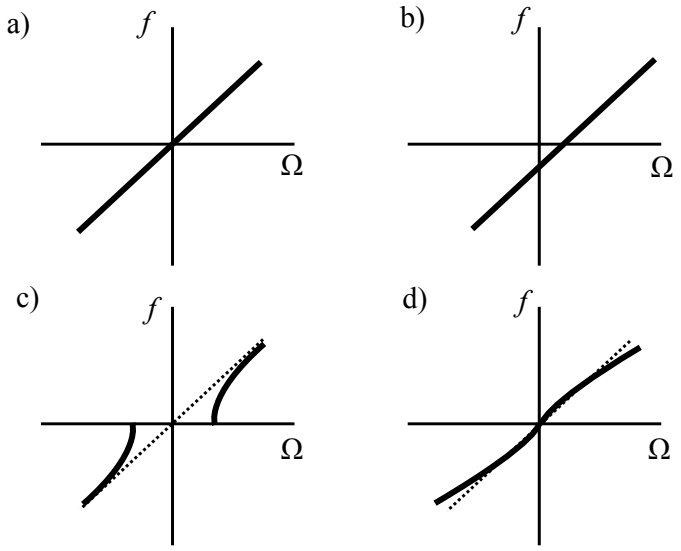

Fig. 3.2.3 – Beat frequency f vs input rotation rate Ω in a ring laser gyro. a) The ideal case, a straight line through the origin; b) A linear relationship with a nonzero null shift; c) Frequency locking; and d) nonlinearities in the response (variable scale factor). [35].

operating at slightly different frequencies lock together. When the two fields have the same frequency the beat frequency is zero. In Fig. 3.2.3 (c) one can see a dead-band where, even though the rotation rate is non-zero , the beat frequency is fixed at zero, i.e. the fringe pattern is stationary.

Nonlinear effects. This means that the linearity in (3.2.17) no longer holds. These effects may arise by dispersive effects in the laser medium (frequency pulling and pushing). Or as a consequence of some of the techniques used to eliminate frequency locking (see Fig. 3.2.3 (d)).

In the paper by Chow et al. [35] an equation of motion is derived from Lamb's semiclassical laser theory assuming $E_+ = E_-$ for the phase angle difference ψ,

$$\dot{\psi} = S\Omega + b\sin\psi \ , \qquad (3.2.18)$$

where Ω is the rotation rate, S is the scale factor and b is the backscattering coefficient. Note that $\dot{\psi}$ is basically the beat frequency, what we called f. If $S\Omega \gg b$ the phase difference ψ grows essentially as a linear function of time, as it would do in absence of backscattering. But if $S\Omega < b$ stationary solutions to (3.2.18) exist, with $\dot{\psi} = 0$, given by

$$\psi_s = \begin{cases} -\arcsin\frac{S\Omega}{b} \\ \pi + \arcsin\frac{S\Omega}{b} \end{cases} \qquad (3.2.19)$$

Of these two solutions the second one, having $b\cos\psi_s < 0$ is stable, this means that no matter what the initial condition is, the evolution of ψ will eventually bring it arbitrarily close to the value ψ_s, for which the right-hand side of equation (3.2.18) equals zero. That is the frequency difference vanishes, in spite of the fact that the rotation rate Ω is nonzero. This is what is called frequency locking in the literature. In [35] a description of techniques used to avoid frequency locking is reported.

III.2.2 Sagnac effect on semiconductor ring lasers

The theoretical analysis is based on the set of dimensionless dynamical equations (3.1.2) and (3.1.3) for the two (slowly varying) complex amplitudes of the counter-propagating fields E_+ and E_-, (3.1.2) is modified to account for inertial rotation effects [31, 55] and the Bloch equation (3.1.3) rests in the same form. So, the modified Eq. (3.1.2) reads

$$\frac{dE_\pm(t)}{dt} = \mathcal{G}_\pm(D(t), |E_\pm(t)|^2)\ E_\pm(t) - \eta\ E_\mp(t) \pm i\Delta E_\pm(t)\ , \tag{3.2.20}$$

where 2Δ is the rotation induced detuning.

Consistently with the standard theory [31], the emission frequency of the two modes (referred to a common optical carrier set to zero) is shifted by the inertial rotation of a dimensionless (because of time rescaling) amount equal to 2Δ, when the rotation vector is orthogonal to the cavity plane,

$$\Delta = \frac{2\pi R\tau_p}{\lambda}\Omega_{rot}\ , \tag{3.2.21}$$

where R is the ring radius, λ is the laser wavelength, and Ω_{rot} is the dimensional rotation angular velocity. First one analyzes the SRL at rest ($\Delta = 0$). From now on we focus on the *in phase* case without loosing generality. If Δ is small, the stationary solution deviate from the solution at rest (3.1.12) and (3.1.8). Assuming symmetric amplitude deviation of the form

$$Q_\pm = Q \pm \delta\ , \tag{3.2.22}$$

and a small deviation θ of the relative phase ϕ, $\phi = \psi_s + \theta$. By substituting the deviations with (3.1.6) in the set (3.2.20) and (3.1.3), at first order in δ and θ, separating the real and the imaginary part one obtains a set of two linear coupled equations for the perturbations δ and θ, i.e.

$$\Delta Q + k_d\theta Q + 2k_c\delta - \alpha Q^2\delta D_{st}(s-c) = 0\ , \tag{3.2.23}$$

$$2k_d\delta - k_c\theta Q - D_{st}Q^2\delta(s-c) = 0\ . \tag{3.2.24}$$

Defining χ as the difference between the fields intensities divided by the total intensity, using (3.1.6) with (3.1.12)-(3.2.22), one obtains

$$\chi = \frac{|E_-|^2 - |E_+|^2}{|E_+|^2 + |E_-|^2} = \frac{2}{Q}\delta = \mathcal{R}\Omega_{rot}\ , \tag{3.2.25}$$

where $\mathcal{R}$ is the responsivity of the system to the dimensional inertial rotation Ω_{rot}, by solving (3.2.23)-(3.2.24) and using (3.2.25), an analytical expression for the dimensional $[Hz^{-1}]$ responsivity function is found,

$$\mathcal{R} = \frac{4\pi k_c R\tau_p}{\lambda(2k_d^2 + 2k_c^2 - (k_d + \alpha k_c)Q^2 D_{st}(s-c))}\ . \tag{3.2.26}$$

The responsivity $\mathcal{R}$ quantifies how the rotation unbalances the counterpropagating fields intensities. In figure 3.2.4 (inset), χ is plotted versus the inertial rotation Ω_{rot} using the analytical expression (3.2.25), and compared to numerical simulations. Fig. 3.2.4 (inset) shows the agreement between numeric results and analytical approximations.

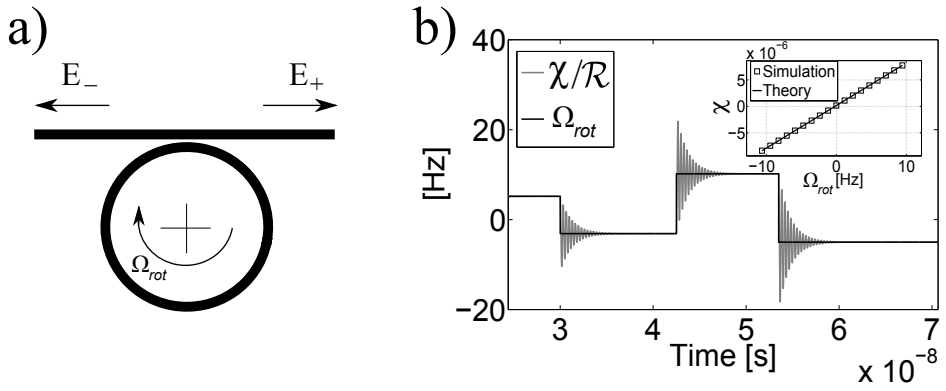

Fig. 3.2.4 – (a) Schematic of the S-RLG. (b) Numerical simulations of the response of the SRL to a time dependent rotation. Inset: System response χ versus inertial rotation Ω_{rot}. The slope is the responsivity $\mathcal{R}$. The ring radius is $R = 600\ \mu m$ and the pump is $\mu = 1.2$, $\alpha = 3.5$, $s = 0.005$, $c = 0.01$, $k_d = -3.27\ 10^{-4}$, $k_c = 4.4\ 10^{-3}$ and $\tau_p = 1\ ps$. The parameter set is taken according to experimental fitting [66].

Fig. 3.2.5 (a) shows the responsivity behavior versus the conservative and dissipative components of the complex backscattering coefficient. Fig. 3.2.5 (b) shows responsivity versus backscattering dissipative coefficient k_d and pump current μ. As a general trend, the responsivity decreases for increasing values for the dissipative backscattering coefficient and decreasing values for the conservative backscattering coefficient.

Physically, the dissipative backscattering stabilizes the locking by damping the perturbations of the phase difference between the two modes. On the other side, conservative backscattering enhances the relative phase dynamics, thus making the system more sensitive to sources of dephasing like the Sagnac effect. Indeed Eq. (3.2.26) shows that the responsivity vanishes if $k_c = 0$. This is so because the relative dephasing accumulated by the two fields is coupled to the field amplitudes via conservative backscattering when Ω_{rot} is within the locking band. This effect is different from the amplitude modulation reported in [137], because in this case the two fields unbalance their CW component. To characterize the response of the device to a rotation variation, the equations set (3.2.20) and (3.1.3) are simulated with a time dependent rotation. The results are shown in Fig. 3.2.4, the response time of the device is a few ns for the parameters choice.

Noise characteristics are also important to characterize the possible implementation of this technique in real gyroscopes. Considering a simple expression for the quantum fluctuations [71] for the optical power in each direction $P_\pm = |E_\pm|^2$,

$$\langle \delta P_\pm^2 \rangle = \frac{2hcBP_\pm}{\lambda} \ , \qquad (3.2.27)$$

where B is the instrument bandwidth, c is the speed of light and h is Planck's constant. Using (3.2.27) with (3.2.25), assuming $P_+ = P_- = P$ by straightforward calculation one obtains the standard deviation of χ,

$$\sigma_\chi = \langle \delta\chi^2 \rangle^{1/2} \simeq \sqrt{\frac{hBc}{\lambda P}} = \mathcal{R}\Omega_{NER} \ , \qquad (3.2.28)$$

where $\langle \delta P_\pm^2 \rangle^{1/2} \ll P$ is assumed. Eq. (3.2.28) permits to calculate the noise equivalent rotation Ω_{NER}. Fig. 3.2.5 (c) shows Ω_{NER} versus backscattering coefficients. The

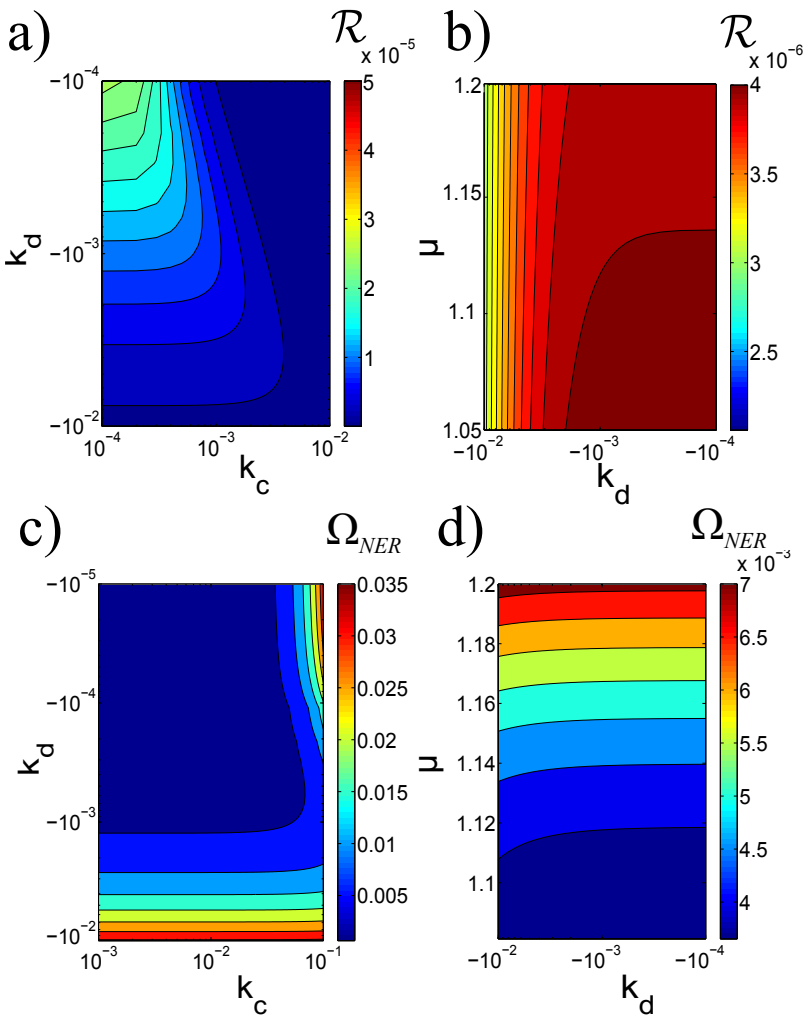

Fig. 3.2.5 – (a) Responsivity contour plot versus backscattering coefficients, $\mu = 1.2$; (b) responsivity contour plot versus backscattering coefficient k_d and pump current μ, $k_c = 10^{-2}$. $\alpha = 3.5$, $s = 0.005$, $c = 0.01$, $\tau_p = 1\ ps$, $R = 600\ \mu m$ and $\lambda = 890\ nm$. (c) Ω_{NER} contour plot versus backscattering coefficients, $\mu = 1.2$; (d) Ω_{NER} contour plot versus backscattering coefficient k_d and pump current μ, $k_c = 10^{-2}$. $\alpha = 3.5$, $s = 0.005$, $c = 0.01$, $\tau_p = 1\ ps$, $R = 600\ \mu m$, $\lambda = 890\ nm$, $B = 10\ Hz$ and $P = 10\ mW$.

order of Ω_{NER} is $\sim 10^{-3} Hz$ for a wide range of parameter values for backscattering coefficients. Ω_{NER} grows with k_c and decreases with k_d. This is so because the conservative backscattering increases the phase-noise [138], whereas the dissipative backscattering dumps phase fluctuations. Fig. 3.2.5 (d) shows how Ω_{NER} grows with the pump current.

III.3 Noise properties in the bidirectional regime

[1]In this part of the thesis, the influence of complex backscattering coefficients and pump current on the noise spectra of a two mode model for semiconductor ring laser in the Langevin formulation is analytically investigated. The system features in the bidirectional regime can be described in terms of the two mode-intensity sum (I-Spectrum) and difference (D-spectrum). The I-Spectrum reflects the energy exchange between the total field and the medium and behaves similarly to the relative intensity noise for single-mode semiconductor lasers. The D-spectrum represents the energy exchange between the two counter-propagating modes and is shaped by the noisy precursor of a Hopf bifurcation induced by the complex backscattering.

An important issue in view of applications is about the effects of fluctuations in ring lasers, as they change the performance as well as the dynamics of these devices. As a matter of fact, noise determines the performance of the ring laser gyroscope [35] and induces spontaneous switching in a bistable SRLs [98, 139]. The main fundamental noise source of a semiconductor laser is represented by spontaneous emission, which yields to fluctuations in the signal intensity and frequency [41]. Different examples of how to model the spontaneous emission noise are shown in [140, 141]. However, *semiconductor* ring lasers show peculiarities in the noise spectra that still deserve attention, such as the presence of an unexpected radio frequency peak, explained in [142] as a mode partition noise effect associated to the intracavity backscattering.

SRLs have some distinctive features respect to other ring lasers such as phase/amplitude coupling, which is known to affect phase noise [41], and strong intermodal gain cross-saturation, which induces anticorrelated dynamics in the mode-power distribution [66]. Also, the light extraction system in integrated SRLs introduces a perturbation of the refraction index [129], which turns out to be a localized reflection enhancing the conservative backscattering. Therefore SRLs experience conservative backscattering stronger than the dissipative one, differently from gas, dye [130] or solid state ring lasers [143]. The influence of backscattering in the noise spectra constitutes a possible strategy to extract backscattering parameters in working conditions, useful for laser characterization.

Here the effects of the spontaneous emission noise in a two mode rate equations model (3.1.2)-(3.1.3) [96, 98, 139] are considered for a SRL operating in the bidirectional regime. In the following, after introducing the model, the operation regimes of SRLs by representation on a Poincaré sphere are reviewed (Sect. III.3.1). Then focussing on the bidirectional regime, the linearized dynamics of the fluctuations and their correlations are calculated analytically (Sect. III.3.2). Noise spectra are obtained for decoupled quantities, that are mode-intensity sum and difference. Correlations are calculated analytically within a linear approximation and compared with simulations of the full non-linear model, showing a very good agreement in the considered regime.

III.3.1 Theoretical model

The model considered is composed by the set of dimensionless rate equations (3.1.2)-(3.1.3) for the time evolution of the electric fields $E_\pm$ and the carrier density D where a spontaneous emission noise term in the field equation (3.1.2) is included,

$$\frac{dE_\pm}{dt} = \mathcal{G}_\pm(D, |E_\pm|^2)\ E_\pm - \eta\ E_\mp + \xi_\pm(t)\ , \qquad (3.3.29)$$

[1]This part is based on the article: "Noise spectra of semiconductor ring laser in the bidirectional regime" by A. Pérez-Serrano, R. Zambrini, A. Scirè and P. Colet, *Phys. Rev. A* **80**, 043843 (2009).

The fluctuations terms $\xi_{\pm}(t)$ are the Langevin forces [144], i.e. white gaussian complex noise sources with non vanishing correlations

$$\langle \xi_{\pm}(t)\xi_{\pm}^{*}(t')\rangle = 2\sqrt{\beta\tau_p D_{st}}\delta(t-t') \ , \qquad (3.3.30)$$

where τ_p is the photon lifetime, D_{st} is the carrier steady state solution (3.1.12) and β represents the fraction of spontaneously emitted photons coupled to the cavity. Noise terms ξ_+ and ξ_- reflect the effect of spontaneous emission in each direction of propagation. For simplicity, a noise source for the carrier density equation is not taken into account, considering the spontaneous emission as the main noise source in semiconductor lasers [41, 140].

According to the experimental fitting [67] through this section the following parameters set is taken (except where otherwise is noticed) $\alpha = 3.5$, $s = 0.005$, $c = 0.01$, $k_d = 3.27\ 10^{-4}$, $k_c = 4.4\ 10^{-3}$, $\tau_p = 10\ ps$ and $\gamma = 2\ 10^{-3}$.

The bifurcation diagram of the SRL is obtained by numerical integration of Eqs. (3.1.2)-(3.1.3) and was shown in Fig. 3.1.1 for increasing values of the pump coefficient μ. As in all the regimes the total intensity is constant and in order to analyze the evolution of the intensity difference and the relative phase between the two counter-propagating fields, new variables are introduced represented in a Poincaré sphere, the relative intensity θ and the relative phase ψ,

$$\theta = 2\ \arctan\left(\frac{|E_+|^2 - |E_-|^2}{|E_+|^2 + |E_-|^2}\right) \ , \qquad (3.3.31)$$

$$\psi = \arctan\left(\frac{Im(\frac{E_+}{E_-})}{Re(\frac{E_+}{E_-})}\right) \ . \qquad (3.3.32)$$

In this context, θ is equivalent to ellipticity in the description of the polarization of the electric field in the sense that it describes how the field is distributed between the two counter-propagating modes (here analogous to the circular polarization modes). Those new variable are projected in the Poincaré sphere by means of the Stokes parameters as follows

$$s1 = \cos\theta\cos\psi \ , \qquad (3.3.33)$$

$$s2 = \cos\theta\sin\psi \ , \qquad (3.3.34)$$

$$s3 = \sin\theta \ . \qquad (3.3.35)$$

Noticing that a fixed value of the total intensity is giving a sphere with unitary radius. The poles represent unidirectional solutions, being the north pole a pure CW operation and the south pole a pure CCW operation. The equator is the line where the two counter-propagating waves have the same intensity but different relative phase. Along the equator, the point $s2 = 0$, $s3 = 0$ represents the two fields in phase while the point $s2 = 1$, $s3 = 0$ represents the two fields with a phase difference equal to π. One can now visualize the instabilities of the SRL on the Poicaré sphere by numerical integration of Eqs. (3.3.29) and (3.1.3) [1]. Above threshold ($\mu > 1$) the first stable regime found is a symmetric solution (bidirectional regime), where the two counterpropagating fields have the same intensity. In Panel (a) of Fig. 3.3.6 one sees a trajectory starting from random initial conditions and ending at the fixed point $s2 = 0$ in the equator. Increasing the pump μ a Hopf bifurcation stabilizes a limit cycle regime (alternate oscillations in [96, 143]), where the two field intensities are

[1] Here noise terms are neglected and a fourth order Runge-Kutta algorithm is used with time discretization $\delta t = 10^{-2}$.

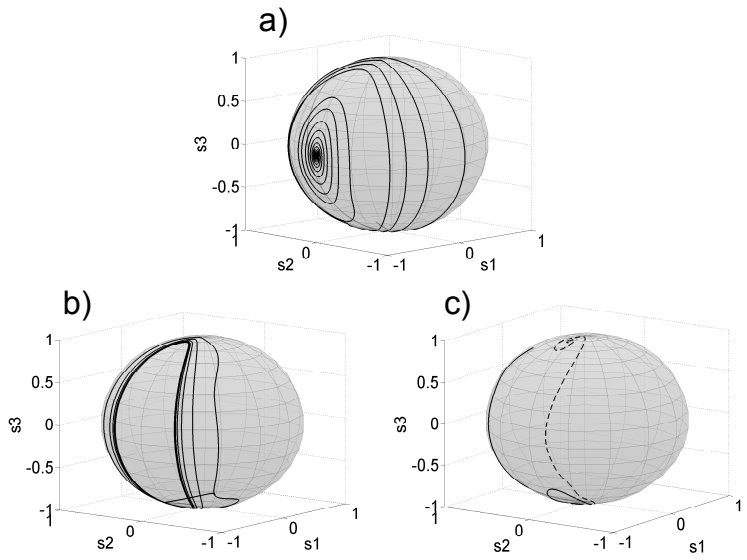

Fig. 3.3.6 – Evolution of the Stokes parameters on the Poincaré spheres for each regime. a) $\mu = 1.2$, b) $\mu = 2$ and c) $\mu = 2.6$.

oscillating in anticorrelated fashion, i.e. when one field reaches its maximum intensity the other reaches its minimum and viceversa. Panel (b) shows the limit cycle on the Poincaré sphere reached from a random initial condition. Increasing further μ an asymmetric solution regime due to a Pitchfork bifurcation is found [131]. Here the two counter-propagating fields have different intensities, and the difference increases with μ. In this regime, depending on the initial conditions, the laser emission is mainly concentrated either in CW or CCW direction. Panel (c) shows two trajectories from different initial conditions and how they are attracted by different fixed points corresponding to the two emission directions. When μ increases the two fixed points move towards the poles.

III.3.2 Fluctuations dynamics and correlations

(a) Linear fluctuations dynamics

Hereby the effect of a perturbation on the stationary solutions is analyzed. One considers a real perturbation n in the carrier density and complex perturbations $a_\pm$ for the fields

$$E_\pm = (Q + a_\pm)e^{i\omega t \pm i\phi} , \tag{3.3.36}$$

$$D = D_{st} + d . \tag{3.3.37}$$

By making use of (3.3.36) and (3.3.37) in (3.3.29) and (3.1.3) the following linear system is derived

$$\begin{aligned} \dot{a}_\pm &= \frac{1}{2}(1 + i\alpha)\{(D_{st}f - 1)a_\pm - D_{st}Q^2[s(a_\pm + a_\pm^*) + c(a_\mp + a_\mp^*)] \\ &+ Qfd\} - i\omega a_\pm - \eta(\cos 2\phi \mp i \sin 2\phi)a_\mp + \xi_\pm , \end{aligned} \tag{3.3.38}$$

$$\begin{aligned} \dot{d} &= -\gamma\{[1 - 2Q^2(s + c)]D_{st}Q(a_+ + a_+^* + a_- + a_-^*) \\ &+ (1 + 2Q^2 f)d\} , \end{aligned} \tag{3.3.39}$$

where $f = 1 - sQ^2 - cQ^2$ and the dot represents the time derivative. At this point a new set of variables to simplify the set (3.3.38)-(3.3.39) in two independent problems by block diagonalization are introduced. The new variables are

$$S = a_+ + a_- \ , \tag{3.3.40}$$

$$R = a_+ - a_- \ . \tag{3.3.41}$$

Those new variables can be related to the typical experimentally measured quantities $|E_+|^2$ and $|E_-|^2$ defining

$$\mathbb{I} = |E_+|^2 + |E_-|^2 \ , \tag{3.3.42}$$

$$\mathbb{D} = |E_+|^2 - |E_-|^2 \ , \tag{3.3.43}$$

and writing those new variables as $\mathbb{I} = I_0 + I$ and $\mathbb{D} = D_0 + D$, where I_0 and D_0 are constants and the perturbations I and D can be expressed in terms of S and R at first order,

$$I = Q(S + S^*) \ , \tag{3.3.44}$$

$$D = Q(R + R^*) \ . \tag{3.3.45}$$

The variable I describes the perturbation of the total intensity of the laser, regardless its distribution between the two modes. Whereas D describes the power exchange between the two counter-propagating fields.

(b) Relative intensity

The equation for the dynamic evolution of the relative intensity R is

$$\dot{R} = (1 + i\alpha)K(R + R^*) - 2\eta R + \xi_R(t) \ \ , \tag{3.3.46}$$

where the fluctuations term is derived from (3.3.40) and (3.3.30), $\xi_R(t) = \xi_+(t) - \xi_-(t)$ with the correlation properties

$$\langle \xi_R(t)\xi_R^*(t')\rangle = 4\sqrt{\beta\tau_p D_{st}}\delta(t - t') \ \ , \tag{3.3.47}$$

and K is a real constant defined by

$$K = \frac{1}{2}N_{st}Q^2(c - s) \ \ . \tag{3.3.48}$$

The corresponding eigenvalues for the differential equations system for R and R^* are

$$\lambda_{1,2} = K - 2k_d \pm [K^2 + 4K\alpha k_c - 4k_c^2]^{\frac{1}{2}} \ \ . \tag{3.3.49}$$

The above eigenvalues are used to construct the stability diagrams shown in Fig. 3.3.7 as functions of the two backscattering parameters. The figure shows how above a certain threshold for the conservative backscattering k_c the eigenvalues become complex conjugate (vertical line in all panels in Fig. 3.3.7). This implies the presence of a new eigenfrequency in the system. In the unstable region A such frequency originates a limit cycle, according to previous works [96], whereas in region B and C perturbations relax to the monochromatic solution. For increasing values of the pump μ the unstable region A becomes less pronounced. The relative intensity in Fourier space reads

$$\widetilde{R}(\omega) = \frac{1}{A(\omega)}[(i\omega - (1 - i\alpha)K + 2\eta^*)\widetilde{\xi}_R(\omega) + (1 + i\alpha)K\widetilde{\xi}_R^*(-\omega)] \ , \tag{3.3.50}$$

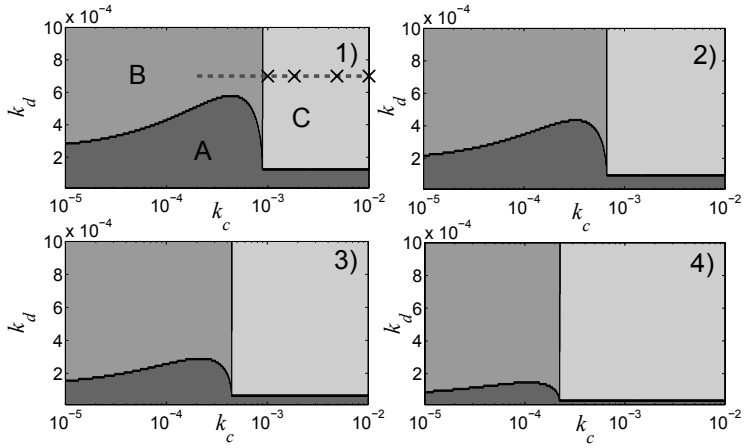

Fig. 3.3.7 – Stability diagrams of the symmetric solution (3.1.9)-(3.1.13) for different values of μ depending on backscattering coefficients. In region A the symmetric solution is unstable, region B is stable with real eigenvalues, and in region C is stable with complex conjugates eigenvalues. The panel 1) corresponds to $\mu = 1.2$, 2) to $\mu = 1.15$, 3) to $\mu = 1.1$ and 4) to $\mu = 1.05$.

where

$$A(\omega) = -\omega^2 + i\omega(4k_d - 2K) - 4(k_d + \alpha k_c)K + 4(k_d^2 + k_c^2) \ ,$$

leading to the two frequency correlation

$$\begin{aligned} \langle \widetilde{R}(\omega)\widetilde{R}^*(\omega')\rangle &= \frac{1}{A(\omega)A(-\omega)}[4k_d^2 - 4K(k_d + k_c\alpha) + 2K^2(1+\alpha^2) \\ &+ 2K\alpha\omega + (\omega - 2k_c)^2]8\pi\sqrt{\beta\tau_p D_{st}}\delta(\omega - \omega') \ . \end{aligned} \qquad (3.3.51)$$

From Eq. (3.3.45) one immediately obtains the D-spectrum

$$\langle \widetilde{D}(\omega)\widetilde{D}^*(\omega')\rangle = Q^2\left(\langle \widetilde{R}(\omega)\widetilde{R}^*(\omega')\rangle + \langle \widetilde{R}(-\omega)\widetilde{R}^*(-\omega')\rangle\right) \ . \qquad (3.3.52)$$

The analytical result is shown in Fig. 3.3.8 for a parameter set in region C of Fig. 3.3.7. The analytic result is compared with numerical simulations of the full nonlinear system [2]. Physically, the backscattering represents the energy exchange rate between the two modes. Such process shows a resonance (the peaks in Figs. 3.3.8, 3.3.9 (a) and (b)) which is more evident for increasing values of gain cross-saturation and conservative backscattering, whereas the resonance is damped for increasing values of gain self-saturation and dissipative backscattering (see continuous black line in Fig. 3.3.9 (a)).

SRLs are well modeled by strong cross-saturation and conservative backscattering. For such parameters choice, the investigation unveils the presence of a resonance peak in the frequency spectrum. Such behavior was reported in a recent experimental work [142]. Fig. 3.3.9 (a) shows how the D-spectrum is modified by conservative backscattering coefficient, using the analytical expression (3.3.51) for parameters values corresponding to the crosses in Fig. 3.3.7. The figure shows that the peak is more pronounced when moving deeper into region C.

[2]Numerical simulations of the stochastic differential equations (3.3.29-3.1.3) performed with a second order Heun algorithm (see appendix B) [140] and with random numbers generator described in [145].

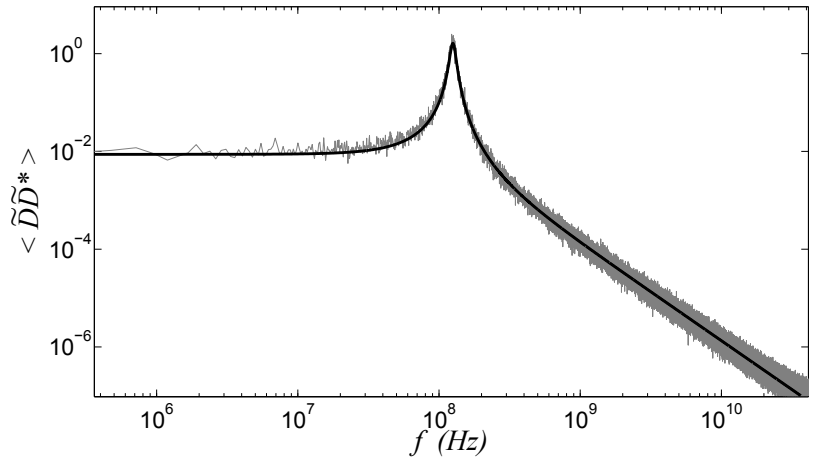

Fig. 3.3.8 – D-spectrum, the grey line corresponds to the numerical simulation for 20 noise realizations the analytical solution is the black line. $\beta = 10^{-3}\ ns^{-1}$, $\alpha = 3.5$, $s = 0.005$, $c = 0.01$, $k_d = 3.27\ 10^{-4}$, $k_c = 4.4\ 10^{-3}$, $\gamma = 2\ 10^{-3}$ and $\mu = 1.2$. The frequency f is found from the dimensionless angular frequency ω, here and in the following figures $f = \frac{\omega}{2\pi\tau_p}$, where $\tau_p = 10ps$ is the photon life time in the ring cavity.

Backscattering parameters are difficult to measure in operating conditions, and they are important to determine the static and dynamic properties of the laser. Such noise spectra, corresponding to measurements of the correlation spectrum of the intensity difference fluctuations, represent a novel and suitable way to extract the actual extent of the backscattering in its dissipative and conservative part, in working conditions. Fig. 3.3.9 (b) shows the D-spectrum dependence on pump current of the analytical expression (3.3.51), for pump values that maintain the SRL in the bidirectional regime. The figure shows the persistence of the resonance peak for increasing pumps.

In time domain, such resonance emerges as a consequence of the system oscillating around the fixed point due to spontaneous emission noise. Fig. 3.3.10 shows the evolution of θ and ψ for the complete set (3.3.29) and (3.1.3) including spontaneous emission noise in the bidirectional regime for different β values. In the absence of noise (see Fig. 3.3.6 panel (2)) the variables θ and ψ end in the fixed point after a transient, but in the presence of noise the transient becomes longer depending on the value of β, and produces slow undamped oscillations around the fixed point, this is reported in literature as Hopf bifurcation precursor [146]. Therefore, a possible interpretation is that the radiofrequency resonance peak experimentally [142] observed is a noise driven excitation near a bifurcation point.

III.3.3 Total intensity and carrier density

The equations for the dynamic evolution of S and n are

$$\dot{S} = (1+i\alpha)\{Cd + \widetilde{K}(S+S^*)\} + \xi_S(t)\ , \qquad (3.3.53)$$

$$\dot{d} = -\gamma\{d + [1-2Q^2(s+c)]D_{st}Q(S+S^*) + 2Q^2[1-sQ^2-cQ^2]d\}\ , \qquad (3.3.54)$$

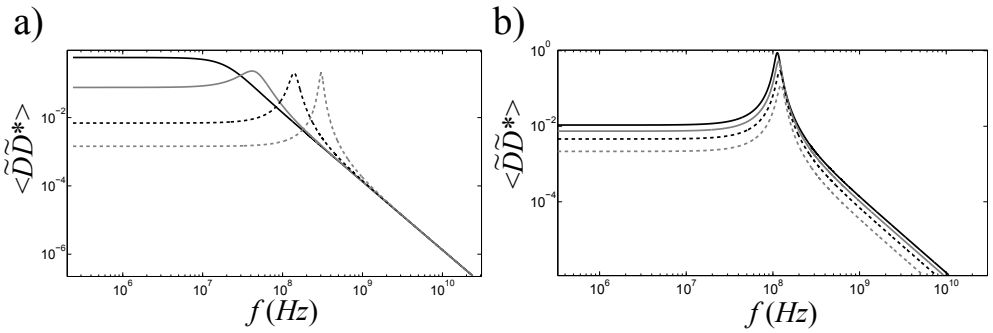

Fig. 3.3.9 – (a) D-spectrum, dependence on conservative backscattering coefficient, k_c. The black curve corresponds to $k_c = 10^{-3}$, the grey to $k_c = 1.83\ 10^{-3}$, the dashed black to $k_c = 4.83\ 10^{-3}$ and the dashed grey to $k_c = 10^{-2}$. Each spectrum corresponds each cross in the panel 1) in Fig. 3.3.7; $\beta = 10^{-3}\ ns^{-1}$, $k_d = 4\ 10^{-4}$ and $\mu = 1.2$. (b) D-spectrum dependence on pump current μ. The black curve corresponds to $\mu = 1.2$, the grey to $\mu = 1.15$, the dashed black to $\mu = 1.1$ and the dashed grey to $\mu = 1.05$; $\beta = 10^{-3}\ ns^{-1}$, $k_c = 4\ 10^{-3}$ and $k_d = 4\ 10^{-4}$.

where the fluctuations term is derived from (3.3.40) and (3.3.30), $\xi_S(t) = \xi_+(t) + \xi_-(t)$ with the same correlation properties shown in the previous section (3.3.47) and $\widetilde{K}$ and C are real constants

$$\widetilde{K} = -\frac{1}{2} D_{st} Q^2 (c+s) \ , \tag{3.3.55}$$

$$C = Q(1 - Q^2(c+s)) \ . \tag{3.3.56}$$

The corresponding eigenvalues for the system (3.3.53)-(3.3.54) are

$$\lambda_0 = 0 \ , \tag{3.3.57}$$

$$\lambda_{1,2} = \widetilde{K} - \frac{\gamma}{2} - \gamma QC \pm \frac{1}{2}[\gamma^2 + 4(\widetilde{K}^2 + \widetilde{K}\gamma + \gamma^2 QC(1+QC)) - 8\gamma(\widetilde{K}QC + D_{st}C^2)]^{\frac{1}{2}} \ . \tag{3.3.58}$$

The presence of a zero eigenvalue indicates that the system (3.3.53)-(3.3.54) is singular. The corresponding neutral eigenmode, known as Goldstone mode [147], appears because the solution in the bidirectional regime breaks the global phase invariance and gives rise to large undamped fluctuations. Here, the Goldstone mode is associated to the imaginary part of S. Interestingly, by using (3.3.44) we can remove this mode by decoupling the fluctuations and reducing the dynamics to a subspace orthogonal to the Goldstone mode itself. Then a linear approximation is well-justified in terms of the variable I, therefore the equations system (3.3.53)-(3.3.54) reads

$$\dot{I} = 2\widetilde{K} I + 2QCd + \xi_I(t) \ , \tag{3.3.59}$$

$$\dot{n} = -\gamma(1 - 2Q^2(s+c)) D_{st} I - \gamma(1 + 2QC)d \ , \tag{3.3.60}$$

where the fluctuation term is derived from (3.3.40) and (3.3.30), $\xi_I(t) = Q\mathbb{R}e(\xi_S(t) + \xi_S^*(t))$ with the correlation properties

$$\langle \xi_I(t)\xi_I(t')\rangle = \langle \xi_I(t)\xi_I^*(t')\rangle = 8Q^2\sqrt{\beta\tau_p D_{st}}\,\delta(t-t') \ . \tag{3.3.61}$$

By Fourier transform, one derives

$$\widetilde{I}(\omega) = \frac{1}{B(\omega)}[i\omega + \gamma(1+2QC)]\widetilde{\xi}_I(\omega) \ , \tag{3.3.62}$$

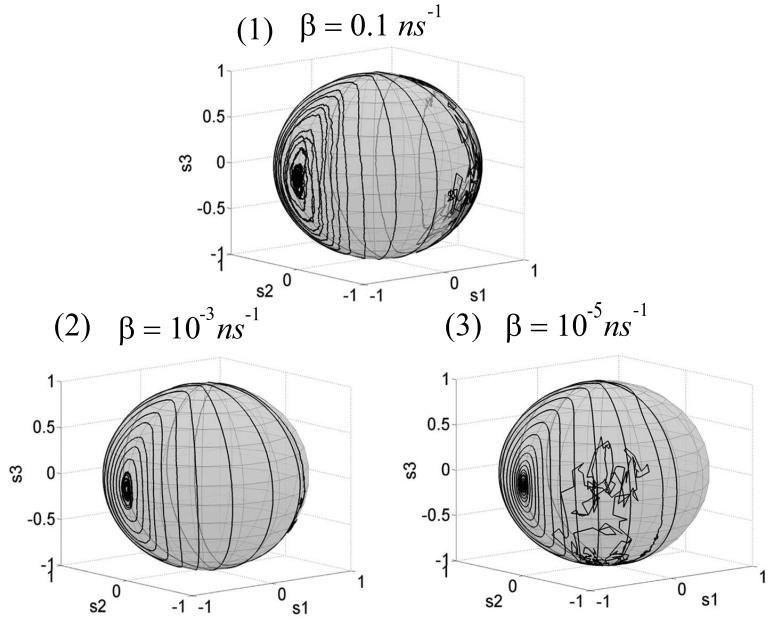

Fig. 3.3.10 – Poincaré spheres for the bidirectional regime in the presence of noise. (1) $\beta = 0.1\ ns^{-1}$, (2) $\beta = 10^{-3}\ ns^{-1}$ and (3) $\beta = 10^{-5}\ ns^{-1}$. $\mu = 1.3$.

and

$$\widetilde{d}(\omega) = \frac{-1}{B(\omega)}\gamma D_{st}[1 - 2Q^2(s+c)]\widetilde{\xi}_I(\omega)\ , \qquad (3.3.63)$$

where

$$B(\omega) = -\omega^2 + i\omega[\gamma(1+2QC) - 2\widetilde{K}] + 2\gamma[QCD_{st} + \widetilde{K}(2Q-1)]\ . \qquad (3.3.64)$$

One is able to find the following ensemble average

$$\begin{aligned}\langle \widetilde{I}(\omega)\widetilde{I}^*(\omega')\rangle &= \frac{Q^2}{\widetilde{B}(\omega)\widetilde{B}^*(\omega)}[\omega^2 + \gamma^2(1+2QC)^2] \\ &\times \ 16\pi\sqrt{\beta\tau_p D_{st}}\delta(\omega-\omega')\ . \end{aligned} \qquad (3.3.65)$$

Fig. 3.3.11 shows the good agreement between I-spectrum from (3.3.65) and numerical simulations. The observed peak corresponds to the typical relaxation oscillations of the field medium-energy exchange process, and its frequency depends on the pump and medium characteristics. The backscattering does not play any role in the field-medium energy exchange process as can be seen from (3.3.65).

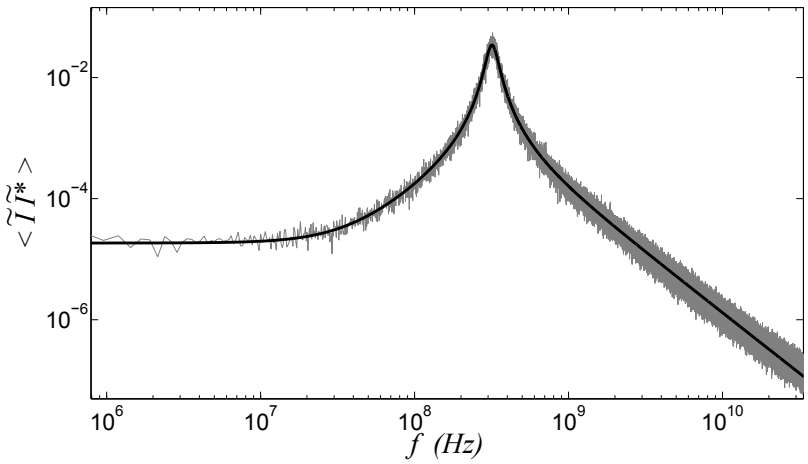

Fig. 3.3.11 – I-spectrum versus frequency. The grey line corresponds to the numerical simulation and the black line is the analytical solution (3.3.65), $\beta = 10^{-3}\, ns^{-1}$.

III.4 Conclusions

Conventional RE model has been modified to account for inertial rotation contribution and used to introduce a simple theory for a new technique to measure inertial rotation using a semiconductor ring laser. Taking into account that the rotation unbalances the intensities of the counter-propagating fields, an analytical expression for the responsivity function of a inertial rotation has been derived. The effect of the backscattering coefficients and the pump current on the responsivity function has been investigated, and the dynamic response of the device when a time dependent rotation rate is applied. Finally, quantum fluctuations in order to calculate the Noise Equivalent Rotation Rate have been considered. Our conclusion is that the proposal of using a semiconductor ring laser as a rotation sensor is theoretically viable, as it is not necessary limited by locking effects, the responsivity and noise performance are quite interesting compared to commercial laser gyroscope, taking into account the cost and size benefits of semiconductor laser technology. Moreover, this technique can be exported to any ring-laser gyroscope, providing a intracavity mechanism of conservative backscattering.

The SRL RE model has been used to study the influence of spontaneous emission noise when SRL is biased in the bidirectional regime. The analysis has been carried out by linearizing the model close to a stable stationary solution, and considering the effect of spontaneous emission as stochastic perturbations expressed by Langevin forces. At a linear level, perturbations concerning the total intensity and carrier inversion dynamics decouple from the energy distribution processes between the two modes. This fact has permitted a full analytic analysis, well confirmed by numerical simulations of the complete non linear system. The analysis showed that semiconductor ring lasers have peculiar noise properties. On one side the total intensity and carrier density show a noise spectrum (I-spectrum) characterized by a resonance induced by the typical field-medium energy exchange process (relaxation oscillations) and the global phase diffusion induced by the Goldstone mode. Besides, the degree of freedom associated to the simultaneous presence of two counter-propagating modes allows for a further process of energy exchange between the two modes. The analysis unveiled that such process presents a resonance influenced mainly by the backscattering parameters, and interpreted as a 'noisy precursor' of a Hopf bifurcation. This opens the possibility to extract the backscattering parameters from the noise spectra.

IV

Traveling wave modeling: Two level atom

This chapter is devoted to investigate on the stability and the dynamics of homogeneously broadened lasers by means of a traveling wave model (TWM) for a two level atom medium. The model allows to investigate beyond the Uniform Field Limit (UFL), where the spatial effects can be important, and to study both ring and Fabry-Pérot (FP) cavities.

For this purpose an algorithm is developed to study the spatiotemporal dynamics that can be applied also to composed cavities retaining their modal properties. Different tools have been developed to obtain the monochromatic solutions of the TWM and to investigate their stability, the numerical tools are described in appendix B. They can be applied to other nonlinear systems based in PDEs. In particular they are applied to Eqs. (2.4.92) and (2.4.94)-(2.4.96), allowing to treat the high number of variables that arise as a consequence of the discretization of the space. In the case where analytical treatment is possible, e.g. the laser threshold or unidirectional operation, it is discussed. Moreover, these analytical results are used to test the numerical algorithms.

In the following sections a method to describe how to find the monochromatic solutions in the general case via a "shooting" method is presented. It allows to find the spatial profiles of the variables: the electric fields, polarizations and carriers. It is also discussed how to perform the Linear Stability Analysis (LSA) of these solutions analytically or numerically in the general bidirectional case. First, it is applied to reach the different modal thresholds, then it is applied to characterize the stability of the different lasing modes. In sect. IV.5, these algorithms help to investigate on the wavelength multistability experimentally demonstrated in ring lasers but never observed in the case of FP lasers. The advantage that the model can be used for ring or FP lasers by changing the boundary conditions is taken. The proposed explanation for the different behaviors of ring a nd FP lasers is that multistability is more easily reached in ring than in FP lasers due the different amount of Spatial-Hole Burning (SHB) in each configuration.

Another advantage of this model is that naturally describes multi-mode behavior. In sect. IV.6, the single-mode dynamics are investigated, first recovering the results in ref. [54] verifying the numerical algorithm used. Then it is used to investigate multi-mode dynamics for different gain bandwidths taking into account the effect of the detuning of the cavity with respect to the atomic frequency. The simulations disclose novel dynamical regimes where the emission in each direction occurs at different wavelengths and a mode-locked emission regime that can coexist with bidirectional emission.

IV.1 Dimensionless model

For numerical purposes it is convenient to rewrite Eqs. (2.4.92)-(2.4.96) in dimensionless form,

$$\pm\frac{\partial A_\pm}{\partial s} + \frac{\partial A_\pm}{\partial \tau} = B_\pm - \alpha_{int}A_\pm \,, \tag{4.1.1}$$

$$\frac{1}{\gamma}\frac{\partial B_\pm}{\partial \tau} = -(1+i\widetilde{\delta})B_\pm + g(D_0 A_\pm + D_{\pm 2}A_\mp) + \sqrt{\beta D_0}\;\xi_\pm(s,\tau)\,, \tag{4.1.2}$$

$$\frac{1}{\epsilon}\frac{\partial D_0}{\partial \tau} = J - D_0 + \Delta\frac{\partial^2 D_0}{\partial s^2} - (A_+B_+^* + A_-B_-^* + c.c.), \tag{4.1.3}$$

$$\frac{1}{\eta}\frac{\partial D_{\pm 2}}{\partial \tau} = -D_{\pm 2} - \frac{\epsilon}{\eta}(A_\pm B_\mp^* + A_\mp^* B_\pm)\,, \tag{4.1.4}$$

where the fields and polarizations are scaled as

$$A_\pm = \sqrt{\frac{4n_{ef}}{\mu\omega_0 c\hbar\gamma_\parallel L}}E_\pm, \qquad B_\pm = -\sqrt{\frac{\mu\omega_0 c}{n_{ef}\hbar\gamma_\parallel L}}P_\pm\,, \tag{4.1.5}$$

and new dimensionless parameters are defined

$$\begin{array}{ccc} g = \frac{\mu\omega_0 c\widetilde{\mu}^2 L}{2n_{ef}\hbar\gamma_\perp}, & \gamma = \frac{\gamma_\perp n_{ef}L}{c}, & \epsilon = \frac{\gamma_\parallel n_{ef}L}{c}, \\ \eta = \frac{(\gamma_\parallel + 4q_0^2\mathbb{D})n_{ef}L}{c}, & \Delta = \frac{\mathbb{D}}{\gamma_\parallel L^2}, & \widetilde{\delta} = \frac{\delta}{\gamma_\perp}, \end{array} \tag{4.1.6}$$

and finally new coordinates are defined

$$\tau = \frac{c}{n_{ef}L}t, \qquad s = \frac{z}{L}. \tag{4.1.7}$$

In this reference frame the general boundary conditions (see Fig. 4.1.1) for the fields in the laser read

$$A_+(0,\tau) = t_+A_+(1,\tau) + r_-A_-(0,\tau)\,, \tag{4.1.8}$$

$$A_-(1,\tau) = t_-A_-(0,\tau) + r_+A_+(1,\tau)\,, \tag{4.1.9}$$

where $r_\pm$ and $t_\pm$ denote the reflectivity and transmissivity of the forward and backward waves respectively. These coefficients can in general be different for the two directions in order to describe the effect of non-reciprocal elements as an optical isolator. Noticing that $|t_\pm|^2 + |r_\pm|^2 = 1 - \varepsilon_\pm$, where $\varepsilon_\pm$ are the losses at the point coupler. Since in the TWM the field evolution is governed by a PDE, it is possible to treat on equal grounds ring and FP cavities simply by supplying for the appropriate boundary conditions. The general boundary conditions reduce to those for an ideal ring if $r_\pm = 0$ and $t_\pm \neq 0$, and to those for a FP cavity if $r_\pm \neq 0$ and $t_\pm = 0$. When $r_+ = r_-$ and $t_+ = t_-$ the device is symmetrical for the two propagation directions. In the following $\gamma\widetilde{\omega}_0 = 2\pi m$ where $m = 0, \pm 1, \pm 2\ldots$ is taken then $e^{i\gamma\widetilde{\omega}_0} = 1$ without loss of generality, it simply means that the carrier frequency ω_0 corresponds to one of the modes of the cavity. Moreover, the analysis is restricted to symmetric devices unless explicitly noted. Therefore $r_+ = r_- = r$ and $t_+ = t_- = t$.

Observe that the effects of diffusion in (4.1.3) are almost negligible because the characteristic length scale of D_0 is 1 (i.e. the cavity length), so Δ almost vanishes in

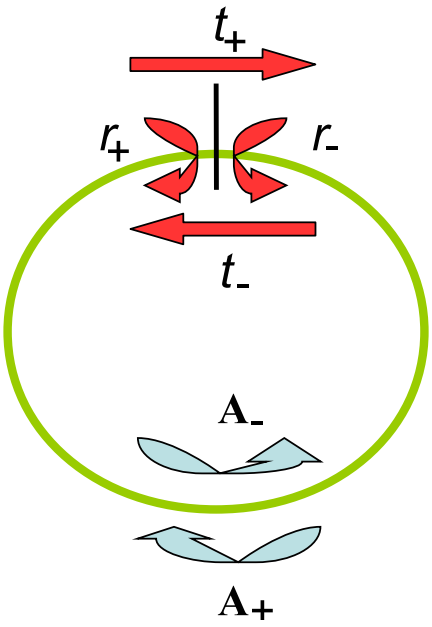

Fig. 4.1.1 – Schematic representation of the ring laser boundary conditions where $t_\pm$ and $r_\pm$ are the the reflectivity and transmissivity for the counter-propagating fields $A+$ and A_- respectively.

(4.1.3). Instead, it is retained in (4.1.4) because the characteristic length scale in this case is the emission wavelength $\lambda_0 = 2\pi c/\omega_0$.

Spontaneous emission is modeled by including Langevin noise terms $\xi_\pm(s,\tau)$ [123]. They are taken to be Gaussian white noise in space and time with zero mean and correlations $\langle \xi_\pm(s,\tau)\xi_\pm(s',\tau')\rangle = \delta(\tau-\tau')\delta(s-s')$, and their intensities are proportional to the population density [41].

IV.2 Laser threshold

The lasing threshold of the system can be readily determined by performing the linear stability analysis (LSA) around the off solution, i.e. $A^{st}_\pm = 0$, $B^{st}_\pm = 0$, $D^{st}_{\pm 2} = 0$ and $D^{st}_0 = J$. Linearizing (4.1.1)-(4.1.4) around this solution by introducing the small perturbations

$$\begin{array}{cc} A_\pm = \varepsilon\, a_\pm(s,\tau), & B_\pm = \varepsilon\, b_\pm(s,\tau), \\ D_0 = J, & D_{\pm 2} = 0. \end{array} \qquad (4.2.10)$$

Where ε is infinitesimally small, then retaining the terms to first order in ε and assuming that the perturbations evolve in time as

$$a_\pm(s,\tau) = \widetilde{a}_\pm(s)e^{\lambda\tau}, \quad b_\pm(s,\tau) = \widetilde{b}_\pm(s)e^{\lambda\tau}, \qquad (4.2.11)$$

we can obtain the eigenvalues λ_m $(m = 0, \pm 1, \pm 2, ...)$ which real part determines whether or not the mode m is stable and which imaginary part determines the modal frequency. The modal threshold is thus given by the current value J^{th}_m such that $Re(\lambda_m) = 0$. In that case, two different branches of solutions ($\sigma = \pm 1$) are obtained

whose modal thresholds read

$$J_m^{th}(\sigma) = \frac{\alpha_{int} - \ln(t+\sigma r)}{g}\left[1 + \left(\frac{\gamma\tilde{\delta} - 2\pi m}{\gamma + \alpha_{int} - \ln(t+\sigma r)}\right)^2\right], \qquad (4.2.12)$$

and which have modal frequencies

$$\Omega_m(\sigma) = \frac{2\pi m + \tilde{\delta}(\alpha_{int} - \ln(t+\sigma r))}{1 + \frac{1}{\gamma}(\alpha_{int} - \ln(t+\sigma r))}. \qquad (4.2.13)$$

The thresholds for the two branches of solutions are shown in Fig. 4.2.2 for typical ring laser parameters. From the Lorentzian shape of the two level gain curve, a curve is obtained for the threshold of the different modes m, as shown in Fig. 4.2.2. The minimum threshold corresponds to the gain peak. The two branches of solutions arise from the non-vanishing reflectivity r, i.e. when $r = 0$, the modes are degenerated in frequency and threshold gain forward and backward waves; however, for $r \neq 0$ the rotational invariance of the system is broken and the modes are given by combinations of the forward and backward waves that lift the degeneracy in both frequency and threshold gain. For $r \to 0$, Eqs. (4.2.12) and (4.2.13) read

$$\begin{aligned} J_m^{th}(\sigma) &= \frac{\alpha_{int} - \ln t}{g}\left[1 + \left(\frac{\gamma\tilde{\delta} - 2\pi m}{\alpha_{int} + \gamma - \ln t}\right)^2\right] \\ &+ \frac{\sigma}{gt}\left[\frac{(\gamma\tilde{\delta} - 2m\pi)^2(\alpha_{int} - \gamma - \ln t)}{(\alpha_{int} + \gamma - \ln t)^3} - 1\right] r + O(r)^2 \end{aligned}, \qquad (4.2.14)$$

and

$$\begin{aligned} \Omega_m(\sigma) &= \frac{\gamma[2\pi m + \tilde{\delta}(\alpha_{int} - \ln t)]}{\alpha_{int} + \gamma - \ln t} \\ &+ \frac{\gamma\sigma(2\pi m - \gamma\delta)}{t(\alpha_{int} + \gamma - \ln t)^2} r + O(r)^2. \end{aligned} \qquad (4.2.15)$$

Such an effect has been experimentally observed in semiconductor ring lasers [129] where the residual reflectivities in the laser cavity induced modal splitting that correspond to the mode-pulling formula (4.2.13). The threshold difference for these doublets is roughly proportional to r for small reflectivities hence the gain difference can be hardly noticeable specially for appreciable internal losses α_{int}. Considering for

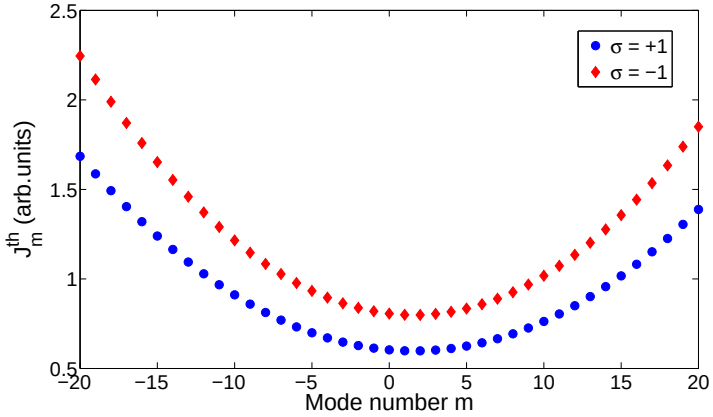

Fig. 4.2.2 – J_m^{th} vs m. $\tilde{\delta} = 0.1$, $g = 1$, $t = 0.5$, $r = 0.05$, $\alpha_{int} = 0$ and $\gamma = 100$. In this case the lowest threshold corresponds to mode $m = 2$ with $J_2^{th} = 0.5981$ for $\sigma = +1$.

instance that the atomic line is resonant with a cavity mode (i.e., $\delta = 0$), for a pure

ring cavity ($r_\pm = 0$), the frequency ($\Omega_m^\pm$) and threshold ($J_m^\pm$) for mode m in each of the counter-propagating directions read

$$\Omega_m^\pm = \frac{2\pi m}{1+\alpha_{tot}^\pm/\gamma}\ , \quad J_m^\pm = \frac{\alpha_{tot}^\pm}{g}\left[1+\left(\frac{\Omega_m^\pm}{\gamma}\right)^2\right]\ , \tag{4.2.16}$$

where $\alpha_{tot}^\pm = \alpha - \ln t_\pm$ accounts for the total distributed loss in each propagation direction. In the same way for a FP cavity ($t_\pm = 0$)—with $\alpha_{tot} = \alpha - \ln\sqrt{r_+ r_-}$—one obtains

$$\Omega_m = \frac{\pi m}{1+\alpha_{tot}/\gamma}\ , \quad J_m = \frac{\alpha_{tot}}{g}\left[1+\left(\frac{\Omega_m}{\gamma}\right)^2\right]\ . \tag{4.2.17}$$

IV.3 Monochromatic solutions

The nontrivial monochromatic solutions read

$$\begin{array}{cc} A_\pm = A_\pm^{st} e^{-i\widetilde{\omega}\tau}, & B_\pm = B_\pm^{st} e^{-i\widetilde{\omega}\tau}, \\ D_0 = D_0^{st}, & D_{\pm 2} = D_{\pm 2}^{st}, \end{array} \tag{4.3.18}$$

where $\widetilde{\omega}$ is the lasing frequency. Using (4.3.18) in (4.1.1)-(4.1.4) one finds

$$\pm\frac{\partial A_\pm^{st}}{\partial s} + (\alpha_{int} - i\widetilde{\omega})A_\pm^{st} = B_\pm^{st}\ , \tag{4.3.19}$$

$$B_\pm^{st} = \frac{g(D_0^{st}A_\pm^{st} + D_{\pm 2}^{st}A_\mp^{st})}{1+i(\widetilde{\delta}-\widetilde{\omega}/\gamma)}\ , \tag{4.3.20}$$

$$D_0^{st} = J - (A_+^{st}B_+^{st*} + A_-^{st}B_-^{st*} + c.c.)\ , \tag{4.3.21}$$

$$D_{\pm 2}^{st} = -\frac{\epsilon}{\eta}(A_\pm^{st}B_\mp^{st*} + A_\mp^{st*}B_\pm^{st})\ . \tag{4.3.22}$$

These equations determine the stationary spatial profiles of the variables.

IV.3.1 Unidirectional solution

Analytical solutions for Eqs. (4.3.19)-(4.3.22) can be found only in the simplest case $r = 0$ and $\alpha_{int} = 0$. In this limit, the two counter-propagating waves are degenerate and a (unstable) bidirectional solution also exists [43, 148]. Focussing on the unidirectional solutions $A_+^{st} \neq 0$ and $A_-^{st} = 0$ without loss of generality (the counter-propagating solution can be directly obtained by replacing + with − in the final results). Using (4.3.20) in (4.3.19) and solving the resulting differential equation, one finds

$$A_+^{st}(s) = A_+^{st}(0)e^{i\widetilde{\omega}s + \frac{g}{1+i(\widetilde{\delta}-\widetilde{\omega}/\gamma)}G(s)}\ , \tag{4.3.23}$$

where

$$G(s) = \int_0^s D_0^{st}(s')ds'\ . \tag{4.3.24}$$

Noticing that $D_0^{st} = \frac{dG(s)}{ds}$, hence using (4.3.20) and (4.3.23) in (4.3.21) yields

$$\frac{dG}{ds} = \frac{J}{1+\frac{2g}{1+(\widetilde{\delta}-\widetilde{\omega}/\gamma)^2}|A_+(0)|^2 e^{\frac{2g}{1+(\widetilde{\delta}-\widetilde{\omega}/\gamma)^2}G(s)}}\ . \tag{4.3.25}$$

In order to integrate Eq. (4.3.25) along the cavity, one needs to impose the boundary conditions of the problem. Clearly, from (4.3.24) at $s = 0$ one obtains: $G(s = 0) = 0$, and using Eq. (4.3.23) with the boundary condition for the field $A_+^{st}(0) = tA_+^{st}(1)$ imposes that

$$G(1) = \frac{-\ln t}{g}[1 + (\widetilde{\delta} - \widetilde{\omega}/\gamma)^2], \tag{4.3.26}$$

$$\widetilde{\omega} = \frac{2\pi m - \widetilde{\delta}\ln t}{1 - \frac{\ln t}{\gamma}} . \tag{4.3.27}$$

Note that (4.3.27) is equivalent to (4.2.13) in this simplified case. Integrating (4.3.25) from one end to the other of the laser cavity and using the boundary conditions for $G(s)$ allows to determine

$$|A_+^{st}(0)|^2 = \frac{J + \frac{\ln t}{g}[1 + (\widetilde{\delta} - \widetilde{\omega}/\gamma)^2]}{e^{-2\ln t} - 1} . \tag{4.3.28}$$

Therefore solving for $G(s)$, one determines the field profile along the laser cavity as shown in Fig. 4.3.3.

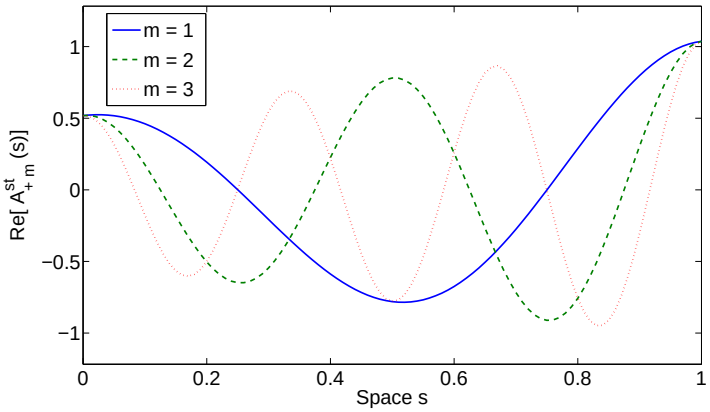

Fig. 4.3.3 – $\mathrm{Re}[A_{+m}^{st}(s)]$ in the unidirectional solution, $\widetilde{\delta} = 0.1$, $g = 1$, $t = 0.5$, $\gamma = 100$ and $J = 1.5$.

IV.3.2 Bidirectional solution

The physical insight gained in the analysis of the simplest case suggests that in the general case, Eqs. (4.3.19)-(4.3.22) can be very efficiently solved by means of a numerical shooting method [149] which is useful since no analytical solution is possible in this case (see appendix B). Here, one can formally solve the system. Considering that the space is formed by a discrete set of N points, then $j = 1, \ldots, N$. Defining a vector for the material variables (and their complex conjugates) for every point in

the discretized space. For the jth point in space, the vector of variables reads

$$\vec{x}_j^{ST} = \begin{pmatrix} B_+^{st} \\ B_+^{st*} \\ B_-^{st} \\ B_-^{st*} \\ D_{+2}^{st} \\ D_{-2}^{st} \\ D_0^{st} \end{pmatrix}_j . \tag{4.3.29}$$

One can write a matrix for the equation system (4.3.20)-(4.3.22),

$$\bar{\bar{M}}_j^{ST} = \begin{pmatrix} l & 0 & 0 & 0 & -gA_-^{st} & 0 & -gA_+^{st} \\ 0 & l^* & 0 & 0 & 0 & -gA_-^{st*} & -gA_+^{st*} \\ 0 & 0 & l & 0 & 0 & -gA_+^{st} & -gA_-^{st} \\ 0 & 0 & 0 & l^* & -gA_+^{st*} & 0 & -gA_-^{st*} \\ A_-^{st*} & 0 & 0 & A_+^{st} & \eta/\epsilon & 0 & 0 \\ 0 & A_-^{st} & A_+^{st*} & 0 & 0 & \eta/\epsilon & 0 \\ A_+^{st*} & A_+^{st} & A_-^{st*} & A_-^{st} & 0 & 0 & 1 \end{pmatrix}_j , \tag{4.3.30}$$

where $l = 1 + i(\widetilde{\delta} - \widetilde{\omega}/\gamma)$ and the system is completed with the solution vector is $\vec{b}_j^{ST} = (0, 0, 0, 0, 0, 0, J)$. Then solving this linear system supposing the electric field as a parameter,

$$\bar{\bar{M}}_j^{ST} \cdot \vec{x}_j^{ST} = \vec{b}_j^{ST} . \tag{4.3.31}$$

The shooting method consists in giving a guess for the electric fields $A_\pm^{st}$ for the spatial point $j = 1$ (i.e. $s = 0$) and a guess for the frequency $\widetilde{\omega}$. The spatial dependence of (4.1.1)-(4.1.4) is solved using standard integration techniques with a spatial step $h = 1/N$ towards the other end of the cavity. For each space point, the system (4.3.31) with $A_\pm^{st}$ and $\widetilde{\omega}$ is solved to find $B_\pm^{st}$, D_0^{st} and $D_{\pm 2}^{st}$ for point j, then solving Eq. (4.3.19) one obtains the fields $A_\pm^{st}$ at point $j + 1$. This process is repeated until the last point of the cavity $j = N$ (i.e. $s = 1$). The propagated values $A_\pm(1)$ must verify the boundary conditions. By using a Newton-Raphson algorithm [149] a new guess for the field amplitudes $A_\pm(0)$ and the modal frequency is proposed and the process is repeated until one reaches convergence. The final trajectory generated by this shooting method provides a discretized representation of the modal profile as a spatial mesh of N points (see appendix B for details). In Fig. 4.3.4 a bidirectional monochromatic solution calculated in this way is shown. This shooting method can be used to quickly find the steady state solutions for different pump values, hence limited bifurcation diagrams as a function of the pump can be readily obtained. For instance, Fig. 4.3.5 depicts the pitchfork bifurcation from a bidirectional solution into two degenerate, almost unidirectional solutions that has been observed in different ring laser systems [96]. It should be noted that, in order to obtain a bifurcation diagram like that in Fig. 4.3.5, it is necessary to perform a double scan, one upwards and one downwards, since the shooting method follows the resulting branches even if they are unstable.

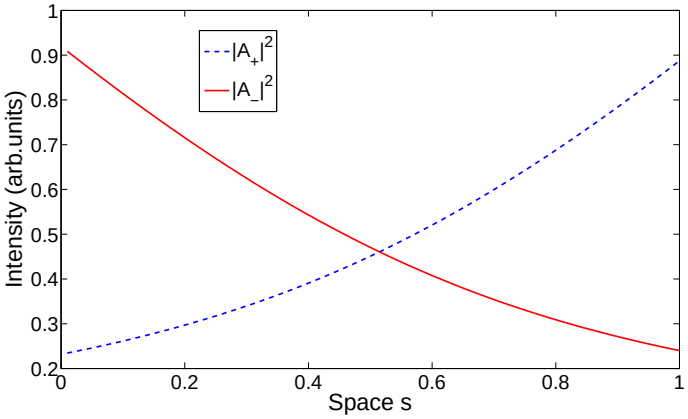

Fig. 4.3.4 – Bidirectional Monochromatic solutions in the general case. Intensity of the fields inside the cavity vs space s. Mesh points $N = 100$, $J = 0.5$, $\widetilde{\delta} = 0.1$, $g = 1$, $\epsilon = \eta = 10^{-2}$, $\beta = 0$, $t = 0.5$, $r = 2\ 10^{-2}$, $\alpha_{int} = 0$ and $\gamma = 100$.

IV.4 Linear stability analysis

The next step in the analysis is to characterize the stability of the steady state solutions. Introducing perturbations as

$$\begin{aligned} A_\pm &= [A_\pm^{st} + a_\pm(s,\tau)]e^{-i\widetilde{\omega}\tau} , && (4.4.32)\\ B_\pm &= [B_\pm^{st} + b_\pm(s,\tau)]e^{-i\widetilde{\omega}\tau} , && (4.4.33)\\ D_0 &= D_0^{st} + d_0(s,\tau) , && (4.4.34)\\ D_{\pm 2} &= D_{\pm 2}^{st} + d_{\pm 2}(s,\tau) . && (4.4.35) \end{aligned}$$

Using (4.4.32)-(4.4.35) in the traveling wave equations (4.1.1)-(4.1.4) and taking to first order in perturbations, one arrives to a new set of equations for the perturbations,

$$\pm \frac{\partial a_\pm}{\partial s} - i\widetilde{\omega} a_\pm + \frac{\partial a_\pm}{\partial \tau} = b_\pm - \alpha_{int} a_\pm , \quad (4.4.36)$$

$$\left[1 + i\left(\widetilde{\delta} - \frac{\widetilde{\omega}}{\gamma}\right)\right] b_\pm + \frac{1}{\gamma}\frac{\partial b_\pm}{\partial \tau} = g[D_0^{st} a_\pm + d_0 A_\pm^{st} + D_{\pm 2}^{st} a_\mp + d_{\pm 2} A_\mp^{st}] , \quad (4.4.37)$$

$$\frac{\partial d_0}{\partial \tau} = -\epsilon[d_0 + (A_+^{st} b_+^* + a_+ B_+^{st*} + A_-^{st} b_-^* + a_- B_-^{st*} + c.c.)] , \quad (4.4.38)$$

and

$$\frac{\partial d_{\pm 2}}{\partial \tau} = -\eta d_{\pm 2} - \epsilon(A_\pm^{st} b_\mp^* + a_\pm B_\mp^{st*} + A_\mp^{st*} b_\pm + a_\mp^* B_\pm^{st}) . \quad (4.4.39)$$

Supposing that the perturbations evolve in time as

$$\begin{aligned} a_\pm(s,\tau) &= \widetilde{a}_\pm(s)e^{\lambda\tau} ,\\ b_\pm(s,\tau) &= \widetilde{b}_\pm(s)e^{\lambda\tau} ,\\ d_0(s,\tau) &= \widetilde{d}_0(s)e^{\lambda\tau} ,\\ d_{\pm 2}(s,\tau) &= \widetilde{d}_{\pm 2}(s)e^{\lambda\tau} . \end{aligned} \quad (4.4.40)$$

Using (4.4.40) in (4.4.36)-(4.4.39) one can write the set of equations as

$$\pm \frac{\partial \widetilde{a}_\pm}{\partial s} + (\lambda + \alpha_{int} - i\widetilde{\omega})\widetilde{a}_\pm = \widetilde{b}_\pm , \quad (4.4.41)$$

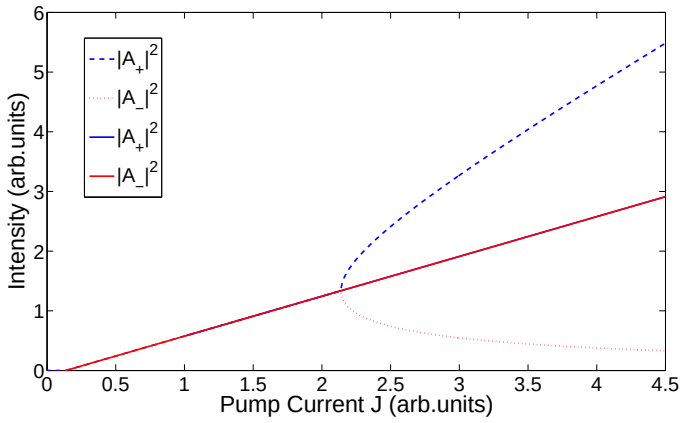

Fig. 4.3.5 – Bifurcation diagram of the monochromatic solutions: for decreasing pump J showing a pitchfork bifurcation (dashed and dotted lines) and for increasing J showing a bidirectional solution (solid lines). For values below $J = 2.15$ all the lines coincide in the bidirectional regime. Mesh points $N = 100$, $\widetilde{\delta} = 0$, $g = 5$, $\epsilon = 10^{-2}$, $\eta = 5$, $\beta = 0$, $t = 0.5$, $r = 5\ 10^{-3}$, $\alpha_{int} = 0$ and $\gamma = 100$.

$$\left[1 + \frac{\lambda}{\gamma} + i\left(\widetilde{\delta} - \frac{\widetilde{\omega}}{\gamma}\right)\right]\widetilde{b}_{\pm} = g[D_0^{st}\widetilde{a}_{\pm} + \widetilde{d}_0 A_{\pm}^{st} + D_{\pm 2}^{st}\widetilde{a}_{\mp} + \widetilde{d}_{\pm 2}A_{\mp}^{st}] \ , \tag{4.4.42}$$

$$(\lambda + \epsilon)\widetilde{d}_0 = -\epsilon(A_+^{st}\widetilde{b}_+^* + \widetilde{a}_+ B_+^{st*} + A_-^{st}\widetilde{b}_-^* + \widetilde{a}_- B_-^{st*} + c.c.) \ , \tag{4.4.43}$$

and

$$(\lambda + \eta)\widetilde{d}_{\pm 2} = -\epsilon(A_{\pm}^{st}\widetilde{b}_{\mp}^* + \widetilde{a}_{\pm} B_{\mp}^{st*} + A_{\mp}^{st*}\widetilde{b}_{\pm} + a_{\mp}^* B_{\pm}^{st}) \ . \tag{4.4.44}$$

IV.4.1 Unidirectional solution

In this case one has to take into account the equation for the whole set of perturbations. Supposing that $A_+^{st} \neq 0$ and $A_-^{st} = 0$, then the set (4.4.41)-(4.4.44) can be written as

$$\pm \frac{\partial \widetilde{a}_{\pm}}{\partial s} + (\lambda - i\widetilde{\omega})\widetilde{a}_{\pm} = \widetilde{b}_{\pm} \ , \tag{4.4.45}$$

$$\widetilde{b}_+ = \frac{g(D_0^{st}\widetilde{a}_+ + \widetilde{d}_0 A_+^{st})}{1 + \frac{\lambda}{\gamma} + i(\widetilde{\delta} - \frac{\widetilde{\omega}}{\gamma})} \ , \tag{4.4.46}$$

$$\widetilde{b}_- = \frac{g(D_0^{st}\widetilde{a}_- + \widetilde{d}_{-2} A_+^{st})}{1 + \frac{\lambda}{\gamma} + i(\widetilde{\delta} - \frac{\widetilde{\omega}}{\gamma})} \ , \tag{4.4.47}$$

$$\widetilde{d}_0 = -\frac{\epsilon}{\lambda + \epsilon}(A_+^{st}\widetilde{b}_+^* + \widetilde{a}_+ B_+^{st*} + c.c.) \ , \tag{4.4.48}$$

$$\widetilde{d}_{+2} = -\frac{\epsilon}{\lambda + \eta}(A_+^{st}\widetilde{b}_-^* + \widetilde{a}_-^* B_+^{st}) \ , \tag{4.4.49}$$

and

$$\widetilde{d}_{-2} = -\frac{\epsilon}{\lambda + \eta}(\widetilde{a}_- B_+^{st*} + A_+^{st*}\widetilde{b}_-) \ . \tag{4.4.50}$$

The analytical treatment of this problem is very difficult. However a semi-analytical treatment can be applied to the stability of the counter-propagating perturbation,

i.e. $\widetilde{a}_-$, because in this case $\widetilde{d}_0$ does not depend on $\widetilde{a}_-$. Using the above equations one can write the differential equation for $\widetilde{a}_-$ as

$$\frac{d\widetilde{a}_-}{ds} = F_m(s,\lambda)\widetilde{a}_- \ , \tag{4.4.51}$$

where

$$F_m(s,\lambda) = \lambda - i\widetilde{\omega} - \frac{g\gamma[D_0^{st}(\eta+\lambda) - \epsilon A_+^{st} B_+^{st*}]}{(\eta+\lambda)(\gamma + i\gamma\delta + \lambda - i\widetilde{\omega}) + g\gamma\epsilon|A_+^{st}|^2} \ . \tag{4.4.52}$$

The solution for (4.4.51) is

$$\widetilde{a}_-(s) = \widetilde{a}_-(0)e^{\int_0^s F_m(s',\lambda)ds'} \ , \tag{4.4.53}$$

and using the boundary condition

$$\widetilde{a}_-(1) = t\widetilde{a}_-(0)e^{i\widetilde{\omega}_0\gamma} \tag{4.4.54}$$

one arrives to the next complex equation

$$\int_0^1 F_m(s',\lambda)ds' - \frac{i\widetilde{\omega}_0}{v} = \ln t + 2\pi m_2 i \ . \tag{4.4.55}$$

This equation is solved numerically and the results for the stability of the mode $m = 2$ are shown in Fig. 4.4.6. In the case of co-propagating perturbations, i.e. $\widetilde{a}_+$,

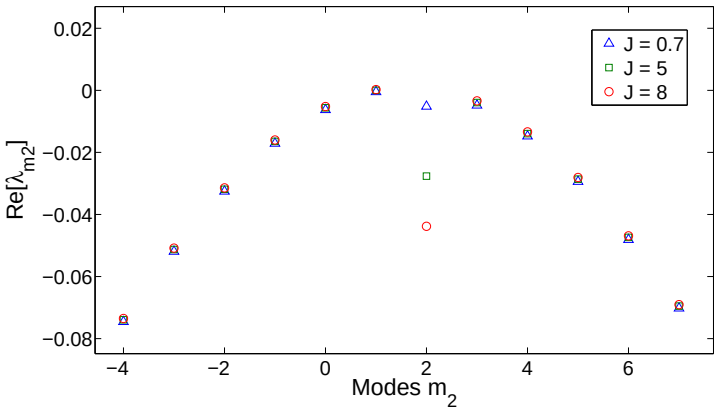

Fig. 4.4.6 – Re[λ_m] vs m_2. $\widetilde{\delta} = 0.1$, $g = 1$, $t = 0.5$, $\epsilon = \eta = 10^{-2}$ and $\gamma = 100$. With respect to $m = 2$, i.e. the mode with lowest threshold for this parameter set.

the problem becomes more complicated. This motivates the numerical treatment of the general bidirectional case.

IV.4.2 Bidirectional solution

In the general bidirectional case a vector for the perturbations can be written as

$$\vec{x}_j^{LSA} = \begin{pmatrix} \widetilde{b}_+ \\ \widetilde{b}_+^* \\ \widetilde{b}_- \\ \widetilde{b}_-^* \\ \widetilde{d}_{+2} \\ \widetilde{d}_{-2} \\ \widetilde{d}_0 \end{pmatrix}_j . \tag{4.4.56}$$

In the same way one can write a matrix for the equation system (4.4.42)-(4.4.44),

$$\bar{\bar{M}}_j^{LSA} = \begin{pmatrix} \widetilde{l}+\lambda & 0 & 0 & 0 & -gA_-^{st} & 0 & -gA_+^{st} \\ 0 & \widetilde{l}^*+\lambda & 0 & 0 & 0 & -gA_-^{st*} & -gA_+^{st*} \\ 0 & 0 & \widetilde{l}+\lambda & 0 & 0 & -gA_+^{st} & -gA_-^{st} \\ 0 & 0 & 0 & \widetilde{l}^*+\lambda & -gA_+^{st*} & 0 & -gA_-^{st*} \\ A_-^{st*} & 0 & 0 & A_+^{st} & (\lambda+\eta)/\epsilon & 0 & 0 \\ 0 & A_-^{st} & A_+^{st*} & 0 & 0 & (\lambda+\eta)/\epsilon & 0 \\ A_+^{st*} & A_+^{st} & A_-^{st*} & A_-^{st} & 0 & 0 & 1+\lambda/\epsilon \end{pmatrix}_j , \tag{4.4.57}$$

where $\widetilde{l} = 1 + i(\widetilde{\delta} - \widetilde{\omega}/\gamma)$ and the vector solution is

$$\vec{b}_j^{LSA} = \begin{pmatrix} g(D_0^{st}\widetilde{a}_+ + D_{+2}^{st}\widetilde{a}_-) \\ g(D_0^{st}\widetilde{a}_+^* + D_{-2}^{st}\widetilde{a}_-^*) \\ g(D_0^{st}\widetilde{a}_- + D_{-2}^{st}\widetilde{a}_+) \\ g(D_0^{st}\widetilde{a}_-^* + D_{+2}^{st}\widetilde{a}_+^*) \\ -(B_-^{st*}\widetilde{a}_+ + B_+^{st}\widetilde{a}_-^*) \\ -(B_+^{st*}\widetilde{a}_- + B_-^{st}\widetilde{a}_+^*) \\ -(B_+^{st*}\widetilde{a}_+ + B_-^{st*}\widetilde{a}_- + B_+^{st}\widetilde{a}_+^* + B_-^{st}\widetilde{a}_-^*) \end{pmatrix}_j . \tag{4.4.58}$$

Solving this system expressions for $\widetilde{b}_+$ and $\widetilde{b}_-$ are found depending on the steady states variables and the perturbations $\widetilde{a}_+$ and $\widetilde{a}_-$, that allows to found the values numerically from the coupled ODEs (4.4.41) solving

$$\bar{\bar{M}}_j^{LSA} \cdot \vec{x}_j^{LSA} = \vec{b}_j^{LSA} . \tag{4.4.59}$$

From the monochromatic solutions, one could in principle compute the eigenvalues from the linearized form of (4.1.1)-(4.1.4) with (4.4.59). However, the resulting system is still a hyperbolic PDE, and a discrete representation of the solution would require to express the gradient operator using finite differences. This approach is not practical: time propagation of hyperbolic PDEs cannot be reliably made for an arbitrary choice of the spatial and of the temporal discretization, because it would lead to large errors in the eigenvalues. Instead, the temporal map $\mathbf{V}_{j+1} = \mathbf{U}(h, \mathbf{V}_j)$ described in in appendix B is used advancing the state vector $\mathbf{V}$ a time step h while verifying the Courant condition [150] and canceling numerical dissipation. Considering all possible perturbations of $\mathbf{V}$ hereby finding the matrix $\mathbf{M} = \partial\mathbf{U}/\partial\mathbf{V}$ representing the linear operator governing the time evolution for the perturbations around one given monochromatic solution. One finally computes the $11 \times N$ Floquet multipliers z_i of $\mathbf{M}$, which determine the eigenvalues as $\lambda_i = h^{-1} \ln z_i$.

The results of this algorithm are shown in Fig. 4.4.7 for the solution $m = 2$ of a symmetric, bidirectional ring laser. $N = 256$ mesh points are used; in this case, determining the spatial profile of the monochromatic solution, generating the matrix $\mathbf{M}$ and diagonalizing it using the QR decomposition method takes 1, 10 and 60 seconds, respectively, on an standard PC using C++ routines based on *Octave* [151]. Stability results have been controlled by direct integration of the TWM [152].

In Fig. 4.4.7 panel a) it is showed that just above the threshold current $J \simeq 0.51$, this solution corresponds to an unstable bidirectional state. At $J_{\in} \simeq 1.5$, a pitchfork bifurcation into unidirectional emission occurs, but the degenerate (almost) unidirectional states are also unstable, as evidenced by the eigenvalues shown in panel b) for $J = 3$. However, for currents above $J > 3.5$, they become stable and all the eigenvalues have $Re(\lambda) < 0$ (see panel c) for $J = 4$). This technique can be applied to investigate the longitudinal mode multistability as it is performed in the following section.

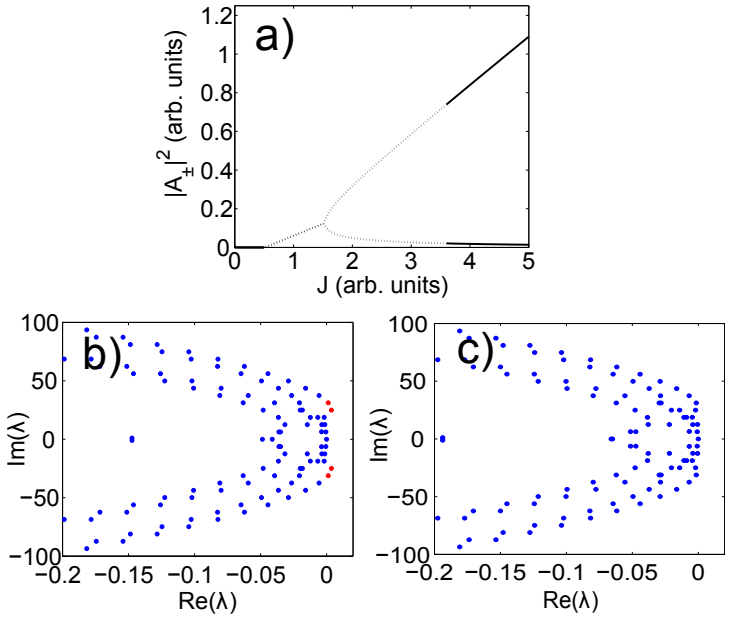

Fig. 4.4.7 – (a) Numerical bifurcation diagram for mode $m = 2$ for a ring laser, $g = 4$, $\gamma = 250$, $\alpha_{int} = 2.03$, $\epsilon = 0.05$, $\eta = 10$, $t_+ = t_- = 0.98$ and $r_+ = r_- = 0.01$. The threshold value is $J_{th} = 0.51$. (b) Real versus imaginary part of the eigenvalues for $J = 3$. Eigenvalues in blue (red) have $Re(\lambda) < 0$ ($Re(\lambda) > 0$). (c) Same as panel (b) for $J = 4$.

IV.5 Wavelength multistability

[1]In this section it is theoretically discussed the impact of the cavity configuration on the possible longitudinal mode multistability in homogeneously broadened lasers. The analysis is based on the most general form of a TWM (4.1.1)-(4.1.4) for which the methods presented in IV.3 and IV.4 are used allowing to evaluate the monochromatic solutions as well as their eigenvalue spectrum. It is found that multistability is more easily reached in Ring than in Fabry-Pérot cavities in agreement with recent experimental reports, which we attribute to the different amount of Spatial-Hole Burning in each configuration.

Recent reports [87, 97, 153] experimentally demonstrate that the emission wavelength of bidirectional SRL can be selected by optical injection among that of several longitudinal modes; upon removal of the optical injection, the emission wavelength remains stable at the chosen value. In addition wavelength multistability in SRLs can coexist with the directional bistability [67], hence it can be of interest for all-optical signal processing applications at a higher-logical level [154]. Although early studies of unidirectional ring lasers, where only one propagation direction was allowed, suggested possible multistability among longitudinal modes [36, 155], this behavior has, to our knowledge, never before been explained or experimentally observed in other types of single-cavity, free-running lasers.

Multistable behavior has been observed in more complex configurations as lasers with optical feedback [156, 157] or with intracavity saturable absorbers [158]. It was shown that a carefully chosen detuning can induce a degeneracy between two adjacent modes and promote bistability in Fabry-Pérot (FP) CO_2 laser [159]. Also, in FP semiconductor lasers, one should mention stochastic mode-hopping between two adjacent modes: this phenomenon consists of random jumps with short characteristic times (below 1 ms) from one stable mode to the other induced either by spontaneous emission noise [160, 161] or, in general, by parameter fluctuations [162] that change the tuning of the gain with respect to the cavity. Yet, at variance with SRL, in these cases there is no evidence that the emission wavelength can be selected at will and remain for long periods.

The different behavior of SRL and FP lasers regarding wavelength multistability calls for an explanation. Ascertaining multistability requires the determination of the monochromatic solutions and the resolution of the LSA. These two problems are known to be difficult if not impossible to implement analytically in the general case, and solutions are only available under strong approximations. Within the Uniform Field Limit (UFL) approximation [36], this can be accomplished via a modal decomposition for either ring [163] or FP lasers[164]. Beyond the UFL, analytical results are available for unidirectional rings if one neglects internal losses [52] and/or invokes singular perturbation techniques [165]. When bidirectional emission, cavity losses or spatially dependent parameters come into play, no general method for the LSA is known, which hinders the study of many devices as bidirectional SRL, FP lasers, or devices for which the UFL or singular perturbations methods are inadequate.

Bidirectional ring and FP lasers are compared regarding the possible multistability of their longitudinal modes. The LSA is obtained by constructing the linearized evolution operator for which one can evaluate the Floquet multipliers and trace back the eigenvalues governing the stability described in section IV.4. This approach is quite general and could also be applied to other dynamical systems described by

[1]This part is based on the article: "Longitudinal mode multistability in Ring and Fabry-Pérot lasers: the effect of spatial hole burning" by A. Pérez-Serrano, J. Javaloyes and S. Balle, *Opt. Express* **19**, 3284 (2011).

partial differential equations (PDEs), and the next results extend and generalize the previous studies performed for unidirectional ring lasers [36, 47, 52, 165, 166]. It is found that multistability is more easily reached in rings as compared to FP cavities, because of the different amounts of Spatial-Hole Burning in each configuration.

Considering homogeneously broadened lasers described by the bidirectional TWM composed by the set (4.1.1)-(4.1.4). Although this model does not correctly describe the asymmetric gain curve typical of semiconductor materials as it lacks the strong amplitude-phase coupling denoted by Henry's linewidth enhancement factor α_H, it still can shed some light on the different behavior of ring and FP lasers regarding multistability. One can expect α_H to induce an asymmetry of the multistability band around the dominant mode, but a precise analysis of semiconductor devices requires modeling the material response as in e.g. [120].

For the sake of simplicity one considers that the atomic line is resonant with a cavity mode (i.e., $\delta = 0$). Assessing modal multistability requires finding the monochromatic solutions of (4.1.1)-(4.1.4) and determining their stability for a given operation point. One computes these solutions for a given cavity configuration via the shooting method presented in IV.3 and perform their LSA with the method presented in IV.4.

In the following pictures, solid (dashed) lines represent the stable (unstable) solutions and parameters are typical of III-V semiconductor systems: a cavity of $L_c = 2.4$ mm and $\tau_c = 25$ ps, a modal gain of 33 cm^{-1}, a gain width of 13 nm, a carrier lifetime 0.5 ns and a diffusion coefficient of 5 cm^2/s.

Repeating the procedure used for Fig. 4.4.7 for all solutions allows to obtain a general view of the stability of the system by plotting the bifurcation diagrams for all modes. In this case, however, it suffices to examine only half of the diagram because the resonance condition implies symmetry for $\pm m$.

Fig. 4.5.8 depicts the general bifurcation diagram for both the ring laser with the parameters in Fig. 4.4.7 (panel a), and an equivalent FP device (panel b). In this sense, a word of caution is in order: for a fair comparison of the behavior of the two devices, both should work with the same degree of gain saturation, hence the pump density and the threshold pump density should be the same in both cases. Since the lasing condition in ring lasers involves a single pass in the cavity, while that of FP lasers implies a roundtrip, the length of the FP cavity should be one half of that of the ring provided that the total distributed losses are the same in both cases. In this way, moreover, the frequency spacing of the modes and their threshold gain difference are the same in both configurations. Thus, the scaled parameters g, γ, ϵ, and η of a ring laser have to be twice their equivalent FP values. For the parameters of Fig. 4.4.7, the ring laser just above threshold has only one stable solution $m = 0$. Upon increasing J, this bidirectional solution becomes unstable first via a Hopf bifurcation at $J \sim 0.7$ and then via a pitchfork bifurcation at $J_\in \sim 1.5$ that leads to two symmetrical, almost unidirectional, solutions. Although the solutions corresponding to $m = 3$ remain unstable over the interval of J shown, solutions $m = 1$ and $m = 2$ become stable for high enough J, hence the system easily displays multistability once in the almost unidirectional regime. The equivalent FP laser behaves remarkably different from the ring laser regarding multistability (see Fig. 4.5.8b). Above threshold, the mode $m = 0$ starts lasing stably, but when the pump is increased it quickly becomes unstable through a multimode instability [164]. All the other modes are unstable over all the pump interval examined.

The results in Fig. 4.5.8 correspond to the UFL, but our methodology allows to easily address their robustness regarding the cavity losses. One can confirm that, in this case, non uniform field amplitudes do not qualitatively modify the multistability scenario as shown in Fig. 4.5.9, where the results obtained are plotted for a high-

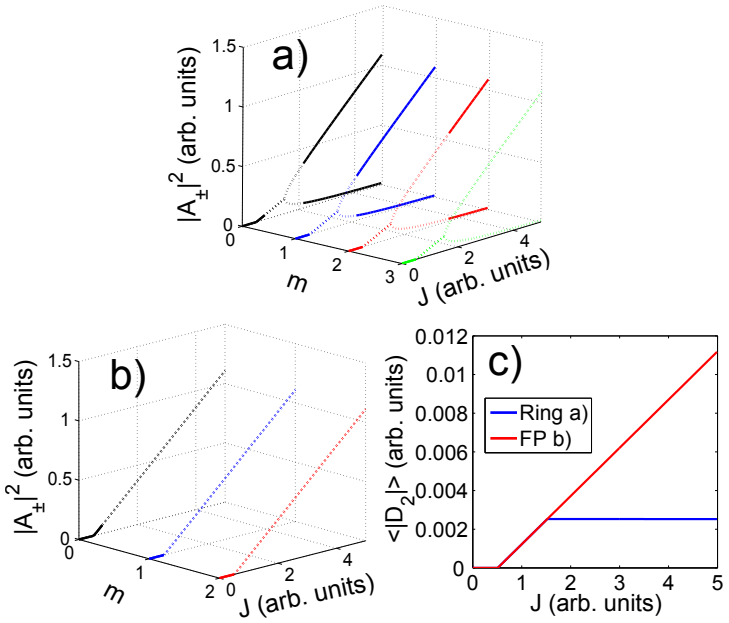

Fig. 4.5.8 – Bifurcation diagram for the first modes of a ring laser (a) with the parameters of Fig. 4.4.7 and for an equivalent FP laser (b), $g = 2$, $\gamma = 125$, $\alpha_{int} = 1.01$, $\epsilon = 0.025$, $\eta = 5$, $t_\pm = 0$ and $r_\pm = 0.99$. (c) $< |D_2| >$ is the average of $|D_2|$ along the cavity for cases (a) and (b).

loss ring laser (panel a) and two equivalent FP lasers, one symmetric (panel b) and one highly asymmetric (panel c). Again, while the ring laser shows multistability, it is never observed multistability for the FP cavities. The physical reason for such a different behavior of FP and ring lasers is the quite different degree of spatial hole burning in the gain, as shown in Figs. 4.5.8 (panel c) and 4.5.9 (panel d), where the absolute value of D_2 averaged along the cavity at different pumping levels is plotted for mode $m = 0$ of the lasers in Figs. 4.5.8 and 4.5.9, respectively. D_2 is almost the same for all modes of a given laser due to the minute modal gain differences. In the ring laser, $|D_2|$ saturates at a comparatively low value as soon as the pitchfork bifurcation leading to unidirectional operation occurs; for FP configurations, instead, the necessarily higher reflectivity of the facets makes $|D_2|$ larger than in the equivalent ring, and it increases continuously with the pump level.

To confirm that the grating term is what destroys multistability in the FP configuration, a system with higher diffusion is considered, which should reduce the values of D_2 (see Eq. (4.1.4)). In fact, as shown in Fig. 4.5.10, now both FP configurations display multistability among longitudinal modes because now the spatial average of D_2 (Fig. 4.5.10 panel c) is half that in Fig. 4.5.9 (panel d).

In order to confirm these results, dynamical simulations of a ring laser are performed injecting a Gaussian pulse at a different frequency. The pulse has the form

$$P_G(t) = \frac{A}{w\sqrt{2\pi}} e^{-\frac{(t-t_0)^2}{2w} - i\Omega(t-t_0)} \quad , \qquad \boxed{4.5.60}$$

where A is the amplitude, w is the width, t_0 is the time where the pulse maximum is situated and Ω is the frequency of the pulse.

Fig. 4.5.11 confirms the scenario shown in Fig. 4.5.8. The laser initially emits at $m = 0$. After the injection at time $t_0 = 750$ rt of a pulse with frequency $\Omega = 2\pi$

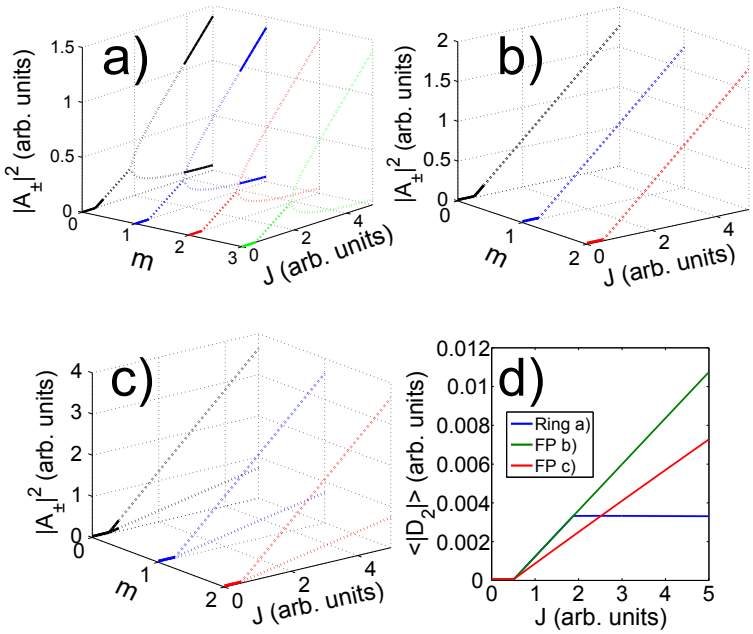

Fig. 4.5.9 – Bifurcation diagram for: (a) ring laser with parameters $g = 4$, $t_{\pm} = 0.6$, $r_{\pm} = 0.01$, $\gamma = 250$, $\alpha_{int} = 1.55$, $\epsilon = 0.05$, $\eta = 10$; (b) equivalent symmetric FP with $\alpha_{int} = 0.51$, $\eta = 5$ and $r_{\pm} = 0.6$; (c) equivalent asymmetric FP with $\alpha = 0.21$, $\eta = 5$ and $r_{+} = 0.99$ and $r_{-} = 0.2$. The threshold value is $J_{th} = 0.51$. (d) $< |D_2| >$ vs J for these lasers.

corresponding to $m = 1$, the laser changes its frequency emitting in $m = 1$.

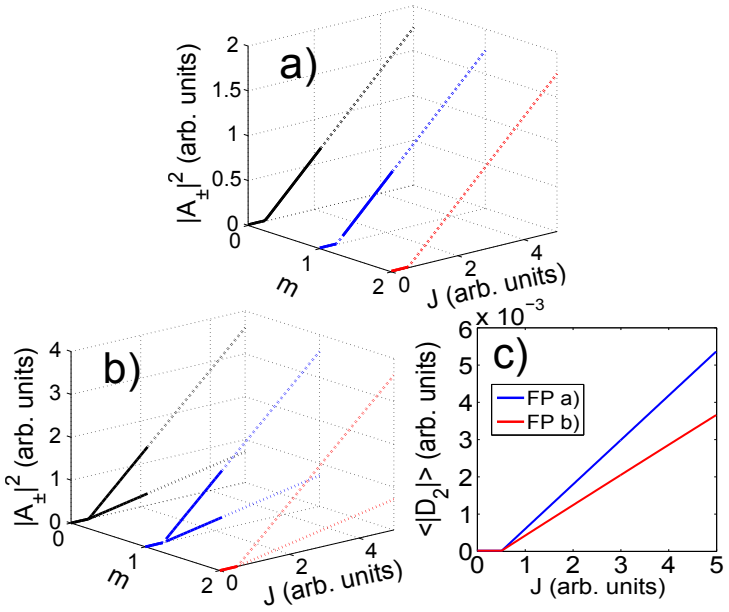

Fig. 4.5.10 – Bifurcation diagram for the first three modes for a symmetric (a) and asymmetric (b) Fabry-Pérot lasers. In both cases $\eta = 10$, for other parameters see Fig. 4.5.9. (c) $< |D_2| >$ vs J for the FPs (a) and (b).

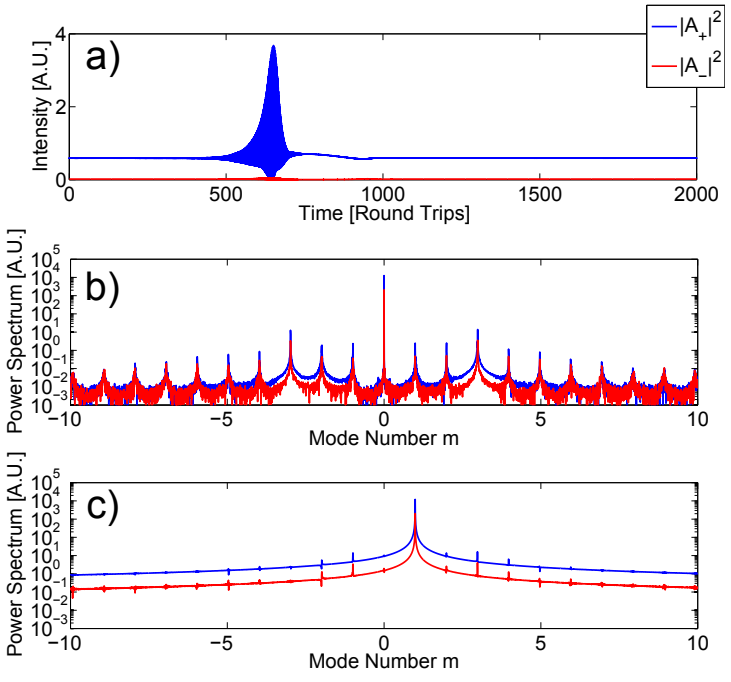

Fig. 4.5.11 – Switching in emission mode. (a) Time trace. (b) Power spectra at $\tau = 12$ rt. (c) Power spectra at $\tau = 1750$ rt. Laser parameters: Mesh points $N = 400$, $J = 2.99$, $\beta = 10^{-3}$, others see Fig. 4.4.7. Pulse parameters: $A = 20$, $w = 100$, $t_0 = 750$ rt, $\Omega = 2\pi$ corresponding to $m = 1$.

IV.6 Spatiotemporal dynamics

[1]The numerical implementation of partial-differential equations always represents a challenge from a technical point of view. In particular, the usual numerical diffusion present in most algorithms has to be carefully taken care of. While numerical dissipation can be helpful in context like e.g. fluid mechanics, to prevent spurious solutions to rise, multi-mode laser dynamics is mainly governed by extremely weak gain differences between consecutive modes that correspond to increasing spatial frequencies. Any weak numerical dissipation would therefore profoundly affect the dynamical scenario and has to be avoided. For this purpose a numerical algorithm is employed that is based on the one presented in [167], which takes advantage of the fact that the equations for the electric fields can be formally solved by integration along the characteristics. The details of the numerical implementation are described in appendix B, where how to impose the boundary conditions are discussed in detail.

IV.6.1 Single-mode dynamics

In this section the test performed in order to check the correctness and accuracy of the numerical algorithm used to implement the TWM is discussed, it is required for controlling potential implementation mistakes.

Clearly, the results in IV.3 and IV.4 provide a first test of the accuracy of the numerical implementation. It has verified that the numerical scheme accurately recovers the lasing threshold yielding monochromatic solutions that match those obtained by the shooting method. A further test, presented below, is provided by comparing the

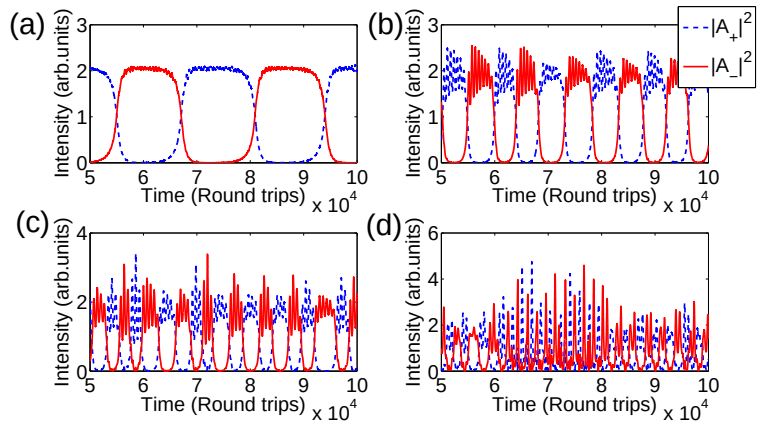

Fig. 4.6.12 – Dynamical behaviors observed for fixed pump $J = 0.5$ while scanning detuning $\widetilde{\delta}$. (a) $\widetilde{\delta} = 0.2$, (b) $\widetilde{\delta} = 0.5$, (c) $\widetilde{\delta} = 0.7$, (d) $\widetilde{\delta} = 0.9$. The parameters correspond to those used in [54] in Figs. 10a - 10i except for the fact that in our case the two modes have equal losses: Mesh points $N = 100$, $g = 1$, $\epsilon = \eta = 1.78\ 10^{-4}$, $\beta = 10^{-4}$, $t = 0.9$, $r = 0$, $\alpha_{int} = 0$ and $\gamma = 1$.

numerical results in the single longitudinal mode limit with the dynamical results previously obtained by Zeghlache et al. [54] with a rate equation model for a CO_2 ring laser. In such a model, obtained in the good cavity limit for a pure single-longitudinal ring laser ($r = 0$), the only term that mixes the counter-propagating fields is the carrier

[1]This part is based on the article: "Bichromatic emission and multimode dynamics in bidirectional ring lasers" by A. Pérez-Serrano, J. Javaloyes and S. Balle, *Phys. Rev. A* **81**, 043817 (2010).

grating, hence the bidirectional regime is unstable [43, 148]. Moreover, the analysis performed in [54] demonstrates that the unidirectional solution can also become unstable in some pump and detuning regimes. For certain values of these parameters, square-wave oscillations between the counter-propagating fields appear followed by regular or even chaotic oscillations. Scanning the pump J for fixed detuning, the system, which is initially stable or bistable, becomes unstable at a certain value, and it eventually recovers stability at high pump values; for fixed pump, instead, stable behavior is not recovered upon increasing detuning although it must be recalled that the single-mode approximation will eventually break down and the model in [54] be no longer valid. A meaningful comparison of these results from those in [54] requires

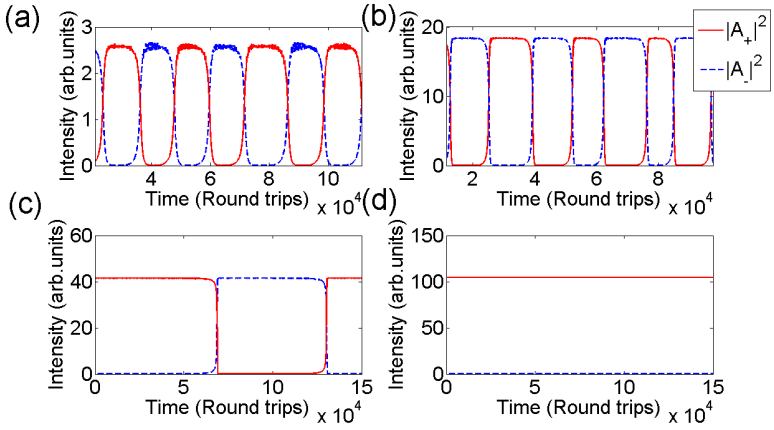

Fig. 4.6.13 – Dynamical behaviors obtained for fixed detuning $\widetilde{\delta} = 0.2$ while scanning J. (a) $J = 0.6$, (b) $J = 3.6$, (c) $J = 8$, (d) $J = 20$ for the same parameters as in Fig. 4.6.12.

to establish the equivalence among the parameters in both models. In order to do so, the model is reduced to that in [54] by neglecting any spatial dependence while redefining the losses in (4.1.1) as $\alpha_T = \alpha - \ln t$ (i.e. the total loss). Then, comparison with Eqs. (3.11) in [54] yields the parameter correspondence rules

$$d_{\parallel} = \tfrac{\epsilon}{\alpha_T}, \quad A = \tfrac{gJ}{\alpha_T}, \quad \Delta = -\widetilde{\delta}. \qquad \boxed{4.6.61}$$

The numerical simulations reproduce accurately the behaviors described in [54]. Simulations fixing the pump and increasing the detuning are performed (see Fig. 4.6.12), in this case, one goes from the unidirectional steady emission to a region of instability where the counter-propagating fields develop a square-wave oscillation with one intensity in anti-phase with the other (Fig. 4.6.12 (a)). Increasing the detuning, the square-waves become distorted and a secondary oscillation appears (Fig. 4.6.12 (b) and (c)), progressing until a chaotic oscillation is obtained for high detunings as shown in Fig. 4.6.12 (d).

On the other hand, when the detuning is fixed and the pump is scanned (see Fig. 4.6.13) one passes from a unidirectional steady solution near threshold into a region of instability where square-waves similar to those in the previous case develop. In contrast with the previous case, now the system recovers stability upon increasing J and returns to one of the unidirectional solutions. The mechanism is a slowing of the square-wave modulation as one increases the pump (see Fig. 4.6.13 (c)), a characteristic behavior of heteroclinic bifurcations.

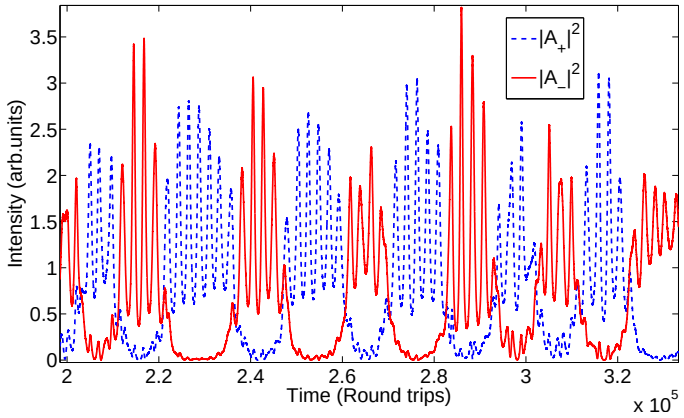

Fig. 4.6.14 – Single mode chaotic behavior. Mesh points $N = 100$, $J = 0.4$, $\widetilde{\delta} = 0.4$, $g = 1$, $\epsilon = \eta = 1.78\ 10^{-4}$, $\beta = 10^{-4}$, $t = 0.9$, $r = 5\ 10^{-4}$, $\alpha_{int} = 0$ and $\gamma = 1$.

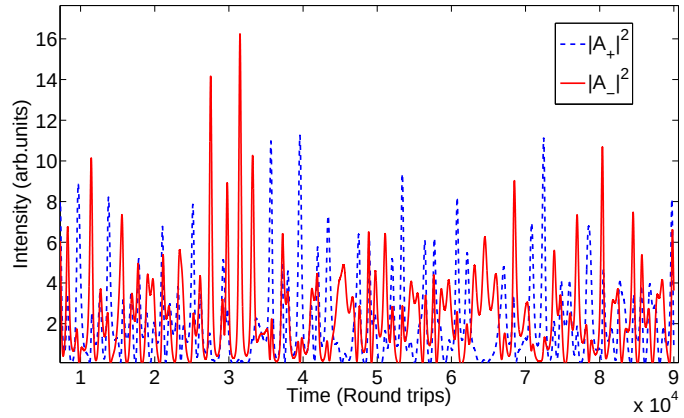

Fig. 4.6.15 – Single mode chaotic behavior. Mesh points $N = 100$, $J = 0.5$, $\widetilde{\delta} = 1$, $g = 1$, $\epsilon = \eta = 1.78\ 10^{-4}$, $\beta = 10^{-4}$, $t = 0.9$, $r = 5\ 10^{-4}$, $\alpha_{int} = 0$ and $\gamma = 1$.

Finally, we remark that the above behaviors are recovered even when putting a small direct reflection and spontaneous emission provided that the good cavity limit still applies (see Fig. 4.6.14 and 4.6.15), i.e. they are robust against small imperfections and noise. However, if the reflectivity is too large, the system emits bidirectionally at threshold and its dynamical behavior is no longer the same [96, 97].

IV.6.2 Multimode dynamics

The rate-equation model described in [54] is very successful at describing the rich variety of dynamics that can be encountered while in single-mode operation. However, in a real laser, increasing the detuning will eventually lead to at least a change in lasing mode which is not accounted for in the RE model. Indeed, the maximum allowed detuning in a real device corresponds to having the gain peak just between two laser modes, i.e. $\widetilde{\delta} = \pi/\gamma$; in this case, the two modes will have the same threshold and lasing can be quite different than when only one mode is active. In addition,

instabilities arising from the multi-mode character of the system as e.g. the Risken-Nummedal instability [47] can develop when the gain curve is broader than the mode spacing and the pump level is high enough.

The dynamics in these cases can readily be analyzed with the traveling wave model, which naturally retains the dynamics of the different modes and the effects of the detuning. Hence it can allow to explore the dynamics of the system in cases where different longitudinal modes are active.

In this section some remarkable dynamical behaviors obtained in these situations are presented and discussed, although note that the large variety of scenarios that are observed calls for the development of a bifurcation tool of our TWM that would allow to better understand the role played by the different parameters. It should be noted, however, that some of them are obtained for very high pumping levels, $J \sim 10{-}100 J_{th}$, which might be difficult or even impossible to achieve in an experiment. First, the situation where a moderate gain bandwidth is taken into account is presented, and how different behaviors arise in this case depending on the pump and the detuning. In the second part of this section the case of a large gain bandwidth is discussed.

(a) Moderate gain bandwidth

Considering the case when the gain spectrum has moderate width, $\gamma = 10$. First the case when the gain spectrum peak lies just between two modes, $\widetilde{\delta} = 0.3141$, is discussed. In this case, modes $m = 0$ and $m = 1$ have exactly the same threshold, so the dynamical scenario at the laser threshold corresponds to a degenerate Hopf bifurcation. It should moreover be noted that for each of these frequencies there are two different solution branches which for small r are also almost degenerate, as discussed in IV.2. This highly degenerated situation allows the system to lase in a great variety of possible states, which can give rise to unexpected dynamical behaviors. The effect of the detuning in this case is subsequently discussed, since varying the detuning allows to reduce the degeneracy of the system.

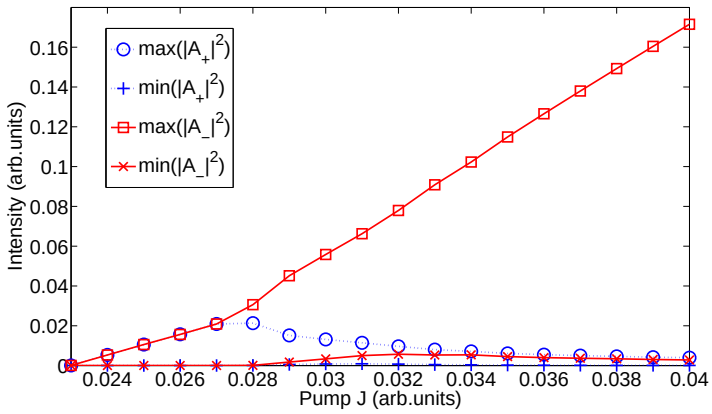

Fig. 4.6.16 – Bifurcation diagram near threshold. The fields begin to emit multi-mode bidirectionally, then after $J = 0.028$ the backward (-) field is favored. Mesh points $N = 100$, $\widetilde{\delta} = 0.3141$, $g = 5$, $\epsilon = 10^{-2}$, $\eta = 0.1$, $\beta = 10^{-4}$, $t = 0.9$, $r = 5\ 10^{-4}$, $\alpha_{int} = 0$ and $\gamma = 10$

Fig. 4.6.16 shows the bifurcation diagram near the threshold for the ring laser with moderate gain bandwidth (laser parameters specified in the caption). First, the

two counter-propagating fields are both emitting with equal intensity in two modes separated by one mode spacing, i.e. the laser starts to emit bidirectionally in consecutive modes, $m = 0$ and $m = 1$. As one increases the pump, one of the directions becomes dominant over the other, and additional modes are excited. For high enough pump (see Fig. 4.6.17), the system emits almost unidirectionally; however, the emission exhibits 100% oscillations at the roundtrip time which correspond to an emission spectrum that involves four dominant modes. Further increasing the pump, the intensity oscillation becomes nonlinear, which corresponds to the locking of a moderate number of modes (see Fig. 4.6.18), this regime can be interpreted as a shallow mode-locked solution.

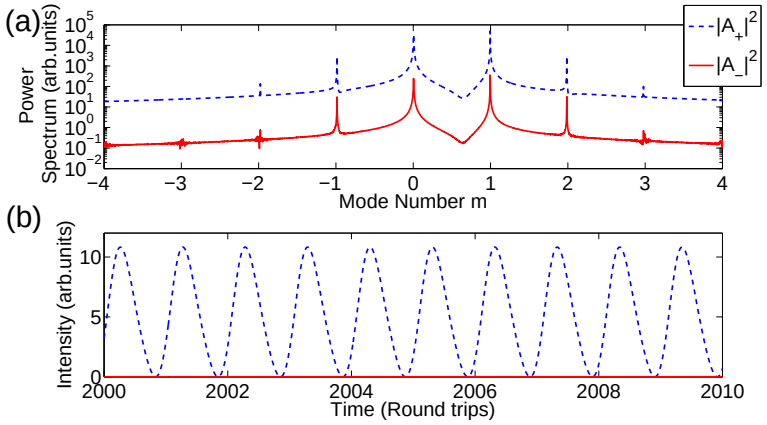

Fig. 4.6.17 – Unidirectional oscillating emission. (a) Power spectra. (b) Time trace. Mesh points $N = 400$, $J = 1$, $\widetilde{\delta} = 0.3141$, $g = 5$, $\epsilon = 10^{-2}$, $\eta = 0.1$, $\beta = 10^{-4}$, $t = 0.9$, $r = 5\ 10^{-4}$, $\alpha_{int} = 0$ and $\gamma = 10$.

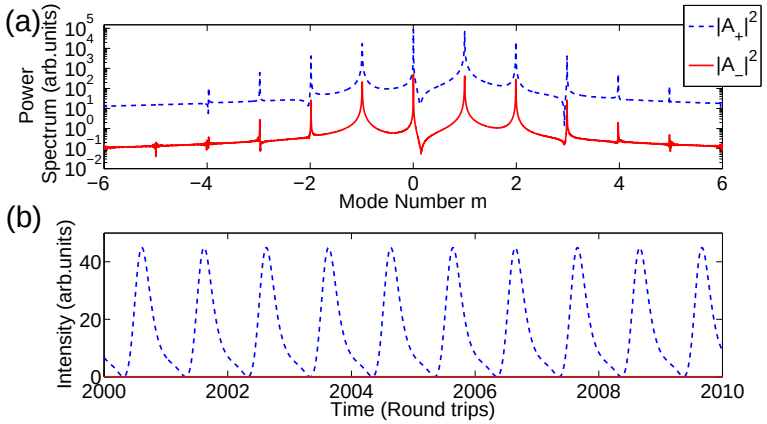

Fig. 4.6.18 – (Color online) Mode-locked solution. (a) Power spectra. (b) Time trace. $J = 3$. Other parameters see fig.4.6.17.

At even higher pumps, the nonlinear oscillation disappears and the emission becomes again bidirectional with both directions emitting stable and with the same power (see Fig. 4.6.19).

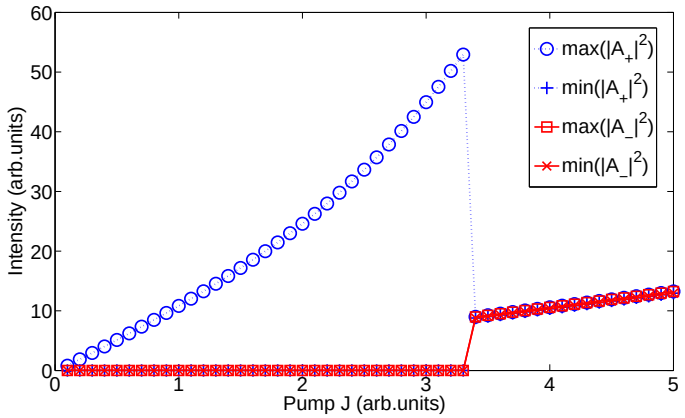

Fig. 4.6.19 – Bifurcation diagram showing the transition from unidirectional oscillating emission to bidirectional emission at different frequencies. (a) Power spectra. (b) Time trace. Mesh points $N = 400$, $\widetilde{\delta} = 0.3141$, $g = 5$, $\epsilon = 10^{-2}$, $\eta = 0.1$, $\beta = 10^{-4}$, $t = 0.9$, $r = 5\ 10^{-4}$, $\alpha_{int} = 0$ and $\gamma = 10$.

However, a closer look at the emission in this regime (see Fig. 4.6.20) reveals that, surprisingly, each emission direction is dominated by a single mode, $m = 0$ for A_+ and $m = 1$ for A_-. Hence each mode contributes in complementary ways to lasing in each direction: while emission in the forward direction is dominated by the redmost mode, the backward direction lases dominantly on the bluest mode. This regime is of course two fold degenerate.

This transition comes from the fact that the population inversion grating tries to favor the almost unidirectionnal emission at the same frequency because it induces an effective cross saturation of the gain between the forward and backward waves [43] which is larger if they have the same frequency (see eqs. (4.1.1)-(4.1.4)). But the power extracted from the system in the bidirectional monochromatic state is not optimal because the atoms located at the nodes of the standing wave do not contribute to stimulated emission. The power extraction can be increased in the case of bichromatic emission when the gain curve is broad enough and the frequency separation between the modes is larger than the decay rate of the population grating ($2\pi \gg \eta$). In this case, the population grating can not develop in response to the counter-propagating fields, hereby effectively reducing cross-gain saturation between the forward and backward waves and restoring the possibility of obtaining stable bidirectional operation. One concludes that this is a pure dynamical effect that allows for bichromatic bidirectional emission at high current.

In order to see the effect of the detuning on the behavior of the laser in the case of moderate gain bandwidth, simulations for different $\widetilde{\delta}$ are performed. For $\widetilde{\delta} = 0.3$, the laser begins to emit bidirectionally in a mode $m = 0$ but it rapidly becomes almost unidirectional with a small amplitude oscillation that corresponds to residual emission in mode $m = 1$ (see inset in Fig. 4.6.21). As one increases the pump, the emission becomes increasingly unidirectional and single mode until $J = 0.4$, where mode $m = 1$ starts to lase and favors the opposite direction. Above this pump value, the laser emits bidirectionally with each direction dominated by a different mode as in the previous subsection. However, the non symmetrical position of the cavity modes respect to the peak of the gain curve produces a sensible difference between the intensities of the two counter-propagating fields (see Fig. 4.6.22).

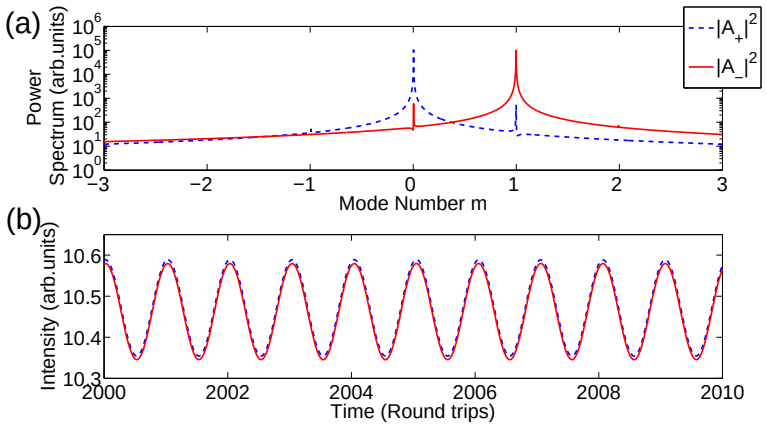

Fig. 4.6.20 – Bidirectional oscillating emission at different frequencies. (a) Power spectra. (b) Time trace. $J = 4$. Other parameters see Fig. 4.6.17.

The above results have been obtained by starting the simulations from a noisy initial condition that does not favor any of the emission directions. However, when the simulations are launched from an initial condition that privileges one of the directions (see Fig. 4.6.23), one finds for some current values an almost unidirectional solution oscillating at the modal beat note with almost 100% amplitude. This solution is the analogous to that in Fig. 4.6.19 in the previous subsection, and it eventually also disappears into the bidirectional solution of Fig. 4.6.21. The former result evidences that the unidirectional oscillating solution and the bidirectional emission at different frequencies can coexist depending on the parameters. We have tried to induce jumps among these two types of solutions by injecting optical pulses, but we have not managed to stably control the emission state of the system: after a relatively long transient, the system returned to the original emission state, indicating that in spite of their coexistence, the perturbation in phase space requires specific characteristics to place the system into the basin of attraction of the other solution.

Finally, in the case that the gain peak is close to one of the cavity modes, multimode dynamics is suppressed because the mode closest to the gain peak takes all the energy provided to the system. For a detuning value $\widetilde{\delta} = 0.15$ the laser emits single-mode unidirectionally as shown in Fig. 4.6.24.

(b) Large gain bandwidth

In this section a large gain bandwidth ($\gamma = 100$) is considered that allows for a rich variety of dynamical behaviors because a large number of modes can become active.

The bifurcation diagram shown in Fig. 4.6.25 summarizes the different behaviors observed when the peak of the gain curve is just between the first two modes, $\widetilde{\delta} = 0.03141$. Close to threshold, the laser emits bidirectionally with two modes active in each direction as in Fig. 4.6.16. Increasing the pump, the forward direction becomes dominant and mode $m = 0$ dominates; conversely, the backwards direction is dominated by mode $m = 1$ (see Fig. 4.6.26). In this regime, both emission directions oscillate in phase, but as the pump is still increased, more modes become excited and the oscillations of the intensity of the counter-propagating fields are out of phase (see Fig. 4.6.27).

Still increasing the pump, a regime of almost single-mode, unidirectional emission

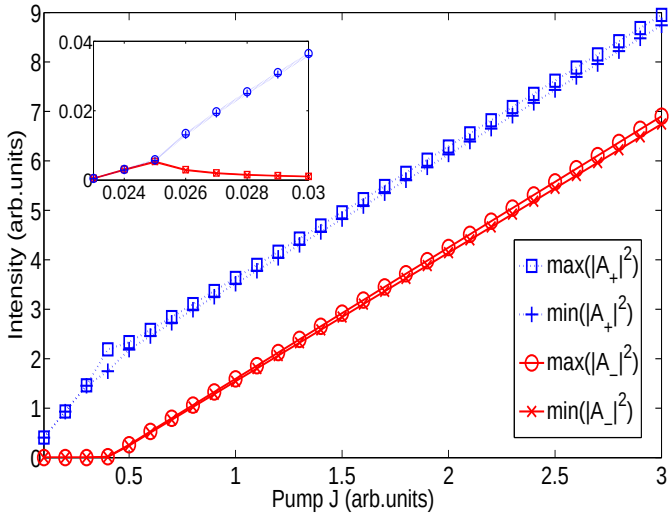

Fig. 4.6.21 – Bifurcation diagram for $\gamma = 10$ and $\widetilde{\delta} = 0.3$. Inset: Bifurcation diagram near the threshold. Mesh points $N = 400$, $g = 5$, $\epsilon = 10^{-2}$, $\eta = 0.1$, $\beta = 10^{-4}$, $t = 0.9$, $r = 5\ 10^{-4}$ and $\alpha_{int} = 0$.

is recovered (see Fig. 4.6.28) for a small range of pump values. One sees that in this case, the depressed emission direction is dominated by mode $m = 2$, with a secondary peak on mode $m = -2$ excited by Four-Wave-Mixing processes. Such a regime indicates that the gain suppression of mode $m = 1$ by emission on mode $m = 0$ is strong enough to inhibit emission on mode $m = 1$. However, the large bandwidth of the gain curve allows modes farther away from mode $m = 0$ to become active when the pump is still increased. As shown in Fig. 4.6.29, this leads again to a bidirectional solution where each direction dominantly lases on different modes separated by twice the mode spacing.

For detuning values above $\widetilde{\delta} = 0.025$, the behavior of the system is qualitatively the same described in the previous subsection (see Fig. 4.6.30). However, the non symmetrical position of the gain curve peak makes the DC component of the fields different and a unidirectional solution is found near threshold.

A different scenario emerges at low detunings. When the detuning is decreased to a value $\widetilde{\delta} = 0.015$ (see Fig. 4.6.31), the laser starts emitting bidirectionally with both directions emitting on two consecutive modes. For slightly higher pump, one emission direction starts to dominate with quasi single-mode emission up to $J \approx 2.4$, where a unidirectional solution arises with a high number of active modes (see Fig. 4.6.32). Although this solution appears very far away from the lasing threshold, it is worth being examined in detail. The solution has the characteristics of a unidirectional mode-locked state, since the laser emits sharp and narrow pulses being in one direction only. Note that this is a harmonic mode-locked state, with pulses occurring at twice the fundamental repetition rate. The duty-cycle of the pulses is around 6%. It is worth remarking that this solution appears without inserting in the cavity any additional element that favors pulsed operation (i.e., a saturable absorber or alike), but it merely arises from an instability of the CW solution occurring when the power level is such that the Rabi frequency of the two-level atoms equals the polarization dephasing rate. From this point of view, then, the mechanism that triggers this solution is analogous to that in the Risken-Nummedal instability. The main difference between this case

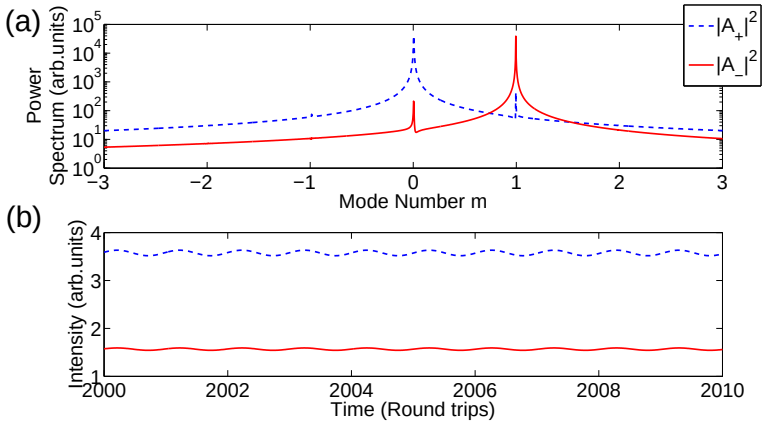

Fig. 4.6.22 – Bidirectional emission. (a) Power spectra. (b) Time trace. Mesh points $N = 400$, $J = 1$, $\widetilde{\delta} = 0.3$, $g = 5$, $\epsilon = 10^{-2}$, $\eta = 0.1$, $\beta = 10^{-4}$, $t = 0.9$, $r = 5\ 10^{-4}$, $\alpha_{int} = 0$ and $\gamma = 10$.

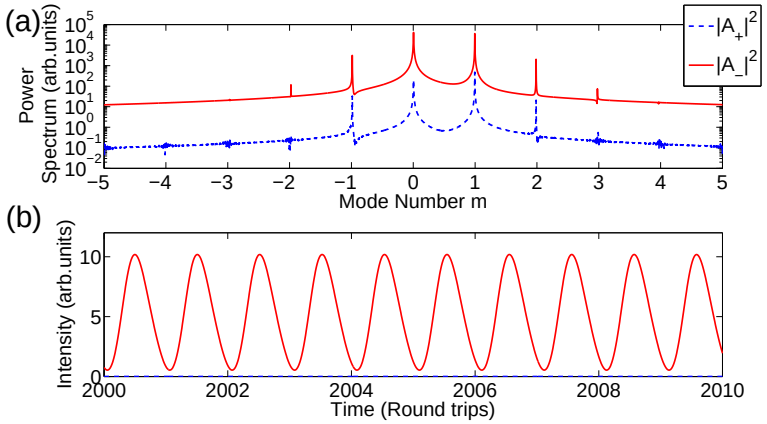

Fig. 4.6.23 – Unidirectional oscillating emission. (a) Power spectra. (b) Time trace. For parameters see Fig. 4.6.22.

and the classical Risken-Nummedal instability is that the large gain curve that we are considering allows for the excitation of additional side-modes through Four-Wave Mixing processes mediated by both D_0 and $D_{\pm 2}$, which give rise to the pulsed emission of the system.

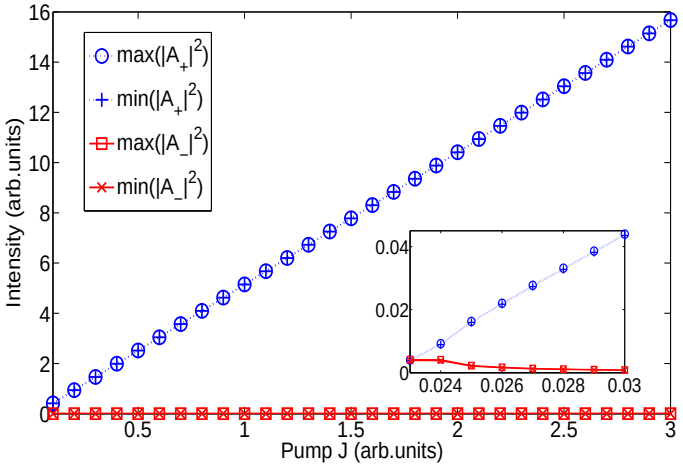

Fig. 4.6.24 – Bifurcation diagram for $\gamma = 10$ and $\widetilde{\delta} = 0.15$. Inset: Bifurcation diagram near the threshold. Mesh points $N = 400$, $g = 5$, $\epsilon = 10^{-2}$, $\eta = 0.1$, $\beta = 10^{-4}$, $t = 0.9$, $r = 5\ 10^{-4}$ and $\alpha_{int} = 0$.

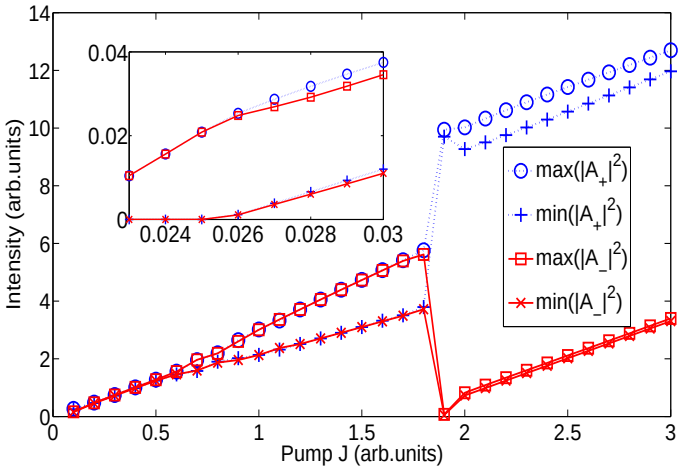

Fig. 4.6.25 – Bifurcation diagram showing different behaviors for $\gamma = 100$ and $\widetilde{\delta} = 0.03141$. Inset: Bifurcation diagram near the threshold. First, close to threshold, the laser emits bidirectionally with both counter-propagating fields emitting at 2 consecutive modes. Then a regime of bidirectional emission at different frequencies appears (see Fig. 4.6.26). Third, a oscillating regime where the counter-propagating fields are out of phase (see Fig. 4.6.27). Fourth, a unidirectional multi-mode solution, composed by not consecutive modes (see Fig. 4.6.28). Fifth, a bidirectional emission at different frequencies at not consecutive modes (see Fig. 4.6.29). Mesh points $N = 400$, $g = 5$, $\epsilon = 10^{-2}$, $\eta = 2\ 10^{-2}$, $\beta = 10^{-4}$, $t = 0.9$, $r = 5\ 10^{-4}$ and $\alpha_{int} = 0$.

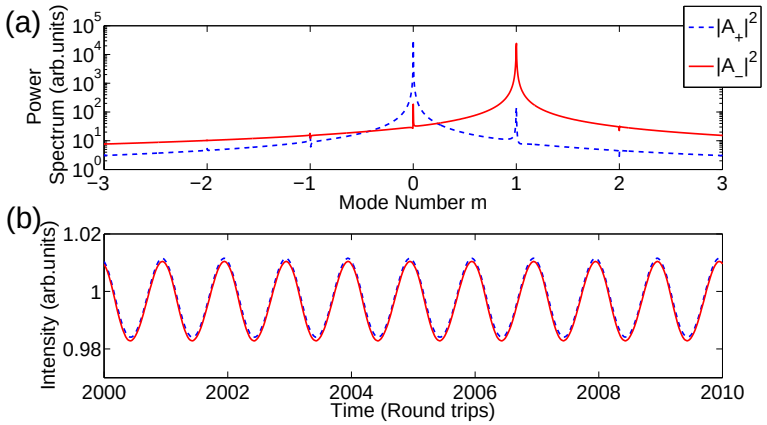

Fig. 4.6.26 – Bidirectional emission at different frequencies. (a) Power spectra. (b) Time trace. Mesh points $N = 400$, $J = 0.4$, $\widetilde{\delta} = 0.03141$, $g = 5$, $\epsilon = 10^{-2}$, $\eta = 2\ 10^{-2}$, $\beta = 10^{-4}$, $t = 0.9$, $r = 5\ 10^{-4}$, $\alpha_{int} = 0$ and $\gamma = 100$.

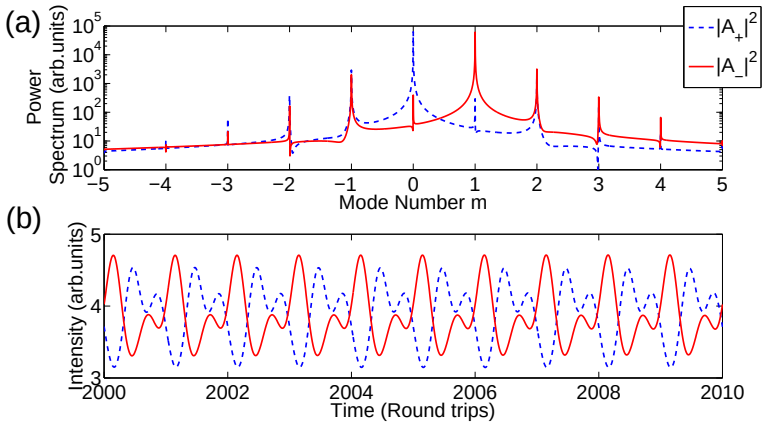

Fig. 4.6.27 – Multi-mode alternate oscillations. (a) Power spectra. (b) Time trace. $J = 1.5$. Other parameters as in Fig. 4.6.26.

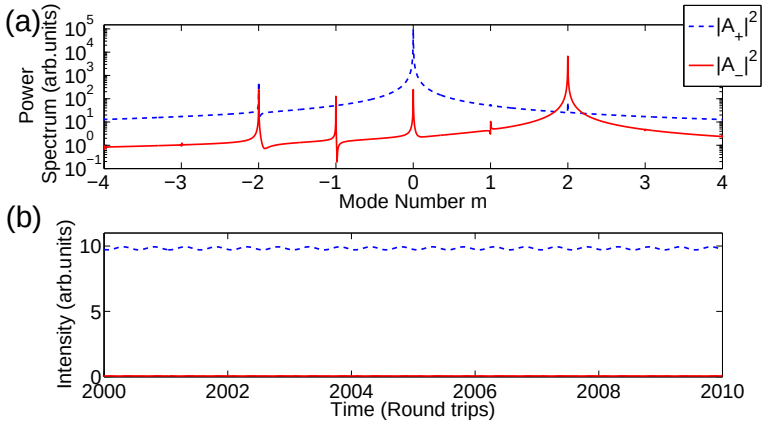

Fig. 4.6.28 – Unidirectional emission. (a) Power spectra. (b) Time trace. $J = 1.9$. Other parameters as in Fig. 4.6.26.

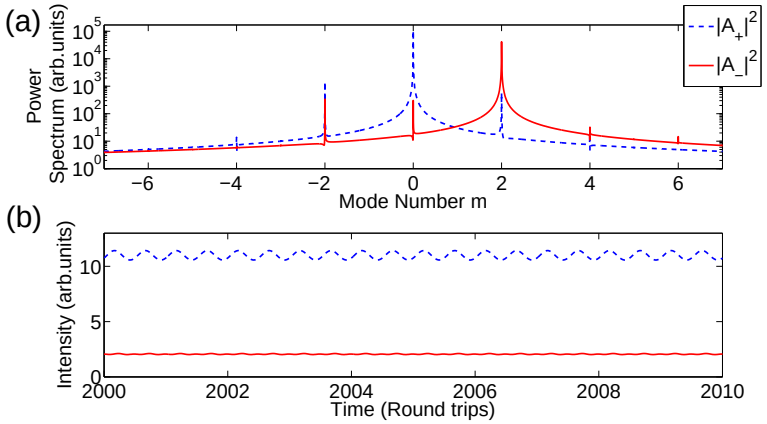

Fig. 4.6.29 – Bidirectional emission at different frequencies. (a) Power spectra. (b) Time trace. $J = 2.5$. Other parameters as in Fig. 4.6.26.

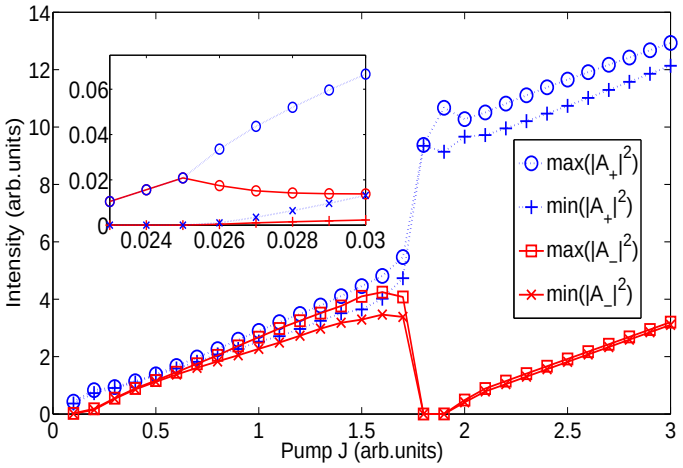

Fig. 4.6.30 – Bifurcation diagram for $\gamma = 100$ and $\widetilde{\delta} = 0.03$. Inset: Bifurcation diagram near the threshold. First, bidirectional emission is found near threshold, then one of the fields is suppressed and a unidirectional regime is found, after that the suppressed field begins to emit at a different frequency respect to the emitted by the no suppressed field and a bidirectional solution appears. Increasing the pump we find a unidirectional solution that end up in a bidirectional solution emitting at not consecutive modes. Mesh points $N = 400$, $g = 5$, $\epsilon = 10^{-2}$, $\eta = 2\ 10^{-2}$, $\beta = 10^{-4}$, $t = 0.9$, $r = 5\ 10^{-4}$ and $\alpha_{int} = 0$.

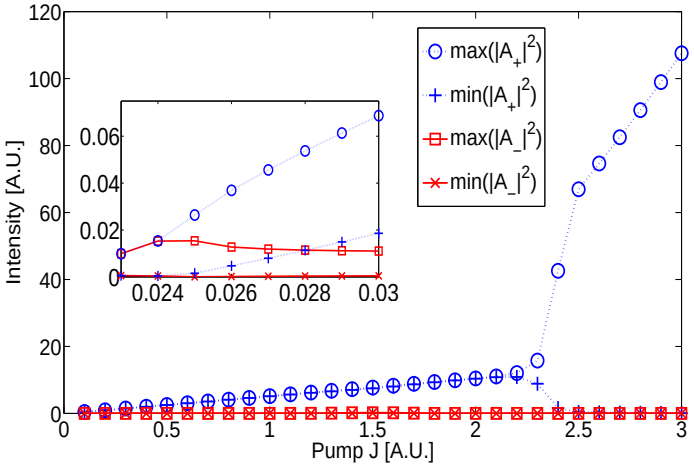

Fig. 4.6.31 – Bifurcation diagram for $\gamma = 100$ and $\widetilde{\delta} = 0.015$. Inset: Bifurcation diagram near the threshold. Near threshold the laser emits bidirectionally but for a wide range on pump the laser emits unidirectionally single-mode, then near $J = 2.2$ different modes start to lase and a mode-locked solution arises (see Fig. 4.6.32). Mesh points $N = 400$, $g = 5$, $\epsilon = 10^{-2}$, $\eta = 2\ 10^{-2}$, $\beta = 10^{-4}$, $t = 0.9$, $r = 5\ 10^{-4}$ and $\alpha_{int} = 0$.

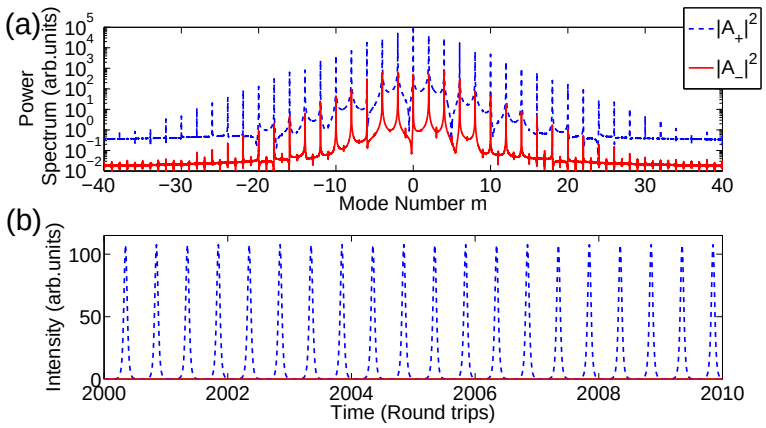

Fig. 4.6.32 – Mode-locked emission. (a) Power spectra. (b) Time trace. Mesh points $N = 400$, $J = 3$, $\widetilde{\delta} = 0.015$, $g = 5$, $\epsilon = 10^{-2}$, $\eta = 2\ 10^{-2}$, $\beta = 10^{-4}$, $t = 0.9$, $r = 5\ 10^{-4}$, $\alpha_{int} = 0$, $\gamma = 100$, $n = 1$ and $L = 1\ m$.

IV.7 Conclusions

In this chapter, a traveling wave (TW) model for a two level atom medium laser is studied. This model retains the spatial dependence of the fields and the material variables and also allow us to model different cavity geometries by introducing the appropriate boundary conditions. Although the model involves a big number of variables that are nonlinearly related, one is able to find some analytical results. The threshold is found analytically, that it is used as first test for the numerical implementation. And also analytical or semi-analytical results for the unidirectional case have been found. On the other hand, the general case was investigated using the numerical tools that are described in appendix B.

This numerical tools have allowed to investigate on the stability of the monochromatic solutions, and the wavelength multistability that was previously reported experimentally [97]. Our conclusion is that high-quality SRL, with low reflectivity couplers, allow to observe longitudinal mode multistability much more easily than their equivalent FP configurations. Lasing in the latter requires high-enough facet reflectivities, which in turn generate substantial gain gratings that impede multistability because the self-saturation of the modal gain is larger than the cross-saturation. The former, instead, easily pass to a regime of almost unidirectional emission where the gain grating is small, and self-saturation is smaller than cross-saturation. FP devices can exhibit multistability if diffusion is strong enough to wash out the grating effectively: in this limit the grating lifetime is much shorter than carrier lifetime, and cross-saturation dominates over self-saturation.

The multimode dynamics of a two-level ring laser has been explored using a spatiotemporal integration numerical algorithm. The algorithm have been tested by reproducing the dynamical results obtained in the single-mode limit by Zeghlache et al. [54]. It has shown that the dynamical regimes reported in [54] are robust against noise and residual reflections provided that the single-mode limit holds. It has been found novel dynamical regimes where the emission in each direction occurs at different wavelengths, each direction being associated to a different longitudinal mode. One thinks that this new regime can be useful in the construction of gyroscopes, however additional investigations both experimental and theoretical are required. Other oscillating regimes have been found, that as far as we know have never been obtained theoretically, however they were reported in solid-state lasers [45].

In addition, the influence of the detuning and the width of the gain spectrum have been thoroughly analyzed, and the onset of unidirectional, mode-locked emission for large gain bandwidth and relatively small detuning has been studied in detail.

V

Traveling wave modeling: Semiconductor

V.1 Modal properties of real devices

[1]SRLs show several unexpected behaviors such as hysteresis in the lasing direction [67, 168] and atypical lasing mode selection rules. In particular, when current or temperature are changed, the lasing mode does not hop between consecutive cavity modes but exhibits sudden jumps between several cavity modes only when the lasing direction reverses. This characteristic strongly enhances the stability of the lasing wavelength against changes in the operating conditions.

In this part of the thesis the measurement of the transfer function of SRL devices in the frequency domain is reported, which provides with a map of the cavity resonances, and the emission wavelength of the SRLs when biased above threshold. The transfer function can be theoretically explained by considering the perturbation induced by the output couplers, which induces a symmetry breaking in the resonant cavity and a modulation of the cavity losses. For the geometry considered, the cavity losses have a wavelength periodicity that corresponds to three ring cavity modes, which explains the measured hops in wavelength as the bias current of the laser is increased.

The device layout consists of a ring cavity with a ring radius of 300 μm, coupled to a straight output waveguide by a point evanescent coupler (see Fig. 5.1.1). The waveguides are 2 μm wide and the gap between the ring and the output waveguides is 750 nm, providing a theoretical coupling ratio of 12%. To minimize the backreflections, the output waveguides are 10° tilted to the cleaved facets.

The wafer used to fabricate the devices is a multiple quantum well AlGaInAs/InP structure, grown by metal-organic chemical vapor deposition (MOCVD). The waveguides were defined by electron beam lithography and transferred to a PECVD (Plasma Enhanced Chemical Vapor Deposition) SiO_2 layer, using CHF_3 reactive ion etching (RIE). A shallow etched ridge-waveguide was then defined by RIE, using a chemistry of $CH_4/H_2/O_2$ process, which is selective to the Al containing core layer and thus ensures a very good control over the etching depth and the power coupling ratio. The etching depth provides an effective refractive index difference of $\Delta n = 0.064$ which makes the bending losses negligible down to ring radii of 140 μm [169]. The subsequent deposition of a SiO_2 layer was followed by contact window definition for current injection. Finally, metal contacts were deposited on both the epitaxial and substrate sides of the wafer section. For analyzing the cavity resonances of the SRL, one injects through port 1 a monochromatic field from a tunable laser, and the photocurrent generated in ports 3 and 4 is measured, which are reverse biased (see Fig. 5.1.1). During

[1]This part is based on the letter: "Modal structure, directional and wavelength jumps of integrated semiconductor ring lasers: Experiment and theory" by S. Fürst, A. Pérez-Serrano, A. Scirè, M. Sorel and S. Balle, *Appl. Phys. Lett.* **93**, 251109 (2008).

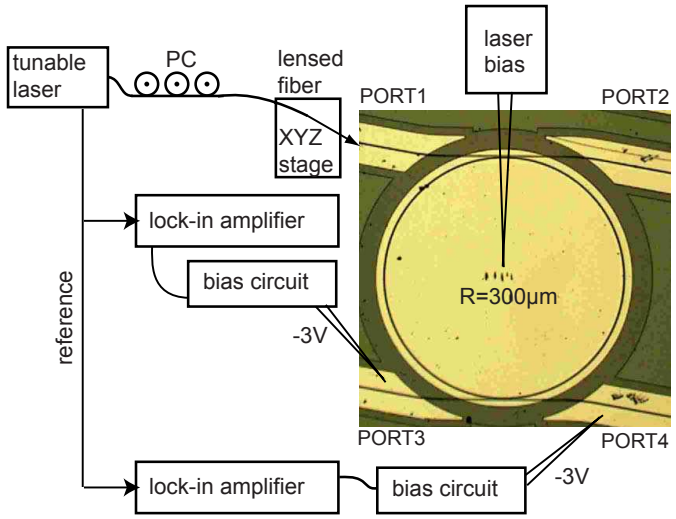

Fig. 5.1.1 – Optical micrograph of a 300 μm-radius ring laser with the corresponding measurement setup.

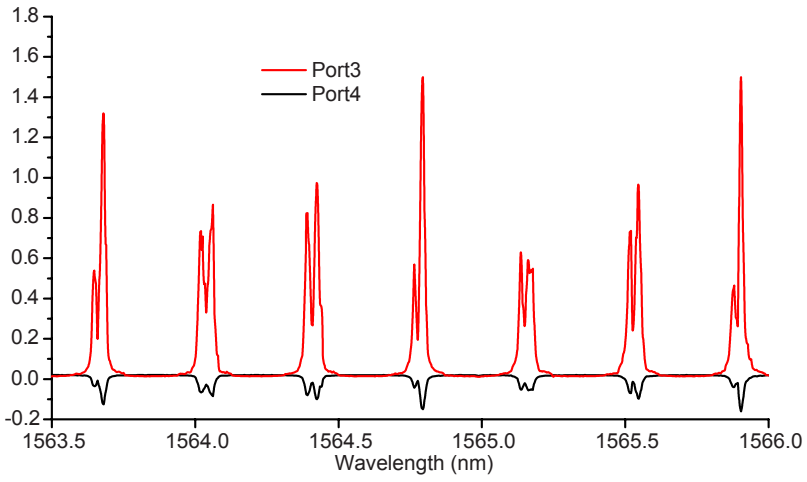

Fig. 5.1.2 – Detected power at port 3 and 4.

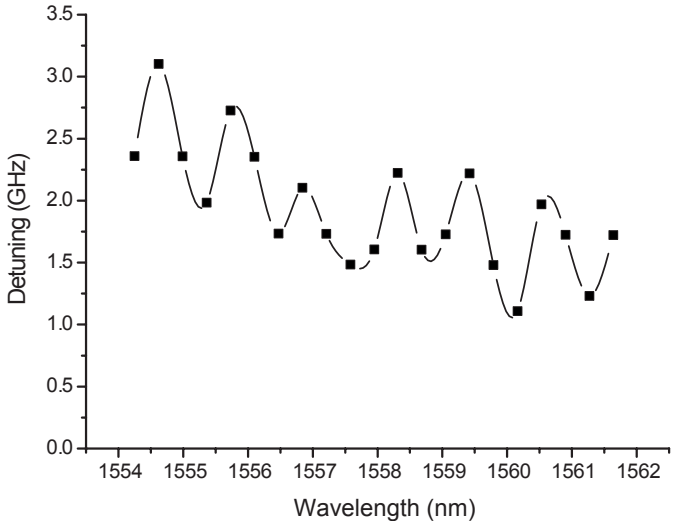

Fig. 5.1.3 – Measured splitting between doublets.

these measurements, the ring is biased close to transparency to minimize the losses. The power collected at port 3 as the input wavelength is scanned (positive peaks in Fig. 5.1.2) displays narrow and well defined peaks at wavelengths equispaced by 0.4 nm. The peak heights show the expected profile defined by the wavelength-dependent gain spectrum in the structure and an additional modulation that occurs every three longitudinal modes.

Measurements over different devices show that the longitudinal modes possess a doublet structure, with the splitting between the two subpeaks varying from 1 to 4 GHz. In addition, for a particular device, the splitting between the subpeaks usually displays a modulation that corresponds with the additional modulation in the longitudinal mode spectrum described above. Fig. 5.1.3 shows the measured doublet splitting for another device, which displays a modulation that also corresponds to a periodicity of roughly three mode spacings. The power collected at port 4 (negative peaks in Fig. 5.1.2) presents a similar structure with the same periodicity, but instead of displaying peaks above a spontaneous-emission noise background, it shows dips on such a background. It is worth remarking that the depth of the dips strongly depends on the bias current in the SRL cavity (see Fig. 5.1.4), the dips cannot be seen for bias currents below 30.5 mA, but they are visible above.

When the laser is biased above the threshold, the main lasing direction does not remain stable for all current values. The L-I curve for the device in Fig. 5.1.3 shows periodic switching between clockwise (CW) and counterclockwise (CCW) emissions for increasing current, a generic behavior in this type of devices [67]. Additionally, the dominant lasing wavelength remains constant except for a small thermal drift between switches, but it suddenly jumps by three cavity modes when the lasing direction reverses, as shown in Fig. 5.1.5. The experimental results below the threshold can be explained by computing the transfer matrix of the complete SRL structure [121]. Assuming that the two couplers are identical, lossless, and with a residual reflectivity due to their pointlike character. Small reflectivity from output facets 1 and 2 is included, but not from facet 3 or 4 since the corresponding output waveguides are reverse biased. From this analysis, the roundtrip condition for the SRL modes in a

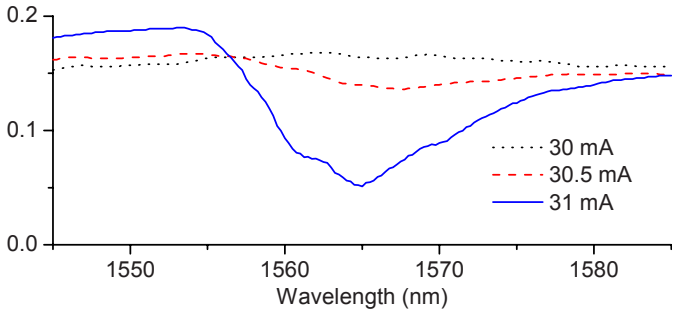

Fig. 5.1.4 – Current dependence of the dips at port 4.

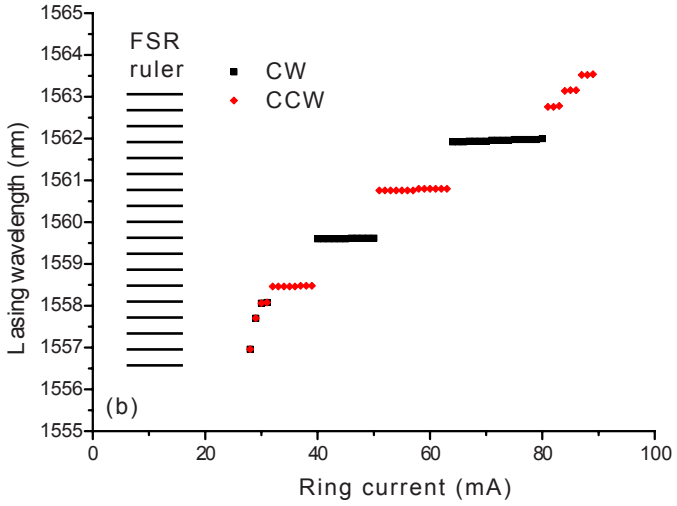

Fig. 5.1.5 – Lasing wavelength as a function of the SRL current.

resonator with equal arms of length $L/2$ can be formulated as

$$e^{2iqL} - ae^{iqL} + b = 0 \,, \tag{5.1.1}$$

where q is the propagation constant. In (5.1.1), $b = (r_u r'_u - t_u t'_u)^{-1}(r_d r'_d - t_d t'_d)^{-1}$, $a = (r_u r_d + r'_u r'_d + t'_u t_d + t_u t'_d)b$ and $t_{u(l)}$ and $r_{u(l)}$ denote the wavelength-dependent transmittivity and reflectivity of the upper (lower) coupler for CW waves, while primed symbols denote the same magnitudes for CCW waves. Thus, the SRL modes are given by

$$q_m^{\pm} L = 2\pi m - i \ln \left[\frac{a}{2} \pm \sqrt{\left(\frac{a}{2}\right)^2 - b} \right] \equiv 2\pi m - i \ln Q_{\pm} \,. \tag{5.1.2}$$

The light-extraction section breaks the circular symmetry of the SRL [170] destroying the pure CW and CCW states at $q_m = 2\pi m$. Two branches of solutions emerge due to the term $-i \ln Q_{\pm}$, which correspond to the experimentally observed doublets. Their splitting, normalized to the free-spectral range of the SRL, is thus given by

$$\Delta = \frac{1}{2\pi} \left\{ Im \left[\ln \left(\frac{Q_-}{Q_+} \right) \right] - \alpha Re \left[\ln \left(\frac{Q_-}{Q_+} \right) \right] \right\} \,, \tag{5.1.3}$$

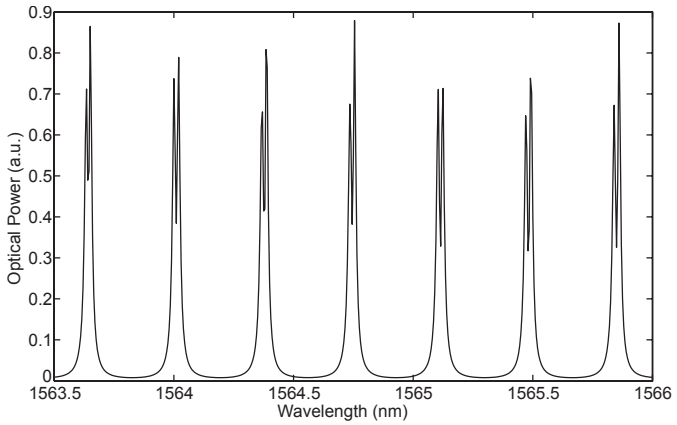

Fig. 5.1.6 – Theoretical calculation of the power collected at port 3.

α being the linewidth enhancement factor. The theoretical results for the power at port 3 are in good agreement with the results shown in Fig. 5.1.2, provided that a small amount of gain in the SRL is included (see Fig. 5.1.6). In these calculations, the section lengths have been taken from the device layout, and facet reflectivities have been adjusted to match the experimental results. The results for the transfer matrix to port 4 show similar trends, and the transfer matrix analysis does not lead to dips on a spontaneous-emission noise background. The reason is that the transfer matrix analysis does not include spontaneous-emission noise in the SRL cavity. Indeed, due to the (slight) gain in the SRL, the power collected at ports 3 and 4 in the absence of external light is the power due to spontaneous emission in the SRL, including amplification and attenuation in the path. In the absence of any reflecting element, light injected into the SRL through port 1 would reach port 3 only after being amplified or attenuated along the path, and no injected light would reach port 4; however, the power at port 4 would be reduced because of amplified spontaneous-emission (ASE) suppression under light injection, thus leading to dips onto the ASE background. It is worth remarking that this effect provides us with a precise way to measure the spectral dependence of the transparency current.

In the same way, one can compute the theoretical detuning for the device used in Figs. 5.1.3 and 5.1.5 (see Fig. 5.1.7). The modulation of the detuning at three mode spacings is apparent, arising from the residual reflectivity at the bends of the output waveguides. In addition, it presents a further slow modulation that arises from the finite effective length of the output couplers and their residual reflectivities. Finally, the wavelength jumps of several modes above the threshold can be partially explained with the same analysis, although a full explanation of the above-threshold phenomenology requires considering nonlinear effects arising from, e.g., four-wave mixing [171] and spatial and spectral hole burning [172]. From Eqs. 5.1.1 and 5.1.3 one sees that for $\alpha > 2 - 3$, the maximum frequency splitting of the doublets almost coincides with their maximum threshold difference, whose modulation for each branch is out of phase. Hence, when the gain spectrum redshifts due to Joule heating, the system will jump from the minimum on one branch to the following minimum on the other branch. For circular SRL, where $L \geq 2R$, this means a jump of $m = int[3\tau_R/\tau_{FP}]$ modes of the SRL, where $\tau_{R(FP)}$ is the roundtrip time in the SRL (Fabry Perot) cavity. Thus, for the device considered here, the modal jumps correspond to m=3.

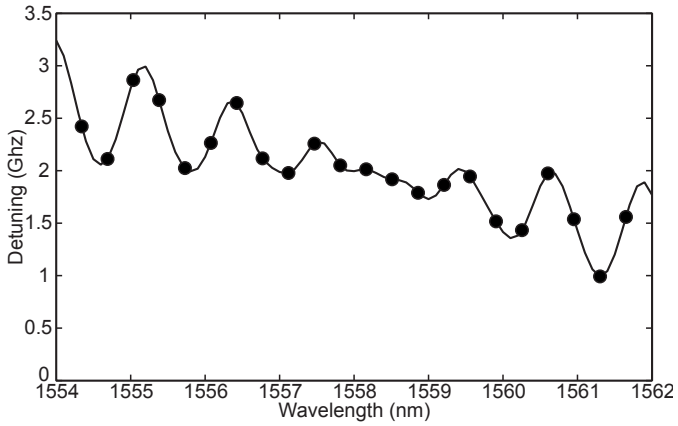

Fig. 5.1.7 – Theoretical detuning between doublets.

V.2 Traveling wave model for quantum well

In this section are presented the effects of taking into account a semiconductor medium in the TW model derived in chapter II. The model used is the one derived in ref. [101]. The differences between this case and the case of a two level atom medium (chapter IV) are discussed.

V.2.1 The model

(a) Equations for the fields

The equation for the longitudinal modes derived in chapter II for a waveguide (2.3.70) reads

$$\frac{\partial^2 \mathcal{E}}{\partial z^2} + \beta^2 \mathcal{E} = -\Gamma \frac{\omega^2}{c^2} \chi_e(\omega, N)\mathcal{E} - i\mu_0 \omega \sigma \mathcal{E} \quad , \tag{5.2.4}$$

that can be written as

$$\frac{\partial^2 \mathcal{E}}{\partial z^2} + \beta^2 \mathcal{E} = -\frac{\omega^2}{c^2} \frac{\mathcal{P}}{\epsilon_0} - i\mu_0 \omega \sigma \mathcal{E} \quad . \tag{5.2.5}$$

Eq. (5.2.5) describes the longitudinal modes in a passive waveguide. One can assume that the waveguide supports a single TE mode whose effective index is $n(\omega)$. Then $\beta = (\omega/c)n(\omega)$. Thinking that inside the core of the waveguide there is a small active region, a quantum well (QW). However, as Eq. (5.2.5) was derived for a passive waveguide one has to introduce the contribution of the QW, removing the contribution of the passive material in the QW region. One can write the polarization in this region as

$$\begin{aligned} \mathcal{P} &= \mathcal{P}_{qw} - \mathcal{P}_{passive} = \epsilon_0 \Gamma \left[\chi_{qw} - (n^2_{passive}(\omega) - 1)\right] \mathcal{E} \\ &= \epsilon_0 \Gamma \left[\chi_{qw} - \mathrm{Re}\{\chi_{qw}\} + \mathrm{Re}\{\chi_{qw}\} - (n^2_{passive}(\omega) - 1)\right] \mathcal{E} \quad , \end{aligned} \tag{5.2.6}$$

that can be written as

$$\mathcal{P} = \epsilon_0 \Gamma [\widetilde{\chi}_{qw} + n_c^2(\omega)]\mathcal{E} \quad , \tag{5.2.7}$$

where

$$\widetilde{\chi}_{qw} = \chi_{qw} - \mathrm{Re}\{\chi_{qw}\} \quad , \tag{5.2.8}$$

$$n_c^2(\omega) = n_{qw}^2(\omega) - n^2_{passive}(\omega) \quad . \tag{5.2.9}$$

Noticing at this point that one can assume the contribution of the QW in two terms, the gain part with a polarization $\widetilde{\mathcal{P}}_{qw} = \epsilon_0 \widetilde{\chi}_{qw} \mathcal{E}$, and the part of the modification of the refractive index in $n_c(\omega)$. These allow to write (5.2.5) as

$$\frac{\partial^2 \mathcal{E}}{\partial z^2} + \frac{\omega^2}{c^2} n^2(\omega)\mathcal{E} = -\frac{\omega^2}{c^2} \left[\frac{\widetilde{\mathcal{P}}_{qw}}{\epsilon_0} + \Gamma n_c^2(\omega)\mathcal{E}\right] - i\mu_0 \omega \sigma \mathcal{E} \quad , \tag{5.2.10}$$

and this imposes the relation of dispersion for the TW as

$$q(\omega) = \frac{\omega}{c} \sqrt{n^2(\omega) + \Gamma n_c^2(\omega)} \quad . \tag{5.2.11}$$

At this point expressing the quasi-monochromatic field as a superposition of left and right TWs

$$\mathcal{E}(z, \omega) = E_+(z, \omega) e^{iq_0 z} + E_-(z, \omega) e^{-iq_0 z} \quad , \tag{5.2.12}$$

substituting it in (5.2.10) and performing the SVEA we obtain

$$\pm \frac{\partial E_\pm}{\partial z} - i\frac{q^2 - q_0^2}{2q_0}E_\pm = i\frac{\omega^2}{2q_0c^2}\frac{P_\pm}{\epsilon_0} - \frac{\mu_0\omega\sigma}{2q_0}E_\pm \quad , \tag{5.2.13}$$

where one defines

$$P_\pm(z,\omega) = \frac{1}{2\Delta}\int_{z-\Delta}^{z+\Delta} dz\ \widetilde{\mathcal{P}}_{qw}(z,\omega)e^{\mp iq_0 z} \quad . \tag{5.2.14}$$

which is the longitudinal average taken over a scale Δ much longer than the optical wavelength but much shorter than the amplification length. Since the fields are quasi-monochromatic around ω_0, the wavenumber q can be written as

$$q \simeq q_0 + \frac{1}{v_g}(\omega - \omega_0) + O(\omega)^2 \quad , \tag{5.2.15}$$

$$q^2 \simeq q_0^2 + \frac{2q_0}{v_g}(\omega - \omega_0) \quad , \tag{5.2.16}$$

then performing the inverse Fourier transform of (5.2.13) using (5.2.15) and (5.2.16), one finds

$$\pm \frac{\partial E_\pm}{\partial z} + \frac{1}{v_g}\frac{\partial E_\pm}{\partial t} = \frac{i\omega_0}{2\epsilon_0 c}P_\pm - \alpha_{int}E_\pm \quad , \tag{5.2.17}$$

where $E_\pm(z,t) = \mathcal{F}^{-1}\{E_\pm(z,\omega)\}$,

$$P_\pm(z,t) = \frac{1}{2\pi}\int_{-\infty}^{+\infty} d\omega\ e^{-i(\omega-\omega_0)t}P_\pm(z,\omega) \quad , \tag{5.2.18}$$

and we have defined the internal losses as

$$\alpha_{int} = \frac{\mu_0\omega_0\sigma}{2q_0} \quad . \tag{5.2.19}$$

(b) Equations for the carriers

In this case Eq. (2.2.46) has to be modified to take into account that in the susceptibility for the semiconductor medium (2.2.48) the imaginary part is providing the gain, while the real part is giving the modification of the refractive index. This is just a modification of the definition of the polarization that leads to an equation for the carriers as

$$\frac{\partial N}{\partial t} = \widetilde{J} - R(N) - i(E^*P - EP^*) + \mathbb{D}\frac{\partial^2 N}{\partial z^2} \quad , \tag{5.2.20}$$

where $R(N) = AN + BN^2 + CN^3$ is the recombination term that includes nonradiative, bimolecular and Auger recombination terms. Using the decomposition of the carriers (2.4.93) one finds

$$\frac{\partial N_0}{\partial t} = \widetilde{J} - R(N_0) + \mathbb{D}\frac{\partial^2 N_0}{\partial z^2} - i(E_+^*P_+ + E_-^*P_- - c.c.) \quad , \tag{5.2.21}$$

and

$$\frac{\partial N_{\pm 2}}{\partial t} = -\left[R'(N_0) + 4\mathbb{D}q_0^2\right]N_{\pm 2} - i(E_\mp^*P_\pm - E_\pm P_\mp^*) \quad . \tag{5.2.22}$$

where $R'(N_0) = dR/dN|_{N_0}$.

(c) Equations for the polarizations

The susceptibility (2.2.48) was modified in [173] to take into account the effect of gain compression due to spectral hole burning. The susceptibility reads

$$\chi_e(\omega, N, |E|^2) = \frac{\hat{\chi} + \hat{\chi}^*}{2} + \frac{\hat{\chi} - \hat{\chi}^*}{2\Lambda} \quad , \tag{5.2.23}$$

where

$$\hat{\chi}(\omega, N, \Lambda) = \chi_0 \left[\ln\left(1 - \frac{b}{\frac{\omega-\omega_{gap}}{\gamma_\perp} + i\Lambda}\right) - 2\ln\left(1 - \frac{\frac{N}{N_t}}{\frac{\omega-\omega_{gap}}{\gamma_\perp} + i\Lambda}\right)\right] \quad . \tag{5.2.24}$$

In (5.2.24) N_t is the transparent carrier density, χ_0 and b are constants characteristic of the material [111] and $\Lambda = \sqrt{1 + \epsilon|E|^2}$, where ϵ is the gain compression parameter due to spectral hole burning. In this case the dominant effect of the spectral hole burning is to reduce the gain in an almost frequency-independent way. The broadening of the gain spectrum can be ignored unless very broadband dynamics are considered [173]. In this case

$$\chi_e(\omega, N, |E|^2) \simeq \chi(\omega, N) - \frac{\Lambda - 1}{2\Lambda}[\chi(\omega, N) - c.c.] \quad , \tag{5.2.25}$$

where $\chi(\omega, N) = \hat{\chi}(\omega, N, 1)$. Then multiplying (5.2.25) by the confinement factor Γ, using (2.2.17), performing the SVAE and taking the first order in small quantities, the equation for the polarizations reads

$$\frac{P_\pm}{\epsilon_0\Gamma} = \chi(\omega, N_0)E_\pm + N_{\pm 2}\frac{\partial\chi(\omega, N_0)}{\partial N}E_\mp - \epsilon g_{nl}(\omega, N_0)\left(|E_\pm|^2 + 2|E_\mp|^2\right)E_\pm \tag{5.2.26}$$

where $g_{nl}(\omega, N) = [\chi(\omega, N) - c.c.]/4$ corresponds to the self- and cross-saturation of the gain, being the self-saturation half the cross-saturation. There is also a term that couples the two counter-propagating field through the grating in the carrier density. However, Eq. (5.2.26) is still in the frequency domain, and no direct inverse Fourier transform can be obtained due to the complicated structure of $\chi(\omega, N_0)$. One possible treatment is to use the (1,1) Padé approximation of the material susceptibility [101] to express (5.2.26) in time domain. The (1,1) Padé approximation for $\chi(\omega, N_0)$ reads

$$\chi(\omega, N_0) \sim \frac{\chi(\omega_0, N_0) + a(N_0)(\omega - \omega_0)}{1 + b(N_0)(\omega - \omega_0)} \quad , \tag{5.2.27}$$

where

$$a(N_0) = \frac{\partial\chi(\omega_0, N_0)}{\partial\omega} + b(N_0)\chi(\omega_0, N_0) \quad , \tag{5.2.28}$$

$$b(N_0) = -\frac{1}{2}\frac{\frac{\partial^2\chi(\omega_0, N_0)}{\partial\omega^2}}{\frac{\partial\chi(\omega_0, N_0)}{\partial\omega}} \quad . \tag{5.2.29}$$

Using the (1,1) Padé approximation one can find the time domain version of (5.2.26) as

$$\begin{aligned} &\tfrac{1}{\epsilon_0\Gamma}\left(P_\pm + ib(N_0)\tfrac{\partial P_\pm}{\partial t}\right) = \chi(\omega_0, N_0)E_\pm + ia(N_0)\tfrac{\partial E_\pm}{\partial t} \\ &+\tfrac{\partial\chi(\omega_0, N_0)}{\partial N}N_{\pm 2}E_\mp - \epsilon g_{nl}(\omega_0, N_0)\left(|E_\pm|^2 + 2|E_\mp|^2\right)E_\pm \quad . \end{aligned} \tag{5.2.30}$$

In order to perform a correct expansion in terms of the Padé approximation and for numerical purposes, it is convenient to choose ω_0 to be the emission frequency at threshold. Changing to this reference frame allow to make the substitution $\chi(\omega_0, D_0) \to \chi(\omega_0, D_0) - \mathrm{Re}\{\chi(\omega_0, D_{th})\}$. Therefore one can use the threshold point as the *expansion point*. The details of this expansion point are discussed in the section V.2.2.

(d) Dimensionless model

The TW equations (5.2.17), (5.2.30), (5.2.21) and (5.2.22) can be written in a dimensionless form as

$$\pm \frac{\partial A_\pm}{\partial s} + \frac{\partial A_\pm}{\partial \tau} = iB_\pm - \alpha A_\pm \ , \tag{5.2.31}$$

$$\begin{aligned} B_\pm \ &+ \ ib(D_0)\frac{\partial B_\pm}{\partial \tau} = \chi(\Omega_0, D_0)A_\pm + ia(D_0)\frac{\partial A_\pm}{\partial \tau} + \frac{\partial \chi(\Omega_0, D_0)}{\partial D} D_{\pm 2} A_\mp \\ &- \ \widetilde{\epsilon} g_{nl}(\Omega_0, D_0)\left(|A_\pm|^2 - 2|A_\mp|^2\right) A_\pm \ + \sqrt{\beta D_0}\xi_\pm(s,\tau) \ , \end{aligned} \tag{5.2.32}$$

$$\frac{\partial D_0}{\partial \tau} = J - R(D_0) - i(A_+^* B_+ + A_-^* B_- - c.c.) \ , \tag{5.2.33}$$

$$\frac{\partial D_{\pm 2}}{\partial \tau} = -\left[R'(D_0) + \eta\right] D_{\pm 2} - i(A_\mp^* B_\pm - A_\pm B_\mp^*) \ , \tag{5.2.34}$$

where the diffusion term in (5.2.33) is neglected but is maintained in (5.2.34) inside the parameter η, and a noise term modeling spontaneous emission is introduced in (5.2.34). The fields, polarizations and carriers are scaled as

$$\begin{array}{cc} A_\pm = \sqrt{\frac{2\epsilon_0 c\tau_f}{\omega_0 L N_t}} E_\pm \ , & B_\pm = \sqrt{\frac{\omega_0 L \tau_f}{2\epsilon_0 c N_t}} P_\pm \ , \\ D_0 = N_0/N_t \ , & D_{\pm 2} = N_{\pm_2}/N_t \ , \end{array}$$

and new dimensionless parameters are defined

$$\begin{array}{cc} \gamma = \widetilde{\gamma}_\perp \tau_f \ , & \Omega_0 = \omega_0 \tau_f \ , \\ \alpha = \alpha_{int} L \ , & \widetilde{\epsilon} = \frac{2\epsilon_0 \tau_f n}{\Omega_0 N_t} \epsilon \ , \\ \eta = 4\mathbb{D} q_0^2 \tau_f \ , & J = \frac{\tau_f}{N_t} \widetilde{J} \ , \end{array}$$

finally. new coordinates are defined

$$s = \frac{z}{L} \ , \quad \tau = \frac{v_g}{L} t = \tau_f^{-1} t \ ,$$

where $\tau_f = L/v_g$ is the time of flight inside the cavity. With these changes the recombination nonlinear function and its derivative reads

$$\begin{aligned} R(D_0) &= (AD_0 + BN_t D_0^2 + CN_t^2 D_0^3)\tau_f \ , \\ R'(D_0) &= (A + 2BN_t D_0 + 3CN_t^2 D_0^2)\tau_f \ . \end{aligned}$$

And the new approximation for the susceptibility reads

$$\chi(\Omega_0, D_0) = \widetilde{\chi}_0 \left[\ln\left(1 - \frac{b}{\frac{\Omega_0 - \Omega_{gap}}{\gamma} + i}\right) - 2\ln\left(1 - \frac{D_0}{\frac{\Omega_0 - \Omega_{gap}}{\gamma} + i}\right)\right] \ ,$$

where $\widetilde{\chi}_0 = \frac{\Gamma \Omega_0}{2n}\chi_0$ and Ω_{gap} is the dimensionless angular frequency corresponding to the energy gap of the quantum well material. The coefficients of the Padé approximation read

$$\begin{aligned} a(D_0) &= \frac{\partial \chi(\Omega_0, D_0)}{\partial \Omega} + b(D_0)\chi(\Omega_0, D_0) \ , \\ b(D_0) &= -\frac{1}{2}\frac{\frac{\partial^2 \chi(\Omega_0, D_0)}{\partial \Omega^2}}{\frac{\partial \chi(\Omega_0, D_0)}{\partial \Omega}} \ , \end{aligned}$$

and the derivatives read as

$$\begin{aligned}\frac{\partial\chi(\Omega_0,D_0)}{\partial D} &= \frac{2\gamma\widetilde{\chi}_0}{\gamma(i-D_0)+\Omega_0}\ ,\\ \frac{\partial\chi(\Omega_0,D_0)}{\partial\Omega} &= \widetilde{\chi}_0\left(\frac{1}{i\gamma+\Omega_0}+\frac{1}{\gamma(i-b)+\Omega_0}-\frac{2}{\gamma(i-D_0)+\Omega_0}\right)\ .\end{aligned}$$

V.2.2 Laser threshold

In order to find the laser threshold one has to encounter the point where the gain equals the total losses of the laser. The frequency of the gain curve is found at,

$$\Omega_{peak}=\Omega_{gap}-\gamma D_0+\gamma\sqrt{2D_0^2-1}\ . \tag{5.2.35}$$

Equalling the gain at peak of the gain curve with the total losses, one obtains a nonlinear equation for D_{th} which is the value of the carriers at threshold,

$$-\Gamma\ \mathrm{Im}\{\chi(\Omega_{peak},D_{th})\}=\alpha-\ln(\max\{t+r,t-r\}), \tag{5.2.36}$$

where $\max\{t+r,t-r\}$ denotes the maximum value between $t+r$ and $t-r$. In Fig. 5.2.8 are plotted the left and right sides terms of Eq. (5.2.36).

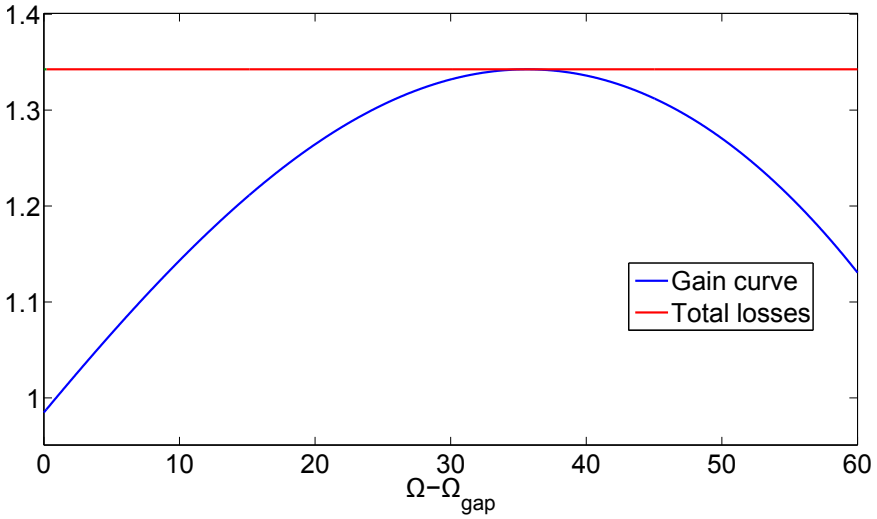

Fig. 5.2.8 – The point were the gain equals to the losses (Eq. (5.2.36)) will be the expansion point for the analysis and simulations, i.e. the laser threshold. In this case $D_{th}=2.0326$ and $\Omega_{th}=35.64$. $\widetilde{\chi}_0=150$, $b=10000$, $\alpha=1$, $\gamma=53.8$, $A=2.2\ 10^{-3}$, $B=1.54\ 10^{-2}$, $C=2.2\ 10^{-4}$, $\widetilde{\epsilon}=0$, $\eta=0.22$, $\Gamma=0.01$, $T=0.7$ and $R=0.01$

Once obtained D_{th} one uses (5.2.35) to calculate the peak frequency at threshold Ω_{th}. This will be used as an expansion point for the refractive index, so

$$\chi(\Omega_0,D_0)\to\chi(\Omega_0,D_0)-\mathrm{Re}\{\chi(\Omega_{th},D_{th})\}. \tag{5.2.37}$$

V.2.3 Numerical analysis

In this case one can use the numerical techniques developed for chapter IV and detailed discussed in appendix B. However the problem to find the steady states now is more

complex due to the nonlinearity of the QW response, and the problem can not be solved via a shooting method. In fact one has to solve all the variables involved with a Newton-Raphson algorithm. This involves a highly multidimensional nonlinear problem that can be difficult to solve unless a good guess solution is provided. The idea is to use the eigenvectors associated to the eigenvalues that change its stability as the guess solution to find the steady state solution.

For example for the parameter set of Fig. 5.2.8, one performs the LSA of the off solution using the evolution operator method described in appendix B, finding the eigenvalue spectra (see Fig. 5.2.9 (a)), in this case for $J = 1.01\ J_{th}$ there is one eigenvalue having $\mathrm{Re}(\lambda) > 0$, $\lambda_0 = 0.010 - 0.014\ i$ and its corresponding eigenvector (see Fig. 5.2.9 (b)-(e)).

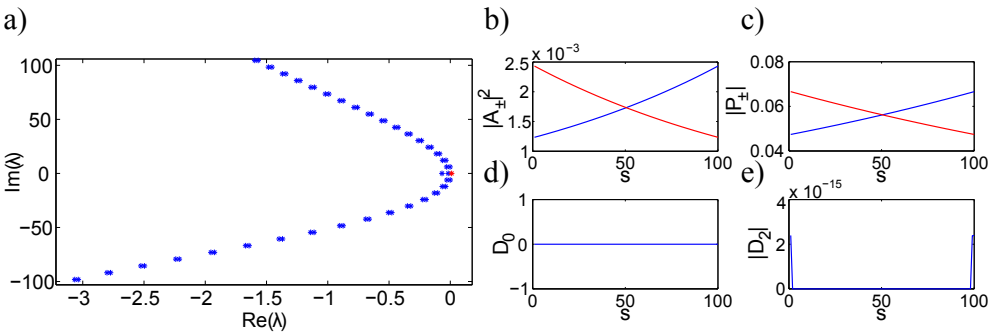

Fig. 5.2.9 – (a) Real vs imaginary part of the eigenvalues λ for $J = 1.01\ J_{th}$. Eigenvalues in blue (red) have $\mathrm{Re}(\lambda) < 0$ ($\mathrm{Re}(\lambda) > 0$). There is one with $\mathrm{Re}(\lambda) > 0$, $\lambda_0 = 0.010 - 0.014\ i$. The complex conjugate eigenvalues have been removed for clarity. (b), (c), (d) and (e) are the intensity of $A_{\pm}$, the modulus of $P_{\pm}$, the carrier density D_0 and the modulus of D_2 respectively, that form the eigenvector associated to λ_0. The parameter set is the one used in Fig. 5.2.8.

Then the eigenvector is used as the guess for the multidimensional nonlinear equation solver and after a few iterations a bidirectional solution corresponding to a lasing branch is found (see Fig. 5.2.10) with a frequency $\Omega = 8.75\ 10^{-7}$.

Once a solution in the lasing branch is known it is easy to continue this branch of solutions by changing the pump current and solving the multidimensional problem with the previous solution as a guess. After that the LSA is performed to know the stability of this solution. Fig. 5.2.11 shows this procedure for the six first modes for the parameter set in Fig. 5.2.8. The first one that corresponds to $m = 0$ it is stable for a pump current range until $J \simeq 1.15\ J_{th}$, the other modes are unstable. For this case, if one repeats the process of branch jumping in the point of change of stability of mode $m = 0$, the solution found after a lot iterations with the multidimensional solver goes to the off solution. It seems that there is not any stable solution and the system goes to a multimode instability, dynamical simulations are required to assure this fact.

The next dynamical simulations where performed using a noisy initial condition and $\beta = 10^{-7}$. Fig. 5.2.12 shows the dynamical behavior for $J = 1.08\ J_{th}$, it shows agreement with Fig. 5.2.11, after a transient which involves modes $m = 0$ and $m = \pm 1$ it arrives to a bidirectional steady state solution for $m = 0$.

Fig. 5.2.13 shows the dynamical behavior for $J = 1.14\ J_{th}$, in this case multimode dynamics are found also in agreement with Fig. 5.2.11.

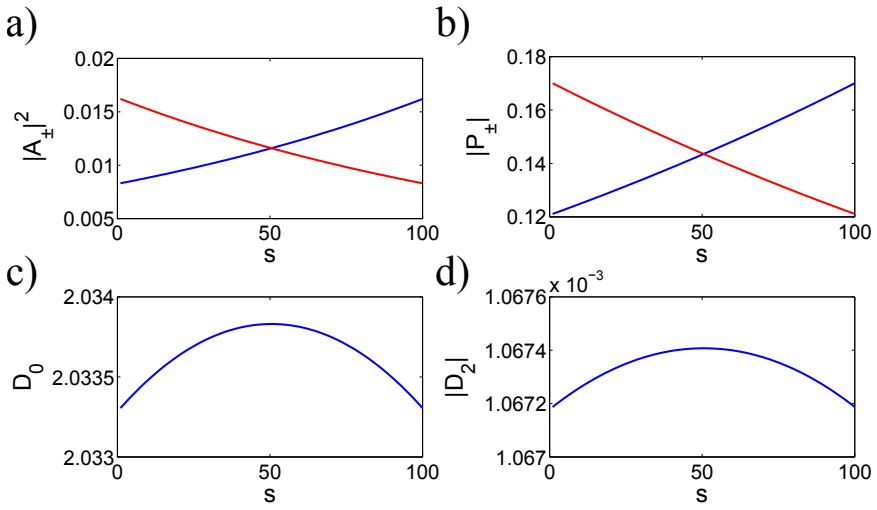

Fig. 5.2.10 – Bidirectional solution obtained from the eigenvector in Fig. 5.2.9. $J = 1.01\ J_{th}$. The frequency of the solution is $\Omega = 8.75\ 10^{-7}$.

(a) Multistability

One of the differences that one can find between this model and the model for the two-level atom it is that a different kind of bifurcation can be found. Fig. 5.2.14 shows a subcritical pitchfork bifurcation. This behavior was previously reported theoretically using a RE model and experimentally [174]. It means that the system has multistability between bidirectional and unidirectional solutions.

Fig. 5.2.15 shows a numerical simulation for the parameter set in Fig. 5.2.14 and $J = 2.1 J_{th}$, i.e. inside the multistability region. A noisy initial condition was used to start the simulation, at the transient the system tends to the unidirectional solution but finally it goes to the bidirectional solution. Fig. 5.2.16 for $J = 3 J_{th}$ shows the opposite situation, at the beginning the system tends to the bidirectional solution (which in this case is unstable) but quickly goes to a unidirectional solution. Increasing the noise to $\beta = 1$ one is able to see the transition between unidirectional and bidirectional solutions (see Fig. 5.2.17). In this case the noise helps the system to jump between the stable solutions. Fig. 5.2.17 shows a dynamical simulation for $J = 2.2 J_{th}$ starting from the unidirectional solution, the noise drives the system to the bidirectional solution in the range between $100 - 400\ \tau_f$ then it returns to the unidirectional solution.

(b) Wavelength multistability

A different situation is found when one increases the carrier diffusion and the gain curve bandwidth. In the same way as in the case for the two level atom (section IV.5) wavelength multistability is found for high carrier diffusion (see Fig. 5.2.18), however in this case due to the asymmetry of the gain curve the system only displays multistability in modes $m = 0$ and $m = +1$.

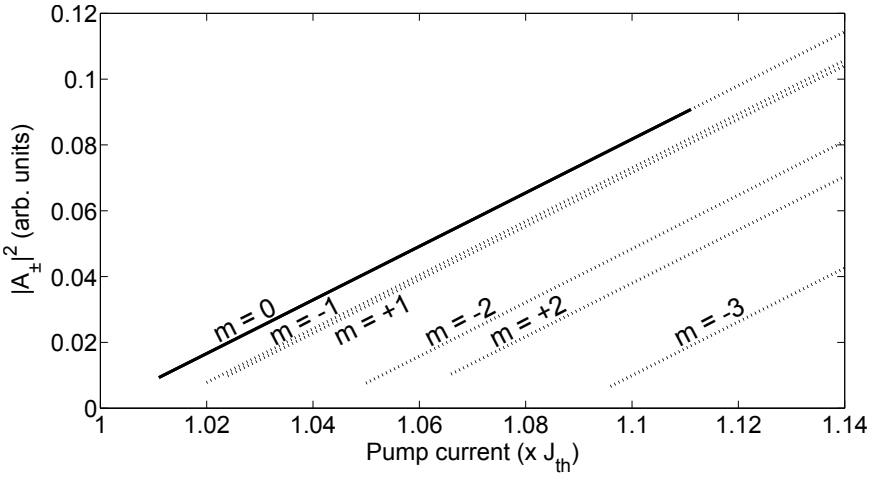

Fig. 5.2.11 – Bidirectional solutions for $m = 0, \pm 1, \pm 2, -3$. The solid (dashed) lines corresponds to a stable (unstable) solution.

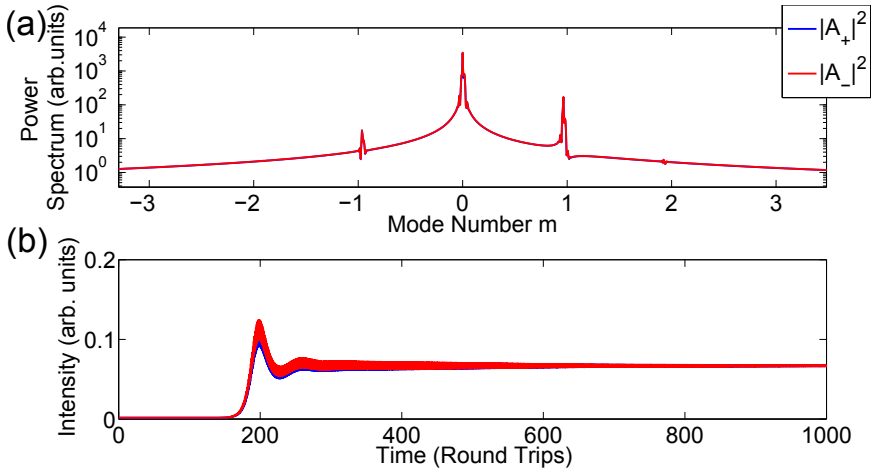

Fig. 5.2.12 – Dynamical simulation for the parameter set used in Fig. 5.2.8 and $J = 1.08 J_{th}$. (a) Power spectra. (b) Time trace.

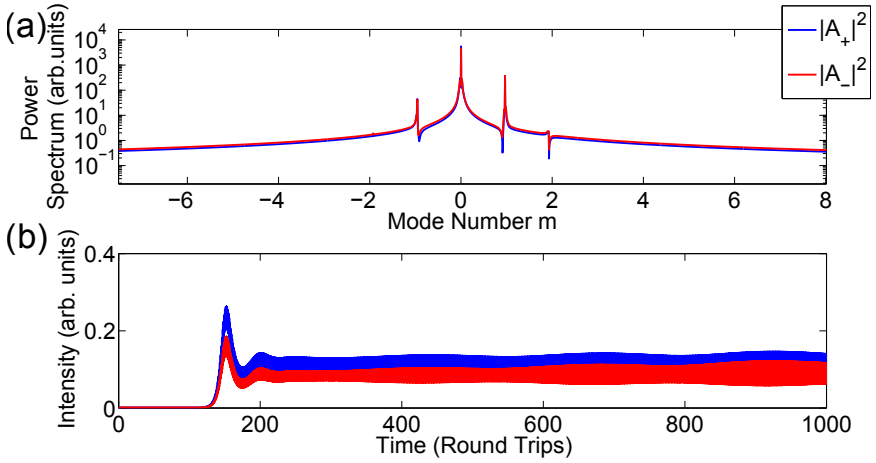

Fig. 5.2.13 – Dynamical simulation for the parameter set used in Fig. 5.2.8 and $J = 1.14 J_{th}$. (a) Power spectra. (b) Time trace.

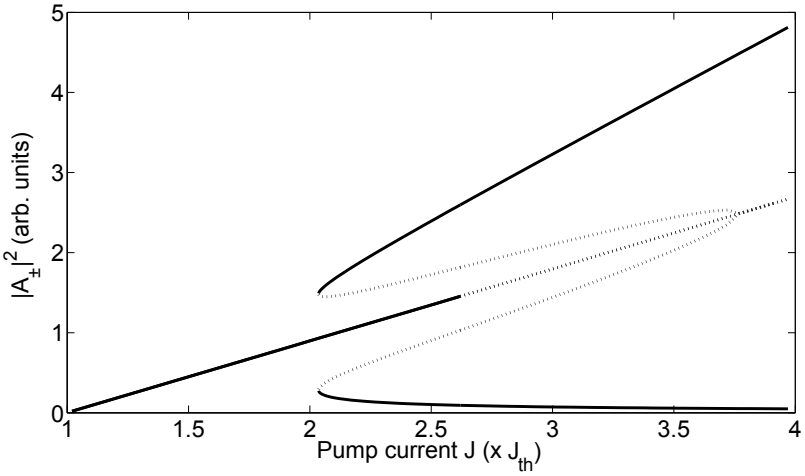

Fig. 5.2.14 – Subcritical pitchfork. $\widetilde{\chi}_0 = 150$, $b = 10000$, $\alpha = 1$, $\gamma = 13.8$, $A = 2.2\ 10^{-3}$, $B = 1.54\ 10^{-2}$, $C = 2.2\ 10^{-4}$, $\widetilde{\epsilon} = 0$, $\eta = 2.2$, $\Gamma = 0.01$, $T = 0.7$ and $R = (8.77 + 4.79i)10^{-3}$.

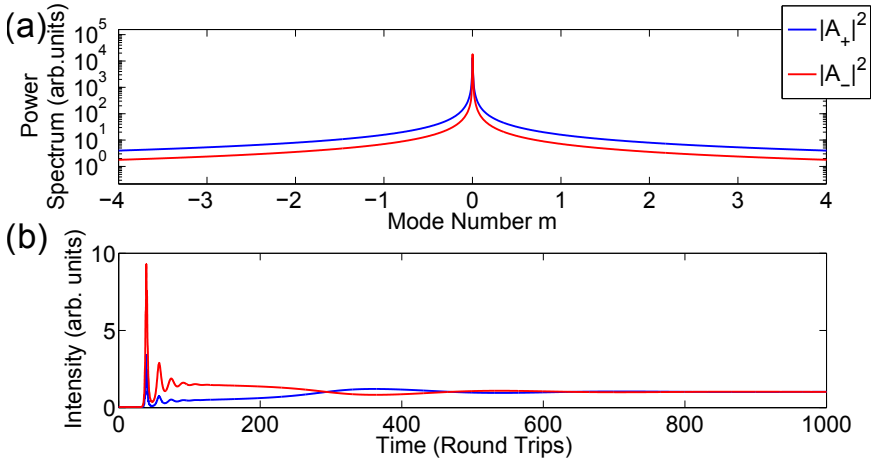

Fig. 5.2.15 – Dynamical simulation for the parameter set used in Fig. 5.2.14 and $J = 2.1J_{th}$. (a) Power spectra. (b) Time trace.

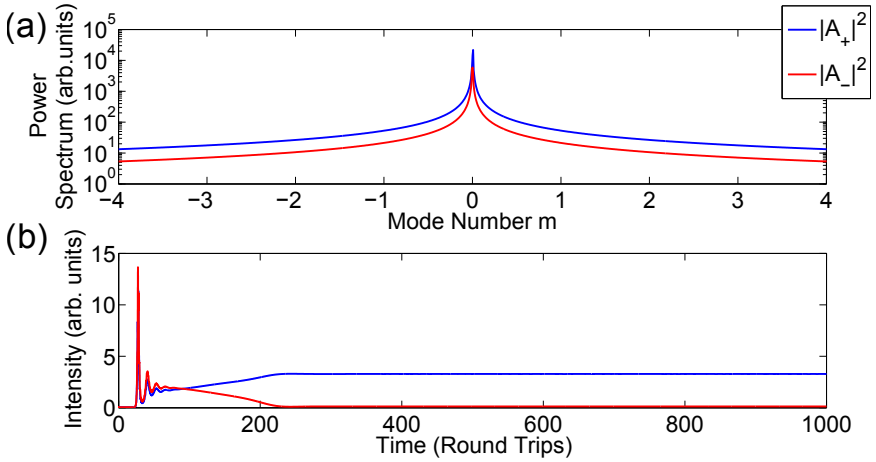

Fig. 5.2.16 – Dynamical simulation for the parameter set used in Fig. 5.2.14 and $J = 3J_{th}$. (a) Power spectra. (b) Time trace.

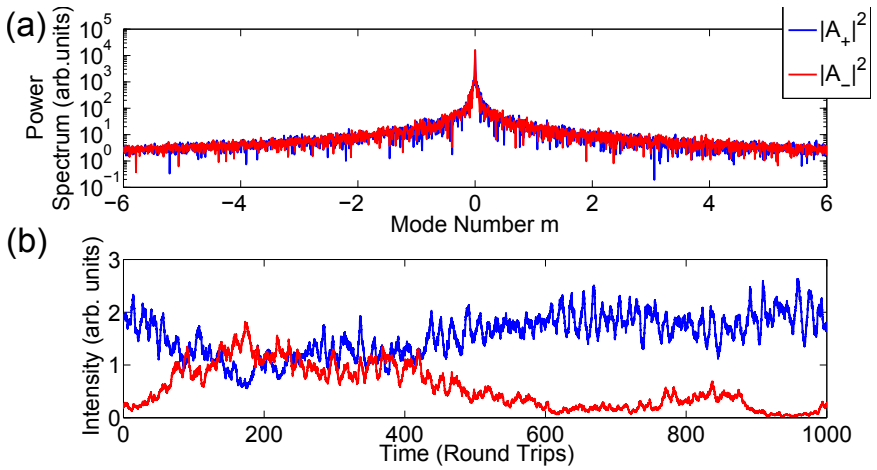

Fig. 5.2.17 – Dynamical simulation for the parameter set used in Fig. 5.2.14, $\beta = 1$ and $J = 2.2 J_{th}$. (a) Power spectra. (b) Time trace.

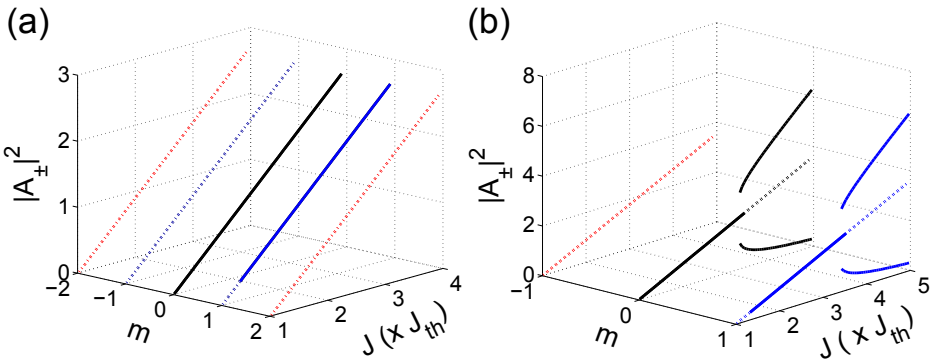

Fig. 5.2.18 – Bifurcation diagrams (a) $\widetilde{\chi}_0 = 150$, $b = 10000$, $\alpha = 1$, $\gamma = 103.8$, $A = 2.2\ 10^{-3}$, $B = 1.54\ 10^{-2}$, $C = 2.2\ 10^{-4}$, $\widetilde{\epsilon} = 0$, $\eta = 222.2$, $\Gamma = 0.01$, $T = 0.7$ and $R = 0.01$.

V.3 Semiconductor Snail Lasers

[1] In this section, a modified ring laser geometry is presented to promote stable unidirectional lasing. The effects of directional coupling and reflectivities are investigated with respect to quantum efficiency, directionality and side-mode suppression ratio of the lasing spectra. Simulation and experimental results are presented showing single mode ($> 20dB$ side-mode suppression ratio), unidirectional lasing on an InP based multiple quantum well material.

Semiconductor ring lasers (SRL) are becoming a mature and versatile technology with applications in telecommunications, optical signal processing and on-chip sensing. Research carried out into SRL devices has demonstrated many of the functions that have been previously presented in Fabry-Pérot (FP) and Distributed Feedback (DFB) lasers; such as tunability [175], master-slave operation [175] and mode-locking [93]. Additionally, directional bistability has been demonstrated [70], with possible future applications in optical memory and delay lines. Further application of SRLs may be made in high power applications, especially where spatially dense arrays of outputs are required, for example in high resolution printing heads. SRLs do not suffer from the Catastrophic Optical Damage (COD) that occurs in FP lasers where the cleaved facets are employed as feedback elements in the laser cavity. In SRLs, the lasing cavity is formed by the closed ring waveguide with light extracted using waveguide coupler structures, avoiding inclusion of facets in the lasing cavity. In addition, SRLs may be spatially separated on chip, allowing better thermal management and contact definition for individual addressing, without the considerations that would be necessary for FP devices, such as waveguide bends or etched cavity mirrors. However, in SRLs it is difficult to realise the equivalent to high and low reflectivity facet coatings, which allow increased quantum efficiency and directionally dependent output power. The symmetric nature of the coupling in SRLs can produce both bidirectional or (fluctuating) bistable directional lasing of the device [96]. Unidirectionality relies on minimising reflections within the laser cavity, which, by coupling energy between counter-propagating modes leads to bidirectional emission. So, the necessity for high output coupling for increased quantum efficiency of SRLs also results in increased feedback into the laser cavity and hence, bidirectional lasing. In this paper an alternative 'snail' ring laser geometry is presented as a means to produce high efficiency, stable unidirectional lasing.

Fig. 5.3.19 shows a schematic of the snail laser device. The structure is similar to that of conventional SRLs, but the cavity is now defined through the crossed ports of the evanescent coupler. The waveguide inside this ring has a cleaved facet, and the one outside is tilted and tapered. This laser geometry is proposed with the objectives of achieving highly directional output with high slope efficiency. The unbalance of the reflectivity of the two facets couples a large fraction of the clockwise (CW) mode (as defined by the schematic in the inset of Fig. 5.3.20) into the counter-clockwise (CCW) mode, so creating unidirectional lasing in this direction. The use of the crossed ports for defining the laser cavity allows us to achieve high slope efficiency with conventional evanescent couplers. In a SRL geometry this would entail producing a directional coupler (DC) with a high coupling fraction, which requires a compromise between small gaps separating the co-propagating waveguides (requiring highly optimised pattern definition and etching) and coupler lengths (leading to device lengths in the order of hundreds of microns.) By using the snail geometry this problem is inverted, and the

[1] This part is based on the letter: "Semiconductor Snail Lasers" by M.J. Strain, G. Mezösi, J. Javaloyes, M. Sorel, A. Pérez-Serrano, A. Scirè, S. Balle, J. Danckaert and G. Verschaffelt, *Appl. Phys. Lett.* **96**, 121105 (2010).

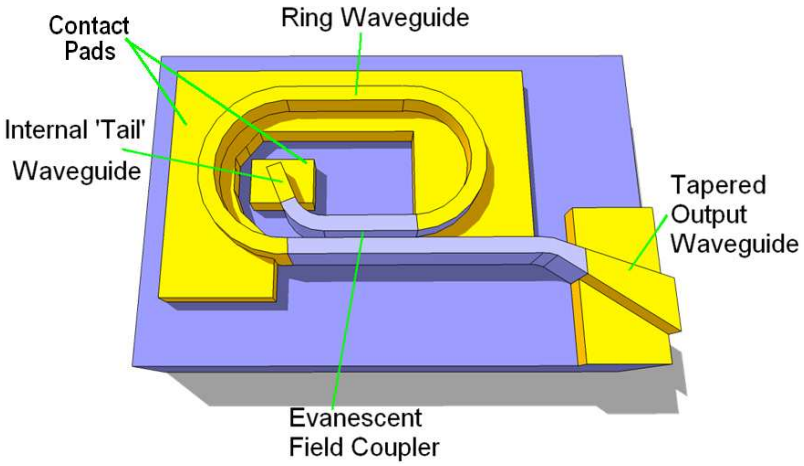

Fig. 5.3.19 – Schematic of a snail laser device.

requirement for low coupling DCs, improves the fabrication tolerances significantly, allowing the production of short, widely spaced co-propagating waveguides.

The theoretical analysis of the snail laser is based on the Travelling-Wave Model (TWM) developed in [101], with the boundary conditions appropriate to this geometry, as depicted in the inset of Fig. 5.3.20, where r_3 (r_2) is the tail (output facet) reflectivity, L_3 (L_2) is the length of the tail (output) waveguide, L is the length of the cavity and δ^2 is the power extraction efficiency of the DC.

The lasing modes of the snail laser can be determined by a transfer-matrix analysis as in [129] (see section V.1). The characteristic equation for the allowed propagation constants q reads

$$Z^2(\delta^2 + Z_2 Z_3) + 2i\delta(1 + Z_2 Z_3)Z - 1 - Z_2 Z_3 \delta^2 = 0 \qquad (5.3.38)$$

where $Z = e^{iqL}$, $Z_{2(3)} = r_{2(3)} e^{i\omega n_{2(3)} L_{2(3)}/c}$, ω is the optical frequency and $n_{2(3)}$ is the effective index of the output (tail) waveguide. The characteristic equation has two branches of solutions $q_m^{\pm}$ which present, for $r_2 r_3 << \delta^2$, a threshold difference given by

$$\Delta Im\left(q_m^{\pm}\right) = 2\frac{1-\delta^2}{\delta L}\sqrt{r_3 r_2} cos\left(\omega \frac{n_3 L_3 + n_2 L_2}{2c}\right) . \qquad (5.3.39)$$

The effective loss modulation due to the compound-cavity effects in the output waveguides may degrade side-mode suppression ratio (SMSR) in the device. Since the amplitude of the loss modulation increases as δ decreases, in order to produce a high output laser source with high SMSR, small reflectivity of the tail and output facet is required.

Fig. 5.3.20 shows the simulated LI curves given the facet reflectivities, and varying δ. In the simulations, the output waveguides have been considered as passive. The TWM shows an inverse relationship between the self-coupling δ and both the threshold current and slope efficiency.

In all of the designs presented here, the waveguide width is $2\,\mu m$, the output waveguide was tapered up to $8\,\mu m$ and the device bar facet cleaved at 80^o to the waveguide normal in order to minimise backreflections. The average ring radius around the snail cavity is $200\,\mu m$. The length of the output waveguides is $450\,\mu m$ and the tail waveguides are $208\,\mu m$ long. The tail waveguide incorporates a contact that allows to control its effective reflectivity by applying a bias. FDTD simulations of the

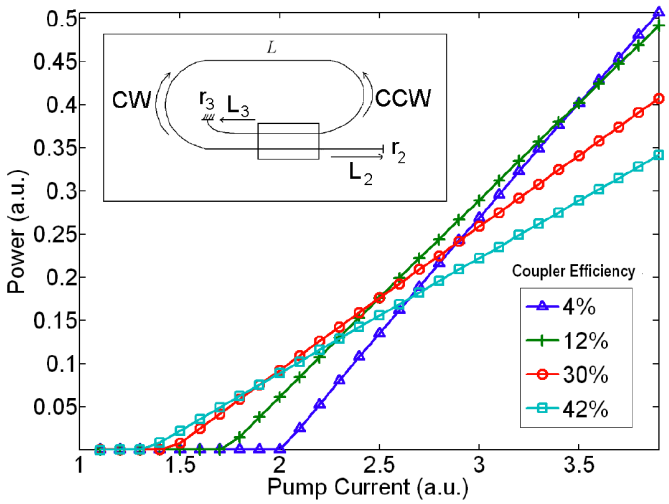

Fig. 5.3.20 – Travelling Wave Model simulation of LI curves outside facet 2 (CCW mode of the ring) for varying δ in a snail laser device.

structures gave values of 6.1% and 0.67% respectively, for the tail and output facet reflectivities at transparency. Devices with coupler lengths of $56.4, 80.5$ and $171\,\mu m$ were produced, giving nominal coupling of $5, 10$ and 40% respectively. The devices were fabricated on a multiquantum-well (QW) InAlGaAs/InP wafer structure with a gain region consisting of five $6\,nm$ compressively strained InAlGaAs wells and six $10\,nm$ slightly tensile strained barriers. The waveguiding core is formed by a $60\,nm$ graded-index layer on either side of the QW region. Hydrogen silsesquioxane (HSQ) was used as a negative tone electron beam resist for definition of the waveguides. After exposure and development the HSQ pattern was used as a hardmask for the etching of the uppercladding layers using a $CH_4/H_2/O_2$ Reactive Ion Etch (RIE).

Experimental LI curves for the lasers were measured by coupling the output from the tapered facet to a broad area Ge photodetector. Fig. 5.3.21 shows LI curves for the snail laser devices with the tail contact biased at $0\,V$. As predicted by the model, the threshold current and slope efficiency of the snail laser devices increase as δ decreases. The abrupt step in power at the lasing thresholds is due to the fact that the DC sections are unpumped, acting as saturable absorbing sections. Photocurrent measurements of the tail waveguide contact confirmed unidirectional operation. Moreover, the LI curves show no evidence of the directional switching that occurs in SRLs (see inset for a comparison) [96]. Directional switching could be observed only for the 40% coupled snail laser for reverse bias $< -2\,V$ on the tail contact, suggesting that as $r_3 \to r_2$, the laser is no longer forced to operate unidirectionally in the CCW direction.

Spectra of the snail laser devices under varying injection current, and reverse bias on the tail waveguide contact, were also recorded. Fig. 5.3.22(a) exhibits the SMSR of the lasers at 2x threshold current for varying reverse bias V_R on the tail waveguide contact.

For $V_R = -3\,V$ (i.e. low r_3), the SMSR is largest for the device with highest δ, in agreement with the theoretical prediction. For the 5% coupler device, the SMSR does not vary greatly with V_R, as expected from the correspondingly large loss modulation amplitude (see eq. 5.3.39). Instead, the SMSR of the 10% and 40% coupler devices strongly varies with V_R, abruptly falling by $\sim 8\ dB$ above $V_R = -2\ V$ and $V_R =$

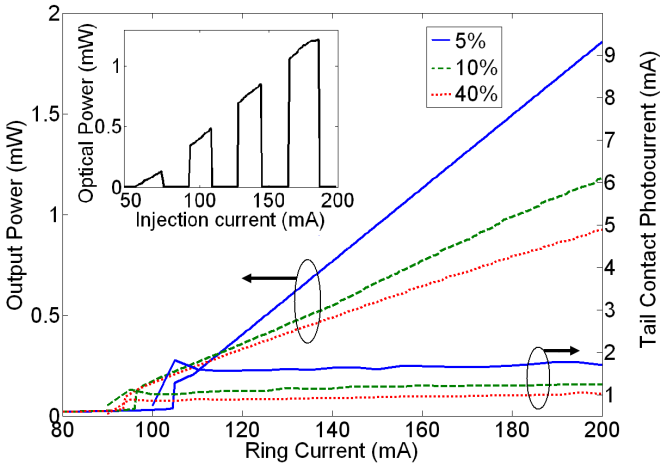

Fig. 5.3.21 – LI curves for snail laser devices with varying self-coupling measured from external facet (CCW mode of the ring), and photocurrent measurement (CW mode of ring) on the tail contact.(Inset: LI curve from a SRL device.)

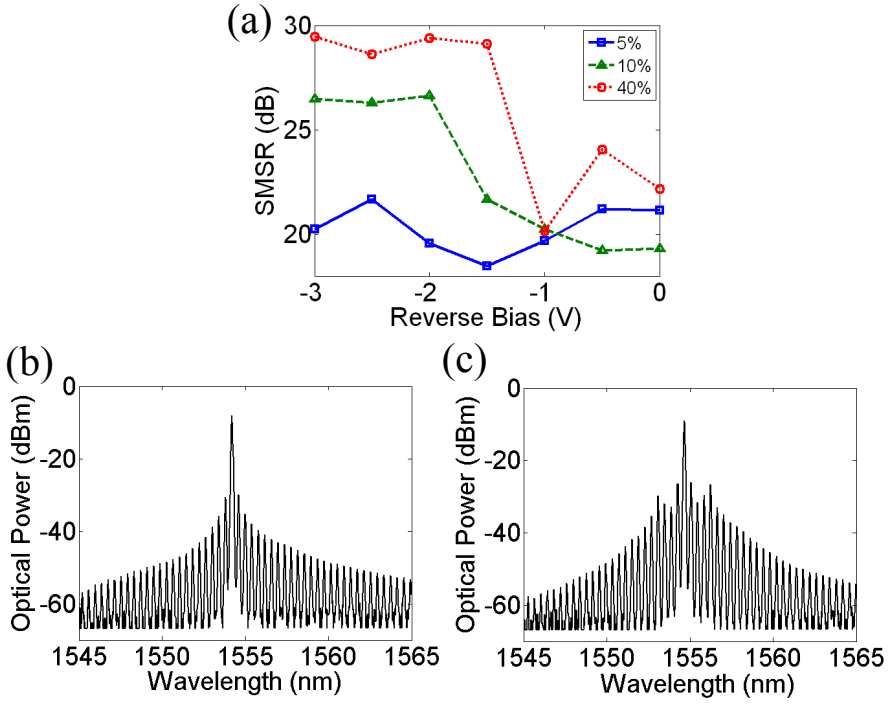

Fig. 5.3.22 – (a) SMSR vs reverse bias on internal waveguide for snail lasers with varying self-coupling, (b) and (c) spectra for snail laser with 10% coupler and $V_R = -3\,V$ and $V_R = 0\,V$, respectively.

$-1.5\ V$. This indicates the crossover to a regime of stronger coupled cavity effects which manifests as an enhancement of secondary modes in the optical spectra. The coupled cavity effect can be clearly identified in Fig. 5.3.22(c) as opposed to the single mode spectra of Fig. 5.3.22(b).

Finally, in order to demonstrate potential of creating dense arrays of these devices on a single chip, a set of four devices were fabricated as shown in Fig. 5.3.23, with an output waveguide pitch of $32\,\mu m$. A near field image is also shown, exhibiting the four distinct output spots of the devices, each of which was individually addressable.

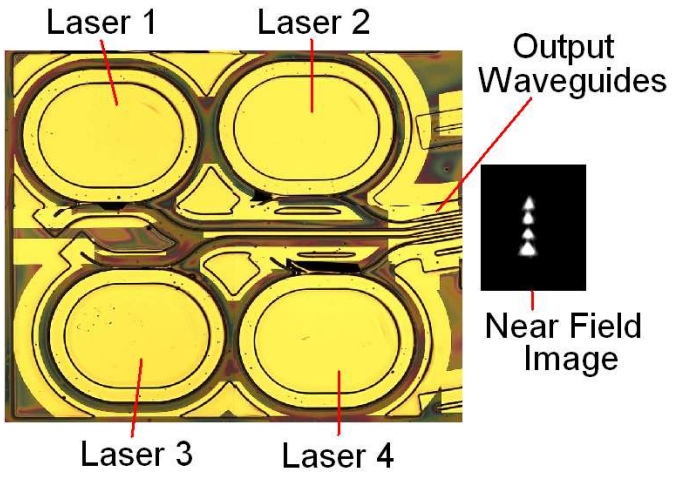

Fig. 5.3.23 – Micrograph of snail laser array, with near field image of emission from four output waveguides.

V.4 Conclusions

In the first section of this chapter, the modal structure of SRLs have been experimentally studied by measuring the transfer properties of the device below the threshold and the wavelength jumps that occur in connection with directional switching above the threshold. A transfer matrix analysis explains the measurements when ASE in the SRL cavity is accounted for. The residual reflectivities in the light-extraction sections determine the frequency splitting and threshold difference between the two branches of solutions. This effect, together with the redshift of the material gain, explains the amount of wavelength jumps displayed by the SRL above the threshold. This work shows that the cavity effects in SRLs are very important and have to be taken into account to develop realistic models.

In section V.2 a TWM for QW material is shown, where the material response in the time domain is found using the (1,1) Padé approximation. This methodology allows to use the tools developed for the case of the two level atom to find the different monochromatic solutions and their stability. Using these tools results previously shown in literature are found, as multistability between unidirectional and bidirectional solutions, and wavelength multistability. This part far from a rigorous analysis of the dynamics of SRL simply shows that the tools developed previously can be helpful in the case of the TWM for QW material.

Finally in section V.3, a modification of a ring laser geometry has been presented in order to produce a high efficiency, unidirectional laser source without suffering from the COD problems associated with FP lasers. SMSRs of over $20\,dB$ were exhibited for all of the devices fabricated, with increased quantum efficiency being exhibited with reducing self-coupling. Increasing the reflectivity from the internal waveguide promotes unidirectionality, but then coupled cavity effects emerge, reducing the SMSR, especially for devices with low δ. The simulations carried out using the TWM, for the threshold, slope efficiency and SMSR behaviour of the devices are in good agreement with the experimental results. An array of four $32\,\mu m$ output pitched, individually addressable snail lasers was also presented.

VI
Concluding Remarks

Semiconductor Ring Lasers (SRLs) dynamics have been investigated through different models. In particular noise properties, wavelength multistability and multimode dynamics of these devices have been studied in detail. As shown in Chapter II, the different models have been derived within the semiclassical approximation and they are divided into two groups: Rate Equation Models (REMs) and Traveling Waves Models (TWMs). The phenomenological approach of REMs provides a useful insight in large size devices; however it cannot describe ps-scale phenomena and can hardly reproduce spatial effects. Instead, TWMs offer a spatiotemporal description that naturally incorporates the spatial effects and the multilongitudinal character of the field, with the geometry of the cavity being incorporated through the boundary conditions for the waves. A consequence of a more detailed description of the physical processes that occur in the laser, either by the inclusion of spatial effects or a better description of the active medium (see Fig. 6.0.1), is an increase of the complexity of the problem. This complexity comes from an increased number of the variables involved and their nonlinear character. This fact makes that the main results in the thesis were found numerically because analytic results are impossible to obtain in the most general cases. Despite the different levels of detail that these descriptions have, each model is useful in certain situations as it has been demonstrated in the previous chapters.

The Ordinary Differential Equations (ODEs) based REMs have historically offered a good description of laser dynamics and particularly to semiconductor devices. These models describe the temporal dynamics of carrier density and electric fields variables, since usually the polarization is adiabatically eliminated. In REMs the spatial dependence is simplified by imposing the Uniform Field Limit (UFL) and/or assuming that the laser operation occurs near the threshold. The solutions of these models show typical relaxation oscillations to a fixed point, e.g. in laser diodes in single-mode operation. As seen in the thesis, in the case of SRLs, these models show a higher dynamic variety due to the presence of two counterpropagating electric fields.

In Chapter III I have presented studies based on REMs. A modified version of the standard model for SRLs taking into account the rotation contribution of the device has been proposed to investigate measuring inertial rotations with a SRL. The main result is that using a SRL as a rotation sensor – gyroscope – is theoretically viable, as it is not necessarily limited by locking effects. The responsivity and noise performance were quite interesting compared to commercial laser gyroscope, taking into account the cost and size benefits of semiconductor laser technology. Also in this chapter, the effects of the spontaneous emission noise in SRLs dynamics were discussed. Specifically the influence of the complex backscattering coefficient and pump current in the dynamics were investigated in the case of a SRL biased in the bidirectional regime. The analysis was carried out by linearizing the model close to a stable stationary

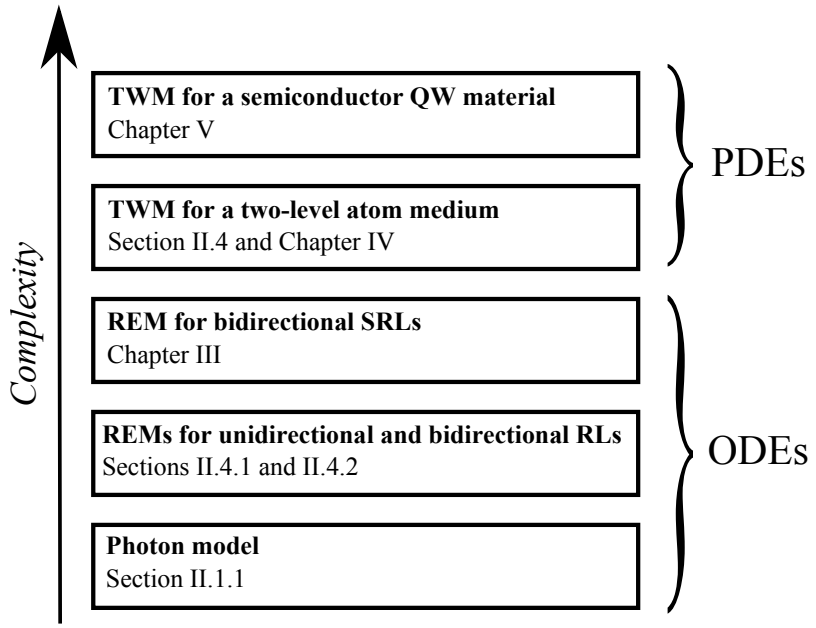

Fig. 6.0.1 – Different models used in the thesis.

solution. At a linear level, perturbations concerning the total intensity and carrier inversion dynamics decouple from the energy distribution processes between the two modes. This fact permits a full analytic analysis, well confirmed by numerical simulations of the complete nonlinear system. The analysis shows that SRLs have peculiar noise properties. The main result is that the energy exchange process between the counter-propagating modes presents a resonance influenced mainly by the backscattering parameters, and interpreted as a 'noisy precursor' of a Hopf bifurcation. This opens the possibility to extract the backscattering parameters from the noise spectra.

Beyond the UFL, the Partial Differential Equations (PDEs) based TWMs describe the longitudinal spatial dependence and they require a temporal description of the response of the active medium. The spatial dependence increases the difficulty in dealing with this type of models; however they allow easily investigating and describing multimode dynamics and spatial effects such as Spatial Hole Burning (SHB) and Four Wave Mixing (FWM). Moreover they are very versatile and can describe different lasers by applying the appropriate boundary conditions to the problem. Tools to analyze these systems have been developed to calculate the monochromatic solutions and their stability. These tools allow to perform direct bifurcation analysis in a more detailed and faster way than using direct numerical time integration of the system of equations. Moreover these techniques can be exported allowing the analysis of other systems based on PDEs. The tools developed in the thesis are the equivalent for PDEs of previously developed tools to analyze other nonlinear systems of equations based on ODEs and Delayed Differential Equations (DDEs), like AUTO [176] or DDEbifTool [177]. In the thesis the TWMs have been classified by the description type of the active medium, the case of the two-level atom being the simplest to treat and the semiconductor the most complex, in particular, I have focused on Quantum Well (QW) materials. The case of the two-level atom, where the simplicity of the active medium allows for a complete temporal description, has been used to develop the tools to analyze and to study multimode dynamics via TWMs. This is done as a first

approximation to the semiconductor devices, however this model does not correctly describe the asymmetric gain curve typical of semiconductor materials as it lacks the strong amplitude-phase coupling denoted by Henry's linewidth enhancement factor α. For the semiconductor medium, QW in particular, the optical response of the medium is described in the frequency domain via mesoscopic approximations that are suitable to describe field dynamics on time scales longer than 1 ps. In the thesis it has been used a Padé approximation of the QW susceptibility to obtain their temporal description, this approach allows to directly use the tools previously developed for the case of the two-level atom.

In Chapter IV the wavelength multistability has been investigated in the case of homogeneously broadened lasers. The purpose of the work was to investigate the impact of the cavity configuration on the possible longitudinal mode multistability. The analysis is based on a general form of a TWM for which a method to evaluate the monochromatic solutions as well as their eigenvalue spectrum was developed. The numerical method consists in using a multidimensional shooting algorithm to find the monochromatic solutions. The linear stability analysis of these solutions is performed using a temporal map that advances the solution one time step including the boundary conditions that allows finding the Floquet matrix that represents the linear operator governing the time evolution for the perturbations around one given monochromatic solution. Finally, the Floquet multipliers that determine the eigenvalues of the system are found. These techniques allow the construction of bifurcation diagrams. The main result found is, in agreement with experimental reports, that multistability is more easily reached in ring than in Fabry-Pérot lasers due to the different amount of SHB in each configuration. Lasing in the Fabry-Pérot configuration requires high-enough facet reflectivities, which generate substantial gain gratings that impede multistability because self-saturation of the modal gain is larger than the cross-saturation. On the other side, ring lasers pass to a regime of almost unidirectional emission where the gain grating is small, and self-saturation is smaller than cross-saturation, thus allowing multistability. Also, it is found that Fabry-Pérot lasers can exhibit multistability if diffusion is strong enough to wash out the grating effectively, then cross-saturation dominates over self-saturation.

Also in Chapter IV the multimode dynamics of a two-level ring laser have been explored numerically using a bidirectional TWM. The numerical algorithm developed is tested reproducing the dynamical results obtained in the single-mode limit previously reported in the literature. The multimode dynamics investigation was focused on the dependence on the detuning of the cavity and the gain bandwidth. Multimode dynamical behaviors previously experimentally reported, e.g. for solid-state ring lasers and fiber ring lasers, were found. The main result is the discovering of dynamical regimes where the emission in each direction occurs at different wavelength. It is found that this bichromatic emission solution can coexist with different multimode behaviors depending on the parameters and the initial conditions. A mode-locked unidirectional regime for large gain bandwidth, that appears without inserting any additional element in the cavity that favors pulsed operation is reported.

In Chapter V an experimental and theoretical work about the modal structure of SRLs with output waveguides has been presented. The purpose of the work was to quantitatively evaluate the coupled cavities effects in SRLs, in order to explain several unexpected reported behaviors such as hysteresis in the lasing direction and atypical lasing mode selection rules. The modal properties were experimentally studied measuring the transfer properties of the device below threshold. The transfer function was theoretically explained by considering the perturbation induced by the light-extraction sections, which induce symmetry breaking in the resonant cavity and

modulation of the cavity losses. Measurements over different devices show that the longitudinal modes possess a doublet structure, with the splitting between the two subpeaks varying from 1 to 4 GHz. In addition, for a particular device, the splitting between the subpeaks usually displays an additional modulation that occurs approximately every three longitudinal modes. I have explained the measured transfer function by including the amplified spontaneous emission in a transfer matrix analysis. Also it was found that the residual reflectivities at the light-extraction sections determine the frequency detuning and threshold difference between the lasing modes. This effect, together with the redshift of the material gain, explains the amount of wavelength jumps displayed by the semiconductor ring laser above threshold.

Chapter V also presents a TWM for QW material, where the material response in the time domain is found using the (1,1) Padé approximation. This allows the use of the tools developed for the case of the two level atom to find the different monochromatic solutions and their stability. Using these tools, results previously reported in literature are found, as multistability between unidirectional and bidirectional solutions, and wavelength multistability. This part, far from a rigorous analysis of the dynamics of SRL, simply shows that the tools developed previously can be helpful in the case of the TWM for QW material. Also in Chapter V I present the demonstration of a new laser based on a modified ring geometry to obtain unidirectional emission, the semiconductor snail laser. The experimental L-I curves of the new device were theoretically reproduced by using a TWM with the coupled cavities effects taken into account. This work exploits the modular character of the TWM.

In summary, two types of models were used in the thesis to study certain characteristics of SRLs. On one side, the REMs have been used to study the spontaneous emission noise properties. And on the other side, a TWM model was developed for a two level atom medium and for QW material. The relative simplicity of the two level atom medium TWM allowed to develop numerical tools or techniques for the analysis and dynamic simulation of TWMs. These techniques allowed analyzing the multimode dynamics and wavelength multistability of the TWM for a two level atom. It has also been shown that these techniques can be used in case of TWM for a QW material, finding wavelength multistability.

The next step is an in-depth analysis of the dynamics and wavelength multistability in SRLs using the TWM. The wavelength multistability is a peculiar feature of SRLs that can be exploited in different ways, e.g. for all-optical signal processing, memory cells, routing in WDM systems, etc. In the future, the plan is to use the tools developed in the thesis to characterize the wavelength multistability and the physical mechanisms that allow it. Also it is planned to adapt the tools developed here to be applied in recently proposed TWMs [120] – based on the calculation of the convolution between the susceptibility of the QW and electric fields – because they offer a better description of the physical processes taking place in the SRL. In Appendix B are found other ways to perform the LSA of the TWM, without using the evolution operator, which can be particularly useful for these new TWMs. Another aspect that I want to exploit in the future, is the modular character of the TWM. This allows the connection of different parts – e.g. waveguides, mirrors, different lasers, saturable absorber sections, Bragg gratings – and the modeling of different laser cavities after minimum modifications. The tools developed in the thesis will be used to study the coupled-cavity effects and the impact of including elements like saturable absorbers or DBRs. Finally, these tools will be helpful to propose new structures based on SRLs for specific applications.

A

Nonlinear dynamical systems

In this appendix are described the basics of nonlinear dynamics and bifurcation theory. Lasers are pumped dissipative systems, this type of systems are not usually in a time-independent state. In general they are in a dynamic state, and the time-dependent change of their variables can be periodic, multiperiodic, or even chaotic. To characterize these behaviors one uses the general concepts of nonlinear dynamics, like the steady states or the Linear Stability Analysis (LSA), they are discussed in the following. On the other hand, the understanding of the laser nonlinear dynamics is done by the construction of bifurcation diagrams. These bifurcation diagrams are constructed by mapping the various steady and oscillating regimes while one – or several – control parameters are varied. This approach has been very successful when one compares the experimental data with the theoretical model. The combination of using the LSA for constructing bifurcation diagrams gives a much quicker and better prediction of the long term dynamics, than the obtained from the direct numerical time integration of the laser system.

A.1 Dynamical stability

Rate equations (RE) models for describing lasers dynamics are a set of Ordinary Differential Equations (ODEs) involving first-order time derivatives. Of course, spatial dependence also exists, but will be not considered here. In general, one can write a dynamical system as

$$\frac{d\vec{x}}{dt} = \vec{F}_{\vec{\mu}}(\vec{x}, t) \ , \qquad \text{A.1.1}$$

where the time dependent vector $\vec{x} = (x_1, \ldots, x_n)$ represent the n dynamical variables describing the system, its evolution defines a trajectory or orbit of the system in the phase-space defined by these variables. The vector function $\vec{F}_{\vec{\mu}}$, depends on several control parameters $\mu_1, \ldots, \mu_p$ that characterize each specific set of experimental conditions.

When the vector function $\vec{F}_{\vec{\mu}}$ does not explicitly depend on time, the system is called *Autonomous*,

$$\frac{d\vec{x}}{dt} = \vec{F}(\vec{x}) \ , \qquad \text{A.1.2}$$

where the vector $\vec{\mu}$ on $\vec{F}$ has been omitted for simplicity. Lasers are autonomous systems, except when a time-modulated external influence is introduced. Given an initial condition $\vec{x}(t = 0) = \vec{x}\ ^0$ is well known that equations such as Eq. (A.1.2) have a unique solution. this means that trajectories in the phase-space never intersect. The only exception to this rule are the *singular points*, at which several trajectories can eventually end (or begin).

A.1.1 Stationary solutions

The stationary solutions of Eq. (A.1.2) are those satisfying

$$\frac{d\vec{x}}{dt} = F(\vec{x}) = 0 \ , \tag{A.1.3}$$

therefore, they remain constant in time,

$$\vec{x}(t) = \vec{x}^{\,0} \ . \tag{A.1.4}$$

For this reason they are also known as *fixed points* in the phase-space. With respect to stability of a fixed point, three kinds of behaviors can be distinguished:

- A stationary solution or fixed point is *stable* (or *asymptotically stable*) if any other solution originating close to $\vec{x}^{\,0}$ approaches it asymptotically, i.e. when any small perturbation added to the stationary solution damps with time. Depending on the way in which the perturbation damps with time, two kinds of stable fixed points are distinguished: *node* and *focus*. In a *node* the damping has an exponential form, instead in a *focus* it shows oscillations around the fixed point, e.g. relaxation oscillations in lasers.

- A fixed point $\vec{x}^{\,0}$ is *marginally stable* (or a *center*) if any other solution originating close to $\vec{x}^{\,0}$ remains there forever, i.e. when any small perturbation neither damps nor amplifies with time.

- Finally, a fixed point $\vec{x}^{\,0}$ is *unstable* if it is neither stable nor marginally stable. If any trajectory originating close to $\vec{x}^{\,0}$ goes away, it is called a *source*, but if some of the trajectories (those going along a certain direction) converge towards $\vec{x}^{\,0}$, then is known as a *saddle point*.

A.1.2 Periodic solutions

A *periodic orbit* or *limit cycle* is a solution of Eq. (A.1.2) that satisfies

$$\vec{x}(t+T) = \vec{x}(t) \ , \tag{A.1.5}$$

for all t and $0 < T < \infty$, where T represent the period. The concepts of stability, marginal stability and instability are identical with those given for a fixed point.

A.1.3 Linear stability analysis

The stability behavior of a stationary or periodic solution is related to the time evolution of small perturbations, therefore it can be determined through a linearization of the set of Eqs. (A.1.2) around the stationary or periodic solution. This method is known as the *linear stability analysis*, which in the case of a periodic solution gives rise to the *Floquet theory*.

Let $\delta\vec{x}(0)$ be a small perturbation added at $t = 0$ to a stationary or periodic solution $\vec{x}^{\,0}(t)$ ($\vec{x}^{\,0}(t) = \vec{x}^{\,0}$ in the stationary case and $\vec{x}^{\,0}(t) = \vec{x}^{\,0}(t+T)$ in the periodic case). The time evolution of the perturbation $\delta\vec{x}(t)$, for $t \geq 0$ can be found by introducing in Eq. (A.1.2) the whole solution

$$\vec{x}(t) = \vec{x}^{\,0}(t) + \delta\vec{x}(t) \ . \tag{A.1.6}$$

If the resulting set of equations is linearized with respect to $\delta\vec{x}(t)$, i.e. ignoring all the non-linear terms, it yields

$$\frac{d\delta\vec{x}(t)}{dt} = J(t)\delta\vec{x}(t) \ , \qquad \text{A.1.7}$$

where $J(t) = [\partial J_i/\partial x_j]_{\vec{x}=\vec{x}\ ^0(t)}$ represents the $n \times n$ matrix of the partial derivatives of the function F of Eq. (A.1.2) with respect to the variables x_n, performed at the point $\vec{x} = \vec{x}\ ^0(t)$. The matrix $J(t)$, called the Jacobian, is constant in the case of a stationary solution, whereas it is periodic (with period T) in the case of a periodic orbit. The set of linear differential equations (A.1.7) has a set of n complex solutions of the form

$$\delta\vec{x}\ ^{(i)}(t) = e^{\lambda_i t}\vec{v}\ ^{(i)}(t) \quad \text{where} \quad i = 1, \ldots, n \ , \qquad \text{A.1.8}$$

where i denotes each one of the solutions, λ_i represents the corresponding characteristic exponent, which has a multiplicity m_i that satisfies $0 < m_i \leq n$, $\sum_{i=1}^{n} m_i = n$, and the vectors $\vec{v}\ ^{(i)}(t)$ are polynomials in t whose highest power is smaller than m_i, i.e.

$$\vec{v}\ ^{(i)}(t) = \vec{v}_0\ ^{(i)}(t) + \vec{v}_1\ ^{(i)}(t)t + \cdots + \vec{v}\ ^{(i)}_{m_i-1}(t)t^{m_i-1} \ . \qquad \text{A.1.9}$$

In the fixed point case, the characteristic exponents λ_i and the vectors $\vec{v}\ ^{(i)}$ are the eigenvalues and the eigenvectors of the constant matrix J respectively. Whereas in the closed orbit case the λ_i are the eigenvalues of a matrix Λ which defines the time periodicity of any solution of Eq. (A.1.7),

$$\delta\vec{x}\ ^{(i)}(t+T) = e^{\Lambda T}\delta\vec{x}\ ^{(i)}(t) \ , \qquad \text{A.1.10}$$

and $\vec{v}\ ^{(i)}(t)$ are T-periodic vectors. The matrix $e^{\Lambda T}$ is known as the Floquet matrix.

The temporal evolution of the initial perturbation $\delta\vec{x}(0)$ is basically ruled by the characteristic exponents λ_i. In particular, $\mathrm{Re}\{\lambda_i\}$ determines the stability behavior of the fixed point or the periodic orbit: if the real parts of all the λ_i are negative then $\vec{x}\ ^0(t)$ is stable, whereas if at least one of these real parts is positive then it is unstable. In the case of a closed orbit there is always an exponent equal to zero, which corresponds to a perturbation along the closed orbit, i.e. phase invariance.

Additional information can be obtained from the characteristic exponents λ_i and vectors $\vec{v}\ ^{(i)}(t)$. For instance, in the case of a fixed point $|\mathrm{Re}\{\lambda_i\}|$ represents the rate at which a small initial perturbation $\vec{v}\ ^{(i)}(t) + \vec{v}\ ^{(i)}(t)^*$ increases ($\mathrm{Re}\{\lambda_i\} > 0$) or decreases ($\mathrm{Re}\{\lambda_i\} < 0$) with time. $|\mathrm{Im}\{\lambda_i\}|$ is the angular frequency at which a small initial perturbation $\vec{v}\ ^{(i)}(t) + \vec{v}\ ^{(i)}(t)^*$ spiral around a stable or unstable focus $\vec{x}\ ^0$, if $\mathrm{Im}\{\lambda_i\} = 0$, then the fixed point is a node instead of a focus. Finally, $\vec{v}\ ^{(i)}(t) + \vec{v}\ ^{(i)}(t)^*$ represents the perturbation whose temporal evolution is exclusively ruled by the exponent λ_i.

The stability behavior of a closed orbit can also be characterized through the eigenvalues ξ_i of the Floquet matrix $e^{\Lambda T}$, which are also known as the *Floquet multipliers*. The closed orbit is stable if all the multipliers lie inside a circle of radius unity in the complex plane (except one of them which is strictly equal to unity), whereas is unstable if at least one multiplier lies outside the circle.

A.2 Bifurcations

Usually, a small variation in one or several parameters produces small (continuous) changes in the position and shape of all the attractors of the system in the phase space. If a one-to-one mapping between each possible trajectory before and after the small variation can be established, the system is said to be *structurally stable*. However, for some specific parameters values, one of the attractors or solutions may suffer a strong qualitative change which prevents such a one-to-one mapping. An example is when a fixed point transforms into two close fixed points. This is called a *bifurcation* and the system is said to be *structurally unstable* in this point.

Here only the different kinds of bifurcations that appear in this thesis are considered, for a more detailed description about bifurcations see for example [178] or [179]. These bifurcations are called local codimension-one bifurcations. *Local* means that the qualitative changes affecting the bifurcation can be analyzed by studying only the region of the phase space close to the solution. The term codimension-one is referred to bifurcations that satisfy the following: (1) they can be found by varying only one (any one) of the control parameters of the system, and (2) a change in any one of the remaining parameters does not cause the bifurcation to disappear, produces only a smooth change of the bifurcation features. Writing Eq. (A.1.2) in its simplest form

$$\frac{dx}{dt} = F(x) \ , \tag{A.2.11}$$

supposing $x \in \mathbb{R}$, the simplest example of bifurcation is the saddle-node bifurcation, Fig. A.2.1 (a). In this case $F(x) = \mu - x^2$, searching for the stationary solution of (A.2.11), one obtains two solutions, one stable and the other unstable.

In the case of a transcritical bifurcation, $F(x) = \mu x - x^2$, the two solutions interchange its stability at point $\mu = 0$, see Fig. A.2.1 (b). This is the case of the laser threshold.

Other bifurcation that it is found as a characteristic of the bidirectional ring laser behavior is the pitchfork bifurcation, $F(x) = \mu x - x^3$. In this case three solutions appear, one of them unstable, see Fig. A.2.1 (c).

Finally, if $x \in \mathbb{C}$ one has the Hopf bifurcation, $F(x) = (\mu + ic) - x|x|^2$ where c is an arbitrary constant. In this case, one fixed point solution bifurcates to a limit cycle. For a given value of μ the $|x|$ is conserved while the phase changes with time, i.e. $\phi\{x\}(t) = \phi\{x\}(t+T)$).

The above described bifurcations are called *supercritical* or *normal* bifurcations. In these bifurcations the nonlinear term is opposite to the constant or linear term. By changing the sign of the nonlinear term one find the *subcritical* or *inverse* bifurcations.

These bifurcations appear in the thesis in many different ways. For example, the RE model described in III.1, varying the pump current parameter μ as shown in Fig. 3.1.1, we found a transcritical bifurcation at $\mu = 1$ that marks the beginning of the laser operation in a bidirectional solution. Further increasing the pump, near $\mu \sim 1.5$ a Hopf bifurcation takes place. While the oscillating solutions are stable after the Hopf bifurcation point, the remaining unstable branch birfurcates through a pitchfork at $\mu \sim 2$. Suddenly at $\mu \sim 1.2$ there is a stability change between the oscillating solutions and those coming from the pitchfork bifurcation. An example of a subcritical pitchfork bifurcation can be found in section V.2.

In the case treated in section IV.5, the bifurcation scenario becomes more complex. When multistability is possible, the different stable modes have different basins of attraction depending on the parameters of the system. Moreover, these solutions can

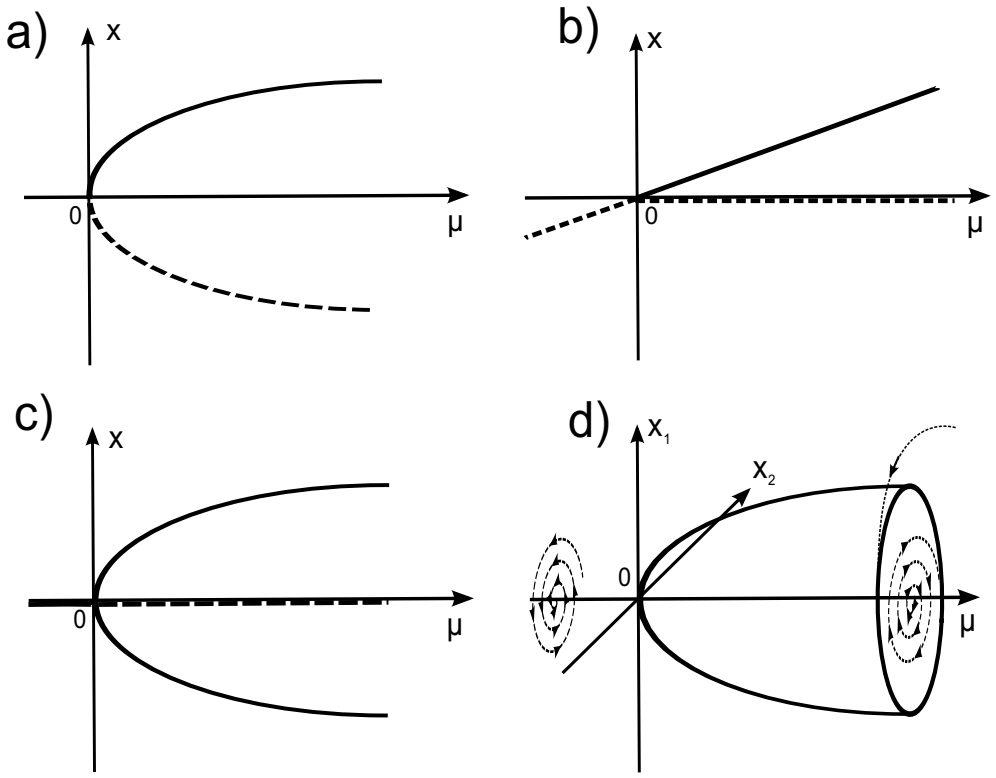

Fig. A.2.1 – (a)A saddle-node bifurcation. $F(x) = \mu - x^2$. (b) A transcritical (or with stability change) bifurcation. $F(x) = \mu x - x^2$. (c) A pitchfork bifurcation. $F(x) = \mu x - x^3$. (d) A Hopf bifurcation. $F(x) = (\mu + ic) - x|x|^2$, where $x = x_1 + ix_2$.

coexists with other solutions that involve the presence of multiple solutions or modes. In this case, the global bifurcation scenario is impossible to be fully characterized.

B
Numerical Algorithms

In this appendix are described the numerical methods used along this thesis. However, the description of some used standard algorithms as the fourth order Runge-Kutta algorithm to solve Ordinary Differential Equations (ODEs), the Newton-Raphson multidimensional root finder or the LU decomposition method to solve linear systems of equations among others are not described here. They can be found in the literature (see for example [149]).

The first algorithm presented is the Heun's algorithm for Stochastic Differential Equations (SDEs). It is used in the simulations of section III.3, where the noise terms model the spontaneous emission of the laser. The following algorithms are those used to perform the spatiotemporal integration, the evaluation of the monochromatic solutions, and the stability of these solutions of the Traveling Wave Model (TWM). Here different methods to perform the Linear Stability Analysis (LSA) are presented. Finally, the advantages and disadvantages of the different methods presented are discussed.

B.1 Heun's algorithm for SDEs

The Heun's algorithm is a method to solve SDEs based on the order two Runge-Kutta method for ODEs. The advantage of this method is that the deterministic part has a convergence of order h^3, therefore, it avoids some instabilities typical of the Euler method. A generic SDE has the following expression for a dynamical variable $x(t)$,

$$\frac{dx(t)}{dt} = q(x,t) + g(t,x)\xi_w(t) \ ,$$

where $q(x,t)$ and $g(x,t)$ are functions, linear or non linear, and $\xi_w(t)$ is a white gaussian noise, which properties are

$$\langle \xi_w(t)\xi_w(t')\rangle = 2D\delta(t-t') \ .$$

When function $g(t,x)$ is independent of x, one talks about additive noise, otherwise, the noise is said to be multiplicative. A possible algorithm [140] to solve the SDE is

$$\begin{array}{rcl} x(t+h) & = & x(t) + \frac{h}{2}\left[q(t,x(t)) + q(t+h, x(t)+l+k)\right] \\ & + & \frac{1}{2}h^{1/2}u(t)\left[g(t,x(t)) + g(t+h, x(t)+k+l)\right] \end{array} \ , \qquad \text{B.1.1}$$

where

$$\begin{array}{rcl} k & = & hq(t,x(t)) \ , \\ l & = & h^{1/2}u(t)g(t,x(t)) \ , \end{array}$$

where h is the temporal step and $u(t)$ is a independent set of random Gaussian numbers with zero mean value and variance equal to one. To compute the random Gaussian numbers, algorithms described in [145] and [149] are used.

B.2 Spatiotemporal integration of the TWM

The TWM is a set of Partial Differential Equations (PDEs). The numerical treatment using finite differences of PDEs is not an easy task. Depending on the problem treated some finite differences schemes can be more accurate than others, and in the worst case can give wrong results if the numerical scheme is unstable.

The stability of numerical schemes is closely associated with numerical error. A finite difference numerical scheme is stable if the errors made at one time step of the calculation do not cause the errors to increase (remain bounded) as the computations are continued. A neutrally stable scheme is one in which errors remain constant as the computations are carried forward. If the errors decay and eventually damp out, the numerical scheme is said to be stable. If, on the contrary, the errors grow with time the solution diverges and thus the numerical scheme is said to be unstable. The stability of numerical schemes can be investigated by performing von Neumann stability analysis [149].

The von Neumann stability analysis (also known as Fourier stability analysis) is a procedure used to verify the stability of finite difference schemes as applied to PDEs. The analysis is based on the Fourier decomposition of the numerical error and it was briefly described first in 1947 article by Crank and Nicolson [180]. Later, it was also published in an article co-authored by von Neumann [181].

For time-dependent problems, stability guarantees that the numerical method produces a bounded solution whenever the solution of the exact differential equation is bounded. Moreover, one has to assure that the time and space steps are appropriate. For this reason, one follows the Courant-Friedrichs-Lewy condition or CFL condition [149], which is a condition for convergence while solving certain partial differential equations (usually hyperbolic PDEs) numerically. It arises when explicit time-marching schemes are used for the numerical solution. As a consequence, the time step must be less than a certain time in many explicit time-marching computer simulations, otherwise the simulation will produce incorrect results. For example, if a wave is crossing a discrete grid, then the time step must be equal than the time for the wave to travel adjacent grid points. As a corollary, when the grid point separation is reduced, the upper limit for the time step also decreases. In essence, the numerical domain of dependence must include the analytical domain of dependence in order to assure that the scheme can access the information required to form the solution. In this case the CFL condition is given by $\Delta\tau = \Delta s = h$.

The numerical algorithm used to perform the simulation of the normalized system of equations (4.1.1)-(4.1.4) is based in the one presented by Fleck in [167]. This algorithm is strongly stable and gives small errors for high frequencies after applying the von Neumann analysis. Moreover it takes advantage of the fact that the equations for the fields can be solved formally in terms of integrals of the polarizations. One discretizes time with time step h, hence the spatial grid has also discretization step h, following the CFL condition. All spatial points $n = 1, ..., N$ are internal, with the first and last points located at $h/2$ from the nearest end (see Fig. B.2.1). We denote by X_j^n the value of variable X at time $\tau = nh$ and gridpoint $s = jh$. The mid-point discretization scheme for the fields is used [167], so they are updated according to

$$A_{+\,j}^{n+1} = \frac{1-q}{1+q} A_{+\,j-1}^{n} + p(B_{+\,j-1}^{n} + B_{+\,j}^{n+1}) \,, \qquad \text{B.2.2}$$

$$A_{-\,j}^{n+1} = \frac{1-q}{1+q} A_{-\,j+1}^{n} + p(B_{-\,j+1}^{n} + B_{-\,j}^{n+1}) \,, \qquad \text{B.2.3}$$

where $q = \alpha h/2$, $p = (h/2)(1+q)^{-1}$. For the polarizations one has

$$\begin{aligned} B_{\pm\ j}^{n+1} &= \mu B_{\pm\ j}^{n} + \nu D_{0\ j}^{n+1/2}(A_{\pm\ j}^{n+1} + A_{\pm\ j}^{n}) \\ &+ \nu D_{\pm 2\ j}^{n+1/2}(A_{\mp\ j}^{n+1} + A_{\mp\ j}^{n}) + \sqrt{\beta h D_0}\ \xi_{\pm}\ , \end{aligned} \tag{B.2.4}$$

where $\mu = [1-(\gamma h/2)(1+i\widetilde{\delta})][1+(\gamma h/2)(1+i\widetilde{\delta})]^{-1}$ and $\nu = (gh\gamma/2)[1+(\gamma h/2)(1+i\widetilde{\delta})]^{-1}$, and where the next approximation has been used

$$\int_t^{t+\Delta t} D_k(t)A_l(t)dt \simeq \Delta t\ D_k\left(t+\frac{\Delta t}{2}\right)\frac{A_l(t+\Delta t)+A_l(t)}{2}\ .$$

At this point noticing that Eq. (B.2.4) needs the values of the carriers (D_0 and $D_{\pm 2}$) at intermediate time steps, hence one uses a temporal grid for the carrier densities which is staggered by half a time step from the fields and polarizations. This is different from the original algorithm in [167], where the carriers are on the same temporal grid than the fields and the polarizations and then interpolation is used to evaluate the carriers at the intermediate times needed in (B.2.2)-(B.2.4). In this case, the finite difference equations for carriers are thus

$$\begin{aligned} D_{0\ j}^{n+3/2} &= \rho D_{0\ j}^{n+1/2} + \theta J \\ &- \theta(A_{+\ j}^{n+1}B_{+\ j}^{*\ n+1} + A_{-\ j}^{n+1}B_{-\ j}^{*\ n+1} + c.c.)\ , \end{aligned} \tag{B.2.5}$$

$$\begin{aligned} D_{\pm 2\ j}^{n+3/2} &= \rho D_{\pm 2\ j}^{n+1/2}\ , \\ &- \theta\left(A_{\pm\ j}^{n+1}B_{\mp\ j}^{*\ n+1} + A_{\mp\ j}^{*\ n+1}B_{\pm\ j}^{n+1}\right)\ . \end{aligned} \tag{B.2.6}$$

where $\rho = \left(1+\frac{\epsilon h}{2}\right)\left(1-\frac{\epsilon h}{2}\right)^{-1}$ and $\theta = \epsilon h\left(1-\frac{\epsilon h}{2}\right)^{-1}$.

B.2.1 Boundary conditions

In order to impose the general boundary conditions (4.1.8) and (4.1.9), one has to consider that the fields propagate during half a step, then experience partial reflection and transmission and then they propagate for another half a step. In addition, recalling the ring structure of the system hence points $j = 1$ and $j = N$ are connected through the boundary conditions. This procedure for A_+ and A_- is implemented as follows:

- Step (1): One uses an explicit Euler method to compute the value of the fields just before arriving at boundary by propagating the fields over half a step

$$\begin{aligned} A_{+\ N+1/2}^{\ n+1/2} - (1-q)A_{+\ N}^{\ n} &= \tfrac{h}{2}B_{+\ N}^{\ n}\ , \\ A_{-\ 1/2}^{\ n+1/2} - (1-q)A_{-\ 1}^{\ n} &= \tfrac{h}{2}B_{-\ 1}^{\ n}\ . \end{aligned} \tag{B.2.7}$$

- Step (2): One applies the boundary conditions and compute the fields just after the boundary, which are denoted as $\widetilde{A}_+$ and $\widetilde{A}_-$

$$\begin{aligned} \widetilde{A}_{+\ 1/2}^{\ n+1/2} &= t_+ A_{+\ N+1/2}^{\ n+1/2} + r_- A_{-\ 1/2}^{\ n+1/2}\ , \\ \widetilde{A}_{-\ N+1/2}^{\ n+1/2} &= t_- A_{-\ 1/2}^{\ n+1/2} + r_+ A_{+\ N+1/2}^{\ n+1/2}\ . \end{aligned} \tag{B.2.8}$$

- Step (3): Finally one uses the implicit Euler method for the remaining half a step to calculate the value of the fields at time $n+1$

$$\begin{aligned} (1+q)A_{+\ 1}^{n+1} - \widetilde{A}_{+\ 1/2}^{n+1/2} &= \tfrac{h}{2}B_{+\ 1}^{n+1}\ , \\ (1+q)A_{-\ N}^{n+1} - \widetilde{A}_{-\ N+1/2}^{n+1/2} &= \tfrac{h}{2}B_{-\ N}^{n+1}\ , \end{aligned} \tag{B.2.9}$$

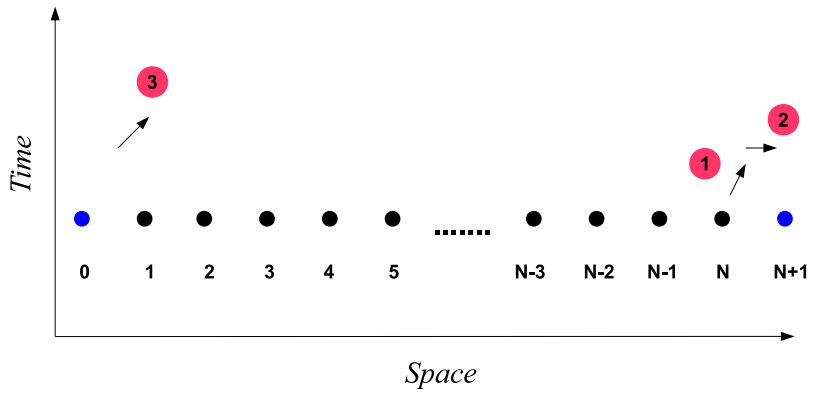

Fig. B.2.1 – Schematic representation of spatial discretization and the implementation of the boundary conditions for the A_+ electric field. In three steps: (1) Half step explicit Euler. (2) Boundary Conditions. (3) Half step implicit Euler. The mesh is composed by N points and N intervals and two auxiliar points at 0 and $N+1$ added for the implementation.

Note that these procedure can be very efficiently implemented by adding to the spatial grid two auxiliary points $j = 0$ and $j = N + 1$ (see Fig. B.2.1) located half a step away from the facets where the fields and polarizations are

$$\begin{array}{rcl} {A_+}^n{}_0 & = & t_+ {A_+}^n{}_N + r_- {A_-}^n{}_1 \ , \\ {B_+}^n{}_0 & = & t_+ {B_+}^n{}_N + r_- {B_-}^n{}_1 \ , \\ {A_-}^n{}_{N+1} & = & t_- {A_-}^n{}_1 + r_+ {A_+}^n{}_N \ , \\ {B_-}^n{}_{N+1} & = & t_- {B_-}^n{}_1 + r_+ {B_+}^n{}_N \ , \end{array} \qquad \text{B.2.10}$$

and updating the fields by means of the standard mid-point integration

$$\begin{array}{rcl} {A_+}^{n+1}{}_1 & = & \frac{1-q}{1+q} {A_+}^n{}_0 + p({B_+}^n{}_0 + {B_+}^{n+1}{}_1) \ , \\ {A_-}^{n+1}{}_N & = & \frac{1-q}{1+q} {A_-}^n{}_{N+1} + p({B_-}^n{}_{N+1} + {B_-}^{n+1}{}_N) \ . \end{array} \qquad \text{B.2.11}$$

Noticing that this algorithm and the procedure of implementing the boundary conditions is very versatile, and it can be applied to different geometries, for example, the snail laser discussed in section V.3. In that section this spatiotemporal integration of the TWM defining three waveguides (two passive and one active) and a point coupler was used. The equivalent expressions of (B.2.10) for a lossless without any reflective element point coupler can be written as

$$\begin{array}{rcl} {A_-}^1{}_{N+1} & = & i\delta {A_-}^4{}_1 + \rho {A_-}^2{}_1 \ , \\ {B_-}^1{}_{N+1} & = & i\delta {B_-}^4{}_1 + \rho {B_-}^2{}_1 \ , \\ {A_+}^2{}_0 & = & i\delta {A_+}^3{}_N + \rho {A_+}^1{}_N \ , \\ {B_+}^2{}_0 & = & i\delta {B_+}^3{}_N + \rho {B_+}^1{}_N \ , \\ {A_-}^3{}_{N+1} & = & i\delta {A_-}^2{}_1 + \rho {A_-}^4{}_1 \ , \\ {B_-}^3{}_{N+1} & = & i\delta {B_-}^2{}_1 + \rho {B_-}^4{}_1 \ , \\ {A_+}^4{}_0 & = & i\delta {A_+}^1{}_N + \rho {A_+}^3{}_N \ , \\ {B_+}^4{}_0 & = & i\delta {B_+}^1{}_N + \rho {B_+}^3{}_N \ , \end{array} \qquad \text{B.2.12}$$

where the superindex denotes the waveguide number, δ^2 is the power extraction efficiency and $\rho = \sqrt{(1-\delta^2)}$. A schematic representation of the point coupler is shown in Fig. B.2.2. One has to define a positive sign that indicates the sign of the propagating electric fields and polarizations in the + direction. The temporal update of the

fields is done with the standard mid-point integration (B.2.11) for every waveguide. In the case of the snail laser the waveguide #4 and #1 are the same one, as shown in Fig. 5.3.20 (inset). Another example of the versatility of the algorithm is that it

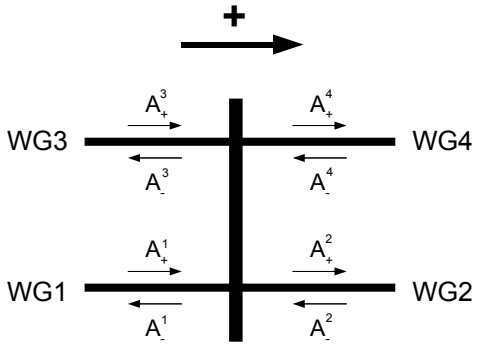

Fig. B.2.2 – Schematic representation of the point coupler. In order to be consistent with the algorithm for integrating the TWM, four waveguides are needed (denoted WG in the figure). The superindex in the counter-propagating electric fields $A_\pm$ indicate the waveguide number.

allow us to implement a laser with saturable absorbers sections by combining different waveguides (passive or active) or by giving a spatial profile of the parameters, in this case the pump current.

B.3 Monochromatic solutions of the TWM: The shooting method

The Shooting method is an iterative method that allow to calculate numerically the spatial profile of the monochromatic solutions of the set (4.1.1)-(4.1.4). It allow us compute L-I curves and bifurcation diagrams in a quicker way than from the spatiotemporal integration scheme. Using the spatiotemporal integration scheme one has to wait a transient time (that varies depending on the parameters of the system and in the proximity of a bifurcation) to obtain the steady state. Therefore, the construction of a bifurcation diagram can cost a long time, longer if one retains the spatial dependence. Fig. 3.1.1 was constructed in this way. Instead, using a Shooting method allow to compute the bifurcation diagrams very quickly because one assumes a time dependence of the variables (see (4.3.18)). The difference between the two approaches is that the shooting method computes the monochromatic solutions of the fields even if they are unstable, whereas using the integration scheme only stable solutions appear even if they are periodic solutions or they involve different modes.

As in the previous algorithm, the same discretization is followed, with j denoting the spatial points $j = 1, ..., N$. The method consists in provide a guess for the fields $A_\pm^{st}(j = 1)$. This guess is used to solve the system (4.3.31) via a LU decomposition method [149]. After solving the system we obtain $\vec{x}_{j=1}^{ST}$. Then one integrates Eq. (4.3.19) using its formal solution,

$$A_\pm(s+\Delta s) = \left[A_\pm(s) \pm \int_s^{s+\Delta s} dx\ P_\pm e^{\mp(i\widetilde{\omega}-\alpha_{int})x}\right] e^{\pm\Delta s(i\widetilde{\omega}-\alpha_{int})}\ , \qquad \text{B.3.13}$$

After integration one obtains $A_\pm^{st}(j = 2)$. This process is iterated until one gets $A_\pm^{st}(j = N)$.

The next step is to verify if the guess $A^{st}_{\pm}(j=1)$ and the calculated fields $A^{st}_{\pm}(j=N)$ fulfill the boundary conditions. If they are fulfilled one haa the spatial profile of a monochromatic solution, i.e. $A^{st}_{\pm}(s)$, $B^{st}_{\pm}(s)$, $D^{st}_{0}(s)$ and $D^{st}_{\pm 2}(s)$. If the boundary conditions are not verified a new guess is proposed from the roots found by the Newton-Raphson method, and the whole process is repeated until convergence is reached. A scheme of the shooting method is depicted in Fig. B.3.3.

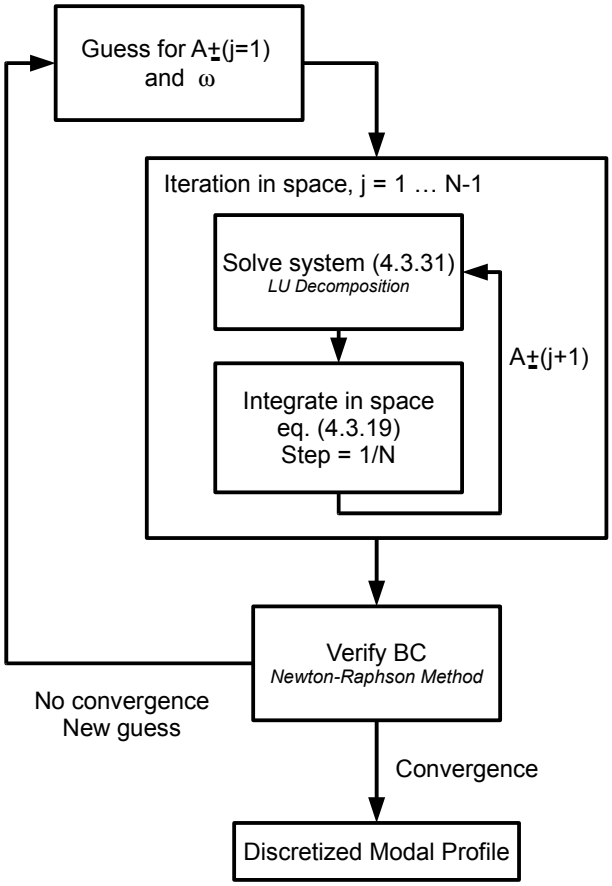

Fig. B.3.3 – Schematic representation of the shooting Method to obtain the monochromatic solutions spatial profile.

B.4 Linear stability analysis of the TWM

From the monochromatic solutions obtained by the shooting method, one could in principle compute the eigenvalues from the linearized form of (4.1.1)-(4.1.4) with (4.4.59). However, the resulting system is still a hyperbolic PDE, and a discrete representation of the solution would require to express the gradient operator using finite differences. This approach is not practical and it leads to large errors in the eigenvalues. Therefore, one has to find another strategy to obtain the eigenvalues of the system.

In this section the different methods to perform the LSA of the system are described and discussed. First, a method that takes profit of the fact that for a two level atom medium the TWM can be fully represented in the time-domain without any approximation of the polarization and field relation is presented. It will use the spatiotemporal integration scheme presented in B.2 for (4.1.1)-(4.1.4) to construct an evolution operator from which one can extract the eigenvalues of the system. However, this method can be difficult to apply in the semiconductor case, and it depends on the approach that one uses to model the response of the semiconductor medium. The problem resides that the time computation of the QR decomposition goes with N^3. Using the Padé approximation for the semiconductor susceptibility [101] this method can be applied (see section V.2), because one has a similar system to the two-level atom. However, this Padé approximation can have problems in some cases, e.g. when one introduces a saturable absorber. The convolution method used to approximate the semiconductor susceptibility [120] is better than the Padé approximation, but it involves a large number of variables that makes the QR decomposition not possible.

This has motivated the search for other methods that do not need the evolution operator. These methods are the homotopy method and Cauchy's theorem method. These methods are used instead of other used standard methods as the IRAM (Implicit Restarted Arnoldi Method), because in our case the eigenvalues are almost degenerated due to the large bandwidth of the gain curve and the doublet structure found in ring lasers. In this case the standard methods show a poor converge.

In the following, we check the homotopy and Cauchy's theorem methods in front of the evolution operator method for the TWM for a two level atom medium. Noticing at this point that by construction of the methods, one will find the double of eigenvalues as a consequence of using real matrices and using the complex conjugates of the variables to solve the problem.

B.4.1 Evolution operator method

In the case of the TWM for a two-level atom (chapter IV), one can use the fact that the Eqs. (4.1.1)-(4.1.4) can be written in time domain. This allow to use the temporal map $\vec{V}_{j+1} = \vec{U}(h, \vec{V}_j)$ formed by Eqs. (B.2.2)-(B.2.6) and (B.2.10) that advances the state vector $\vec{V}$ a time step h while verifying the CFL condition [150] and canceling numerical dissipation. Considering all possible perturbations of $\vec{V}$ hereby finding the matrix $\mathbf{M} = \partial\vec{U}/\partial\vec{V}$ representing the linear operator governing the time evolution for the perturbations around one given monochromatic solution: $A^{st}_{\pm}(s)$, $B^{st}_{\pm}(s)$, $D^{st}_{0}(s)$ and $D^{st}_{\pm 2}(s)$.

Numerically, one separates the perturbations $\widetilde{a}_{\pm}(s)$, $\widetilde{b}_{\pm}(s)$ and $\widetilde{d}_{+2}(s)$ in real and imaginary parts, one uses the fact that $\widetilde{d}_{-2}(s) = \widetilde{d}_{+2}(s)*$ and that the $\widetilde{d}_{0}(s)$ is real. Then a number of 11 variables for each point space is treated. Taking into account the spatial discretization, the total number of variables is $11 \times N$.

To obtain the evolution operator $\mathbf{M}$, a $(11 \times N) \times (11 \times N)$ matrix, one calculates each row by introducing a perturbation, i.e. one of the $11 \times N$ variables is set to 1 whereas the others are zero. Then this state is evolved over one time step according to section B.2 and taking into account the monochromatic solutions calculated by the shooting method. This process is repeated for all variables, obtaining $\mathbf{M}$. One finally computes the $11 \times N$ Floquet multipliers z_n of $\mathbf{M}$ via a QR decomposition method, which determine the eigenvalues as $\lambda_n = h^{-1} \ln z_n$. An schematic representation of the evolution operator method is depicted in Fig. B.4.4.

If one of these computed eigenvalues has a positive real part, then one concludes that this monochromatic solution is unstable. If none of them has a positive real part, then the monochromatic solution is stable. Noticing that using this approach for computing the stability of a monochromatic solution different from the off solution will always give a zero eigenvalue corresponding to the phase invariance of the system.

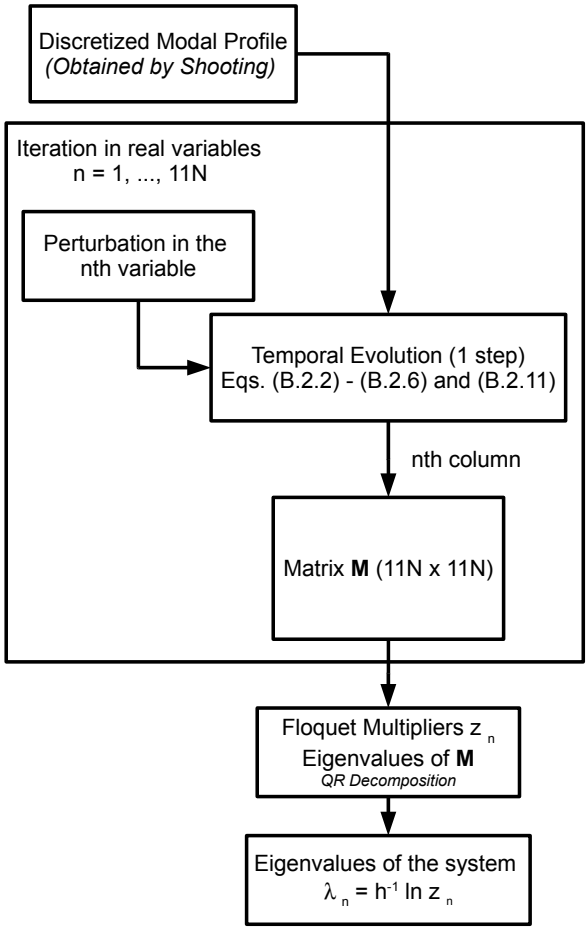

Fig. B.4.4 – Schematic representation of the LSA numerical method, using the evolution operator.

B.4.2 Homotopy method

Another strategy that can be used to compute the stability of a monochromatic solution of the system without using the evolution operator is the homotopy method. This method consists first in calculate the eigenvalues of the linear part of Eq. (4.4.41), i.e. the part without the material components, that can be done analytically. Once one has these eigenvalues, which are the ones corresponding to the perturbations of the electric fields, one adds the material part of Eq. (4.4.41) multiplied by an homotopy parameter ρ. For $\rho = 0$ one reobtains the version of Eq. (4.4.41) without the material components, and for $\rho = 1$ one has the complete system. Finally, one follows the eigenvalues obtained analytically via a Newton-Raphson root finder by iterating in ρ using as initial guess the previous value of λ in each ρ step, until $\rho = 1$.

Going into the details, Eqs. (4.4.41) for the perturbations of the different field components and their complex conjugates can be written as

$$\frac{\partial \widetilde{a}_+}{\partial s} = (i\widetilde{\omega} - \lambda - \alpha_{int})\ \widetilde{a}_+ + \widetilde{b}_+ \ , \tag{B.4.14}$$

$$\frac{\partial \widetilde{a}_-}{\partial s} = -(i\widetilde{\omega} - \lambda - \alpha_{int})\ \widetilde{a}_- - \widetilde{b}_- \ , \tag{B.4.15}$$

$$\frac{\partial \widetilde{a}^*_+}{\partial s} = (-i\widetilde{\omega} - \lambda - \alpha_{int})\ \widetilde{a}^*_+ + \widetilde{b}^*_+ \ , \tag{B.4.16}$$

$$\frac{\partial \widetilde{a}^*_-}{\partial s} = (i\widetilde{\omega} + \lambda + \alpha_{int})\ \widetilde{a}^*_- - \widetilde{b}^*_- \ , \tag{B.4.17}$$

Where the perturbations of the polarizations $\widetilde{b}_\pm$, can be written in general as

$$\widetilde{b}_\pm = f_\pm\ \widetilde{a}_+ + g_\pm\ \widetilde{a}_- + h_\pm\ \widetilde{a}^*_+ + i_\pm\ \widetilde{a}^*_- \ , \tag{B.4.18}$$

$$\widetilde{b}^*_\pm = j_\pm\ \widetilde{a}_+ + k_\pm\ \widetilde{a}_- + l_\pm\ \widetilde{a}^*_+ + m_\pm\ \widetilde{a}^*_- \ . \tag{B.4.19}$$

To obtain the expressions for $f_\pm$, $g_\pm$, etc... — which in fact depend on the space, the frequency of the monochromatic solution and the eigenvalues, i.e. $f_\pm = f_\pm(z, \omega, \lambda)$ — one solves the system (4.4.59) for every j point in the space. Solving this system one finds expressions for $\widetilde{b}_+$ and $\widetilde{b}_-$ depending on the steady states variables and the perturbations $\widetilde{a}_+$ and $\widetilde{a}_-$ for every point in the space.

One can write Eqs. (B.4.14)-(B.4.17) for the perturbations of the fields in a vector form

$$\vec{v}(s) = \begin{pmatrix} \widetilde{a}_+(s) \\ \widetilde{a}_-(s) \\ \widetilde{a}^*_+(s) \\ \widetilde{a}^*_-(s) \end{pmatrix} \ , \tag{B.4.20}$$

and their spatial evolution is given by

$$\frac{\partial \vec{v}(s)}{\partial s} = \mathbf{Q}\ \vec{v}(0) \ , \tag{B.4.21}$$

where

$$\mathbf{Q} = \rho\ \mathbf{F}_2 + \mathbf{F}_1 \ , \tag{B.4.22}$$

where the homotopy parameter ρ is introduced. The matrices $\mathbf{F}_1$ and $\mathbf{F}_2$ have the form

$$\mathbf{F}_1 = \begin{pmatrix} i\omega - \lambda - \alpha_{int} & 0 & 0 & 0 \\ 0 & -i\omega + \lambda + \alpha_{int} & 0 & 0 \\ 0 & 0 & -i\omega - \lambda - \alpha_{int} & 0 \\ 0 & 0 & 0 & i\omega + \lambda + \alpha_{int} \end{pmatrix} \ , \tag{B.4.23}$$

and

$$\mathbf{F}_2 = \begin{pmatrix} f_+ & g_+ & h_+ & i_+ \\ -f_- & -g_- & -h_- & -i_- \\ j_+ & k_+ & l_+ & m_+ \\ -j_- & -k_- & -l_- & -m_- \end{pmatrix} . \qquad \text{B.4.24}$$

The problem has to be completed with the boundary conditions

$$\vec{v}(L) = \mathbf{B}\ \vec{v}(0) , \qquad \text{B.4.25}$$

where

$$\mathbf{B} = \begin{pmatrix} \frac{1}{T} & -\frac{R}{T} & 0 & 0 \\ \frac{R}{T} & \frac{T^2-R^2}{T} & 0 & 0 \\ 0 & 0 & \frac{1}{T} & -\frac{R}{T} \\ 0 & 0 & \frac{R}{T} & \frac{T^2-R^2}{T} \end{pmatrix} . \qquad \text{B.4.26}$$

The problem corresponds to $\rho = 1$, however, one can find the analytical solutions for $\rho = 0$,

$$\lambda_m^{\pm}(\rho = 0) = \ln(t \pm r) - \alpha_{int} + i(2\pi m - \omega) , \qquad \text{B.4.27}$$

$$\lambda_m^{\pm}(\rho = 0) = \ln(t \pm r) - \alpha_{int} + i(2\pi m + \omega) . \qquad \text{B.4.28}$$

Noticing that the these four solutions come from the fact that one is using the complex conjugates of our perturbations in $\vec{v}(s)$. The method consist in following the solutions for $\rho = 0$ while increasing ρ. For this one uses a Newton-Raphson algorithm with a guess obtained from the previous value of ρ, and iterating until $\rho = 1$. Numerically the system (B.4.21) can be solved as

$$\vec{v}_{j+1} - \vec{v}_j = \frac{h}{2} \left(\mathbf{Q}_{j+1} \vec{v}_{j+1} + \mathbf{Q}_j \vec{v}_j \right) , \qquad \text{B.4.29}$$

therefore

$$\vec{v}_{j+1} = \left(\mathbf{I} - \frac{h}{2} \mathbf{Q}_{j+1} \right)^{-1} \cdot \left(\mathbf{I} + \frac{h}{2} \mathbf{Q}_j \right) \vec{v}_j , \qquad \text{B.4.30}$$

where $\mathbf{Q}_j$ depends on the homotopy parameter ρ and $\mathbf{F}_2$ depends on the space

$$\mathbf{Q}_j = \rho\ \mathbf{F}_2^j + \mathbf{F}_1 . \qquad \text{B.4.31}$$

Finally, for the last point in the space $j = N$,

$$\vec{v}_N = \left[\prod_{j=N}^{2} \left(\mathbf{I} - \frac{h}{2} \mathbf{Q}_j \right)^{-1} \cdot \left(\mathbf{I} + \frac{h}{2} \mathbf{Q}_{j-1} \right) \right] \vec{v}_0 , \qquad \text{B.4.32}$$

and applying the boundary conditions and taking the determinant, one obtains the equation to solve for the eigenvalues λ depending on ρ,

$$f(\lambda, \rho) = \det \left\{ \mathbf{B} - \prod_{j=N}^{2} \left(\mathbf{I} - \frac{h}{2} \mathbf{Q}_i \right)^{-1} \cdot \left(\mathbf{I} + \frac{h}{2} \mathbf{Q}_{i-1} \right) \right\} = 0 . \qquad \text{B.4.33}$$

Finally, one can improve the method by deflation of the determinant to assure that one does not find the same value or if one finds it is because in some cases the roots will have a multiplicity.

B.4.3 Cauchy's theorem method

To know if a monochromatic solution is stable or unstable one does not need explicitly the values of all the eigenvalues, one just needs to know if there are some of them that have real positive parts. From complex analysis [182], one can use the Cauchy's theorem combined with the residue theorem and the logarithm residues to count the number of zeros in a region of the complex plane, in this case the region with positive real part.

From the previous section one can construct a function $f(\lambda, \rho)$ which in this case includes all the material components, i.e. $\rho = 1$,

$$f(\lambda, 1) = \det \left\{ \mathbf{B} - \prod_{j=N}^{2} \left(\mathbf{I} - \frac{h}{2}\mathbf{Q}_i \right)^{-1} \cdot \left(\mathbf{I} + \frac{h}{2}\mathbf{Q}_{i-1} \right) \right\} . \tag{B.4.34}$$

This function has to be analytical inside and over a closed simple contour C, which is positively orientated. In this case from complex analysis one gets

$$\frac{1}{2\pi i} \oint_C \frac{f'(\lambda, 1)}{f(\lambda, 1)} dz = N_f(C) - P_f(C) , \tag{B.4.35}$$

where C is a closed simple contour, $f'(\lambda, 1)$ denotes the derivative of $f(\lambda, 1)$ respect to λ, $N_f(C)$ is the number of zeros of $f(\lambda)$ inside C and $P_f(C)$ is the number of poles inside C.

One cannot assure that $f(\lambda, 1)$ will not have poles in the complex plane, but as far as we know from the previous methods, we can assure that in the plane with positive real part, one will found only zeros if the monochromatic solutions are unstable. The procedure that we follow is to compute $f(\lambda, 1)$ as in the homotopy method section with $\rho = 1$. Then we compute numerically the derivative respect to λ. To compute (B.4.35) we use a Matlab function to approximate the integral of the function over the contour C using a recursive adaptive Simpson quadrature method [149].

B.4.4 Discussion

Here we focus in the case described in Fig. B.4.5. In this situation we treat a ring laser that shows multistability in various modes. This situation is interesting because one has a large gain bandwidth $\gamma = 100$, therefore the number of points N of our space grid will play a crucial role. First, we will discuss the robustness of these methods against the space discretization. Finally, we will compare between them.

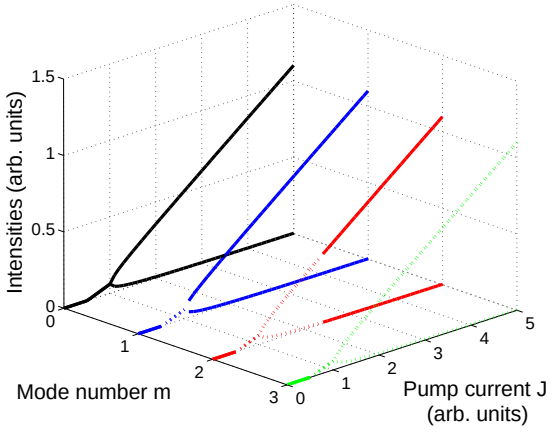

Fig. B.4.5 – Bifurcation diagram for the first modes of a ring laser. $g = 4$, $\gamma = 100$, $\alpha = 2.03$, $\epsilon = 0.2$, $\eta = 10$, $t_+ = t_- = 0.98$ and $r_+ = r_- = 0.01$. The threshold value is $J_{th} = 0.51$. Solid (dashed) lines indicate stable (unstable) monochromatic solution. The stability analysis was performed with the evolution operator method, $N = 512$.

(a) Dependence on space discretization

Fig. B.4.6 shows the results of performing the LSA with the evolution operator method, to the monochromatic solution corresponding to mode $m = 2$ at $J = 2$, for different values of N. It is a unstable solution. One can see the expected effect of the aliasing produced by the discretization for those eigenvalues with $|Im(\lambda)| > 30$ corresponding to modes $m = \pm 5, \pm 6, \pm 7, \ldots$. The effect is notable for $N = 128$, while it is minimum for $N = 256$. The computing time in each case is: approx. 90 s for $N = 128$, approx. 727 s for $N = 256$ and approx. 3000 s for $N = 512$, running on a standard PC.

Fig. B.4.7 shows the results for the same case showed in Fig. B.4.6 but in this case using the homotopy method for 11 modes, $m = -5 \ldots 5$. Being the homotopy parameter step $\Delta\rho = 0.01$. We have choose this value for $\Delta\rho$ in order to not loose the eigenvalues or to end in another branch of eigenvalues, however this will increase the computing time significantly. From the Fig. B.4.7 one can see that the effect of the discretization is bigger using the homotopy method than the evolution operator method, one can see that for $N = 128$ and $N = 256$ six eigenvalues with real positive part are found, while with $N = 512$ four eigenvalues in agreement with the evolution operator method are obtained. Moreover, this effect does not scale with N as expected. For example, the eigenvalues found around zero for $m = \pm 2$, i.e. $\mathrm{Im}(\lambda) = \pm 12$, show a peculiar behavior that can be related to the deflation and to the flat shape of the function $f(\lambda, \rho)$ around their zeros. This effect is minimized when N is bigger, however the computing cost increases drastically. The computing time in each case is: approx. 3000 s for $N = 128$, approx. 5500 s for $N = 256$ and approx. 13000 s for $N = 512$.

Continuing in the same case, table 2.4.1 shows the results depending on N using the Cauchy's theorem method. The integration contour was defined in four lines, from $0.001 - 30i$ to $0.02 - 30i$, from $0.02 - 30i$ to $0.02 + 30i$, from $0.02 + 30i$ to $0.001 + 30i$, and finally, from $0.001 + 30i$ to $0.001 - 30i$. We can see that except for $N = 64$ the rest of the results are right, finding the expected result of four eigenvalues.

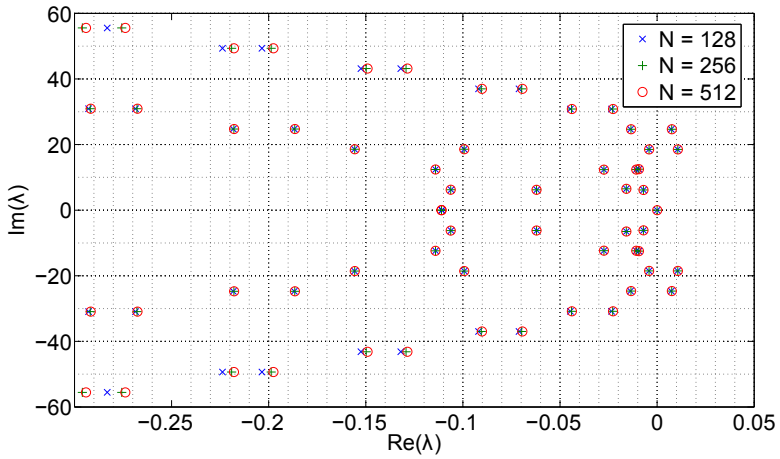

Fig. B.4.6 – Comparison between the results obtained using the evolution operator method with different spatial discretization. This corresponds to an unstable solution, mode $m = 2$ and $J = 2$.

N	Integral value $/2\pi i$	Computing time (s)
64	2.00000020743705 + 0.000000007107681	443
128	4.00000223625788 + 0.000000074022401	757
256	4.00000193269392 + 0.000000055903761	1533
512	4.00000193269392 + 0.000000086662941	2895

Table 2.4.1 – Cauchy's theorem method results for $m = 2$ and $J = 2$.

(b) Comparison between methods

Fig. B.4.8 shows the results from the evolution operator method and the homotopy method, for the LSA of the off solution $m = 0$ at $J = 0.49$, i.e. under threshold.

Fig. B.4.9 shows the results from the evolution operator method and the homotopy method, for the LSA of the off solution $m = 0$ at $J = 0.55$, i.e. above threshold. The eigenvalues found via the homotopy method show in Figs. B.4.8 and B.4.9 show a deviation with respect to the ones found with the evolution operator. This deviation can be a consequence of using deflation.

Fig. B.4.10 shows the comparison between the results obtained with the evolution operator and the homotopy method for a monochromatic solution $m = 2$ and $J = 2$. In fact these correspond to the cases with $N = 512$ in Figs. B.4.6 and B.4.7 respectively. Here the differences are bigger than in the case for the off solution. The modes which are more affected are $m = \pm 1, \pm 2, \pm 3$. Fig. B.4.11 also shows these differences.

Therefore, one can conclude that the evolution operator method is a stable, robust and low consuming method for performing numerically the LSA of the TWM for a two level atom medium. However, it can be very costly in the case of a semiconductor medium, due to the lack of a time-domain relation between the polarization and the field. And alternative can be the Cauchy's theorem method rather than the homotopy method. However in this thesis we have used the evolution operator method to perform the LSA of the TWM for the semiconductor medium using the Padé approximation (see section V.2).

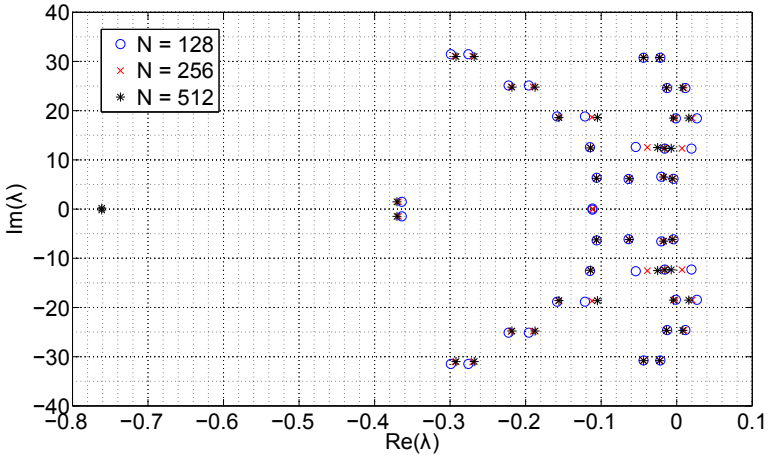

Fig. B.4.7 – Comparison between the results obtained using the homotopy method $\Delta\rho = 0.001$ with different spatial discretization. This corresponds to an unstable solution, mode $m = 2$ and $J = 2$.

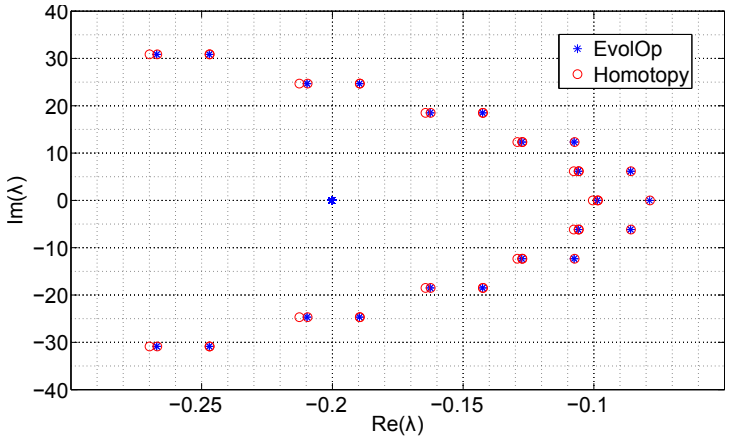

Fig. B.4.8 – Comparison between the results obtained using the evolution operator method and the homotopy method with $\Delta\rho = 0.01$. This corresponds to the off solution which is stable for mode $m = 0$ and $J = 0.49$. $N = 512$.

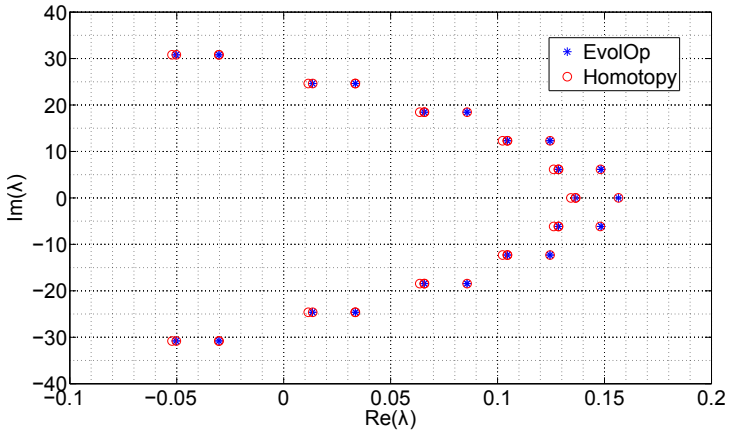

Fig. B.4.9 – Comparison between the results obtained using the evolution operator method and the homotopy method with $\Delta\rho = 0.01$. This corresponds to the off solution which is unstable for mode $m = 0$ and $J = 0.55$. $N = 512$.

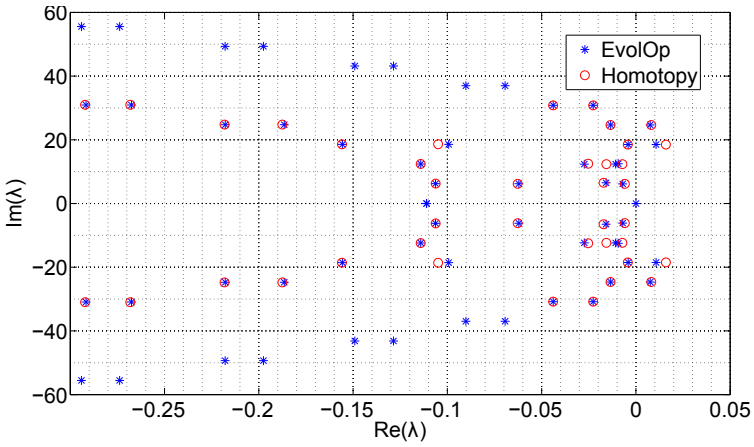

Fig. B.4.10 – Comparison between the results obtained using the evolution operator method and the homotopy method with $\Delta\rho = 0.01$. This corresponds to a lasing solution which is unstable for mode $m = 2$ and $J = 2$. $N = 512$.

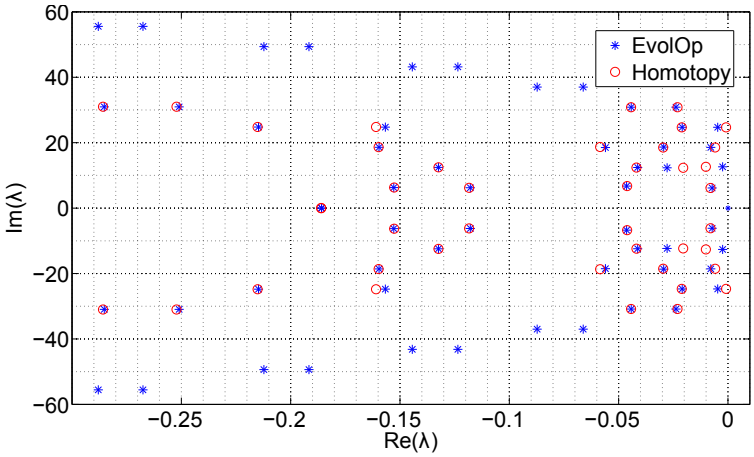

Fig. B.4.11 – Comparison between the results obtained using the evolution operator method and the homotopy method with $\Delta\rho = 0.01$. This corresponds to a lasing solution which is stable for mode $m = 2$ and $J = 3$. $N = 512$.

Bibliography

[1] B. Mukherjee. WDM optical communication networks: progress and challenges. *Selected Areas in Communications, IEEE Journal on*, 18(10):1810 – 1824, Oct 2000.

[2] T. H. Maiman. Stimulated optical radiation in ruby. *Nature*, 187(4736):493–494, 1960.

[3] K. Böhringer and O. Hess. A full-time-domain approach to spatio-temporal dynamics of semiconductor lasers. I. Theoretical formulation. *Progress in Quantum Electronics*, 32(5-6):159 – 246, 2008.

[4] T. L. Koch and U. Koren. Semiconductor lasers for coherent optical fiber communications. *Lightwave Technology, Journal of*, 8(3):274 –293, Mar 1990.

[5] J. Hecht. The bubble legacy. *Physics World*, 23(5):36–40, May 2010.

[6] H. J. R. Dutton. *Understanding Optical Communications*. IBM Corporation, Prentice-Hall, New Jersey, 1998.

[7] H. A. Haus. Mode-locking of lasers. *Selected Topics in Quantum Electronics, IEEE Journal of*, 6(6):1173 –1185, Nov/Dec 2000.

[8] B. K. Garside and T. K. Lim. Laser mode locking using saturable absorbers. *Journal of Applied Physics*, 44(5):2335–2342, 1973.

[9] H. Kogelnik and C. V. Shank. Coupled-wave theory of distributed feedback lasers. *Journal of Applied Physics*, 43(5):2327–2335, 1972.

[10] R. D. Dupuis and P. D. Dapkus. Room-temperature operation of distributed-Bragg-confinement $Ga_{1-x}Al_xAs$-GaAs lasers grown by metalorganic chemical vapor deposition. *Applied Physics Letters*, 33(1):68–69, 1978.

[11] J. L. Jewell, J. P. Harbison, A. Scherer, Y. H. Lee, and L. T. Florez. Vertical-cavity surface-emitting lasers: Design, growth, fabrication, characterization. *Quantum Electronics, IEEE Journal of*, 27(6):1332 –1346, jun 1991.

[12] M. Saruwatari. All-optical signal processing for terabit/second optical transmission. *Selected Topics in Quantum Electronics, IEEE Journal of*, 6(6):1363 –1374, nov/dec 2000.

[13] P. Y. Fonjallaz, H. G. Limberger, and R. P. Salathe. Bragg gratings with efficient and wavelength-selective fiber out-coupling. *Lightwave Technology, Journal of*, 15(2):371 –376, feb 1997.

[14] J. E. Johnson, L. J. P. Ketelsen, D. A. Ackerman, Z. Liming, M. S. Hybertsen, K. G. Glogovsky, C. W. Lentz, W. A. Asous, C. L. Reynolds, J. M. Geary, K. K. Kamath, C. W. Ebert, M. Park, G. J. Przybylek, R. E. Leibenguth, S. L. Broutin, J. W. Stayt Jr., K. F. Dreyer, L. J. Peticolas, R. L. Hartman, and T. L. Koch. Fully stabilized electroabsorption-modulated tunable DBR laser transmitter for long-haul optical communications. *Selected Topics in Quantum Electronics, IEEE Journal of*, 7(2):168 –177, mar/apr 2001.

[15] G. T. Paloczi, Y. Huang, and A. Yariv. Free-standing all-polymer microring resonator optical filter. *Electronics Letters*, 39(23):1650–1651, 2003.

[16] G. Griffel. Synthesis of optical filters using ring resonator arrays. *Photonics Technology Letters, IEEE*, 12(7):810 –812, Jul 2000.

[17] D. G. Rabus, Z. Bian, and A. Shakouri. Ring resonator lasers using passive waveguides and integrated semiconductor optical amplifiers. *Selected Topics in Quantum Electronics, IEEE Journal of*, 13(5):1249 –1256, sept.-oct. 2007.

[18] V. Van, T. A. Ibrahim, P. P. Absil, F. G. Johnson, R. Grover, and P. T. Ho. Optical signal processing using nonlinear semiconductor microring resonators. *Selected Topics in Quantum Electronics, IEEE Journal of*, 8(3):705 –713, may/jun 2002.

[19] M. Mancinelli, R. Guider, P. Bettotti, M. Masi, M. R. Vanacharla, and L. Pavesi. Coupled-resonator-induced-transparency concept for wavelength routing applications. *Opt. Express*, 19(13):12227–12240, Jun 2011.

[20] J. S. Levy, M. A. Foster, A. L. Gaeta, and M. Lipson. Harmonic generation in silicon nitride ring resonators. *Opt. Express*, 19(12):11415–11421, Jun 2011.

[21] R. Soref. The past, present, and future of silicon photonics. *Selected Topics in Quantum Electronics, IEEE Journal of*, 12(6):1678 –1687, nov.-dec. 2006.

[22] A. Argyris, S. Deligiannidis, E. Pikasis, A. Bogris, and D. Syvridis. Implementation of 140 Gb/s true random bit generator based on a chaotic photonic integrated circuit. *Opt. Express*, 18(18):18763–18768, Aug 2010.

[23] M. Bougioukos, Ch. Kouloumentas, M. Spyropoulou, G. Giannoulis, D. Kalavrouziotis, A. Maziotis, P. Bakopoulos, R. Harmon, D. Rogers, J. Harrison, A. Poustie, G. Maxwell, and H. Avramopoulos. Multi-format all-optical processing based on a large-scale, hybridly integrated photonic circuit. *Opt. Express*, 19(12):11479–11489, Jun 2011.

[24] C. Xiong, W. Pernice, K. K. Ryu, C. Schuck, K. Y. Fong, T. Palacios, and H. X. Tang. Integrated GaN photonic circuits on silicon (100) for second harmonic generation. *Opt. Express*, 19(11):10462–10470, May 2011.

[25] A. Szöke, V. Daneu, J. Goldhar, and N. A. Kurnit. Bistable optical element and its applications. *Applied Physics Letters*, 15(11):376–379, 1969.

[26] M. Okada and K. Nishio. Bistability and optical switching in a polarization-bistable laser diode. *Quantum Electronics, IEEE Journal of*, 32(10):1767 –1776, oct 1996.

[27] J. Sakaguchi, T. Katayama, and H. Kawaguchi. High switching-speed operation of optical memory based on polarization bistable vertical-cavity surface-emitting laser. *Quantum Electronics, IEEE Journal of*, 46(11):1526 –1534, nov. 2010.

[28] C. H. Rowe, U. K. Schreiber, S. J. Cooper, B. T. King, M. Poulton, and G. E. Stedman. Design and operation of a very large ring laser gyroscope. *Appl. Opt.*, 38(12):2516–2523, 1999.

[29] R. B. Hurst, G. E. Stedman, K. U. Schreiber, R. J. Thirkettle, R. D. Graham, N. Rabeendran, and J. P. R. Wells. Experiments with an 834 m^2 ring laser interferometer. *Journal of Applied Physics*, 105(11):113115, 2009.

[30] W. E. Lamb. Theory of an optical maser. *Phys. Rev.*, 134(6A):A1429–A1450, Jun 1964.

[31] L. N. Menegozzi and W. E. Lamb. Theory of a ring laser. *Phys. Rev. A*, 8(4):2103–2125, Oct 1973.

[32] M. Choi, T. Tanaka, S. Sunada, and T. Harayama. Linewidth properties of active-passive coupled monolithic InGaAs semiconductor ring lasers. *Applied Physics Letters*, 94(23):231110, 2009.

[33] H. Yanagi, R. Takeaki, S. Tomita, A. Ishizumi, F. Sasaki, K. Yamashita, and K. Oe. Dye-doped polymer microring laser coupled with stimulated resonant raman scattering. *Applied Physics Letters*, 95(3):033306, 2009.

[34] W. M. Macek and D. T. M. Davis Jr. Rotation rate sensing with traveling-wave ring lasers. *Applied Physics Letters*, 2(3):67–68, 1963.

[35] W. W. Chow, J. Gea-Banacloche, L. M. Pedrotti, V. E. Sanders, W. Schleich, and M. O. Scully. The ring laser gyro. *Rev. Mod. Phys.*, 57(1):61, Jan 1985.

[36] L. M. Narducci, J. R. Tredicce, L. A. Lugiato, N. B. Abraham, and D. K. Bandy. Mode-mode competition and unstable behavior in a homogeneously broadened ring laser. *Phys. Rev. A*, 33(3):1842–1854, Mar 1986.

[37] F. Aronowitz. Loss lock-in in the ring laser. *Journal of Applied Physics*, 41(6):2453–2456, 1970.

[38] F. Zarinetchi and S. Ezekiel. Observation of lock-in behavior in a passive resonator gyroscope. *Opt. Lett.*, 11(6):401–403, 1986.

[39] H. Haus, H. Statz, and I. Smith. Frequency locking of modes in a ring laser. *Quantum Electronics, IEEE Journal of*, 21(1):78 – 85, jan 1985.

[40] L. S. Kornienko, N. S. Kravtsov, and A. N. Shelaev. Optical bistability and hysteresis in a solid-state ring laser. *Proceedings of the society of photo-optical instrumentation engineers*, 473:215–218, 1984.

[41] K. Petermann. *Laser Diode Modulation and Noise*. Kluwer Academic Publishers, Norwell, MA, 1988.

[42] S. Schwartz, G. Feugnet, P. Bouyer, E. Lariontsev, A. Aspect, and J. P. Pocholle. Mode-coupling control in resonant devices: Application to solid-state ring lasers. *Phys. Rev. Lett.*, 97(9):093902, Aug 2006.

[43] M. Sargent. Theory of a multimode quasiequilibrium semiconductor laser. *Phys. Rev. A*, 48(1):717–726, Jul 1993.

[44] T. J. Kane and R. L. Byer. Monolithic, unidirectional single-mode Nd:YAG ring laser. *Opt. Lett.*, 10(2):65–67, 1985.

[45] N. V. Kravtsov, E. G. Lariontsev, and A. N. Shelaev. Oscillation regimes of ring solid-state lasers and possibilities for their stabilization. *Laser Physics*, 3(1):21–62, 1993.

[46] H. Haken. Analogy between higher instabilities in fluids and lasers. *Physics Letters A*, 53(1):77 – 78, 1975.

[47] H. Risken and K. Nummedal. Self-pulsing in lasers. *Journal of Applied Physics*, 39(10):4662–4672, 1968.

[48] E. M. Pessina, G. Bonfrate, F. Fontana, and L. A. Lugiato. Experimental observation of the Risken-Nummedal-Graham-Haken multimode laser instability. *Phys. Rev. A*, 56(5):4086–4093, Nov 1997.

[49] K. Tamura, J. Jacobson, E. P. Ippen, H. A. Haus, and J. G. Fujimoto. Unidirectional ring resonators for self-starting passively mode-locked lasers. *Opt. Lett.*, 18(3):220–222, 1993.

[50] K. Tamura, E. P. Ippen, H. A. Haus, and L. E. Nelson. 77-fs pulse generation from a stretched-pulse mode-locked all-fiber ring laser. *Opt. Lett.*, 18(13):1080–1082, 1993.

[51] P. B. Hansen, G. Raybon, M.-D. Chien, U. Koren, B. I. Miller, M.G. Young, J.-M. Verdiell, and C. A. Burrus. A 1.54-μm monolithic semiconductor ring laser: CW and mode-locked operation. *Photonics Technology Letters, IEEE*, 4(5):411 –413, May 1992.

[52] L. A. Lugiato, L. M. Narducci, and M. F. Squicciarini. Exact linear stability analysis of the plane-wave maxwell-bloch equations for a ring laser. *Phys. Rev. A*, 34(4):3101–3108, Oct 1986.

[53] L. A. Lugiato, F. Prati, D. K. Bandy, L. M. Narducci, P. Ru, and J. R. Tredicce. Low threshold instabilities in unidirectional ring lasers. *Optics Communications*, 64(2):167–171, OCT 15 1987.

[54] H. Zeghlache, P. Mandel, N. B. Abraham, L. M. Hoffer, G. L. Lippi, and T. Mello. Bidirectional ring laser: Stability analysis and time-dependent solutions. *Phys. Rev. A*, 37(2):470–497, Jan 1988.

[55] R. J. C. Spreeuw, R. Centeno Neelen, N. J. van Druten, E. R. Eliel, and J. P. Woerdman. Mode coupling in a he-ne ring laser with backscattering. *Phys. Rev. A*, 42(7):4315–4324, Oct 1990.

[56] S. Zhu. Saturation effects in a two-mode ring laser. *Phys. Rev. A*, 50(2):1710–1715, Aug 1994.

[57] B. McNamara, K. Wiesenfeld, and R. Roy. Observation of stochastic resonance in a ring laser. *Phys. Rev. Lett.*, 60(25):2626–2629, Jun 1988.

[58] G. Vemuri and R. Roy. Stochastic resonance in a bistable ring laser. *Phys. Rev. A*, 39(9):4668–4674, May 1989.

[59] I. I. Zolotoverkh, N. V. Kravtsov, E. G. Lariontsev, and S. N. Chekina. Stochastic effects during the action of the pump noise on bistable self-modulation oscillations in a solid-state ring laser. *Quantum Electronics*, 39(6):515–520, JUN 2009.

[60] I. I. Zolotoverkh, N. V. Kravtsov, E. G. Lariontsev, and S. N. Chekina. Nonlinear stochastic effects during the action of noise on relaxation oscillations in a ring solid-state laser. *Quantum Electronics*, 39(1):53–58, JAN 2009.

[61] W. T. Silfvast. *Laser Fundamentals*. Cambridge University Press, Cambridge, 1996.

[62] S. V. Zhukovsky, D. N. Chigrin, and J. Kroha. Bistability and mode interaction in microlasers. *Phys. Rev. A*, 79(3):033803, Mar 2009.

[63] S. L. McCall, A. F. J. Levi, R. E. Slusher, S. J. Pearton, and R. A. Logan. Whispering-gallery mode microdisk lasers. *Applied Physics Letters*, 60(3):289–291, 1992.

[64] V. M. Apalkov and M. E. Raikh. Directional emission from a microdisk resonator with a linear defect. *Phys. Rev. B*, 70(19):195317, Nov 2004.

[65] S. Koseki, B. Zhang, K. De Greve, and Y. Yamamoto. Monolithic integration of quantum dot containing microdisk microcavities coupled to air-suspended waveguides. *Applied Physics Letters*, 94(5):051110, 2009.

[66] M. Sorel, P. J. R. Laybourn, A. Scirè, S. Balle, G. Giuliani, R. Miglierina, and S. Donati. Alternate oscillations in semiconductor ring lasers. *Opt. Lett.*, 27(22):1992–1994, 2002.

[67] M. Sorel, P. J. R. Laybourn, G. Giuliani, and S. Donati. Unidirectional bistability in semiconductor waveguide ring lasers. *Applied Physics Letters*, 80(17):3051–3053, Apr 2002.

[68] J. P. Hohimer, G. A. Vawter, and D. C. Craft. Unidirectional operation in a semiconductor ring diode laser. *Applied Physics Letters*, 62(11):1185–1187, Mar 1993.

[69] H. Nakatsuka, S. Asaka, H. Itoh, K. Ikeda, and M. Matsuoka. Observation of bifurcation to chaos in an all-optical bistable system. *Phys. Rev. Lett.*, 50(2):109–112, Jan 1983.

[70] M. T. Hill, H. J. S. Dorren, T. de Vries, X. J. M. Leijtens, J. H. den Besten, B. Smalbrugge, Y. S. Oei, H. Binsma, G. D. Khoe, and M. K. Smit. A fast low-power optical memory based on coupled micro-ring lasers. *Nature*, 432(7014):206–209, Nov 2004.

[71] S. Donati. *Electro-optical Instrumentation*. Prentice Hall, New Jersey, 2004.

[72] D. Botez, L. Figueroa, and S. Wang. Optically pumped GaAs-$Ga_{1-x}Al_xAs$ half-ring laser fabricated by liquid-phase epitaxy over chemically etched channels. *Applied Physics Letters*, 29(8):502–504, 1976.

[73] A. S. Liao and S. Wang. Semiconductor injection lasers with a circular resonator. *Applied Physics Letters*, 36(10):801–803, May 1980.

[74] J. Jahns, Q. Cao, and S. Sinzinger. Micro- and nanooptics - an overview. *Laser & Photonics Reviews*, 2(4):249–263, Aug 2008.

[75] T. Krauss, P. J. R. Laybourn, and J. Roberts. CW operation of semiconductor ring lasers. *Electronics Letters*, 26(25):2095–2097, Dec. 1990.

[76] A. Behfar-Rad, J. M. Ballantyne, and S. S. Wong. Etched-facet AlGaAs triangular-shaped ring lasers with output coupling. *Applied Physics Letters*, 59(12):1395–1397, Sep 1991.

[77] S. Oku, M. Okayasu, and M. Ikeda. Low-threshold CW operation of square-shaped semiconductor ring lasers (orbiter lasers). *Photonics Technology Letters, IEEE*, 3(7):588 –590, july 1991.

[78] T. F. Krauss, R. M. De La Rue, and P. J. R. Laybourn. Impact of output coupler configuration on operating characteristics of semiconductor ring lasers. *Lightwave Technology, Journal of*, 13(7):1500–1507, Jul 1995.

[79] H. Han, D. V. Forbes, and J. J. Coleman. InGaAs-AlGaAs-GaAs strained-layer quantum-well heterostructure square ring lasers. *Quantum Electronics, IEEE Journal of*, 31(11):1994–1997, Nov 1995.

[80] C. Ji, M. H. Leary, and J. M. Ballantyne. Long-wavelength triangular ring laser. *Photonics Technology Letters, IEEE*, 9(11):1469–1471, Nov. 1997.

[81] G. Griffel, J. H. Abeles, R. J. Menna, A. M. Braun, J.C. Connolly, and M. King. Low-threshold InGaAsP ring lasers fabricated using bi-level dry etching. *Photonics Technology Letters, IEEE*, 12(2):146 –148, Feb 2000.

[82] L. Bach, J. P. Reithmaier, A. Forchel, J. L. Gentner, and L. Goldstein. Wavelength stabilized single-mode lasers by coupled micro-square resonators. *Photonics Technology Letters, IEEE*, 15(3):377 –379, March 2003.

[83] H. Cao, H. Ling, C. Liu, H. Deng, M. Benavidez, V. A. Smagley, R. B. Caldwell, G.M. Peake, G.A. Smolyakov, P.G. Eliseev, and M. Osinski. Large s-section-ring-cavity diode lasers: directional switching, electrical diagnostics, and mode beating spectra. *Photonics Technology Letters, IEEE*, 17(2):282 –284, Feb. 2005.

[84] Z. Wang, G. Verschaffelt, Y. Shu, G. Mezosi, M. Sorel, J. Danckaert, and S. Yu. Integrated small-sized semiconductor ring laser with novel retro-reflector cavity. *Photonics Technology Letters, IEEE*, 20(2):99 –101, jan.15 2008.

[85] Z. Wang, G. Yuan, and S. Yu. Directional bistability in novel semiconductor ring lasers with retro-reflector microcavity. *Photonics Technology Letters, IEEE*, 20(12):1048 –1050, june15 2008.

[86] Z. Wang, G. Yuan, G. Verschaffelt, J. Danckaert, and S. Yu. Injection locking and switching operations of a novel retro-reflector-cavity-based semiconductor micro-ring laser. *Photonics Technology Letters, IEEE*, 20(20):1673 –1675, oct.15 2008.

[87] Z. Wang, G. Yuan, G. Verschaffelt, J. Danckaert, and S. Yu. Storing 2 bits of information in a novel single semiconductor microring laser memory cell. *Photonics Technology Letters, IEEE*, 20(14):1228 –1230, july15 2008.

[88] G. Mezosi, M.J. Strain, S. Furst, Z. Wang, S. Yu, and M. Sorel. Unidirectional Bistability in AlGaInAs Microring and Microdisk Semiconductor Lasers. *Photonics Technology Letters, IEEE*, 21(2):88 –90, jan.15 2009.

[89] K. Thakulsukanant, B. Li, T. Memon, G. Mezosi, Z. Wang, M. Sorel, and S. Yu. All-optical label swapping using bistable semiconductor ring laser in an optical switching node. *Lightwave Technology, Journal of*, 27(6):631 –638, march15 2009.

[90] B. Li, M.I. Memon, G. Mezosi, G. Yuan, Z. Wang, M. Sorel, and S. Yu. All-optical response of semiconductor ring laser to dual-optical injections. *Photonics Technology Letters, IEEE*, 20(10):770 –772, may15 2008.

[91] B. Li, D. Lu, M.I. Memon, G. Mezosi, Z. Wang, M. Sorel, and S. Yu. All-optical digital logic and and xor gates using four-wave-mixing in monolithically integrated semiconductor ring lasers. *Electronics Letters*, 45(13):698 –700, 18 2009.

[92] S. Furst and M. Sorel. Cavity-enhanced four-wave mixing in semiconductor ring lasers. *Photonics Technology Letters, IEEE*, 20(5):366 –368, march1 2008.

[93] Y. Barbarin, E. A. J. M. Bente, M. J. R. Heck, Y. S. Oei, R. Nötzel, and M. K. Smit. Characterization of a 15 GHz integrated bulk InGaAsP passively modelocked ring laser at 1.53μm. *Opt. Express*, 14(21):9716–9727, Oct 2006.

[94] C.-F. Lin and P.-C. Ku. Analysis of stability in two-mode laser systems. *Quantum Electronics, IEEE Journal of*, 32(8):1377 –1382, Aug 1996.

[95] T. Numai. Analysis of signal voltage in a semiconductor ring laser gyro. *Quantum Electronics, IEEE Journal of*, 36(10):1161 –1167, Oct 2000.

[96] M. Sorel, G. Giuliani, A. Scire, R. Miglierina, S. Donati, and P. J. R. Laybourn. Operating regimes of GaAs-AlGaAs semiconductor ring lasers: experiment and model. *Quantum Electronics, IEEE Journal of*, 39(10):1187–1195, Oct. 2003.

[97] M. Sorel C. Born and S. Yu. Linear and nonlinear mode interactions in a semiconductor ring laser. *Quantum Electronics, IEEE Journal of*, 41(3):261 – 271, March 2005.

[98] T. Perez, A. Scirè, G. Van der Sande, P. Colet, and C. R. Mirasso. Bistability and all-optical switching in semiconductor ring lasers. *Optics Express*, 15(20):12941–12948, Oct 1 2007.

[99] G. Yuan and S. Yu. Bistability and switching properties of semiconductor ring lasers with external optical injection. *Quantum Electronics, IEEE Journal of*, 44(1):41 –48, jan. 2008.

[100] G. Yuan, Z. Wang, and S. Yu. Dynamic switching response of semiconductor ring lasers to nrz and rz injection signals. *Photonics Technology Letters, IEEE*, 20(10):785 –787, may15 2008.

[101] J. Javaloyes and S. Balle. Emission directionality of semiconductor ring lasers: A traveling-wave description. *Quantum Electronics, IEEE Journal of*, 45(5):431 –438, May 2009.

[102] H. Haken. *Laser Light Dynamics*, volume 2. North-Holland Physics Publishing, Amsterdam, 1985.

[103] M. Homar, S. Balle, and M. San Miguel. Mode competition in a Fabry-Perot semiconductor laser: Travelling wave model with asymmetric dynamical gain. *Optics Communications*, 131(4-6):380–390, Nov 1 1996.

[104] M. Rossetti, P. Bardella, and I. Montrosset. Time-domain travelling-wave model for quantum dot passively mode-locked lasers. *Quantum Electronics, IEEE Journal of*, 47(2):139 –150, feb. 2011.

[105] J. R. Tredicce, F. T. Arecchi, G. L. Lippi, and G. P. Puccioni. Instabilities in lasers with an injected signal. *J. Opt. Soc. Am. B*, 2(1):173–183, 1985.

[106] A. Einstein. Quantum theory of radiation. *Physikalische Zeitschrift*, 18:121–128, 1917.

[107] J. C. Maxwell. *A Treatise on Electricity and Magnetism*, volume 2. Claredon Press, Oxford, 1873.

[108] H. Romer. *Theoretical Optics, An Introduction.* Wiley-VCH Verlag GmbH & Co. KGaA, Weinheim, 2005.

[109] N. W. Ashcroft and N. D. Mermin. *Solid State Physics.* Harcourt College Publishers, Fort Worth, 1973.

[110] J.J. Sakurai and S.F. Tuan. *Modern quantum mechanics.* Addison-Wesley Pub. Co., Massachussetts, 1994.

[111] S. Balle. Simple analytical approximations for the gain and refractive index spectra in quantum-well lasers. *Phys. Rev. A*, 57(2):1304–1312, Feb 1998.

[112] K. J. Vahala. Optical microcavities. *Nature*, 424:839–846, 2003.

[113] W. W. Chow and S. W. Koch. *Semiconductor-Laser Fundamentals.* Springer-Verlag, Berlin, Heidelberg, New York, 1999.

[114] M. Osinski and J. Buus. Linewidth broadening factor in semiconductor lasers–an overview. *Quantum Electronics, IEEE Journal of*, 23(1):9 – 29, jan 1987.

[115] C. Henry. Theory of the linewidth of semiconductor lasers. *Quantum Electronics, IEEE Journal of*, 18(2):259 – 264, Feb 1982.

[116] A. Villafranca, G. Giuliani, and I. Garces. Mode-Resolved Measurements of the Linewidth Enhancement Factor of a Fabry Pérot Laser. *Photonics Technology Letters, IEEE*, 21(17):1256 –1258, sep. 2009.

[117] W. S. C. Chang. *Principles of Lasers and Optics.* Cambridge University Press, Cambridge, 2005.

[118] H. P. Zappe. *Introduction to Semiconductor Integrated Optics.* Artech House, Boston, London, 1995.

[119] T.D. Visser, H. Blok, B. Demeulenaere, and D. Lenstra. Confinement factors and gain in optical amplifiers. *Quantum Electronics, IEEE Journal of*, 33(10):1763 –1766, oct 1997.

[120] J. Javaloyes and S. Balle. Quasiequilibrium time-domain susceptibility of semiconductor quantum wells. *Phys. Rev. A*, 81(6):062505, Jun 2010.

[121] A. E. Siegman. *Lasers.* University Science Books, Mill Valley, California, 1986.

[122] S. Haroche and F. Hartmann. Theory of saturated-absorption line shapes. *Phys. Rev. A*, 6(4):1280–1300, Oct 1972.

[123] M. Homar, J. V. Moloney, and M. San Miguel. Travelling wave model of a multimode fabry-perot laser in free running and external cavity configurations. *Quantum Electronics, IEEE Journal of*, 32(3):553 –566, Mar 1996.

[124] J. Ohtsubo. *Semiconductor Lasers. Stability, Insability and Chaos.* Springer-Verlag Berlin Heidelberg, 2005.

[125] C.O. Weiss and R. Vilaseca. *Dynamics of Lasers*. VCH, Weinheim, 1991.

[126] G. L. Oppo and A. Politi. Improved adiabatic elimination in laser equations. *EPL (Europhysics Letters)*, 1(11):549, 1986.

[127] E. N. Lorenz. Deterministic nonperiodic flow. *Journal of the Atmospheric Sciences*, 20(2):130–141, 1963.

[128] G. H. M. van Tartwijk and G. P. Agrawal. Laser instabilities: a modern perspective. *Progress in Quantum Electronics*, 22(2):43 – 122, 1998.

[129] S. Fürst, A. Pérez-Serrano, A. Scirè, M. Sorel, and S. Balle. Modal structure, directional and wavelength jumps of integrated semiconductor ring lasers: Experiment and theory. *Applied Physics Letters*, 93(25):251109, 2008.

[130] C. Etrich, Paul Mandel, R. Centeno Neelen, R. J. C. Spreeuw, and J. P. Woerdman. Dynamics of a ring-laser gyroscope with backscattering. *Phys. Rev. A*, 46(1):525–536, Jul 1992.

[131] G. Van der Sande, L. Gelens, P. Tassin, A. Scirè, and J Danckaert. Two-dimensional phase-space analysis and bifurcation study of the dynamical behaviour of a semiconductor ring laser. *Journal of Physics B: Atomic, Molecular and Optical Physics*, 41(9):095402, 2008.

[132] L. Gelens, S. Beri, G. Van der Sande, J. Danckaert, N. Calabretta, H. J. S Dorren, R. Notzel, E. A. J. M. Bente, and M. K. Smit. Optical injection in semiconductor ring lasers: backfire dynamics. *Optics Express*, 16(15):10968–10974, JUL 21 2008.

[133] K. Taguchi, K. Fukushima, A. Ishitani, and M. Ikeda. Optical inertial rotation sensor using semiconductor ring laser. *Electronics Letters*, 34(18):1775–1776, Sep 1998.

[134] M. Ikeda, K. Taguchi, K. Fukushima, and A. Ishitani. Semiconductor ring laser gyroscopes. In *Lasers and Electro-Optics Europe, 1998. 1998 CLEO/Europe. Conference on*, pages 156–156, Sep 1998.

[135] K. Taguchi, K. Fukushima, A. Ishitani, and M. Ikeda. Experimental investigation of a semiconductor ring laser as an optical gyroscope. *Instrumentation and Measurement, IEEE Transactions on*, 48(6):1314–1318, Dec 1999.

[136] R. Wang, Y. Zheng, and A. Yao. Generalized sagnac effect. *Phys. Rev. Lett.*, 93(14):143901, Sep 2004.

[137] V. Annovazzi-Lodi, S. Donati, and M. Manna. Chaos and locking in a semiconductor laser due to external injection. *Quantum Electronics, IEEE Journal of*, 30(7):1537 –1541, jul. 1994.

[138] A. Pérez-Serrano, R. Zambrini, A. Scirè, and P. Colet. Noise spectra of a semiconductor ring laser in the bidirectional regime. *Phys. Rev. A*, 80(4):043843, Oct 2009.

[139] S. Beri, L. Gelens, M. Mestre, G. Van der Sande, G. Verschaffelt, A. Scirè, G. Mezosi, M. Sorel, and J. Danckaert. Topological insight into the non-arrhenius mode hopping of semiconductor ring lasers. *Phys. Rev. Lett.*, 101(9):093903, Aug 2008.

[140] M. San Miguel and R. Toral. *Stochastic effects in physical systems*. Instabilities and nonequilibrium structures VI. Kluwer Academic Publishers, Norwell, MA, 2000.

[141] H. Haug and S.W. Koch. *Quantum theory of the optical and electronic properties of semiconductors*. World Scientific, Singapore, 2004.

[142] C. Ji, M. F. Booth, A. T. Schremer, and J. M. Ballantyne. Characterizing relative intensity noise in InGaAsP-InP triangular ring lasers. *Quantum Electronics, IEEE Journal of*, 41(7):925–931, July 2005.

[143] N. V. Kravtsov and N. N. Kravtsov. Non-reciprocal effects in spatially inhomogeneous, nonlinear media. *Journal of Russian Laser Research*, 17(5):457–464, Sep-Oct 1996.

[144] C. W. Gardiner. *Handbook of Sthocastic Methods for Physics, Chemistry and the Natural Sciences*. Springer-Verlag, Berlin, 2nd edition, 1990.

[145] R. Toral and A. Chakrabarti. Generation of gaussian distributed random numbers by using a numerical inversion method. *Computer Physics Communications*, 74(3):327–334, Mar 1993.

[146] K. Wiesenfeld. Virtual hopf phenomenon: A new precursor of period-doubling bifurcations. *Phys. Rev. A*, 32(3):1744–1751, Sep 1985.

[147] D. Foster. *Hydrodynamic Fluctuations, Broken Symmetry, and Correlation Fluctuations*. Addison Wesley, Redwood City, Ca, 1983.

[148] P. Mandel and G. P. Agrawal. Mode-instabilities in a homogeneously broadened ring laser. *Optics Communications*, 42(4):269–274, 1982.

[149] W.H. Press. *Numerical recipes: the art of scientific computing*. Cambridge University Press, Cambridge, 2007.

[150] R.J. LeVeque. *Finite difference methods for ordinary and partial differential equations: steady-state and time-dependent problems*. Classics in Applied Mathematics. Society for Industrial and Applied Mathematics, Philadelphia, 2007.

[151] J.W. Eaton. *Gnu Octave Manual*. A GNU manual. Network Theory, 2002.

[152] A. Pérez-Serrano, J. Javaloyes, and S. Balle. Bichromatic emission and multimode dynamics in bidirectional ring lasers. *Phys. Rev. A*, 81(4):043817, Apr 2010.

[153] C. Born, M. Hill, S. Yu, and M. Sorel. Study of longitudinal mode coupling in a semiconductor ring laser. In *2004 IEEE LEOS Annual Meeting Conference Proceedings, Vols 1 and 2*, IEEE Lasers and Electro-Optics Society (LEOS) Annual Meeting, pages 27–28. IEEE Lasers & Electro Opt Soc; IEEE, IEEE, November 2004. 17th Annual Meeting of the IEEE-Lasers-and-Electro-Optics-Society, Rio Grande, PR, Nov 07-11, 2004.

[154] Koen Huybrechts, Bjoern Maes, Geert Morthier, and Roel Baets. Tristable all-optical flip-flop using coupled nonlinear cavities. In *2008 IEEE/LEOS Winter Topical Meeting Series*, pages 16–17, January 2008. IEEE/LEOS Winter Topical Meeting, Sorrento, Italy, Jan 14-16, 2008.

[155] L. A. Kotomtseva and S. G. Rusov. Mechanism of formation of undamped pulsations around several equilibrium states in a laser with a saturable absorber. *Quantum Electronics*, 28(2):155, 1998.

[156] R. Lang and K. Kobayashi. External optical feedback effects on semiconductor injection laser properties. *Quantum Electronics, IEEE Journal of*, 16(3):347 – 355, mar 1980.

[157] A. Loose, B. K. Goswami, H.-J. Wünsche, and F. Henneberger. Tristability of a semiconductor laser due to time-delayed optical feedback. *Phys. Rev. E*, 79(3):036211, Mar 2009.

[158] K. P. Komarov. Multistable single-mode emission from solid-state lasers. *Quantum Electronics*, 24(11):975, 1994.

[159] N. B. Abraham D.K Bandy J. R. Tredicce, L. M. Narducci and L.A. Lugiato. Experimental-evidence of mode competition leading to optical bistability in homogeneously broadened lasers. *Optics Communications*, 56(6):435–439, Jan 15 1986.

[160] M. Yamada. Theory of mode competition noise in semiconductor injection lasers. *Quantum Electronics, IEEE Journal of*, 22(7):1052 – 1059, jul 1986.

[161] F. Pedaci, S. Lepri, S. Balle, G. Giacomelli, M. Giudici, and J. R. Tredicce. Multiplicative noise in the longitudinal mode dynamics of a bulk semiconductor laser. *Phys. Rev. E*, 73(4):041101, Apr 2006.

[162] T. Acsente. Laser diode intensity noise induced by mode hopping. *Romanian Reports in Physics*, 59(1):87–92, 2007.

[163] Y.A.I. Khanin. *Fundamentals of Laser Dynamics*. Cambridge International Science Publishing, 2005.

[164] H. Fu and H. Haken. Multifrequency operations in a short-cavity standing-wave laser. *Phys. Rev. A*, 43(5):2446–2454, Mar 1991.

[165] G. J. de Valcarcel, E. Roldan, and F. Prati. Risken-Nummedal-Graham-Haken instability in class-B lasers. *Optics Communications*, 163(1-3):5–8, May 1999.

[166] R. Graham and H. Haken. Quantum theory of light propagation in a fluctuating laser-active medium. *Zeitschrift fur Physik*, 213(5):42, 1968.

[167] J. A. Fleck. Ultrashort-pulse generation by q-switched lasers. *Phys. Rev. B*, 1(1):84, Jan 1970.

[168] M. F. Booth, A. Schremer, and J. M. Ballantyne. Spatial beam switching and bistability in a diode ring laser. *Applied Physics Letters*, 76(9):1095–1097, 2000.

[169] S. Furst, M. Sorel, A. Scire, G. Giuliani, and S. Yu. Technological challenges for CW operation of small-radius semiconductor ring lasers - art. no. 61840R. In Lenstra, D and Pessa, M and White, IH, editor, *Semiconductor Lasers and Laser Dynamics II*, volume 6184 of *Proceedings of the Society of Photo-optical Instrumentation Engineers (SPIE)*, page R1840, April 2006. Conference on Semiconductor Lasers and Laser Dynamics II, Strasbourg, France, Apr 03-06, 2006.

[170] E. J. D'Angelo, E. Izaguirre, G. B. Mindlin, G. Huyet, L. Gil, and J. R. Tredicce. Spatiotemporal dynamics of lasers in the presence of an imperfect O(2) symmetry. *Phys. Rev. Lett.*, 68(25):3702–3705, Jun 1992.

[171] C. Born, G. Yuan, Z. Wang, M. Sorel, and S. Yu. Lasing mode hysteresis characteristics in semiconductor ring lasers. *Quantum Electronics, IEEE Journal of*, 44(12):1171 –1179, dec. 2008.

[172] A. Uskov, J. Mork, and J. Mark. Wave mixing in semiconductor laser amplifiers due to carrier heating and spectral-hole burning. *Quantum Electronics, IEEE Journal of*, 30(8):1769 –1781, aug 1994.

[173] S. Balle. Analytical description of spectral hole-burning effects in active semiconductors. *Opt. Lett.*, 27(21):1923–1925, 2002.

[174] L. Gelens, S. Beri, G. Van der Sande, G. Mezosi, M. Sorel, J. Danckaert, and G. Verschaffelt. Exploring multistability in semiconductor ring lasers: Theory and experiment. *Phys. Rev. Lett.*, 102(19):193904, May 2009.

[175] S. Furst, S. Yu, and M. Sorel. Fast and Digitally Wavelength-Tunable Semiconductor Ring Laser Using a Monolithically Integrated Distributed Bragg Reflector. *Photonics Technology Letters, IEEE*, 20(23):1926 –1928, Dec 1 2008.

[176] E. Doedel, A. R. Champneys, T. F. Fairgrieve, Y. A. Kuznetsov, B. Sand-stede, and X. Wang. Auto: Software for continuation and bifurcation problems in ordinary differential equations, http://indy.cs.concordia.ca/auto/.

[177] K. Engelborghs, T. Luzyanina, G. Samaey, D. Roose, and K. Verheyden. DDE-bifTool v.2.03: A Matlab package for bifurcation analysis of delay differential equations, http://twr.cs.kuleuven.be/research/software/delay/ddebiftool.shtml.

[178] R.C. Hilborn. *Chaos and nonlinear dynamics: an introduction for scientists and engineers*. Oxford University Press, Oxford, 2000.

[179] S.H. Strogatz. *Nonlinear dynamics and chaos: with applications to physics, biology, chemistry, and engineering*. Studies in nonlinearity. Westview Press, Colorado, 1994.

[180] J. Crank and P. Nicolson. A practical method for numerical evaluation of solutions of partial differential equations of the heat conduction type. *Proc. Phil. Soc.* **43**, *50-67 (1947),* Reprinted version *Advances in Computational Mathematics* **6**, *207-226 (1996).*

[181] J. G. Charney, R. Fjørtoft, and J. von Neumann. Numerical integration of the barotropic vorticity equation. *Tellus*, **2**:237–254, 1950.

[182] J.W. Brown and R.V. Churchill. *Complex variables and applications*. Churchill-Brown series. McGraw-Hill, New York, 1996.

Curriculum Vitae

Personal information

Surname(s) / First name(s)	**Pérez-Serrano , Antonio**
Address(es)	Pare Guillem Vives 9 3D, 07006, Palma de Mallorca (Spain)
Telephone(s)	(Office) +34 971 25 98 82 (Mobile) +34 629 155 309
Email(s)	antonio@ifisc.uib-csic.es
Nationality(-ies)	Spanish
Date of birth	6 October 1978
Gender	Male

Lines of investigation

Laser Physics, Semiconductor Lasers, Non-linear Dynamics, Optoelectronics, Optical Communications

Current position

Since	November 2006
Position	PhD Student / Govern Balear Grant (since October 2009)
Institution	Instituto de Física Interdisciplinar y Sistemas Complejos, IFISC (UIB-CSIC), Campus UIB, E-07122 Palma de Mallorca (Spain).

Academic formation

Date	September 2007
	Master in Physics
Master Thesis Title	Correlations in semiconductor ring laser in the bidirectional regime.
Center	Universitat de les Illes Balears (UIB), Palma de Mallorca (Spain).
Date	September 2006
	Degree in Physics
Center	Universitat de les Illes Balears (UIB), Palma de Mallorca (Spain).

Complementary formation

Date	18-23 May 2008
Short-course	Nanoscale & Ultrafast Photonics (24 hours)
Place	Cost 288 Training School, Cetraro (Italy)
Date	July 2006
Short-course	El clima de la Tierra, del Sistema Solar y de la Galaxia (20 hours)
Place	Universitat de les Illes Balears (UIB), Palma de Mallorca (Spain).
Date	July 2005
Short-course	Vida e Inteligencia en el Universo: Una Perspectiva Multidisciplinar (20 hours)
Place	Universitat de les Illes Balears (UIB), Palma de Mallorca (Spain).
Date	1997-1998
Course	Sound Engineering (300 hours)
Place	Microfusa, Barcelona (Spain).

Participation in research projects

Project	IOLOS (Integrated Optical Logic and Memory using Ultra-fast Micro-ring Bistable Semiconductor Lasers)
Funding	EU 6th FWP IST-2005-2.5.1 Photonic components
Date	2006-2009
Principal investigator	Dr. Alessandro Scirè, IFISC (Spain)
Project	QULMI (Luz cuántica en micro-dispositivos)
Funding	Govern Balear (PROGECIB-5A)
Date	2007-2008
Principal investigator	Dr. Roberta Zambrini, IFISC (Spain)
Project	PhoDeCC
Funding	Ministerio de Educación y Ciencia (TEC2006-10009/MIC)
Date	2007-2008
Principal investigator	Dr. Pere Colet, IFISC (Spain)

Languages

Spanish (native language)
Catalan (very good)
English (good)

Publications

Authors	Colet, P.; Fischer, I.; Mirasso, C.R.; **Pérez-Serrano, A.**; Scirè, A.;
Title	Semiconductor laser dynamics at IFISC
Journal	Optica Pura y Aplicada vol.44 n.3 pp. 519-525
Date	2011
Authors	**Pérez-Serrano, A.**; Javaloyes, J.; Balle, S.;
Title	Longitudinal mode multistability in Ring and Fabry-Pérot lasers: the effect of spatial hole burning
Journal	Optics Express vol.19 n.4 pp. 3284-3289
Date	2011
Authors	**Pérez-Serrano, A.**; Javaloyes, J.; Balle, S.;
Title	Bichromatic emission and multimode dynamics in bidirectional Ring Lasers
Journal	Physical Review A 81, 043817
Date	2010
Authors	Strain, M.; Mezosi, G.; Sorel, M.; **Pérez-Serrano, A.**; Scirè, A.; Balle, S.; Verschaffelt, G.; Danckaert, J.;
Title	Semiconductor Snail Lasers
Journal	Applied Physics Letters 96, 121105
Date	2010
Authors	**Pérez-Serrano, A.**; Zambrini, R.; Scirè, A.; Colet, P.;
Title	Noise Spectra of a Semiconductor Ring Laser in the Bidirectional Regime
Journal	Physical Review A 80, 043843
Date	2009

Authors	**Pérez-Serrano, A.**; Scirè, A.;
Title	Theoretical Analysis of a New Technique for Inertial Rotation Sensing Using a Semiconductor Ring Laser
Journal	IEEE Photonics Technology Letters 21, 917
Date	2009

Authors	Furst, S.; **Pérez-Serrano, A.**; Scirè, A.; Sorel, M.; Balle, S.;
Title	Modal Structure, Directional and Wavelength Jumps of Integrated Semiconductor Ring Lasers: Experiment and Theory
Journal	Applied Physics Letters 93, 251109
Date	2008

Authors	Latorre, M. J.; Furst, S.; Mezosi, G.; Sorel, M.; **Pérez-Serrano, A.**; Scirè, A.; Balle, S.; Giuliani, G.;
Title	Experimental and theoretical analysis of the optical spectra of directionally bistable semiconductor ring lasers
Journal	Proceedings of SPIE 6997, 699725
Date	2008

Authors	**Pérez-Serrano, A.**; Zambrini, R.; Scirè, A.; Colet, P.;
Title	Noise properties of semiconductor ring lasers
Journal	Proceedings of SPIE 6997, 69971Q
Date	2008

Authors	**Pérez-Serrano, A.**; Furst, S.; Javaloyes, J.; Scirè, A.; Balle, S.; Sorel, M.;
Title	Modelling Strategies for semiconductor Ring Lasers
Journal	Proceedings of SPIE 6997, 69971N
Date	2008

Authors	Scirè, A.; **Pérez-Serrano, A.**; Pérez, T.; Van der Sande, G.; Colet, P.; Mirasso, C.R.; Balle, S.;
Title	Bistability and All Optical Switching in Semiconductor Ring Lasers
Journal	Conference proceeding of 9th International Conference on Transparent Optical Networks, 2007. ICTON '07. 10.1109-ICTON.2007.4296129
Date	2007

Stays in internationally recognized centers

Center	Dept. of Electronics and Electrical Engineering, University of Glasgow (UK)
Duration	1 February 2009 - 10 March 2009
Theme	Modeling of semiconductor ring lasers
	Stay collaboration in the framework of the project IOLOS

Conferences

Type	Oral Contribution
Authors	Javaloyes, J.; **Pérez-Serrano, A.**; Balle, S.;
Title	Bifurcation Diagram of Travelling Wave Models
Conference	NUSOD, Rome (Italy)
Organizers	IEEE and Universita' degli studi di Roma
Date	5-8 September 2011

Type	Oral Contribution
Authors	**Pérez-Serrano, A.**; Javaloyes, J.; Balle, S.;
Title	Bichromatic Emission and Coexisting Multimode Dynamics in Ring Lasers
Conference	CLEO Europe - EQEC 2011, Munich (Germany)
Organizers	European Optical Society (EPS), IEEE and OSA
Date	22-26 May 2011

Type	Oral Contribution
Authors	**Pérez-Serrano, A.**; Javaloyes, J.; Balle, S.;
Title	Wavelength Multistability in Ring and Fabry-Pérot Lasers: The Effect of Spatial Hole Burning
Conference	CLEO Europe - EQEC 2011, Munich (Germany)
Organizers	European Optical Society (EPS), IEEE and OSA
Date	22-26 May 2011

Type	Oral Contribution
Authors	**Pérez-Serrano, A.**; Javaloyes, J.; Balle, S.;
Title	Wavelength Multistability in Lasers: The Effect of Spatial Hole Burning
Conference	IONS 9 - Salamanca (Spain)
Organizers	OSAL - OSA
Date	7 - 8 April 2011

Type	Oral Contribution
Authors	**Pérez-Serrano, A.**; Javaloyes, J.; Balle, S.;
Title	Multistability and multimode dynamics in lasers
Conference	Dynamics Days Europe 2010, Bristol (UK)
Organizers	University of Bristol
Date	6-10 September 2010

Type	Oral Contribution
Authors	**Pérez-Serrano, A.**; Scirè, A.; Javaloyes, J.; Balle, S.;
Title	Travelling Wave Model for Ring Lasers
Conference	LPHYS09, Barcelona (Spain)
Organizers	RAS - ICFO
Date	13-17 July 2009

Type	Oral Contribution (invited)
Authors	Strain, M.; Mezosi, G.; **Pérez-Serrano, A.**; Scirè, A.; Balle, S.; Verschaffelt, G.; Danckaert, J.; Sorel, M.;
Title	Semiconductor Snail Lasers
Conference	CLEO Europe - EQEC 2009, Munich (Germany)
Organizers	European Optical Society - IEEE
Date	15-19 June 2009

Type	Oral Contribution
Authors	**Pérez-Serrano, A.**; Furst, S.; Scirè, A.; Javaloyes, J.; Sorel, M.; Balle, S.;
Title	Modal structure of integrated semiconductor ring laser with output waveguides
Conference	CLEO Europe - EQEC 2009, Munich (Germany)
Organizers	European Optical Society - IEEE
Date	15-19 June 2009

Type	Poster Contribution
Authors	**Pérez-Serrano, A.**; Scirè, A. ; Zambrini, R. ; Colet, P.;
Title	Noise spectra of semiconductor ring lasers in the bidirectional regime
Conference	CLEO Europe - EQEC 2009, Munich (Germany)
Organizers	European Optical Society - IEEE
Date	15-19 June 2009

Type	Poster Contribution
Authors	**Pérez-Serrano, A.**; Scirè, A.; Furst, S; Javaloyes, J.; Balle, S.; Sorel, M.;
Title	Modal structure of semiconductor ring lasers
Conference	IEEE International Semiconductor Laser Conference 2008, Sorrento (Italy)
Organizers	IEEE
Date	14-18 September 2008

Type	Poster Contribution
Authors	**Pérez-Serrano, A.**; Scirè, A.; Furst, S.; Javaloyes, J.; Balle, S.; Sorel, M.;
Title	Modal structure of semiconductor ring lasers
Conference	Cost 288 Training School 'Nanoscale & Ultrafast Photonics', Cetraro (Italy)
Organizers	Cost 288
Date	18-23 May 2008

Type	Poster Contribution
Authors	Latorre, M. J.; Furst, S.; Mezosi, G.; Sorel, M.; **Pérez-Serrano, A.**; Scirè, A.; Balle, S.; Giuliani, G.;
Title	Experimental and theoretical analysis of the optical spectra of directionally bistable semiconductor ring lasers
Conference	SPIE Europe 2008, Strasbourg (France)
Organizers	SPIE
Date	7-10 April 2008

Type	Poster Contribution
Authors	**Pérez-Serrano, A.**; Scirè, A.; Furst, S.; Javaloyes, J.; Balle, S.; Sorel, M.;
Title	Modelling strategies of semiconductor ring lasers
Conference	SPIE Europe 2008, Strasbourg (France)
Organizers	SPIE
Date	7-10 April 2008

Type	Poster Contribution
Authors	**Pérez-Serrano, A.**; Scirè, A.; Zambrini, R.; Colet, P.;
Title	Noise properties of semiconductor ring laser
Conference	SPIE Europe 2008, Strasbourg (France)
Organizers	SPIE
Date	7-10 April 2008

Type	Poster Contribution
Authors	**Pérez-Serrano, A.**; Scirè, A.; Zambrini, R.; Colet, P.;
Title	Noise spectra and correlation in semiconductor ring laser in the bidirectional regime
Conference	FisEs 08: XV Congreso de Física Estadística, Salamanca (Spain)
Organizers	Real Sociedad Española de Física
Date	27-29 March 2008

Type	Oral Contribution
Authors	Scirè, A; **Pérez-Serrano, A**; Furst, S; Javaloyes, J; Zambrini, R; Balle, S; Sorel, M;
Title	Semiconductor Ring Laser Modelling
Conference	Nonlinear Dynamics in Semiconductor Lasers Workshop, Berlin (Germany)
Organizers	Weierstrass Institute for Applied Analysis and Stochastics (WIAS)
Date	19-21 October 2007
Type	Oral Contribution
Authors	**Pérez-Serrano, A.**; Scirè, A.; Javaloyes, J.; Balle, S.; Sorel, M.;
Title	Modal properties of a ring laser with imperfections
Conference	European semiconductor laser workshop ESLW 2007, Berlin (Germany)
Organizers	Heinrich Hertz Institute Berlin
Date	14-15 September 2007
Type	Poster Contribution
Authors	**Pérez-Serrano, A.**; Scirè, A.; Zambrini, R.; Colet, P.;
Title	Noise properties of semiconductor ring laser
Conference	Red temática óptica cuántica y no lineal, 2o encuentro general en Salamanca, Salamanca (Spain)
Organizers	Red temática óptica cuántica y no lineal
Date	5-7 September 2007
Type	Oral Contribution
Authors	**Pérez-Serrano, A**; Scirè, A.; Zambrini, R.; Colet, P.;
Title	Noise properties of semiconductor ring laser
Conference	CLEO Europe - EQEC 2007, Munich (Germany)
Organizers	European Optical Society - IEEE
Date	17-22 June 2007

Computer skills

Languages	C++, Fortran, LaTeX 2_ε
	Matlab, Mathematica, Octave
Others	Office, graphics, sound and video manipulating programs

Reviewer

Journals	Optics Express, Optics Letters and Applied Physics Letters

Others

Talk	Multimode Dynamics in Ring Lasers
Institution	Instituto de Física Interdisciplinar y Sistemas Complejos, IFISC (UIB-CSIC), Palma de Mallorca (Spain).
Date	18 November 2009
Student Group	Founder Member 'OSA-IFISC Student Chapter' 18 February 2009
	Secretary (from 18 February 2009 to 1 May 2010)
	President (from 1 May 2010 to 1 May 2011)
Outreach talk	Dinámica de Láseres
	II Modern Optics Days / II Jornadas de óptica moderna IFISC-OSA
Organizers	OSA-IFISC Student Chapter and IFISC
Date	6 July 2010

Outreach talk	Historia del láser y sus principios físicos II Modern Optics Days / II Jornadas de óptica moderna IFISC-OSA
Organizers	OSA-IFISC Student Chapter and IFISC
Date	5 July 2010
Outreach talk	La luz, los láseres y sus aplicaciones tecnológicas IFISC Open Days 2009
Organizers	IFISC and OSA-IFISC Student Chapter
Date	9 to 13 November 2009
Outreach talk	Dinámica de Láseres Modern Optics Days / Jornadas de óptica moderna IFISC-OSA
Organizers	OSA-IFISC Student Chapter and IFISC
Date	6 July 2009